# The Physics of Interdigitated Dielectrometry Sensors and Application as *In-Situ* Oil Oxidation Monitoring

by

## Alex Risos

B.Sc. Physical Technologies, 2011
M.Sc. Optical Engineering and Photonics, 2013

A thesis submitted to the

## Victoria University of Wellington

in fulfilment of the requirements for the degree of

## Doctor of Philosophy in Physics

March, 2018

To my late honourable dad

Alexander Risos

14.11.1944 - 09.05.2017

## Acknowledgements

**Abstract:** Monitoring of hydrocarbon oxidation is of great importance in many industry applications and reliable *in-situ* measurements are a challenge. In literature, it was shown that new versus degraded hydrocarbons show a change in their dielectric properties. In this thesis, the degradation of the oil was investigated by means of two thermal oil degradation experiments and the Fourier transform infrared spectroscopy. In addition, the impact on the dielectric properties were determined using a novel type of a dielectric test cell that is temperature compensated. It was found that ketones, acids and moisture were generated through a thermal oil aging process. These products have been found to change in the dielectric properties of the liquid which are reflected through the complex permittivity. Ketones increased largely the real part of the permittivity and organic acids affected predominantly the imaginary part of the complex permittivity in a non-linear fashion, which could be described using a modified polaron theory model. These measurements served as the base for the development of a novel kind of interdigitated sensor that can measure the dielectric properties such as the relative permittivity and the intrinsic conductivity with high accuracy and precision, without being affected by temperature. This is a crucial step in the development of a suitable in-situ sensor, as it does not need to undergo a complicated temperature curve compensation or calibration using calibration-liquids. The interdigitated sensor, made using cost efficient printed circuit board technology, exhibited an accuracy in measuring the complex permittivity of about 99%. The sensing precision was practically limited by the measurement instrumentation using a developed Faraday shield for the sensor. The sensor was used in an oil degradation experiment to verify the *in-situ* capability. These measurements of the relative permittivity and conductivity yielded values such as a degree of oxidation and acidity number. For the first time, it was possible to measure *in-situ* the complex dielectric properties of liquids at temperatures between 20 °C to 140 °C using interdigitated sensors.

# Table of Contents

# List of important abbreviations, units (non-italic) and variables (italic)

| | |
|---|---|
| IDS | Interdigitated dielectrometry sensor |
| SCM | Schwarz Christoffel Mapping (conformal transformation) |
| FTIR | Fourier-transform infrared spectroscopy |
| A | Electrical current, Ampere |
| kg | Mass, Kilogram |
| m | Meter, length |
| s | Second, time |
| K | Kelvin, temperature |
| mol | Mole, amount of substance |
| S | Siemens [$kg^{-1} \cdot m^{-2} \cdot s^3 \cdot A^2$] |
| F | Farads [$s^4 \cdot A^2 \cdot m^{-2} \cdot kg^{-1}$] |
| V | Volts [$kg \cdot m^2 \cdot s^{-3} \cdot A^{-1}$] |
| C | Coulomb [$A \cdot s$] |
| J | Joule [$C \cdot V$] |
| eV | Electron volts [J] |
| $C$ | Capacitance [F] |
| $E$ | The electric field in [$V \cdot m^{-1}$] |
| $Q$ | Arbitrary surface charge [$C \cdot m$] |
| $q$ | Arbitrary quantized charge [C] |
| $\alpha$ | Polarizability [$C \cdot m^2 \cdot V^{-1}$] |
| $A$ | Area [$m^2$] |
| $c$ | Speed of light [$m \cdot s^{-1}$] |
| $\hbar$ | Planck constant (reduced) [$eV \cdot s$] |
| $W_p$ | Hopping energy [J] |
| $E_a$ | Activation energy [J] |
| $k_b$ | Boltzmann constant [eV] |
| $\lambda$ | Wavelength [m] |
| $\Psi$ | Electric potential field [V] |
| $\omega$ | Angular frequency in [$s^{-1}$] |
| $\sigma$ | Conductivity [$S \cdot m^{-1}$] |
| $\nabla$ | Nabla operator ($\partial/\partial x_1$, ..., $\partial/\partial x_n$) |
| $\Delta$ | Laplace operator $\nabla^2$ |
| $\delta$ | Angle between imaginary and real value |
| $v$ | Wavenumber, e.g. for infra-red spectroscopy in $1/\lambda$ |
| $\mu$ | Electron mobility [$m^2 \cdot V^{-1} \cdot s^{-1}$] |
| $\mu_x$ | Dipole moment with subscript "$x$" [$C \cdot m$] |
| $w, g, h, l$ | Length parameter [m] |
| $\chi$ | Electric susceptibility; $\varepsilon_r$ - 1 |
| $\varepsilon_0$ | Permittivity of free space [$F \cdot m$] |
| $\varepsilon_r$ | Relative permittivity, $\in \mathbb{R}$ |
| $\upsilon$ | Number operator for spectroscopy, natural number $\in \mathbb{N}$ |
| $N_a$ | Avogadro's number |
| $K$ | Elliptical integral first kind |
| $k, c_n$ | Constants |

# 1 Introduction

## 1.1 Background

In a simplified view, we can say that our electrical grid consists of power generators and transformers. These transformers can be differentiated into two classes: a power transformer and a distribution transformer (henceforth "transformer"). The latter, the distribution transformers, for instance are units which transform high voltage electricity down to 220 V or 110 V for the customer. Hence, such transformers are present in many cases. For example, they are used as a pole mounted transformer for street lights, for industry facilities or for a small area of domestic houses. Hence, they have to be cost efficient.

Due to electrical conversion losses, they generate heat which needs to be dissipated. In the case of a distribution transformer, this heat is dissipated through radiators by an insulating liquid. Such a liquid is often mineral oil, such as paraffin.
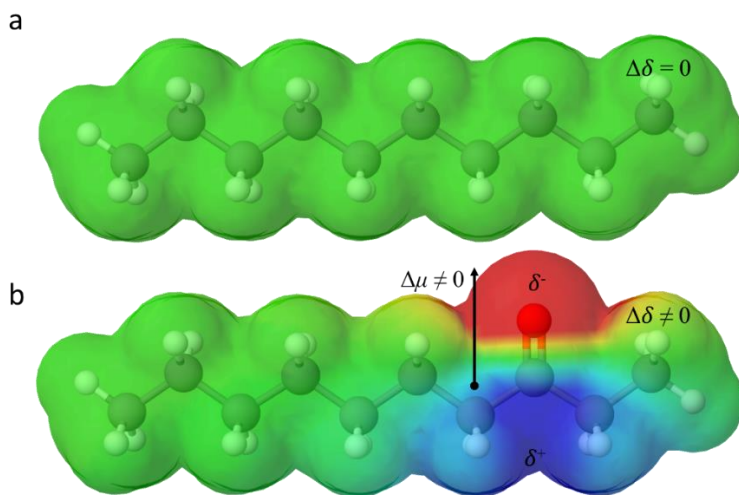


Figure 1.1. The hydrocarbon and its electrostatic potential. An example for an alkane is (a) decane showing its balanced charges (green everywhere). A ketone example is (b) Decanone and its unbalanced electrostatic potential exhibiting a permanent dipole moment (red and blue).

However, hydrocarbons are susceptible to oxidation. Such oxidation is detrimental to their function and can even be present at moderately low

temperatures. This in particular is an issue when used in oil filled transformers [1-3]. For instance, the thermal degradation of the liquid generates ketones, organic acids or water. These components, especially acids, are harmful for the transformer environment (e.g. copper conductors) and decrease the insulating capability (e.g. the DC conductivity), which eventually cause a transformer malfunction. An example for a molecular change of paraffin is shown in Figure 1. Hydrocarbons such as a paraffin (Figure 1.1a) are non-polar. This has special properties such as a very low conductivity, making them suitable for transformers. However, oxidation changes their molecular structure, making them a polar molecule and changing the desired insulating properties, Figure 1.1b.

Thus, such transformers have to be maintained in order to avoid a malfunction. This requires man-power and is effectively not undertaken for all of them as the number of transformers is very large. Transformers for a larger district have a higher priority in contrast to pole mounted ones for street lights, and hence are maintained in regular intervals. A usual way is taking a sample of the oil and carrying it to a laboratory for offline analysis. For example, optical [4, 5] or dielectric and chemical analysis of a sample [1, 6] can give insight in various aging indicators. If this can be measured online *in-situ*, this will be tremendously attractive for engineers and the industry worldwide.

Chemical sensors which are responding to specific molecules can be found in literature [7-11]. The sensing of hydrocarbon degradation products is hence a challenging undertaking as the complexity of generated compounds can be large [12], especially for low thermal oxidation [13]. This implies the use of multiple sensors at the same time. Infra-red spectroscopy is commonly used to investigate hydrocarbons and their degradation products [14], but this approach does not fit well as a robust and long term *in-situ* measuring solution in harsh environments [4]. Using dielectrometry, a measurement of the hydrocarbon liquid and its

degradation products can be done using capacitive probes. A capacitor consists of two electrodes driven by alternating current, of which its impedance is dependent on the employed dielectric, e.g. the hydrocarbon liquid. This dielectric can change its properties when it undergoes a chemical change such as the oxidation. Therefore, if using the hydrocarbon liquid as a dielectric for a capacitive probe, a change in the chemical composition of hydrocarbons (Figure 1.1a to Figure 1.1b) will change the measured capacitance. This change will be due to all oxidation products, eliminating the use for multiple sensors.

A promising advance for this type of sensing was made in the literature using interdigitated dielectrometry sensors (IDS) as capacitive probes [15-21]. A principle design of such a sensor is shown with its distributed electric field across its electrodes in Figure 1.2. Their advantage lays in their cost efficiency, due to a very simple design and material choice. This potentially enables their usage for all distribution transformers. However, such sensors were developed for various purposes and may not be optimised for sensing hydrocarbon oxidation.

Understanding the physics of such sensors using electrostatics was a particular challenge in this thesis for developing an accurate and precise sensor. With the support of infra-red spectroscopy measurements, the dielectric response of oxidation products were identified. This information was used to design and fabricate a suitable interdigitated dielectrometry sensor. This sensor development lead to a positive additional outcome. It was found for the first time that, besides the relative permittivity, the conductivity of the liquid hydrocarbon could also be measured with such sensors. This parameter is shown to be related to the acidity number of the oil.
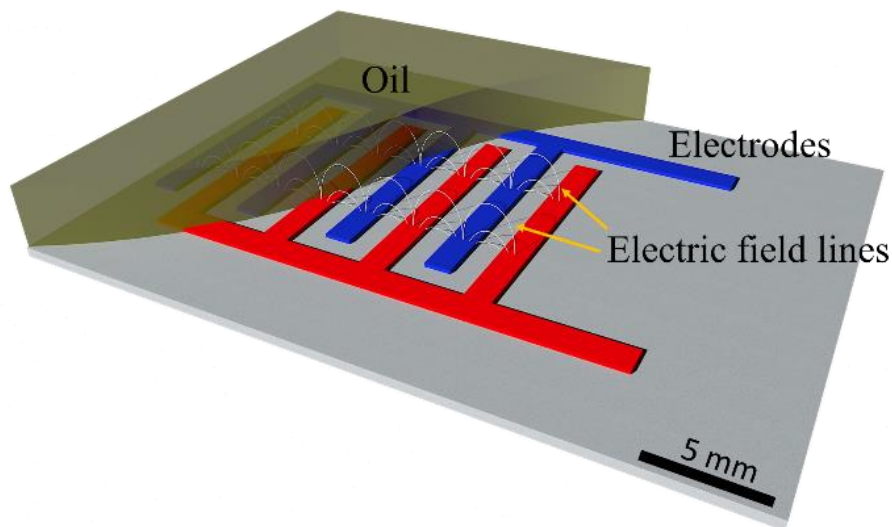
Figure 1.2. A simplified picture of an interdigitated dielectrometry sensor showing its electrodes on a common substrate, color coded (red and blue have different potentials). Those emanate an electric field which is depicted via white lines across the electrodes. With this electric field, they sense a material under test (MUT) such as an insulation liquid, e.g. alkanes or ketones, by penetration.

## 1.2 Thesis structure

The second chapter in this thesis is the literature review and elaborates the hydrocarbon oxidation to a necessary extent in order to understand the measurements. It discusses the decomposition path of hydrocarbons and its measurements with techniques such as Fourier-transformed infra-red spectroscopy (FTIR). The theoretical discussion of the FTIR measurements of hydrocarbons concludes with a brief overview of literature results. A linkage between the FTIR measurements and the relative permittivity of a dielectric is discussed subsequently. It elaborates the possibility to use FTIR measurements as a complementary technique together with dielectric measurements. The background chapter introduces the principle in sensing the hydrocarbon liquid with interdigitated sensors.

The third chapter starts the research in this thesis. It shows dielectric and infra-red measurements of the hydrocarbon liquid. These were necessary to understand the properties of the oil in order to develop a suitable sensor. The

dielectric measurements were conducted with a custom made dielectric test cell in order to yield reference values to characterise the hydrocarbon liquid and its oxidation products. These values were determined during a 600 hour artificially accelerated oxidation experiment of the hydrocarbon liquid via FTIR. The change in the dielectric properties of the liquid during this experiment were measured using the test cell. Identified oxidation products (moisture, ketones and organic acids) and their impact on the dielectric properties were separately investigated to identify the impact on the permittivity. The experimental data could be explained using established mobility models for electronic properties of insulating liquids - the polaron theory.

The fourth chapter focusses on the development of the interdigitated sensor. It starts the development-series for finding an optimised interdigitated dielectrometry sensor for sensing the dielectric changes during the oxidation of hydrocarbon liquids. A total of four design iterations, were necessary in order to find sufficiently high sensor performance. This performance was evaluated in theory using analytical expressions and finite element modelling (FEM) method, as well as in practice though measurements.

The fifth chapter used the IDS3.0 as an *in-situ* probe through a second oxidation experiment having three IDS in this oxidative environment. Such an experiment was not found in past known literature. The acquired data by measuring the liquid with the IDS could be successfully linked to the degree of oxidation through a linear increase in the permittivity. The oil acidity was directly proportional to the measured non-linear increase in the conductivity.

Finally, chapter six summarizes the findings and draws a conclusion of this work. It emphasises the potential impact it can have in the industry using this type of a developed interdigitated sensor.

## 1.3 Contribution

As a major outcome in this thesis, it could be shown that an oxidation of hydrocarbons leads to the formation of several compounds which affect the dielectric properties of the liquid. A suitable sensor could be developed measuring the permittivity and conductivity in an *in-situ* oxidation experiment. The relative permittivity can be used to infer the state of oxidation in various applications such as oil filled transformers or various hydrocarbon processing facilities. The conductivity was found to be related to the acidity concentration. This opens new applications, such as replacing time and cost intensive laboratory measurements for determining the acidity content of such a liquid. Applications which utilize conductive polymers onto such sensors, which are reacting to moisture, nitrites or various gases, can turn this developed sensor into a highly selective sensing apparatus.

## 1.4 Disseminations

From this thesis, the following disseminations have been produced:

1. A. Risos, N. Long, A. Hunze, and G. Gouws, "A 3D Faraday Shield for Interdigitated Dielectrometry Sensors and Its Effect on Capacitance" *MDPI Sensors*, 2017. Reference: [22].

2. A. Risos, N. Long, A. Hunze, and G. Gouws, "Interdigitated Sensors: A Design Principle for Accurately Measuring the Permittivity of Industrial Oils" *IEEE Sensors* Journal, 2017. Reference: [23].

3. A. Risos, N. Long, A. Hunze, and G. Gouws, "MID-IR absorbance and its relation to static permittivity as a robust in-field tool tracking oil deterioration" in *Proc. SPIE Defence & Commercial Sensing*, 2017. Reference: [24].

4. A. Risos, N. Long and G. Gouws, "A Temperature Compensated Dielectric Test Cell for Accurately Measuring the Complex Permittivity of Liquids" in *Review of Scientific Instruments*, 2017. Reference: [25].

5. Accepted for publication: Interdigitated Sensors: The Next Generation "Measuring The Permittivity and Conductivity of Liquids - Unaffected by Temperature" in *IEEE Sensors* Journal.

6. In preparation: "In-Situ Aging Monitoring of Transformer Oil and Paper Using Interdigitated Dielectrometry Sensors" in *Sensors and Actuators B: Chemical.*

7. Talk: "Measuring dielectric properties of liquids" *IEEE IMS Workshop Victoria University Wellington*, New Zealand

8. Poster: "Interdigitated Sensors as Dielectric Probes" *Robinson Research Institute Kyoto Workshop*, New Zealand.

9. Talk: "MID-IR absorbance and its relation to static permittivity as a robust in-field tool tracking oil deterioration" *SPIE Defence & Commercial Sensing*, California, USA.

# 2 Background

This chapter first discusses hydrocarbons and its oxidation. The thermally driven decomposition of the hydrocarbon described is elaborated according to known literature. This includes an infra-red analysis of hydrocarbons and their oxidation products, for which a review is provided to understand the infra-red spectra. This chapter also describes the relationship between the infra-red absorbance and relative permittivity.

The structure of this background chapter is as follows. Section 2.1 describes the hydrocarbon and its properties and section 2.2 elaborates the FTIR technique as applied in the literature (section 2.3), to analyze the hydrocarbon oxidation products. In section 2.4 the dielectric properties of the hydrocarbon liquid is described and section 2.5 introduces the IDS as a potential in-situ measurement system. This is followed by section 2.6, which gives an introduction into literature findings via dielectric measurements of liquid hydrocarbons, and an overview of the IDS developments in literature over the past decades.

## 2.1 The hydrocarbon molecule

The mission of oxidation product analysis and sensing firstly requires a fundamental understanding of the material under test - the paraffinic hydrocarbon - and its behaviour when subject to deterioration - the paraffinic oxidation. This chapter focuses on the necessary understanding of hydrocarbon oxidation when subject to thermal stresses. An example of a hydrocarbon molecule is depicted in Figure 2.1. It shows a linear array of $CH_2$ atoms terminating with methyl ($CH_3$) groups. Such molecules are also referred to as paraffinic molecules as they represent only alkanes ($CH_2$-$CH_2$). These molecules can originate from crude oil, but there are also several other variations of hydrocarbons such alkenes ($CH$=$CH$) or aromatic rings ($C$-$C$). For simplification, the discussions are limited to alkanes.
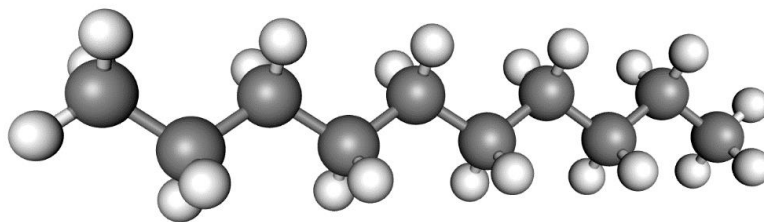
Figure 2.1. 3D illustration of an example alkane (decane) consisting of 10 carbon (dark) and 22 hydrogen (bright) atoms.

### 2.1.1  Oxidation of hydrocarbons

Decane (chemical formula: $C_nH_{2n+2}$, $n = 10$) is used as an example to explain the paraffinic properties, Figure 2.1. Such a symmetric group balances the electric charges and thus an entire alkane molecule is understood to exhibit no total molecule polarity and hence no permanent dipole moment. Consequently, it repels polar water due to its hydrophobic nature, but organic compounds are very much soluble. Paraffin, due to its insulating properties is commonly used as an insulator and coolant fluid in a high voltage environment [1, 3, 26, 27].

The paraffin can be altered under the presence of oxygen. A substitution reaction takes place when the atomic oxygen replaces the hydrogen by forming carbonyls (**H-C-H → C=O**). The pathway of liquid paraffinic oxidation is well described in common literature [12, 13]. Predominant reactions and end products are shown in the schematic pathway in Figure 2.2.

In this figure the standard oxidation pathway of hydrocarbons is shown [12]. A first step of oxidation of the alkane 0.) leads to a peroxide 1.) from which alcohols 2.) can be formed. Carbonyls such as ketones 3.) are present in further decomposing steps which are subject to further oxidation 4.), ultimately resulting in acidic compounds 5.) also consisting of a carbonyl groups. Oxidation products such as water are known to be generated when the hydro-peroxide 1.) forms a ketone 3.). It can be deduced that **C=O** groups emerge predominantly from paraffin oxidation and thus reflecting a degree of deterioration [12, 13].

9

The formation of polar and acidic compounds as well as water is not only detrimental to electrical equipment, it also reduces the electrical insulating capability of the paraffin. This potentially causes malfunction of the electrical equipment [1, 3, 26-30].
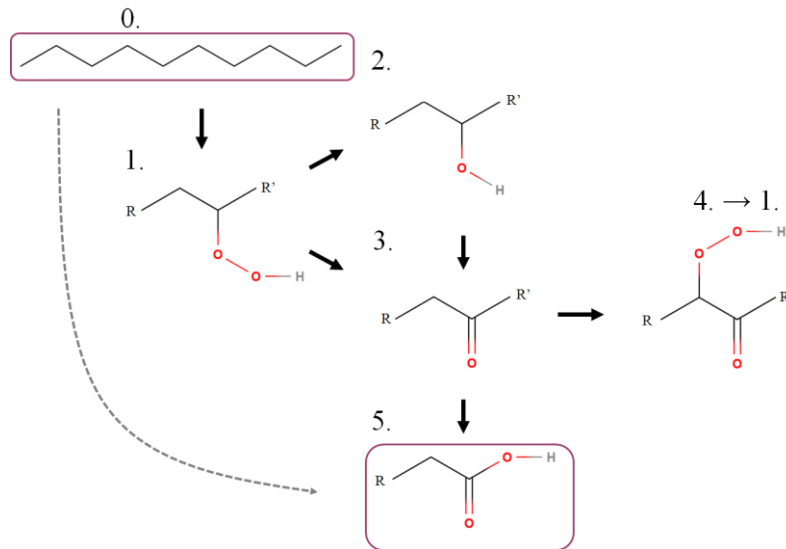


Figure 2.2. Pathway of a paraffinic oxidation. 0.) The hydrocarbon, subject to oxidation, is turning into a 1.) hydro-peroxide. The formation of 2.) alcohols can be a parallel process for the formation of a 3.) carbonyl bond. 4.) This carbonyl can be subject to further peroxidation which returns to the hydro-peroxide 1.). 5.) Acidic compounds are formed eventually.

Transformers are designed for 30 to 40 years at about 60 °C operating temperature [3, 31]. In order to simulate this time in a laboratory, an increase in the oil temperature may accelerate this process. In general, reaction rates are often referred to as an Arrhenius type equation [12] for a temperature $T$ and activation energy $E_a$ with the Boltzmann constant $k_b$,

$$f(T, E_a) = A \exp\left(-\frac{E_a}{k_b T}\right) t \,, \tag{2.1}$$

where $t$ is the time. A plot of this function with Temperature $T$ is shown in Figure 2.3. The exponential nature flattens out for large temperatures due to the $T$ in the denominator in the exp-function and approaches the (arbitrary) coefficient $A = 1$.
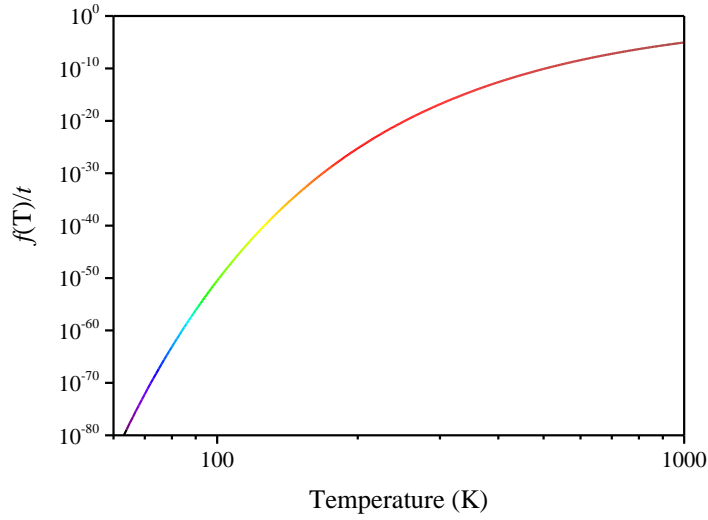
Figure 2.3: Relative oxidation reaction rate of hydrocarbon as function of $T$.

This is only an approximate but illustrates two facts. Firstly, the temperature affects the rate of which hydrocarbons oxidise to ketones and secondly, this dependence is exponential with temperature allowing it to simulate the oil's lifetime by an accelerated aging experiment in the laboratory during few weeks. For $E_a = E_{oil} = 0.9$ - $1.1$ eV [32], the oxidation acceleration factor can then be calculated by [12];

$$A\exp\left(\frac{-E_{oil}}{k_bT_1}\right)t_1 = A\exp\left(\frac{-E_{oil}}{k_bT_2}\right)t_2$$

$$t_1 = \frac{\exp\left(\frac{-E_{oil}}{k_bT_2}\right)}{\exp\left(\frac{-E_{oil}}{k_bT_1}\right)} \quad \text{if} \ \ t_2 = 1 \tag{2.2}$$

If the normal operating temperature of a transformer is about 60 °C and a laboratory aging temperature at 140 °C, Equation 2.2 yields an acceleration factor of about 870. Hence, about 1 year (8760 hours) of hydrocarbon insulating liquid being aged in transformers in the field can be reduced to about 10 hours in the laboratory.

11

## 2.2  FTIR spectroscopy of hydrocarbons

FTIR is a powerful analytical technique to determine functional compounds of hydrocarbons [4, 5, 14, 33-35]. It is challenging to predict the exact composition of oxidised hydrocarbon products due to the complexity of the possible reaction pathways. This problem is particularly elevated due to the fact that the hydrocarbon liquid typically containing various forms of hydrocarbons, with inconsistent molecular weights. However, infra-red spectroscopy such as FTIR can identify functional groups via oscillation excitation of their diatomic bonding. This technique does not alter the molecular composition of the oxidation products due to insufficient photonic energy [33].

In FTIR spectroscopy, the material under test is placed between an optical interferometer and a detector. Such spectrometers are commercially available such as the "Spectrum One FTIR Spectrometer" from Perkin Elmer which is employed in the present study. A schematic is shown in Figure 2.4. Infra-red light from a thermal emitter is collimated into the interferometer (Figure 2.4a) which is split into two paths via a beam splitter. One path is varied in distance from which a difference $\delta_x$ in the path length is achieved. This difference causes an interference pattern dependent on all available infra-red frequencies. The longer the interferogram path length difference, $\delta_x$, the better the instrument resolution. Placing a sample into the beam path, this sample will only absorb specific frequencies and thus creating a unique interference pattern. With the aid of the Fourier Transformation, these specific frequencies can be decoded and plotted over the wavenumber $v$ $(\text{cm}^{-1}) = 1/\lambda$, where $\lambda = c/f$ with $c$ the speed of light and $f$ the frequency of the light. A comparison of the background (e.g. air) and the sample test gives the frequency dependent absorption of the sample. The infra-red absorption using the Beer-Lambert-law can be written as a wavenumber dependent parameter $\beta(v)$;

$$A_v = \beta(v)cd \,, \qquad\qquad\qquad (2.3)$$

which is linearly proportional to a molar concentration $c$ assuming the molecular attenuation coefficient $\beta(v)$ and cell distance $d$ (Figure 2.4b) to be constant. This is the case for values of $c \lesssim 0.1$ (mol/l) [33]. Figure 2.5 shows typical absorption bands of organic molecules (such as oils) and their approximate absorption strengths over a mid-infra-red band as an intuitive overview. A good overview is shown in [36]; the absorption strength $A$ is predominantly dependent on type of the diatomic bond.
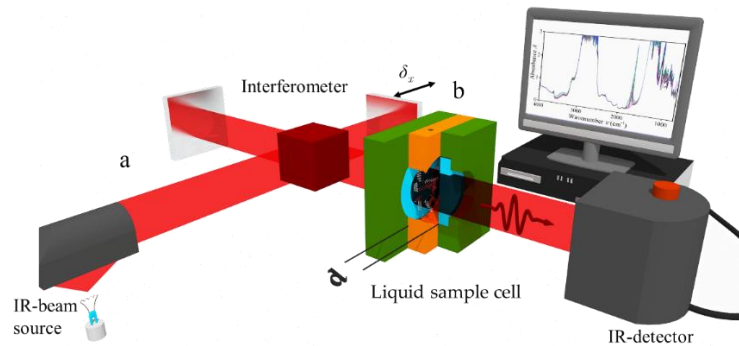


Figure 2.4. A typical setup of an FTIR spectrometer. (a) The infra-red source light is collimated and divided via a beam splitter. The interferogram, generated through two mirrors from which one is variable in its longitudinal distance $\delta_x$, is sent through the liquid sample cell (b) towards the IR-detector.
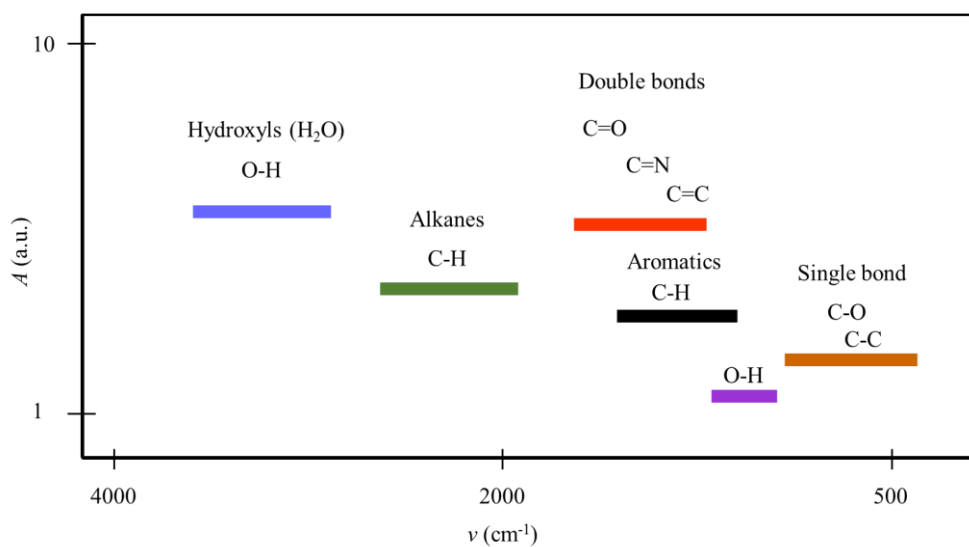


Figure 2.5. Typical absorbance strengths and appearance of organic molecules along the mid-IR wavenumbers.

13

### 2.2.1 Infra-red absorption wavenumber

Infra-red spectra can contain information of the molecular composition by the absorption $A$ as a function of the wavenumber $v$ (cm$^{-1}$). Figure 2.6 displays one typical absorbance mode at $v_0$ with infra-red light coming from the left to the right. Broadband infra-red light is passed through a sample containing the displayed molecule having a polar bond ($C=O$). This bond can oscillate at $v_0$ yielding the infra-red intensity $v_n$ minus $v_0$ on the right hand side. This is called an absorbance spectrum which can be used to yield information about temperature, bond lengths, possible isotopes or the entire molecular structure [33]. A molecular potential energy model can give information about the molecular composition by predicting the absorption wavenumber. The Born-Oppenheimer approximation describes this potential energy of molecules via quantum mechanics [33], consequently describing quantum-mechanically the infra-red spectra. A brief insight into the generation of spectra is given now.
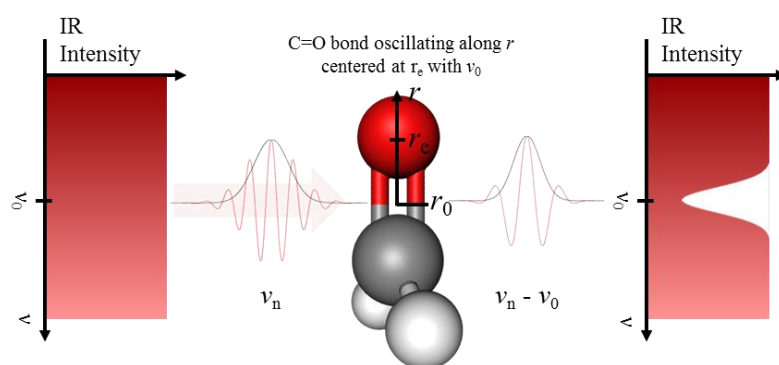


Figure 2.6. Schematics of the principle of vibrational absorption spectroscopy of molecules. Infra-red light having a wide spectrum of $n$ wavenumbers $v_n$ (cm$^{-1}$) pass through a sample (a ketone in this figure). This sample absorbs a specific wavenumber at $v_0$.

Temperature has an impact on the infra-red spectrum. This is due to thermal energy determined by the Boltzmann population density of the $J$ rotational states of a diatomic molecule. These states can have integer values; $J = 0, 1, 2, ... N$. These states are quantized in discrete $J(J+1)$ values exhibiting multiple peaks in the infra-red spectra following $v_{rot}(J) = BJ(J+1)$ with $B = h/(8\pi^2 cl) = $ const. having a

rotational energy separation of $\nu_{rot}(\Delta J=1)= 2B$ with $l$ = momentum of inertia and $c$ = speed of light in cm/s. In liquids, the molecular collision causes a continuum spectrum around $\nu_0$, resulting in a centered and broadened absorbance peak. A change in temperature can affect the mean value and the shape of $\nu_0$, therefore it is required to compare the infra-red spectra at the same temperatures [33]. Measuring the spectra at the same temperature allows setting the temperature impact as constant across the measurements. This simplifies the infra-red spectra analysis tremendously. The covalent bonds of molecules can thus be reduced to diatomic molecules which are held together via a bond strength, or force constant, $k$. Such a diatomic system can oscillate which is called vibrational spectroscopy. Infra-red radiation at such a frequency $\nu_0$ can excite this bond to oscillate. In order to find the vibrational (absorbance) wavenumber $\nu_{vib}$ the quantum mechanics shows that the force constant $k$ of a diatomic molecule is defined through its potential energy $U(r) \cong k(r-r_e)^2$ and thus the force constant becomes a function of the diatomic system, $k = d^2U(r)/dr^2$. The eigen-frequency of such a diatomic system having the mass $m_1+m_2$ is $\omega_0 = (k/\mu_{mass})^{1/2}$, with $\mu_{mass} = m_1m_2/(m_1+m_2)$. The vibrational states $(\upsilon+\frac{1}{2})$ are quantized with the quantum number $\upsilon = 0, 1, 2, ..., N$ with the Greek letter upsilon. Hence, the frequency of this harmonic oscillator is $\propto (\upsilon+\frac{1}{2})\omega_0$. The energy $E$ required to excite the vibration from a ground state $\upsilon_0$ to $\upsilon_1$ is therefore $\Delta E = E((\upsilon+1)+\frac{1}{2}) - E(\upsilon+\frac{1}{2}) = E(\upsilon)$, which is also $E = \omega_0\hbar$. For the excitation of the dominant first harmonic ($\upsilon = 1$), we thus yield the distinct absorption of the corresponding bond having the wavenumber [35] (Greek letter nu)

$$\nu_{vib} = \omega_0 / (2\pi c).$$

(2.4)

The wavenumber $\nu$ is typically expressed in cm$^{-1}$, therefore $c$ has units of cm/s.

## 2.2.2 Intensity of infra-red absorption

We have seen how and at what frequency absorption occurs, but the magnitude of infra-red absorption is yet unclear. An interaction with electromagnetic radiation takes place when a dipole moment changes its oscillation states; eg. $\upsilon = 0 \rightarrow \upsilon = 1$. This process requires electromagnetic energy. These $\upsilon$-states are wavefunctions such as $\psi(x,t)$, consisting of trigonometric functions which are quantum mechanically written as ket; $|\psi\rangle$, using the bra-ket notation for simplification [35]. In term of infra-red analysis, the oscillation states are called $\upsilon$ and therefore the $\upsilon$-associated wavefunction can be written as $|\upsilon\rangle$. Thus, the transition dipole moment integral from state $|\upsilon_0\rangle$ to $|\upsilon_1\rangle$ must be non-zero: $\langle\upsilon_1|\mu_t|\upsilon_0\rangle \neq 0$, where $\mu_t$ is the dipole of the diatomic molecule (the dipole $\mu$ is elaborated in section 2.4.1). The radiated electric field is proportional to the dipole, $E \propto \mu$ and if such a dipole absorbs radiation, $I \propto E^2$ (Intensity), the absorbance $A \propto I$ will be dependent of the square of the dipole moment relative to the equilibrium state distance $r_e$ [35]. One can thus write;

$$A \propto \mu_t^2(r),\tag{2.5}$$

where

$$\begin{aligned}\mu_t(r) &= \langle\upsilon_1|\mu_t|\upsilon_0\rangle \\ &\cong (\partial\mu(r)/\partial r)\langle\upsilon_1|r-r_e|\upsilon_0\rangle\end{aligned},\tag{2.6}$$

plus overtone terms which are of orders of magnitudes lower.

The term $\langle\upsilon_1|r-r_e|\upsilon_0\rangle$ has the selection rule $\upsilon_1 = \pm 1$ (and $\pm 2$ for the first overtones) which can be mathematically acquired using the Taylor series [37]. At the same time, the harmonic oscillator Hamiltonian dictates a discrete wavenumber, $v$, dependence (c.f. p. 90 in Ref [35]). The exact strength of absorption is given in theory [35] & [33, 35, 38] which eventually yields the spectral absorption $A$ which is dependent on the oscillating frequency, which in turn is dependent on the diatomic dipole moment;

$$A(\nu) = \mu_t^2 \left( \nu_{vib} \right) \beta c \, d \,, \tag{2.7}$$

with assumed constants such as $\beta$ as infra-red absorption probability coefficient or cross section, $c$ the molar concentration of the material under test and the optical transmission length $d$. **The** optical transmission length $d$ is effectively the cell distance in Figure 2.4. This molecular dipole is leading to an infra-red absorption which is of importance for linking the relative permittivity to the infra-red absorbance.

### 2.2.3 Infra-red absorbance spectra of hydrocarbons

As discussed, $k$ was a parameter for the potential $U(r)$. However, $U(r)$ can change even for the same kind of diatomic bond. This affects the bond strength of the **C=O** bond in molecules such as hexanone or decanone. An explanation for this is the distortion of the electron configuration of the entire molecule. Consequently, hetero atomic configurations, such as **C-H** or **C=O**, will exhibit a slightly different $\nu_{vib}$ among similar molecules. Thus, the exact wavenumber (-shift) can yield information of the participating molecule.

The absorbance can also be affected by temperature. Hence, stable temperature conditions during the infra-red measurement are important for comparison of the measured spectra [33, 35].

A hydrocarbon such as decane possess absorption in the **C-H** bending and **C-H** stretching bands at $\nu_{C-H} = 730$ and $2950\ \text{cm}^{-1}$ as well as a **C-C** stretching band at $\nu_{C-C} = 1400\ \text{cm}^{-1}$. Fermi resonance is an effect described in Ref. [35] which causes the **C-H** stretching at $2950\ \text{cm}^{-1}$ to split into three bands close to $2950\ \text{cm}^{-1}$. Carbonyls such as ketones and organic acids are known to absorb at $\nu_{C=O} \approx 1710$ - $1730\ \text{cm}^{-1}$. A typical gas absorbance spectrum for decane ($C_{10}H_{22}$) is shown by the National Institute of Standards and Technology (CAS Registry Number: 124-18-5, NIST, USA) in Figure 2.7a. This demonstrates broadened peaks and skeletal coupling [35] visible for the $\nu_{C-H}$-stretching band. The spectrum for 2-decanone

($C_{10}H_{20}O$) (CAS Registry Number: 693-54-9, NIST, USA) exhibits additional peaks as shown in Figure 2.7b. The predominant difference between both spectra are the $\nu_{C=O}$-region at around 1720 cm$^{-1}$. This is due to the formation of carbonyls.
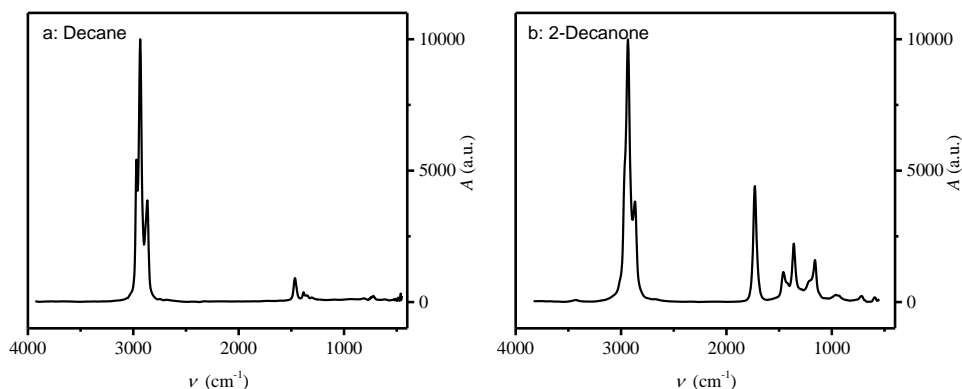


Figure 2.7. (a) Decane infra-red absorbance spectrum from 500 to 4000 cm$^{-1}$. (b) The absorbance spectrum from 2-decanone showing additional peaks between 2000 and 1000 cm$^{-1}$. Image produced from the NIST infra-red database.

## 2.3  Previous work using FTIR for hydrocarbon detection

Investigations on the thermal oxidation of liquid hydrocarbons were done in many studies [3, 12, 13, 28, 39, 40]. A study of paraffinic insulating liquid oxidation at 130° C [40] (Figure 2.8) shows how the oxidation products increase with time when subject to thermal decomposition. The oxidation products such as peroxides, alcohols, ketones, aldehydes, acids and esters were determined using infra-red spectroscopy by integrating the absorbance peaks of the oxidation products. A significant increase in carbonyls such as aldehydes and ketones was noticed during the experiment, but the hydro-peroxide value dropped after a first rise with the experiment time. This is in accordance with theory [12, 13], as the peroxides exhibit a low bond energy and thus they decompose under thermal energy rapidly. This study also investigated the formation of oxidation products from an insulating liquid under the name Yubase 4 (YB4) with and without an inhibitor (alkylated diphenylamine; ADPA). Seemingly, the oxidation of

18

hydrocarbons cannot be avoided with inhibitors. Such results were found in similar studies using infra-red spectroscopy [4, 5, 14, 33, 34, 39].
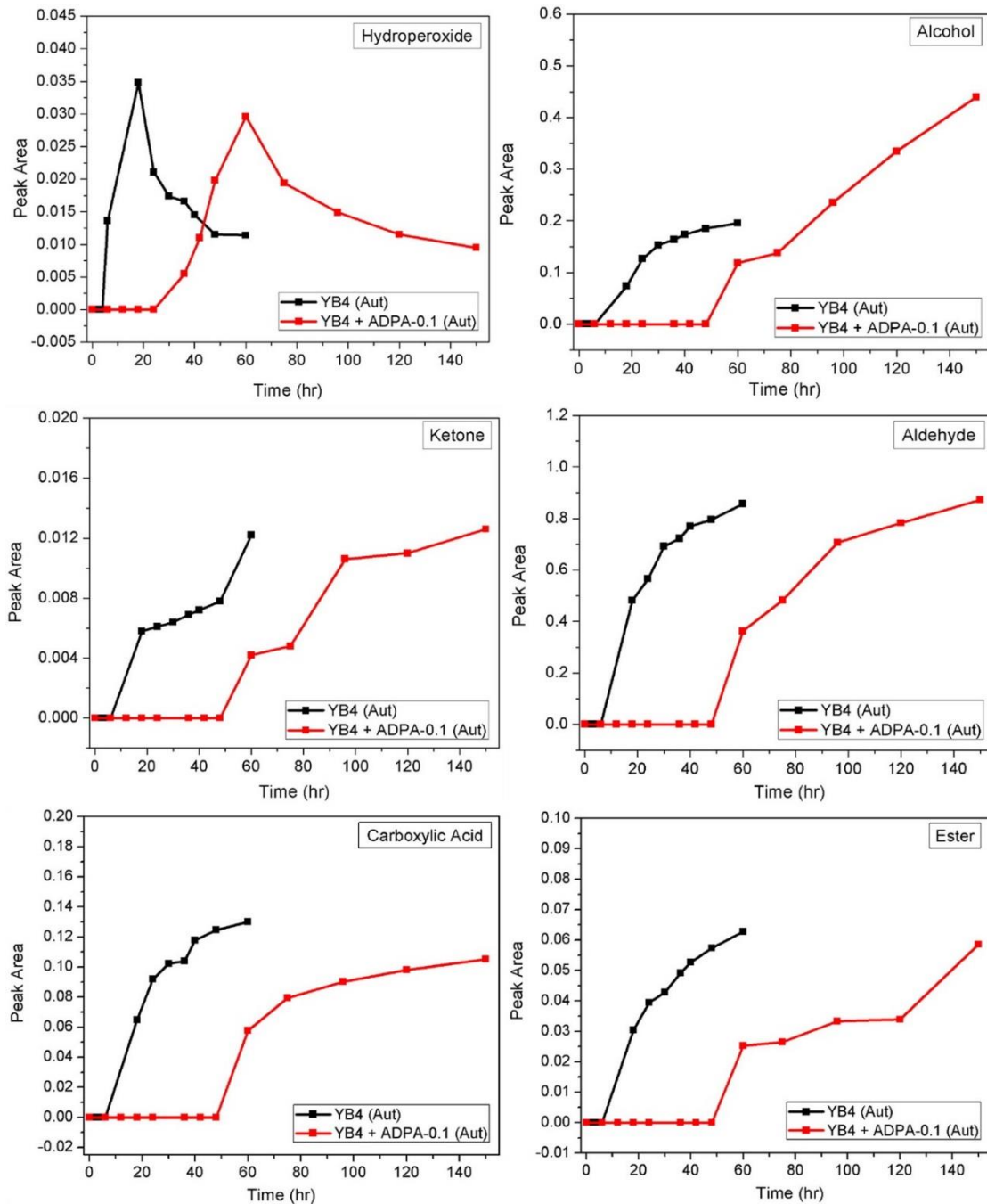


Figure 2.8. The formation of various oxidation products (peroxides, alcohols, ketones, aldehydes, acids, esters) via FTIR spectroscopy with time of an oxidation experiment with and without inhibitor YB4. Figure from Ref. [40].

Previous research in detecting oxidation products via infra-red spectroscopy is numerous [5, 14, 34, 36]. In Ref. [14] the study of oxidation products was done using FTIR on hydrocarbon based insulating liquids with different compositions

19

which is shown Figure 2.9. This figure shows the qualitative absorption for seven different hydrocarbon insulating liquids. This research gives a deeper insight in the generation of products during oxidation with time at elevated temperatures. A distinct broad absorbance around 1720 cm⁻¹ was found for seven different hydrocarbon liquids. Also, a hydroxyl increase was noted. This demonstrated a detectable absorbance in the carbonyl region that was a prominent mechanism occurring during oxidation.
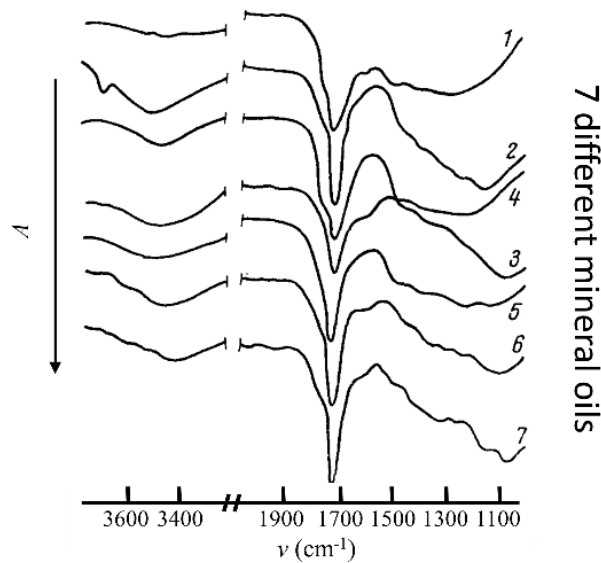


Figure 2.9. The infra-red absorbance of seven different hydrocarbon liquids showing the carbonyl absorbance at around 1720 cm⁻¹ after subject to thermal oxidation (modified from Ref. [14]).

This oxidation was attributed to a large variety of generated carbonyls such as aldehydes, ketones, organic acids and esters. Interestingly, an increase in the moisture region, 3200 to 3600 cm⁻¹ was found. However, it was not proven whether this region was caused by water or free hydroxyl. A similar study was done oxidising insulating liquid such as paraffinic transformer oil [5]. One observation was a clear absorption also at 1718 cm⁻¹. This research associated the absorbance peaks from oxidation to certain carbonyl compounds. The carbonyl absorbance was integrated and plotted over its oxidation time showing a linear dependency.

A study about organic acids and their infra-red response was done in Ref. [34]. It showed how FTIR can potentially be used to determine the absolute

concentration of acids and moisture. Figure 2.10 illustrates the organic acids having different moisture concentrations. The difference in the moisture concentration (0 - 2000 ppm) is visible in the (a) 3600 $cm^{-1}$ and (c) 1600 $cm^{-1}$ region. As organic acids contain one or more carbonyl groups this absorbance (b) is distinctively visible in the 1700 $cm^{-1}$ area. This will be adopted in this thesis to a) confirm the presence of moisture via FTIR spectroscopy and b) to determine the quantity using FTIR spectroscopy.
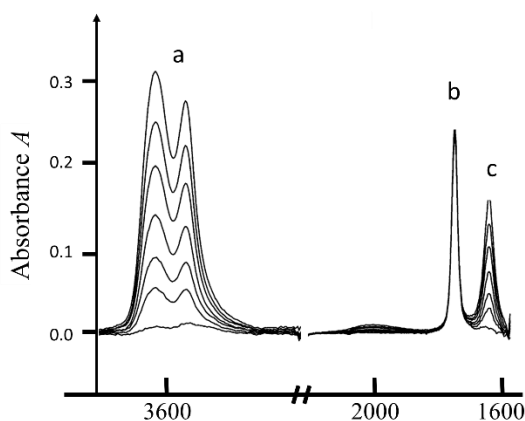


Figure 2.10. The infra-red spectrum of organic acids, modified from Ref. [34]. These acids exhibiting a different infra-red absorbance dependent on their (a, c) moisture concentration. (b) Organic acids are shown as peak around 1700 $cm^{-1}$.

## 2.4 Dielectric properties of hydrocarbons

This section is a brief review of the properties of dielectrics, polarisation and the relative permittivity which is held consistent with the literature [41], but limited to the need for this thesis. With focus of a generic understanding, it firstly introduces the definition of a dipole important for a dielectric measurement and what relation it has to the oxidised alkane. This is followed by a brief section of how this dipole can be measured over the relative permittivity at low frequencies. A detailed review is given in common text books [37, 38, 42, 43].

### 2.4.1 The permanent dipole moment of molecules

The familiar equation for a plane parallel capacitor with geometry $A/d$ is given by

$$C = \varepsilon_0 \varepsilon_\mathrm{r} A / d \quad , \tag{2.8}$$

where $\varepsilon_0$ is the vacuum permittivity. For a medium within the parallel plates, the capacitance is proportional to the value of $\varepsilon_\mathrm{r}$. In literature [41], this is described due to a macroscopic polarisation, $p \sim N\alpha \sim \varepsilon_\mathrm{r}$, of a medium due to separation of $N$ positive and negative charges dependent on their polarisability $\alpha$ [38, 43]. A larger number of separated charges increases $p$ and thus $\varepsilon_\mathrm{r}$. Under certain conditions, the $\varepsilon_\mathrm{r}$ is not constant anymore and then yields a real part $\varepsilon_\mathrm{r}$ and an imaginary part $\varepsilon_\mathrm{r}$. This can be due different types of polarisation which are illustrated in Figure 2.11. Space charge polarisation describes the interaction of charges such as in ionic liquids. A polarisation can be due to mobile charge carriers such as anions, Cl⁻, and cations, Na⁺. These can move under an applied electric field between two plates leading to a collection of those charge carriers on each plate with opposite polarity. When their mobility time constant is in the range of a measurement frequency, then those charge carriers cause electrical losses in the system. Molecular dipoles tend to align to an applied electric field. When the frequency is lower than the time constant of the alignment, then the dipoles contribute to the relative permittivity. If the frequency is in the range of the alignment time constant, those molecules are permanently accelerated, causing joule heating due to molecular movement. When the frequency is higher, then the dipoles fail to align and we enter the region of ionic polarisation. In systems such as crystals such as NaCl, which are non-polar, polarisation due to an electric field is caused by an induced charge separation of the electrons from the nucleus. Also here, the ionic anions and cations follow the frequency up to a certain limit until resonance. If the frequency is high enough, these ions are too heavy to follow the rapid oscillations. In this Figure 2.11, only the much lighter electrons are capable of following the rapidly changing electric field, and the frequency to measure permanent dipoles, e.g. for C=O bonds, via a dielectric

measurement of the $\varepsilon_r$ is therefore in the range of $10^1$ to $10^4$ Hz. This will be discussed in some more detail now.
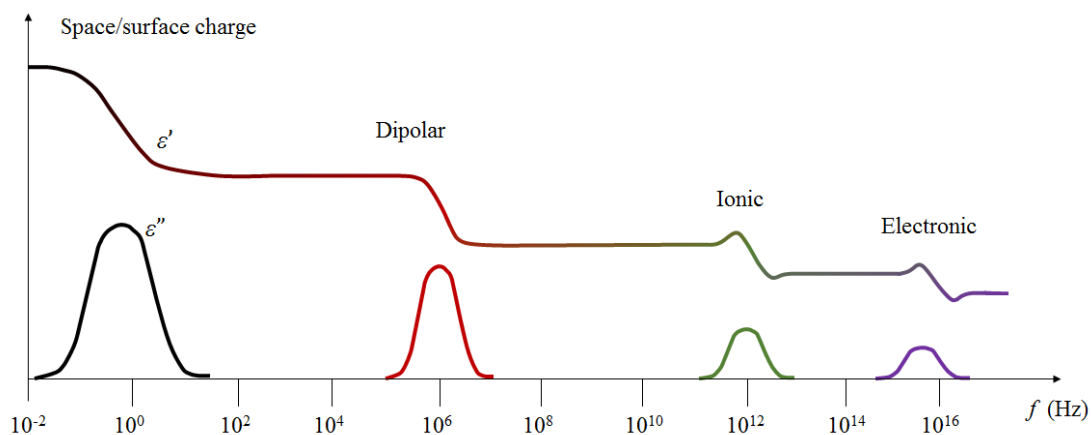


Figure 2.11. The types of polarizations and their resulting permittivity ($\varepsilon_r$) and losses, $\varepsilon_r$, as function of frequency.
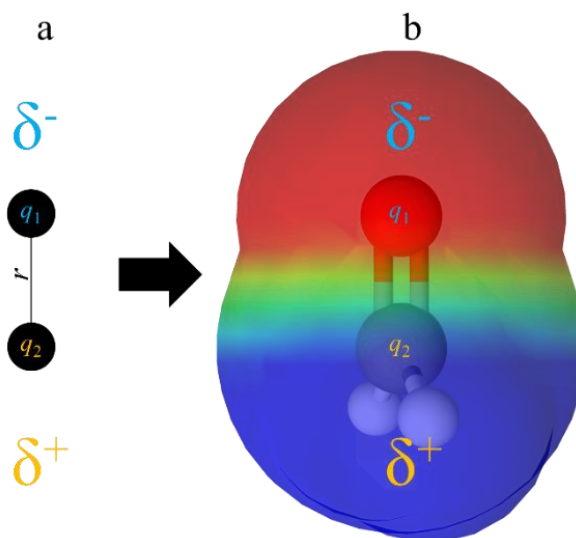


Figure 2.12. A permanent dipole. (a) Two point-charges ($q$) separated by a distance $r$ and (b) an electrostatic charge distribution for a simple molecule, formaldehyde, containing a carbonyl (C=O) group.

A molecular dipole having a **C=O** bond is depicted in Figure 2.12. A permanent dipole can exist in diatomic molecules due to the separation of two charges ($q_1$ negative, $\delta^-$, and $q_2$ positive, $\delta^+$), Figure 2.12a. The dipole moment can be calculated using electron negativities of each atom and their respective angles to each other. This dipole moment will be valid for $q_n$ point charges. Real molecules e.g. formaldehyde (Figure 2.12b) exhibit a charge distribution density,

$q \rightarrow \rho(\mathbf{r})$. Predominantly due to covalent bonds, the dipole moment can be more generally expressed by the static dipole moment as integral of the charge distribution density $\rho(\mathbf{r})$,

$$\mu_{\mathrm{s}} = \int_V \mathbf{r}\rho(\mathbf{r})\mathrm{d}r . \tag{2.9}$$

Such a permanent dipole moment can interact with electric fields. If placed between two charges plates e.g. in a plane parallel capacitor they will orient to the electric field $E$ in parallel. This orientational (= dipolar) polarizability, derived by Debye with the aid of the Langevin function (c.f. Ref. [37] for details), is defined by

$$\alpha_{\mathrm{o}} = \mu_{\mathrm{s}}^2 E / \left(3k_{\mathrm{b}}T\right) . \tag{2.10}$$

It can be seen that the orientation polarizability, $\alpha_0$, (Equation 2.10) is inversely proportional to the Boltzmann constant $k_{\mathrm{b}}$ and the temperature $T$ in kelvin. Temperature induces a kinetic molecular energy, e.g. rotation, which makes it more difficult to orient to the applied field. The factor $1/3$ is due to the average dipole orientation when using the Lorentz sphere (c.f. Ref. [37, 43] for details) as a dipole model within the electric field.

An orientation of 2-decanone between two charged plates is depicted in Figure 2.13. First the non-polar molecules are depicted with a random orientation in Figure 2.13a. Replacing some of these molecules with ketones in Figure 2.13b (e.g. due to oxidation), the permanent dipole aligns to the electric field in parallel. In this example, the permanent dipole moment is drawn as a vector $\boldsymbol{\mu}$ pointing in parallel to the electric field. The electrode charges (pink and blue dots named $q$) are increased due to the presence of the dipoles.
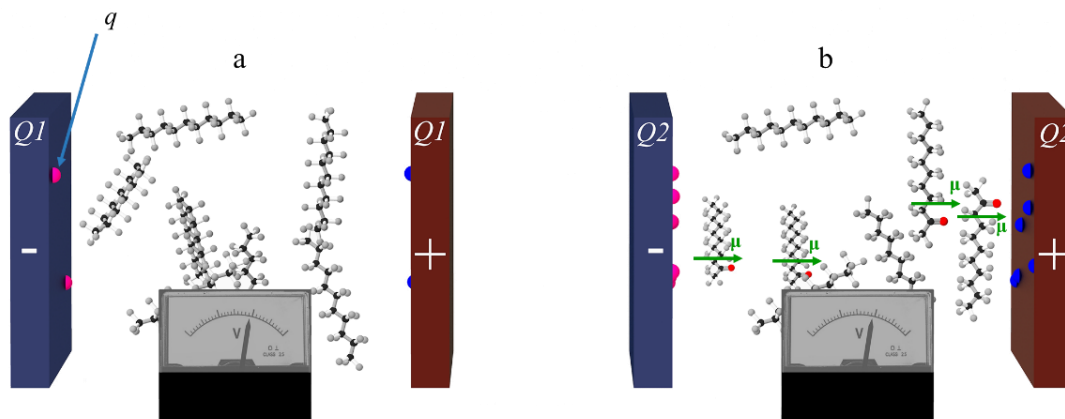
Figure 2.13. Working principle of measuring $\varepsilon_r$. (a) Non-polar molecules are randomly distributed between two electrodes with a potential applied. Only a few charges $q$ (pink and blue dots) on the electrodes are present. (b) Polar molecules, having a dipole moment (vector) $\boldsymbol{\mu}$, align to the applied electric field and causing an significant increase in the total electrode charge $Q_2 > Q_1$ using same electric potential. Modified from [24].

### 2.4.2 Relation from the permanent dipole moment to the permittivity

In section 2.4.1, it was argued that the polarization, the polarizability and the relative permittivity are connected to each other. This connection can be shown via the Clausius-Mosotti equation (C-M), which links the dipole moment, $\mu$, to the relative static permittivity, $\varepsilon_r$ (c.f. section 2.4 in [38]),

$$\frac{\varepsilon_r - 1}{\varepsilon_r + 2} = \frac{N_A \rho}{M} \frac{\mu_s^2}{9\varepsilon_0 k_b T} \; . \tag{2.11}$$

This equation is independent of the electrical field *E*. The volume density *N/V* of a material under test is expressed by $N_A \rho / M$. With *M* as the molar mass and $N_A$ is the Avogadro number and density $\rho$. An increase in the volume density, e.g. oxidised compounds, causes $\varepsilon_r$ to increase. The C-M equation is however only valid for very small concentrations. For high polar liquids for instance, various other equations based on C-M have been determined [38]. Here, C-M is used as indicative dependency between $\varepsilon_r$, *T* and $\mu$.

The relative permittivity can be obtained via two capacitive measurements $C_0$ and $C_1$ from which one of them, such as $C_0$, must be of a known permittivity

value. It is common to measure the air capacitance as $C_0$, since $\varepsilon_{r,Air} = 1.0007 \approx$ 1. Then, the ratio of two capacitive measurements yields the relative permittivity;

$$\varepsilon_r = C_1 / C_0. \tag{2.12}$$

### 2.4.3 Relation of the permittivity to the infra-red absorbance

It was shown that the intensity of the infra-red absorption is proportional to the transitional dipole moment in section 2.2. This included the permanent dipole moment $\mu_t$. The infra-red absorbance requires a change in the existing permanent dipole moment $\mu_s$ [37, 38] and thus we can write $\mu_t \rightarrow \mu_s$ and then the condition that the dipole interacts with an infra-red light is [33, 35],

$$<\upsilon_1|\mu_t|\upsilon_0> \rightarrow <\upsilon_1|\mu_s|\upsilon_0> \neq 0. \tag{2.12}$$

This system was evaluated with the appropriate Hamiltonian and its matrix elements in Ref. [35]. It can be shown that a permanent dipole $\mu_s$ must be present. When using static electric fields, where no transition occurs; $\upsilon_1 = \upsilon_0$, the transitional dipole moment must become

$$<\upsilon_0|\mu_s|\upsilon_0> = <\mu_s> \neq 0, \tag{2.13}$$

and as

$$<\upsilon_0|\upsilon_0> = 1, \tag{2.14}$$

a permanent dipole must be present;

$$\mu_s \neq 0. \tag{2.15}$$

This result is somewhat obvious when looking at Equation 2.10. What it says however is that a change in the relative permittivity must be accompanied by a change in the infra-red absorption (but not strictly vice versa). As oxidation products are polar, these can be detected though the infra-red spectroscopy and a permittivity measurement.

### 2.4.4 Measurements of dielectrics

The permittivity and its relation to the permanent dipole was discussed under DC electric fields. In practice, the capacitance is measured via AC fields

with impedance analysers (Hioki IM3590) yielding a measurement of the impedance $Z$ as described in common text books [41, 43]. This impedance can be written simplified as $Z = C^{-1}\omega^{-1}$ with $\omega = 2\pi f$, $f = 50$ Hz throughout in the thesis, unless stated otherwise. The dielectric constant of free space is $\varepsilon_0$ the relative complex permittivity of the material under test $\varepsilon_r$. The impedance can be complex and yielding a real component and an imaginary component, as the permittivity also contains real and imaginary components. The real part is reflecting the energy stored through the capacitor which results in an imaginary impedance. The imaginary part represents a proportionality to physical resistive losses. Such dielectric losses can be due to various effects such as charge carrier conduction for frequencies below the MHz regime or dielectric relaxation above the MHz regime. For instance, space charges are accelerated due to the electric field and move from one electrode to another. This is dependent on a time constant relative to the excitation frequency (c.f. Ref. [43]). Dielectric relaxation occurs due to permanent molecular dipoles which start to rotate and induce joule heating under certain frequencies as this also has a time constant of orientation (c.f. Ref. [43]). When the particle aligns to an electric field, this will consume energy for the time the particle is accelerated. For molecules, they rotate to the field in parallel, while rotation, they consume energy. When they start to align to an electric field which changes its direction in a time scale equal to the time the molecule needs to rotate, this system consumes work permanently. This is exploited in microwave ovens operating at GHz. The frequency range in this study is in Hz to kHz regime, and so this discussion can be limited to charge carrier conduction from which the complex permittivity can be written as,

$$\varepsilon_r = \varepsilon_r^{'} - i\varepsilon_r^{''}. \tag{2.16}$$

The real part of the permittivity $\varepsilon_r$ describes the static polarizability due to static dipoles $\mu_s$ and the losses $\varepsilon_r$ describe the conduction though charge carrier mobility.

An angle $\delta = 90° - \varphi$, where $\varphi$ is the measured angle between voltage and current across a capacitor, is used to describe the dielectric losses by the dielectric loss factor [43, 44],

$$\tan\delta = \varepsilon_r'' / \varepsilon_r'. \tag{2.17}$$

The complex permittivity, $\varepsilon_r$, contains information about the complex conductivity [43],

$$\sigma = i\omega\varepsilon_0\varepsilon_r \tag{2.18}$$

The DC conductivity is understood to be a process of electron conduction via hopping [42] and will be discussed in more detail in section 3.3.2 where it becomes relevant to model the data. The DC conductivity, $\sigma_{DC}$, can be calculated by this loss factor and the frequency at which the loss factor was measured, assuming no other types of losses are present. Together with the permittivity [43] one finds;

$$\sigma_{DC} = \omega\varepsilon_0\varepsilon_r' \tan\delta. \tag{2.19}$$

Since the loss factor is inversely proportional to the frequency, $\tan\delta = \varepsilon_r''/\varepsilon_r' = (\sigma_{DC}/\varepsilon_0\omega)/\varepsilon_r'$, the frequency cancels out in the Equation 2.19. This conductivity and the complex permittivity can be measured through the phase angle $\varphi$ and the magnitude of the impedance $Z$ only. The permittivity varies for different substances. However, in order to give an impression of the magnitude, a selection of approximate values for the insulators, polar molecules and ionic liquids is given in Table 2.1. Polar compounds are larger in their permittivity.

Table 2.1. An overview of values for the relative permittivity for non-polar and polar liquids

| Type | Material | Permittivity |
|------|----------|--------------|
| **Insulating liquids** | Paraffin oils | 2.1~2.3 [1, 3, 17, 29, 45-47] |
| | Cyclohexane | 2 [48] |
| | Vegetable oils | 2.9~3.8 [29, 49] |
| **Polar liquids** | $H_2O$ | 78[48] |
| | Methanol | 32 [48] |
| | Levulinic acid | 18 [50] |
| | Acetone | 21 [51] |

### 2.4.5 Permittivity of mixtures of liquid dielectrics

The Clausius-Mosotti equation can be used to describe mixtures of dielectrics. This is satisfactory for gases or ideal liquids with no or low dipole interaction and low conductivities such as paraffin. For pure polar liquids, more specific equations have been derived such as the Onsager equation, the Raleigh's formula or Bottcher's formula [37, 38]. The oxidation process increases the concentration of dissolved polar compounds such as water or carbonyls. Important in these equations is the lack of molecular permanent dipole-dipole interaction. Thus, this **C-M** equation holds approximately well for dissolved products in low concentrations. Hence, it is possible to state the resulting permittivity (c.f. p. 200 in Ref. [37]) as a linear combination of the participating dielectrics;

$$\varepsilon_\mathrm{r} = \sum_k N_k \varepsilon_{\mathrm{r},k} \,. \tag{2.20}$$

The normalized molar fraction is $N_k$, and $\varepsilon_{\mathrm{r},k}$ is the participating permittivity of this fraction. Experimental verification of this equation was shown in Ref. [37], p. 201.

## 2.5 Previous work on dielectric sensing of liquid hydrocarbons

The current effort in measuring $\varepsilon_\mathrm{r}$ of insulating liquids is numerous [1-3, 6, 15, 17, 26, 28, 39, 44, 46, 47, 52-57]. Representative for this vast research are studies from Dervos et. al. [1] & [6]. They characterised about 200 used oil samples regarding its $\varepsilon_\mathrm{r}'$ and $\tan\delta$ value using a low frequency impedance analyzer, into three deterioration categories. This was done according to standardized test methods and conditions for insulating liquid classifications. The permittivity measurements for $\varepsilon_\mathrm{r}'$, in the region 20 Hz to 1 MHz showed a featureless line across various deteriorated liquids, Figure 2.14a. The observed range of the oil value, $\varepsilon_\mathrm{r}'$ = 2.1 to 2.5, is described due to thermal aging effects. The $\tan\delta$ values exhibited an increase with progressed deterioration, Figure 2.14b. With increasing

frequency, this dissipation factor value decreased monotonically. A complementary chemical analysis of the ca. 200 in field samples revealed the typical characteristic of hydrocarbon liquid deterioration; the dielectric breakdown strength decreased while values such as moisture, acidity, density and color have steadily increased.
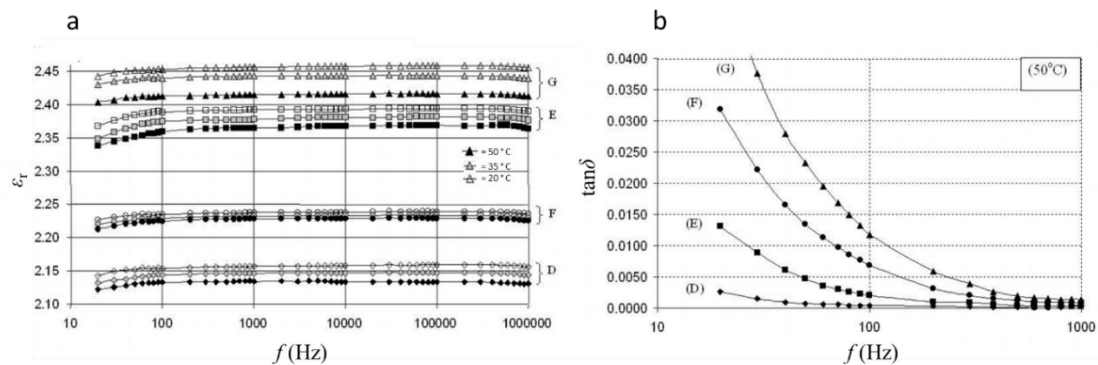


Figure 2.14. (a) The permittivity as a function of temperature and frequency for in-field samples D to G. Darker colored marker indicates temperature from 20 °C to 50 °C. (b) Dissipation factor as a function of frequency for in-field samples D to G. Alphabetic order represents an increased hydrocarbon deterioration. Figure from Ref. [1].

One preceding study showed the impact of hydrocarbon oxidation products on the tan$\delta$ value (60 Hz) [58]. Properties of various ketones and carboxylic acids as well as alcohols were determined dependent on temperature and concentration. It was found that with temperature the tan$\delta$ values increased among all experiments as well as with an increase in concentration, Figure 2.15. In particular, the investigated propionic acids showed a significant increase in its loss factor with temperature when compared to the results from stearic and naphthenic acids. Aldehydes such as valeraldehyde and heptaldehyde showed a significant impact on the loss factor and concentration. Ketones and alcohols exhibited a low impact on the dielectric loss factor.
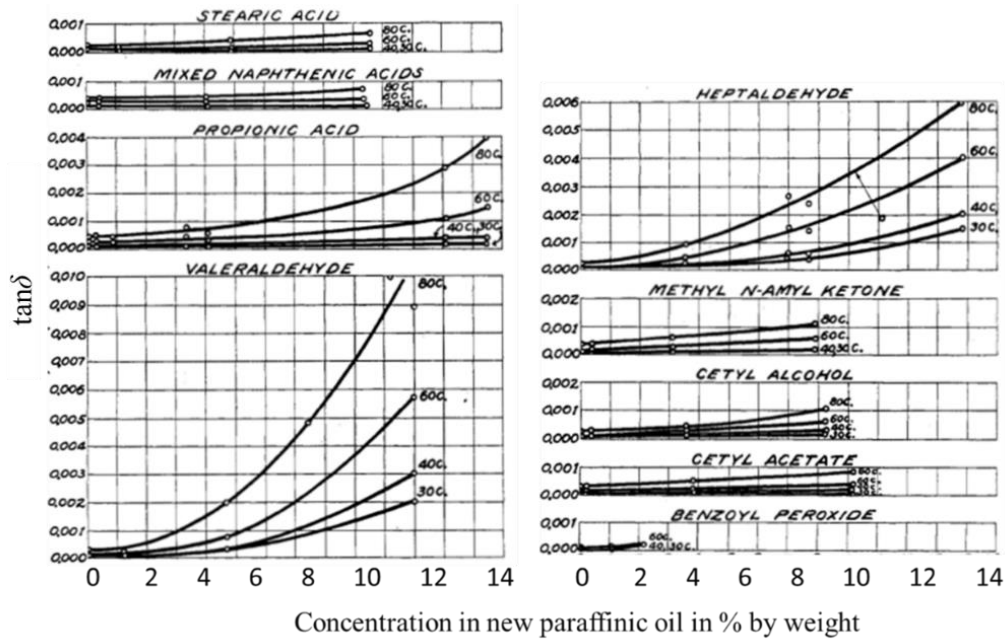
Figure 2.15: $\tan(\delta)$ at 60 Hz as function of temperature and concentration in % by weight for oxidation products. Figure from Ref. [58].

## 2.6 Sensing with Interdigitated Dielectrometry Sensors

Interdigitated Dielectrometry Sensors, IDS, have the potential to be used as dielectric probes in particular for *in-situ* measurements of insulating liquids measuring the complex permittivity $\varepsilon_r$, including the $\tan\delta$ value and hence their conductivity. A major difference to plane parallel designs are fixed electrodes on one plane, which need otherwise be mounted in a complex and fragile way in space. This chapter will briefly introduce the working principle, the current achievements for IDS and their limitations.

Such a dielectrometry sensor measures a dielectric with electric fields. The electric field from a point charge $q$ at $y = y'$ is known to be propagated inversely to its radial distance in free space according to $E = q/(y\text{-}y')^2$, Figure 2.16a. For an infinite large plane, the electric field is proportional to $1/y$; however, between two infinite large plane parallel plates, the electrical field $E$ is constant, Figure 2.16b. Having two alternatingly charged strips in parallel, the electric field from the surface charge $Q = \Sigma q$ is then emanated into space from one electrode to another, Figure 2.16c (here the electrode is only partially shown with $w/2$ due to

31

symmetry). Thus, the sensing electric field and its distribution is not straightforward and depends on the specific geometry of IDS electrodes.
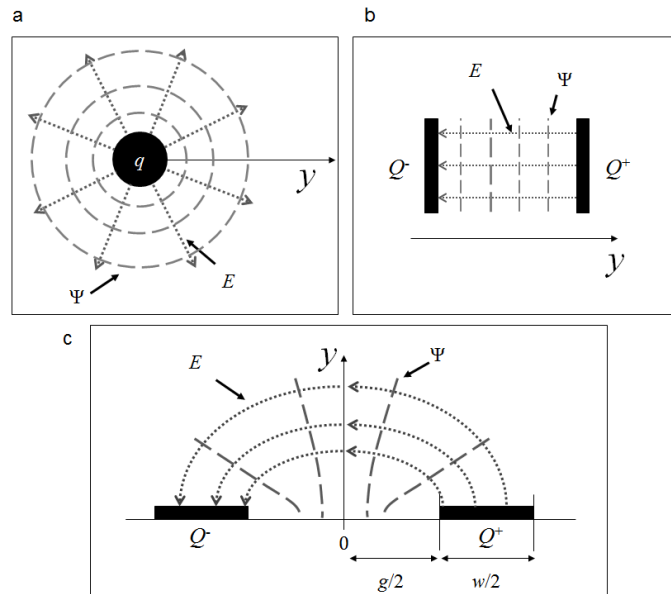


Figure 2.16: (a) A point change is emanating its electric $E$ and potential field $\Psi$ in free space is proportional to $1/y^2$. (b) The electrical field between two electrodes is constant along $y$. (c) An electrical field across the gap, $g$, from two coplanar electrodes, $w/2$, is distributed in space but spatially limited by the presence of the oppositely charged electrodes.

Figure 2.17 shows an IDS top view of the cross sectional view from Figure 2.16c having a periodicity which is called wavelength of $\lambda = 2g+2w$, where $g$ is the spacing of the electrode with width $w$. These electrodes are driven by a four wire measurement system yielding the impedance $Z$ and the phase between current and voltage across the electrodes.
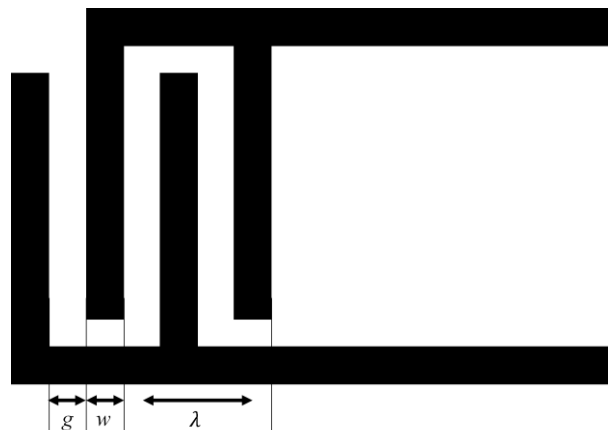


Figure 2.17. A top view of four coplanar electrode fingers and their separation $g$ as well as width $w$.

Vast research about IDS and their structure is available in literature and attempts have been made measuring the relative permittivity of hydrocarbon based insulating liquids using impedance measurements [15-21, 59, 60]. However, this has remained challenging to date. A chronological research about IDS is given now.

One theoretical approach in 1968 was studying the electrostatic potential via conformal mapping methods [61]. It showed that changing the electrode structure to a narrower gap increased the capacitance and that an approximation of zero electrode height is well adequate. Furthermore, the electrical field distribution distance for a fixed magnitude above the coplanar strips was determined to be proportional to the wavelength $\lambda$.

The IDS development in 1994 was advanced by the Massachusetts Institute of Technology under Markus Zahn for using IDS to track moisture in pressboard via an $\varepsilon_r$ measurement [15]. The used IDS was made of electrodes on a flexible polyimide substrate coated with parylene. The wavelength $\lambda$ was chosen to be 1 mm 2.5 mm and 5 mm. With aid of this setup it was possible to penetrate three different lengths into the pressboard. As moisture has about ten-fold greater permittivity than pressboard, the response of each $\lambda$ could be extracted enabling spatial tracking of moisture within the cellulose.

Optimisations of such IDS structures have been done by A. Mamishev in 1998 [16]. This led to an improved design of a three-wavelength IDS. Here a ground plane was used to prevent sensing beneath the electrodes, improving unidirectional sensing above the IDS. Contrary to the previous design, polytetrafluoroethylene (PTFE, also called under the branded name "Teflon") as an insulator underneath the electrodes was used. Here, insulating liquids such as various insulating liquids have been investigated via a gain and phase measurement with proprietary read-out electronics. It was found that insulating

liquids exhibit a featureless flat gain and phase response. Parasitic capacitances and cross coupling did not allow measuring the absolute permittivity with sufficient accuracy. A wider application range was examined in [17] showing measurements for various polymers and insulating liquids.

More theoretical analysis was done in 2001 using Green's Functions [60] to describe the electric field above the coplanar electrodes giving relatively simple analytical expressions. In 2002, the electrode surface charge was calculated by Matthijs W. Den Otter et. al. [62]. Mamishev et. al. examined the uncertainty in practical measurements with IDS [19]. He has shown that the IDS possess strong parasitic effects leading to non-linear dependencies between capacitance and the permittivity under test. In 2006, Xiaobei Li under A. Mamishev had elaborated few design principles to overcome these issues [59]. Few experimental designs were suggested in order to improve signal to noise ratio (SNR), crosstalk, and field distribution depth and sensitivity.

The work done on IDS still needs a detailed understanding of the dependence between the electrode structure on the figures of merit such as capacitance, sensitivity and accuracy to date. Since 2006, no major advances were found in literature that could give sufficient insight in such sensors in order to derive a structure for being directly suitable for a specific application. The presented thesis will investigate this particular point.

## 2.7 Summary

The oxidative deterioration of hydrocarbons was found to be driven by temperature. While a catalyst can accelerate this process, the dependence to temperature remains unchanged. Ketones and organic acids are the end result of the oxidation. This is molecularly different from the paraffin as it contains a **C=O** bond which exhibits a strong polarity. In particular, acids increase the acidity of

the solution. Acids are generally harmful in particular for metallic compounds while ketones have the potential to dissolve polymers.

The polar **C=O** group can be detected via infra-red spectroscopy such as FTIR. The carbonyl bond interacts with electric field oscillation present at its molecular resonance frequency at around 1720 cm$^{-1}$. Due to the Beer-Lambert law, absorption $A$ is related to a concentration. Thus FTIR is a potential resource to identify molecular changes within the material under test.

The FTIR spectroscopy has its advantage of being related to polar compounds such as **C=O** that exhibits a strong permanent polarity. This polarity can be measured over dielectrometry, i.e. the permittivity - which can be measured with IDS.

One critical aspect in order to use IDS in-field for measuring the dielectric properties is accurately measuring the permittivity. Without sufficient accuracy it will always be challenging to interpret the results and distinguish them from secondary impacts such as sensor effects. These effects may not always be stable under practical conditions. Thus, if effects such as a parasitic capacitance are removed, a measurement will only be dependent on the material under test. Therefore, one focus in this thesis is to develop an IDS capable of measuring the complex permittivity most accurately.

# 3 Laboratory analysis of the hydrocarbon

Although the ultimate goal of this study was the development of sensors with the potential *in-situ* use in a hydrocarbon based insulating liquid within transformers, the initial measurements in the characterisation of aging hydrocarbons were performed using a bench-top laboratory instrumentation. This approach had two advantages: 1) it allowed an analysis of these complex liquids via very reliable instrumentation, thus gaining insight into the chemistry and physics of the aging process. 2) the initial use of the instrument also served as valuable calibration points for the low cost IDS sensor that will be developed later in this study.

Hence, this laboratory analysis chapter examines the physical properties such as the permittivity, the conductivity and the infra-red absorbance of the liquid and its oxidation products. In order to measure these properties accurately and precisely, a dielectric liquid test cell was developed in section 3.1. In section 3.2, this cell was then used to measure the permittivity and the conductivity from an accelerated artificial insulating liquid oxidation experiment. Also, FTIR measurements were used to analyse the oxidation products during this experiment. This FTIR technique was utilised in section 3.3 to qualitatively reproduce the infra-red absorbance from the oxidation experiment by adding selected oxidation compounds to the unused liquid. Then, the quantitative analysis of the infra-red and dielectric response was investigated in experiments, for which moisture, ketones and acids were added to unused liquid.

## 3.1 Temperature Compensated Dielectric Test Cell

This section is similar to the publication in Ref. [25] by the authors Alex Risos, Nick Long and Gideon Gouws. All authors agreed with the use of the publication in this thesis.

In order to measure the dielectric properties, a novel dielectric test fixture had to be developed that is accurate and precise and does not show a capacitance affected by temperature. An accurate and precise measurement of the value of $\varepsilon_r$ is difficult to obtain, as the measurement may be influenced by the introduction of parasitic capacitances due to design issues. In addition, both the material under test as well as the test cell's geometry can show a temperature dependence, hindering a precise acquisition $\varepsilon_r$ over a wide temperature range [52, 56, 57, 63]. As a solution to this problem, the cross capacitor was proposed by Thomson and others [57, 64, 65]. This particular alignment of four electrodes for two capacitors in theory can make the capacitance independent of a change in the geometry and thus temperature, enabling sample measurements over a continuous temperature range. However, other effects such as electrode polarization and parasitic capacitances do change with the cell geometry and therefore with temperature. Further issues are the total capacitance per length of a cross capacitor which is a constant but small value of about 0.02 pF/cm [64]. At the same time the cross capacitor configuration requires the simultaneous measurement of two very high impedance values at low frequency which may be problematic for many commercial impedance analyzers.


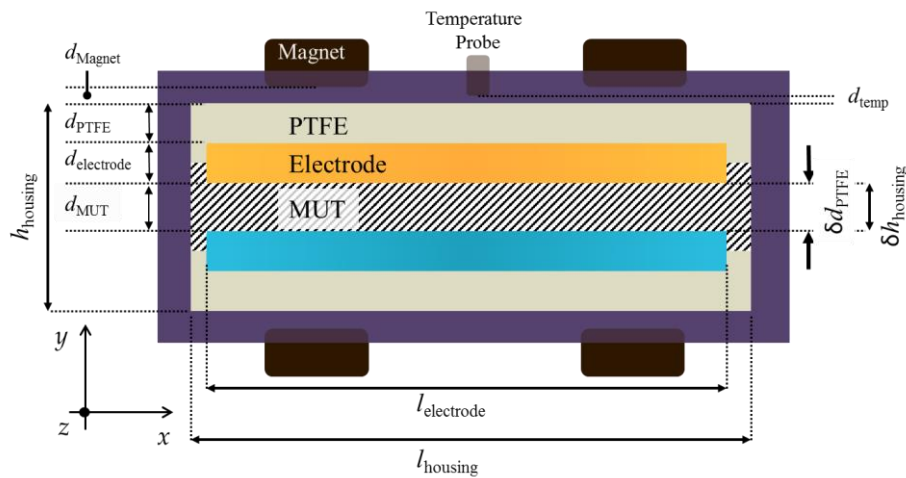
Figure 3.1. Schematic top view of the plane parallel test cell with labelled dimensions. Due to different expansion coefficients, the PTFE expansion $\delta d_{\text{PTFE}}$ is equal to the housing expansion $\delta h_{\text{housing}}$ keeping the electrodes at a constant separation, $d_{\text{MUT}}$.

37

In this work we solve some remaining issues using a parallel plate capacitor cell design. This design of a highly accurate and precise dielectric test cell exploits the thermal expansion of the different standard materials employed in this cell geometry. This minimizes dimensional changes over a wide temperature range. The design is evaluated according to various figures of merit that are obtained by calculations and the finite element (FEM) analysis. This is followed by the construction of the cell and the measurement of several dielectric liquids in the cell to show consistency with the expected behavior.

The dielectric cell in this work consists of the parallel plate capacitor design shown in Figure 3.1. Polymers in between the electrodes are often required as a support for the measurement electrodes and are used to provide electrical isolation. However, the use of polymers between the electrodes will introduce parasitic capacitances. This parasitic effect requires calibration techniques to compensate and increased temperature causes such polymers to expand and changes the geometry, thus affecting the capacitance. In the present design we have utilized the thermal expansion of the different parts in order to minimize temperature induced fluctuations in the cell geometry. As illustrated in Figure 3.1 (left), the PTFE spacers of thickness $d_{PTFE}$ are located on the outside of the electrodes instead of in-between the electrodes. The thermal expansion of $d_{PTFE}$ can compensate the thermal expansion of the steel housing, $h_{housing}$; as the housing expands, the PTFE spacer pushes the electrodes towards each other. These competing effects can compensate the thermal expansion when the absolute expansion of housing and PTFE is equal ($\delta d_{PTFE} = \delta h_{housing}$) as shown in Figure 3.1. Here, $\delta$ is the length difference (non-italic). This will result in a constant separation of the electrodes, $d_{MUT}$, exhibiting a capacitance independent of the temperature $T$. This also reduces the parasitic capacitance of the PTFE as the spacers are located away from the measurement area.

Table 3.1: Thermal expansion coefficients over the range of 20 to 100 °C for the materials used in the cell construction.

| Material | CTE $\alpha$ in $\mu$m K$^{-1}$ m$^{-1}$ |
|---|---|
| Steel 316 | $\cong 16$[66] |
| PTFE | $\cong 111$[67, 68] |
| SuperInvar 32-5 | $\cong 0.63$[69] |

The thermal expansion coefficients of different materials used in the cell construction can be seen in Table 3.1. PTFE is an inert polymer, resistant to swelling and with a large and linear temperature coefficient of thermal expansion over 30° to 90 °C [67, 68]. The stainless steel 316 housing exhibits a linear and small thermal coefficient of expansion [66]. The electrodes were manufactured from the material SuperInvar 32-5 (provided by Vulcan Steel, Auckland, New Zealand). This particular alloy of Iron and Nickel exhibits a very low thermal expansion coefficient ($\sim 1/25$[th] of that of the 316 stainless steel) from 0 – 100 °C and is thus negligible compared to the other two materials.

### 3.1.1 Theoretical calculations

The dependence of cell capacitance on the temperature $T$ in vacuum can be written as

$$C(T) = \varepsilon_0 A_{\text{electrode}}(T) / d_{\text{MUT}}(T) \; , \tag{3.1}$$

where the electrode area is the length along the $x$-axis ($l_{\text{electrode}}$) of the electrodes times its length in the $z$-axis ($z_{\text{electrode}}$): $A_{\text{electrode}}(T) = l_{\text{electrode}}(T) \, z_{\text{electrode}}(T)$. The electrode separation is therefore the difference of thicknesses in $y$-direction (see Figure 3.1): $d_{\text{MUT}}(T) = h_{\text{housing}}(T) - 2d_{\text{PTFE}}(T) - 2d_{\text{electrode}}(T)$. The thermal length expansion of these dimensions can now be calculated based on the values given in Table 3.1. To find starting conditions for the calculations, a minimum capacitance $C_{\text{min}}$ was defined, based on the upper impedance limit of the employed commercial impedance analyzer (a Hioki IM3590), using 1 Hz as the lower frequency limit.

In order to achieve the vacuum capacitance $C_{min} \sim 30$ pF, the dimension parameters were: $d_{electrode} = 6.52$ mm, $l_{electrode} = 100.5$ mm, $z_{electrode} = 48.0$ mm, $l_{housing} = 102.0$ mm and $d_{PTFE} = 1.16$ mm. The dimension $h_{housing}$ was calculated to find the iso-capacitive, $\delta C(T) = 0$, condition for the cell. Taking the derivative with respect to $T$ of Equation 3.1, and setting the right hand side to zero,

$$dC(T)/dT = 0 \ , \tag{3.2}$$

and solving for $h_{housing}$ at e.g. $T = 50°$ C, we find $h_{housing} = 16.666$ mm, returning a $d_{MUT} = 1.326$ mm and a vacuum capacitance $C = 32.21$ pF.

To understand the effect of manufacturing tolerances on the temperature compensation, we calculated the capacitance for the case where the housing and PTFE dimensions vary from the iso-capacitive condition with $h_{housing} = \pm 0.10$ mm and $d_{PTFE} = \pm 0.01$ mm, see Table 3.2. The PTFE tolerance is smaller as this is the thickness measurement precision of the commercially available PTFE sheet. These calculations show that the maximum effect is a change in capacitance of 0.004 pF across the temperature range. A housing with manufacturing tolerance significantly less than $\pm 0.10$ mm is easily possible with precision manufacturing techniques, if more accurate temperature compensation is required.

The simplified cell structure of Figure 3.1 has been simulated with the aid of finite element modelling (FEM) in Comsol Multiphysics version 4.2 using the electrostatics module. This module calculates the potential field according to Dirichlet boundary conditions solving the Laplace equation in the presence of dielectrics. The electrode potential was set to 1 V for the positive electrode and 0 V for the neutral electrode and housing. The capacitance is calculated from the ratio of total surface charge on each electrode to the voltage. In addition to the calculations, this simulation provides an understanding of the accuracy of the cell with different MUT; recorded as the deviation $D = (\varepsilon_{r,cell} - \varepsilon_r)/\varepsilon_r$.

**a**

Housing

PTFE ($\varepsilon_r = 2.1$)

Positive electrode

MUT, e.g. oil

Negative electrode

PTFE

Log($E/E_0$)

**b**

$\varepsilon_r = 1$

**c**

$\varepsilon_r = 20$

PTFE lip

$y$

$z$

$x$
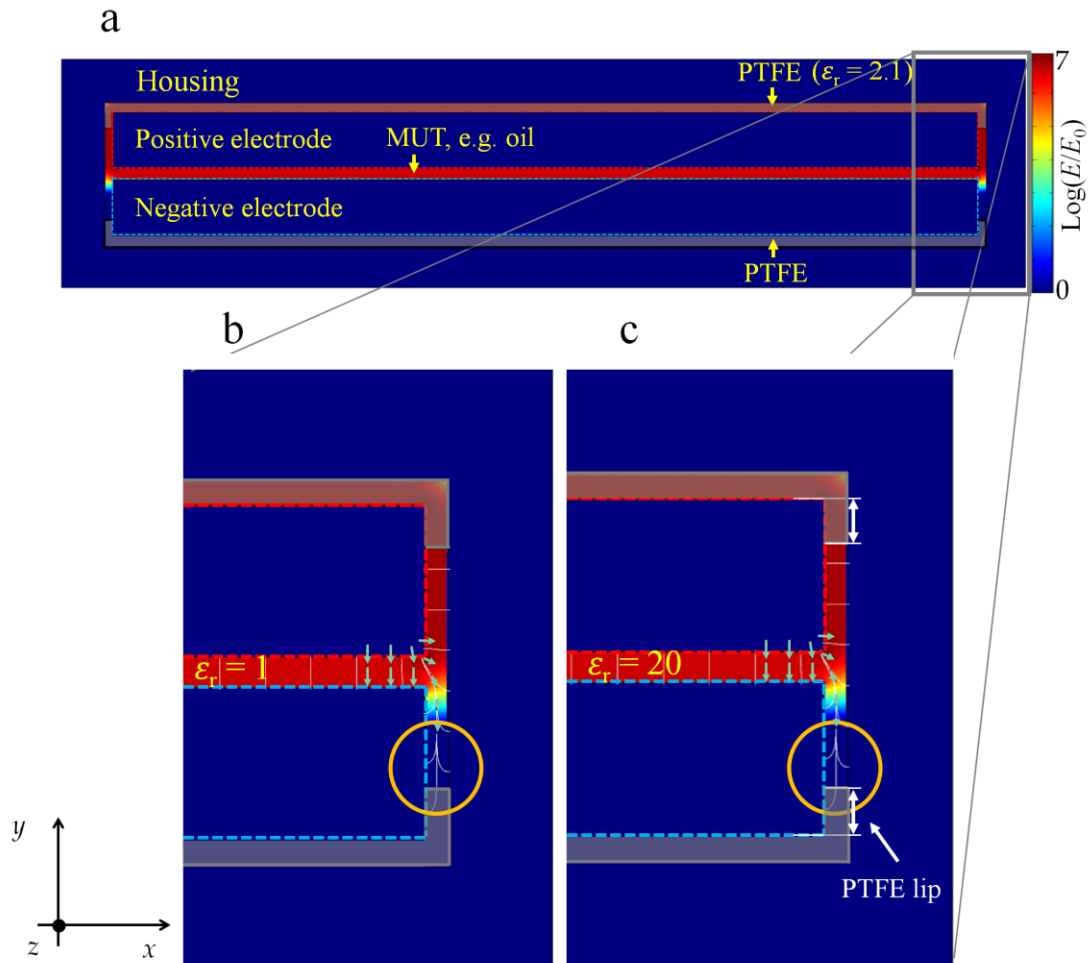
Figure 3.2. (**a**) Top view of the electric field distribution as a log scale ($E_0 = 1$ V/m) within the cell's domain with a closer view of the right hand side for $\varepsilon_r$ = 1 (**b**) and for $\varepsilon_r$ = 20 (**c**) as MUT. Arrows and streamlines (green and white) indicating the electric field direction and path. The electric field strength drops rapidly on the side of the grounded electrode and thus less affected by the presence of the PTFE when using different $\varepsilon_r$ (circles). The dotted lines indicate the electrode boundaries. The PTFE region in (**b**) and (**c**) is shaded grey.



Sample fill-in holes

Gold plated electrodes

BNC 4-wire contacts

Magnet

PTFE
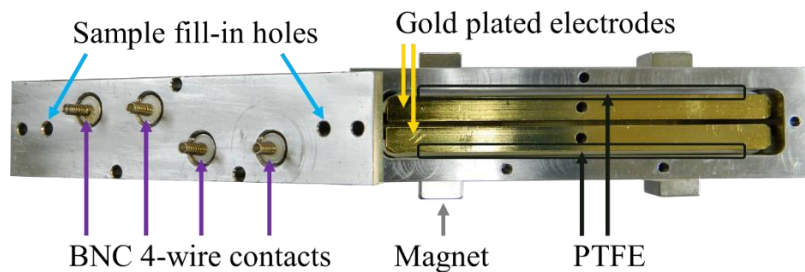
Figure 3.3. Top view of assembled cell with lid open (downside is shown upwards) showing inlet and outlet for liquids, gold plated electrodes, electrical contact of the BNC connector through springs and ½" Neodymium magnets keeping the electrodes pressed against the housing separated by the PTFE layer.

41

Table 3.2. Potential manufacturing tolerances and its impact on the cell capacitance with temperature.

| Tolerance | $C(T = 20\ °C)$ | $C(T = 90\ °C)$ |
|---|---|---|
| $\delta h_{\text{housing}} = +0.10$ mm | 29.952 pF | 29.949 pF |
| $\delta h_{\text{housing}} = -0.10$ mm | 34.837 pF | 34.841 pF |
| $\delta d_{\text{PTFE}} = +0.01$ mm | 32.704 pF | 32.707 pF |
| $\delta d_{\text{PTFE}} = -0.01$ mm | 31.732 pF | 31.728 pF |

In Figure 3.2a, the electric field distribution within the housing, the PTFE, the electrodes and the MUT is plotted via FEM. Dielectrics such as the PTFE can cause a parasitic capacitance, thus altering the measurement as the electric flux is proportional to $\varepsilon_r$ [22, 23]. In order to reduce the interference with the $\varepsilon_r$ measurement, the height of the PTFE lip, that is the thickness of the PTFE that extends in the $y$-direction between the electrodes, should be minimized. However, this lip height must be sufficiently large to hold the electrodes rigidly in position (Figure 3.2c). The PTFE lip height was then chosen to be $d_{\text{electrode}}/3$ as depicted in Figure 3.2b and 3.2c, resulting in a constant $D = 0.005\%$ for $\varepsilon_r = 2$ to 20. The electric field is emphasized via black vector arrows and white streamlines indicating the direction and path of the electric field.

These results are consistent with the field distribution observed within the test cell highlighted via circles in Figure 3.2b ($\varepsilon_r = 1$) and Figure 3.2c ($\varepsilon_r = 20$). It can be seen that the simulated field distribution does not exhibit a change in the electric field distribution through a change in $\varepsilon_r$. Thus, the simulated capacitance matches the calculations and results in a sensitivity directly proportional to the $\varepsilon_r$ of a MUT with $S = \partial C/\partial \varepsilon_r = 32.210$ pF.

### 3.1.2 Parts and assembly

The assembled cell with its components is shown in Figure 3.3. The inlet and outlet for liquid samples is via two 3 mm holes. The two gold plated electrodes have electrical contact through stainless steel metal springs attached to four BNC connectors on the lid for the four wire measurement principle. Small magnets

keep the electrodes in place, allowing the required free expansion of the PTFE. The housing is machined from one block of non-magnetic stainless steel grade 316. The electrodes made of SuperInvar 32-5 were plated via an electrochemical deposition process with 10 µm nickel and 1 µm gold. This combination of diffusion barrier and gold provides sufficient inertness at elevated temperatures. The cell temperature was determined via a PT100 sensor submerged into the housing as shown in Figure 3.1. The measured dimensions after manufacturing were $h_{housing}$ = 16.57 mm, $d_{electrode}$ = 6.52 mm and $d_{PTFE}$ = 1.16 mm. The temperature probe was separated by $d_{temp}$ = 0.39 mm to the inside of the housing. The measurement uncertainties of these dimensions were ± 0.01 mm.

Parasitic effects such as stray capacitances or external electric fields can also interfere with the measurement [16, 22, 59]. This problem is addressed through an electric shield, a 3D Faraday housing, that is connected to the ground of the measurement instrument. A sample exchange arrangement provides the option to measure the air capacitance and the MUT capacitance without interfering with the mechanical arrangement of the setup. This increases the reliability and allows thermal expansion of the MUT. Parasitic effects due to measurement leads were reduced by using a four wire measurement system, consisting of current and voltage leads connected directly to the electrodes.

### 3.1.3 Theory verification

In order to verify the calculations and simulations, a series of measurements with the test cell were performed. First, the temperature dependence of the cell capacitance was measured and compared with the calculations. Secondly, an insulating liquid (non-polar) and an organic acid (polar) liquids were used to demonstrate the accuracy and range of applicability.

The measurements with our cell were done in the following way: The disassembled cell was cleaned by washing with dichloromethane until no residue

of the previous liquid could be found. All parts (electrodes, PTFE, housing, lid) were placed in a 50 °C heated environment to vaporize potential traces and moisture. The subsequent assembly of the cell was accompanied by a measurement of the air capacitance at 30 °C cell temperature. The MUT was inserted through one of the two holes in the lid via a syringe. The $\varepsilon_r$ value was determined by the ratio of the air capacitance and the capacitance with MUT.

The measurement settings were: 1 $V_{RMS}$ between the electrodes, 0 V for the ground housing potential, a total of 204 data points were recorded and averaged for each temperature measurement.

The impedance measurements were done with our four wire impedance analyzer and the cell's capacitance was calculated from these measurements over the relation to its impedance $Z = C^{-1}\omega^{-1}$. The temperature was regulated via a temperature controller and two heating elements with total power 30 W, attached to each long side of the housing. The precision of each temperature set point was ± 1 mK using the "TEC Temperature Controller TCLV" (Electron Dynamics Ltd, UK) while the absolute accuracy was determined to be ± 10 mK.

In order to estimate the magnitude of the thermal lag from $T_{housing}$ (temperature probe within the housing) to $T_{MUT}$, we performed an experiment with two PT100 temperature probes, one within the housing and another inside the cell, within the MUT. The cell was heated to set points of 30, 50, 70 and 90 °C. It was found that the temperature difference was about $T_{housing}$ - $T_{MUT} = 0.1$ °C during heating. After $T_{housing}$ reaches a set point, the time to equilibrate $T_{housing} = T_{MUT}$ was about $\tau \approx 20$ seconds. Based on these observations we waited at least 5 minutes before conducting $\varepsilon_r$ measurements.

Figure 3.4 shows the air capacitance vs. temperature measured by the test cell together with the calculated values of the vacuum capacitance. The capacitance measurements were carried out at 5 kHz over three temperature

cycles from 20 °C to 90 °C. The capacitance measurements over three cycles, within a 24 h test, were stable at $C_{air}$ = 35.322 pF with a standard deviation of about ± 0.001 pF. The cell's capacitance variation due to multiple cleaning and assembly was stable at $C_{air}$ = 35.32 ± 0.01 pF.
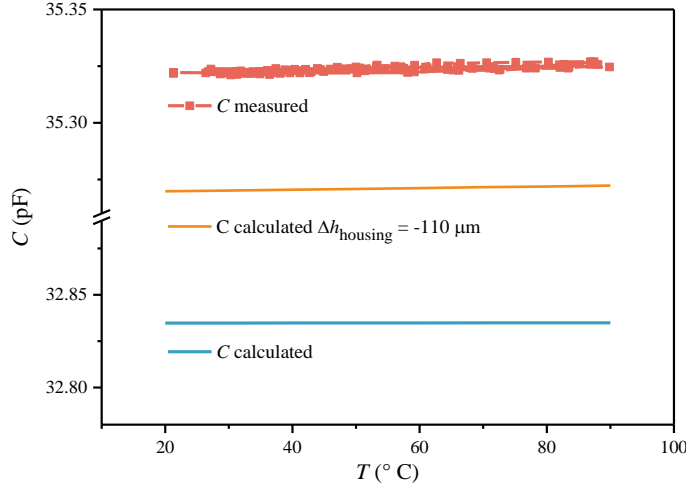


Figure 3.4. The vacuum capacitance as calculated for a cell with ideal dimensions (bottom line), the calculated capacitance for the actual cell dimensions (middle line) and the actual measured cell capacitance (top line).

A larger capacitance was measured than that predicted by the calculations for the iso-capacitance condition. This was predominantly due to tolerances of the geometry that reduced the electrode separation. The housing dimension, $h_{housing}$, was designed to be 16.666 mm while the manufactured version was measured to be 16.57 ± 0.01 mm. The difference of 96 ± 10 µm resulted in a closer electrode separation $d_{MUT}$ = 1.326 mm → 1.23 mm. The calculated capacitance using the measured dimensions is plotted in Figure 3.4. This shows an agreement of the housing measurement with our calculations; the capacitance magnitude increased and a slight slope of $\partial C / \partial T \approx$ 0.00003 pF/K occurred. Over the temperature range from 30 to 90 °C, this yields a maximum difference of 0.006% which was measurable but also lies within the noise of this experiment, i.e. 0.005%. The remaining difference between the calculated and measured

capacitance of 0.05 pF in Figure 3.4 is due to measurement uncertainties of the geometry which propagates into the calculations.

### 3.1.4 Measurement examples

The performance of the cell was evaluated by measuring the temperature dependent permittivity of common liquids used in industry. In addition, we measured recommended standard liquids such as water, cyclohexane and methanol and compared them with literature values [48].

An insulating liquid (BS 148 class - I, Savita Oil Tech. Ltd., Mumbai, India) represents a MUT which is non-polar and insulating. It is used in industry for high voltage insulation and cooling [3]. The insulating liquid was measured at 50 Hz and up to 90 °C according to the standard for insulating liquids [44], Figure 3.5. A comparison with values obtained from a standard industry instrument (DTL C - Dissipation Factor Oil Tester, BAUR GmbH, Sulz, Austria) shows a good agreement with the test cell's measurements. The DTL C measurements were repeated 3 times from which the average has been taken with a standard deviation $\Delta\varepsilon_r \pm 0.02$ and $\Delta(\tan\delta) \leq 13\%$.

Levulinic acid was measured as this compound exhibits a stronger polarity and dielectric loss factor than compared to insulating liquid [50]. This substance is widely used and of great importance for processing e.g. in the food industry and pharmaceutical industry [70]. The permittivity of this substance has been investigated previously [50] and therefore a comparison with literature values is possible. The measurements on the Levulinic acid (Sigma Aldrich, L2009, 98% purity) were done at a measurement frequency of 100 kHz similar to the conditions of Ref. 36. We measured $\varepsilon_r$ values which were consistently 0.001 less than the reported literature values. The standard deviation in this experiment was $\pm$ 0.0008. Thus, the extracted literature values (c.f. Fig. 9 in Ref. 36) are consistent with the cell measurements plotted in Figure 3.6.

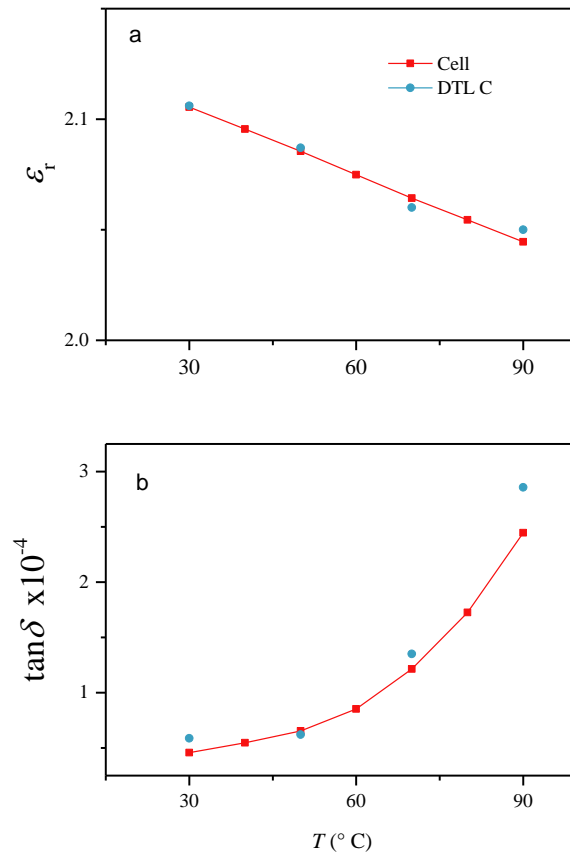Figure 3.5. (a) The measured permittivity $\varepsilon_r(T)$ over the temperature $T$ of insulating liquid for the cell and an industry device DTL C. (b) $\tan\delta$ over temperature $T$ of the same insulating liquid as measured via the cell and compared with DTL C measurements.
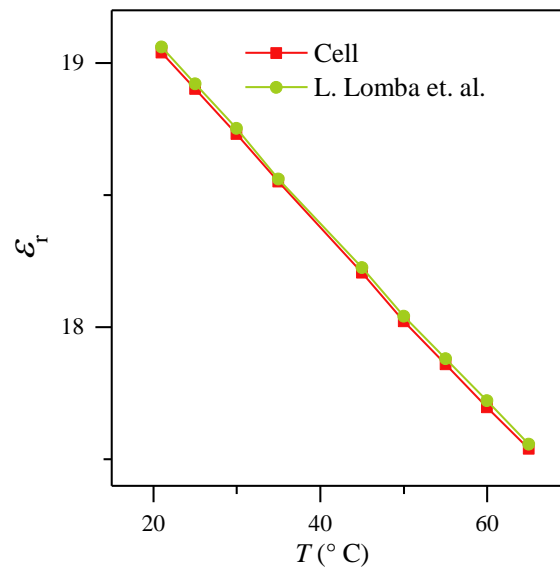


Figure 3.6. The measured permittivity over the temperature of Levulinic acid compared with literature values [50].

Table 3.3 shows the measured $\varepsilon_r$ of liquids via our cell: insulating liquid, Levulinic acid as well as cyclohexane and methanol. These values are compared with literature values. Cyclohexane (227048 Aldrich) was measured at 50 Hz and 30 °C, as this is an insulating liquid. Methanol (322415 Aldrich) and deionized water from our laboratory were measured at 100 kHz and 25 °C and 0.1 $V_{RMS}$. Deionized water and methanol has a high dielectric loss factor compared to insulating liquids. In addition, electrode polarization effects can be significant during low frequency measurements on such liquids but will be reduced when using higher frequencies. To compare the permittivity of water with literature values [48] we calculated the real part of the measured complex permittivity $\varepsilon_r$.

Table 3.3. Measurements with standard liquids and Levulinic acid at 25 °C.

| MUT | $\varepsilon_r$ measured | $\varepsilon_r$ literature |
|---|---|---|
| Cyclohexane | $2.0112 \pm 0.0008$ | $2.008 \pm 0.006$[48] |
| Methanol | $32.751 \pm 0.015$ | $32.65 \pm 0.03$[48] |
| Levulinic acid | $18.732 \pm 0.009$ | $18.75 \pm 0.05$[50] |
| Water | $78.541 \pm 0.018$ | $78.35 \pm 0.05$[48] |

The permittivity values measured on the different liquids are well within the reported literature values. The uncertainty in the measurements was about $\pm$ 0.005% due to the noise of the impedance analyzer which explains the larger absolute error for larger values of $\varepsilon_r$. This observed noise is within the reported value given in the specifications of this instrument. A slight difference in the magnitude may be due to a different measurement frequency, as well as the impurity content of the liquids. However, in these measurements the precision in measuring $\varepsilon_r$ after cleaning and reassembly stays within $\pm$ 0.005%.

### 3.1.5 Conclusion of the test cell development

A design for a temperature insensitive parallel plate dielectric test cell was proposed. This iso-capacitive cell exhibited remarkably high performance in terms of accuracy and precision over a temperature range of 20 °C to 90 °C. The FEM

simulated high accuracy (99.995%) and the measured high precision ($\Delta C = \pm 0.01$ pF) after multiple test cycles was confirmed through experiments using insulating and conducting liquids. These measured permittivity values were consistent with literature values to $> 99.7\%$. Large manufacturing tolerances up to $\pm$ 100 µm have a small impact on the iso-capacitance making this design viable across a wide range of studies. This cell can be used for yielding reference values of the complex permittivity of liquids at various temperatures.

## 3.2 Hydrocarbon oxidation analysis

The background chapter introduced liquid hydrocarbons in some detail, in particular the oxidation mechanism. However, this lacked an experimental verification using an insulating liquid. Accelerated oxidation for instance, can also be achieved through artificial degradation experiments [28, 30]. The paraffinic oxidation is a well-understood hydrocarbon decomposition process when subjected to thermal energy and oxygen [12]. It was mentioned that the hydrocarbon may not be a perfect linear paraffinic molecule [27] and in combination with multiple possible oxidation pathways [13], making an exact prediction of the oxidation products is difficult. However, the oxidation can be studied through artificial degradation experiments of insulating liquids [28, 30]. This chapter will artificially degrade an insulating liquid, measure its FTIR response and its dielectric properties.

The results described in this chapter have been published by the author of this thesis in Ref. [24]. Some paragraphs are similar to this publication. The permission of reprinting the published work is granted due to shared copyright under the condition that the original research is credited.

### 3.2.1 Oxidation experiment setup

In order to develop a sensitive device for detecting insulating liquid oxidation, the generation of oxidation products with the employed insulating liquid had to

49

be investigated via an experiment. The increase of these products was artificially achieved by an accelerated oxidation process utilizing elevated temperatures and oxidation catalysts. This experiment also included components which are expected to be present in environments where such liquids are used, such as coolant fluids for energized conductors within oil transformer environments [3]. This method was similar to previous reports [28, 30, 39, 45]; six liter of insulating liquid (BS 148 class - I, Savita Oil Tech. Ltd., Mumbai, India) was subject to oxidation at 140 °C for about 600 hours. In addition, one liter air headspace, 500g insulating paper (Weidmann Diamond Dotted 380 µm, ten 10-by-10 cm sheets, Weidmann Electric Technology Inc., St. Johnsbury, VT, U.S.A.) and industrial grade copper (40 cm$^2$) as an oxidation catalyst were introduced. Copper accelerates the oxidation by providing a free oxygen radical through the copper oxide on its surface [13]. Samples of 20 ml each were taken weekly via a glass syringe. These samples were stored in glass-sealed vials, flushed with nitrogen. A reduction in the headspace pressure while extracting the samples was balanced by injecting gaseous nitrogen. Figure 3.7 shows the experimental setup for the accelerated oxidation process.
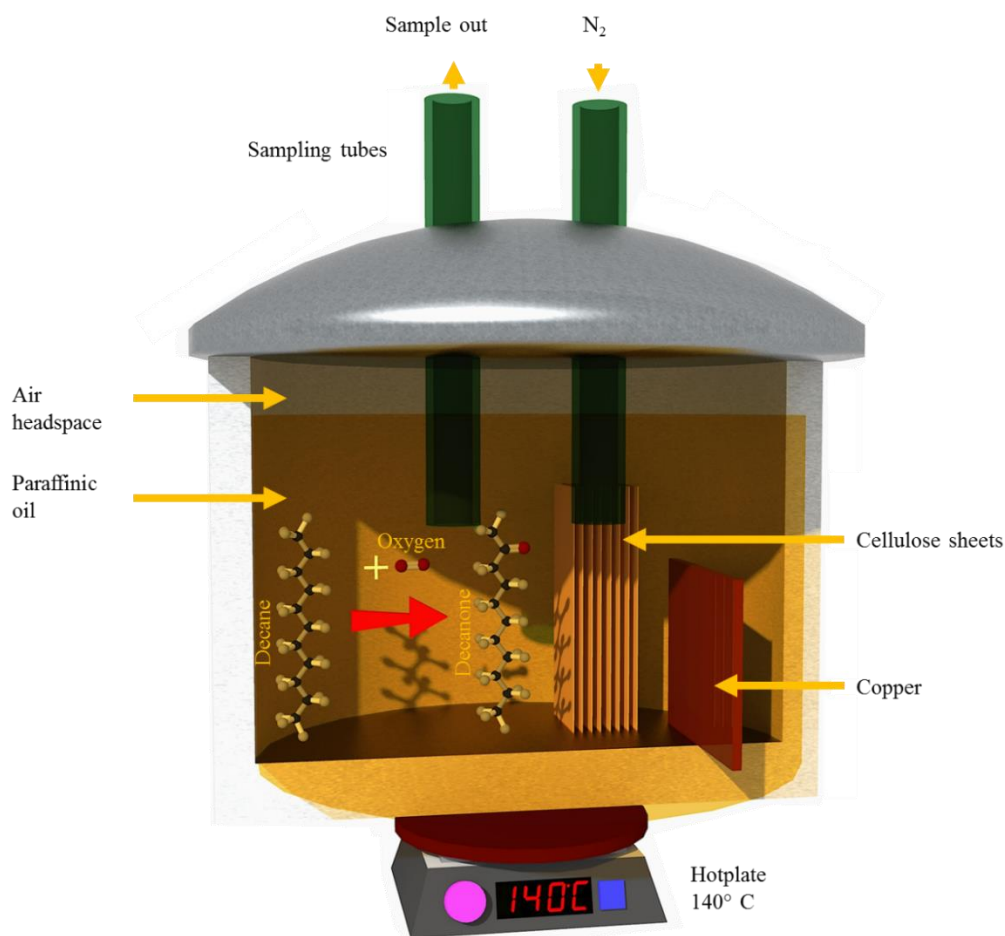
Figure 3.7. The environment containing six liters of paraffinic insulating liquid, copper and transformer winding paper. This was heated to 140 °C for 600 h for the accelerated oxidation experiment. A simplified, unidirectional reaction of an alkane with oxygen to a ketone is shown [24].

### 3.2.2 FTIR measurements & setup

The FTIR absorbance, $A$, was measured via an FTIR spectrometer (Figure 3.8a) with a custom made liquid sample cell (Figure 3.8b) which consisted of a rigid PTFE cell housing and 20 mm diameter KBr-windows having a thickness of 5 mm. The sample thickness was $d = 1.000 \pm 0.005$ **mm**. The mechanism of the FTIR absorbance working principle is described in section 2.2. Here, the absorbance is the total absorbance of the substance subtracted from the atmospheric background and the KBr windows;

$$A = A_{\mathrm{MUT}} - A_{\mathrm{bg}}. \tag{3.3}$$

A FTIR spectrometer (Spectrum One, PerkinElmer Inc., Waltham, MA, U.S.A.) was used to acquire the spectra of 15 measurements per sample with a 0.5 cm$^{-1}$ resolution at a 21 $\pm$ 1 °C room temperature. These were the *standard* settings for the FTIR measurements in this thesis unless specified otherwise.
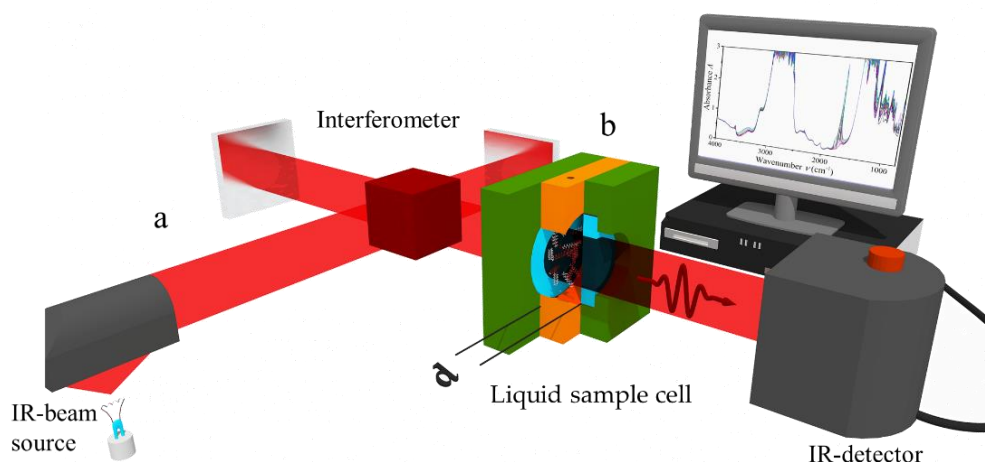


Figure 3.8. (a) The FTIR spectrometer beam path is shown schematically. (b) Custom made sample cell for the infra-red measurement having transmission line $d = 1$ mm (false color for visualisation purpose) [24].

The insulating liquid was measured during the oxidation process. Figure 3.9a shows the background reduced infra-red spectra of the initial (0 hours) and the last (600 hours) sample. The region around $v = 3000$ to 2700 cm$^{-1}$ and $v = 1450$ to 1200 cm$^{-1}$ represent strong alkyl absorptions which are obscured due to the limited instrument sensitivity due to a very strong absorbance. The presence of absorptions below 3000 cm$^{-1}$ indicates paraffinic hydrocarbons. Aromatics are known to show a strong absorbance between 1500 to 1650 cm$^{-1}$ [33] which was not observed in this experiment. In the molecular infra-red fingerprint region (< 1000 cm$^{-1}$), the long chain methyl rock oscillation at around $v \approx 750$ to 800 cm$^{-1}$ was observed, indicating a major presence of saturated hydrocarbon molecules. The region from 750 to 1000 cm$^{-1}$ exhibited a general absorbance increase but additional peaks were absent. The most notable change, when comparing the

spectra before and after oxidation, is in the carbonyl region (1780 to 1650 cm$^{-1}$) where a strong absorption peak has occurred. In addition, a small absorbance for free hydroxyl is emerging at $v \approx 3600\,\mathrm{cm}^{-1}$. A minor absorption in the water region (3600 to 3300 cm$^{-1}$) was observed after 605 hours at 140 °C. The time evolution of the infra-red absorbance is shown as a 3D plot in Figure 3.9b illustrating the change of the absorbance spectra with time.

During this oxidation process, various states of hydrocarbon oxidation are reached. The complexity of the hydrocarbon species present (e.g. methyl, di-methyl or tri-methyl) and the following variation of oxidation products, causes absorption in multiple neighbored regions leading to a wide absorption band. This wide absorption band with a center of 1720 cm$^{-1}$ is due to the decomposition of the paraffin which causes a formation of low molecular weight hydrocarbons, absorbing at a higher wavenumber region than 1720 cm$^{-1}$. The formation of high molecular weight hydrocarbons shift towards a lower wavenumber region than 1720 cm$^{-1}$ [5, 12, 13, 33]. The **C=O** bond strength is weaker for longer chained molecules but for small molecules the **C=O** bond is stronger and oscillates at a higher frequency. Additionally, multiple oxidation states of a hydrocarbon can be initiated, affecting the line width and position of the **C=O** absorbance.

Figure 3.9c shows the gradual increase of the integrated carbonyl and the moisture absorbance region, as well as the total increase in the infra-red absorbance (4000 to 500 cm$^{-1}$) with oxidation time. The three lines in this figure show a linear increase with time. It can be seen that the absorbance change within the carbonyl absorbance region is about +300%.
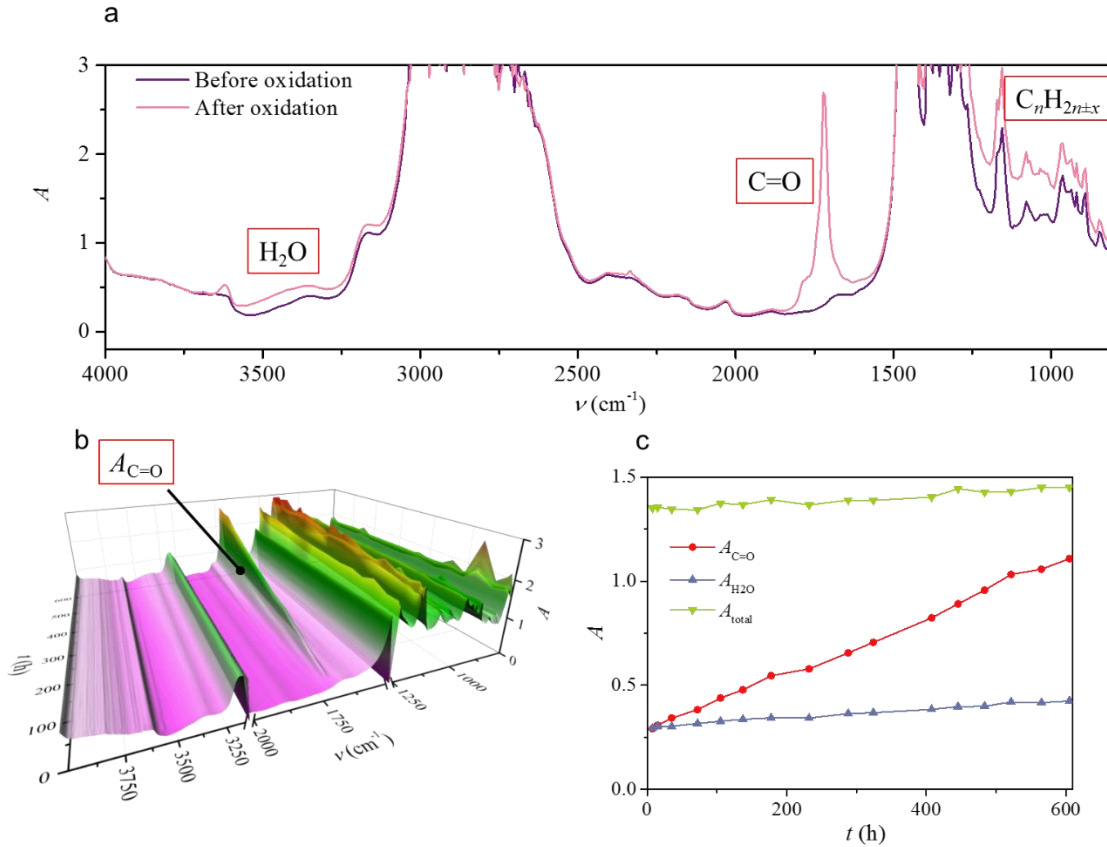
Figure 3.9. (a) Infra-red absorbance A over the wavenumber $\nu$ of the insulating liquid before and after oxidation experiment. (b) FTIR absorbance A over the $\nu$ and oxidation time $t$ of the oxidation experiment showing a distinct increase at 1720 cm$^{-1}$. (c) Integrated $A$ of the carbonyl region, the moisture region and the total integral of the spectrum over time of the oxidation experiment [24].

### 3.2.3 Moisture measurements

Because of the observed increase in the FTIR absorbance of 50% in the moisture region, the moisture value in weight as parts per million was then determined though eNZOil Ltd, (Lower Hutt, New Zealand) by means of a standard coulometric Karl-Fisher titration method (831 Coulometer, Metrohm AG, Switzerland).

Both the moisture and the infra-red absorbance was steadily increasing with oxidation time, Figure 3.10. A comparison of both values gave a correlation coefficient of 97%. While the FTIR spectra indicates the generation of hydroxyl

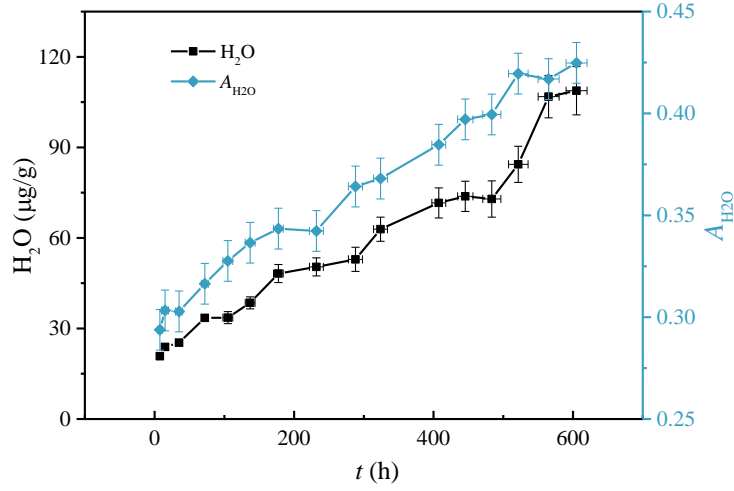compounds during oxidation, the moisture results show that water is indeed formed in this oxidation process.



Figure 3.10. Moisture concentration and the corresponding infrared absorbance of the insulating liquid as function of the experiment duration.

## 3.2.4 Dielectric measurements of the permittivity and DC conductivity

The dielectric measurement of $\varepsilon_r$ was done over a frequency range from 1 Hz to 10000 Hz at room temperature (21 ± 1 °C) using the parallel plate dielectric test cell connected to the impedance analyzer IM3590. The measurement theory to acquire the dielectric properties from an impedance measurement is described in section 2.4. Here, a potential of 1 $V_{RMS}$ across the test cell's electrodes was applied to gain the impedance and the phase to calculate the complex permittivity from the capacitance. From this permittivity, the real part of the permittivity and the conductivity was calculated (The appendix A shows the raw measurements for the impedance $Z$, the phase $\varphi$, the $\tan\delta$ and the magnitude of the permittivity $\varepsilon_r = \sqrt{(\varepsilon_r' - i\varepsilon_r'')}$).

The featureless lines in Figure 3.11 show that the permittivity, $\varepsilon_r'$, is constant across the measurement frequency and scales proportionally with aging time. The conductivity shown in Figure 3.12 shows a similar picture. The conductivity measurements, $\sigma_{DC} = \omega\varepsilon_0\tan\delta$, show no dependence with frequency. Hence, both

55

these parameters can be regarded as static relative permittivity and DC conductivity as anticipated in section 2.4. However, it was required to prove that this is indeed the case and that the theory (section 2.4) is applicable for this thesis. Thus, the permittivity and conductivity can be plotted at 50 Hz more intuitively over time, Figure 3.13. A linear increase in $\varepsilon_r^?$ and a non-linear dependency of the conductivity with time was found in this experiment. These values indicate a monotonic generation of impurities with experiment duration. The standard deviation of the permittivity and conductivity measurements were $\leq 0.02\%$ with a total accuracy of $\leq 0.08\%$. The accuracy of the time was within $\pm 2\%$.
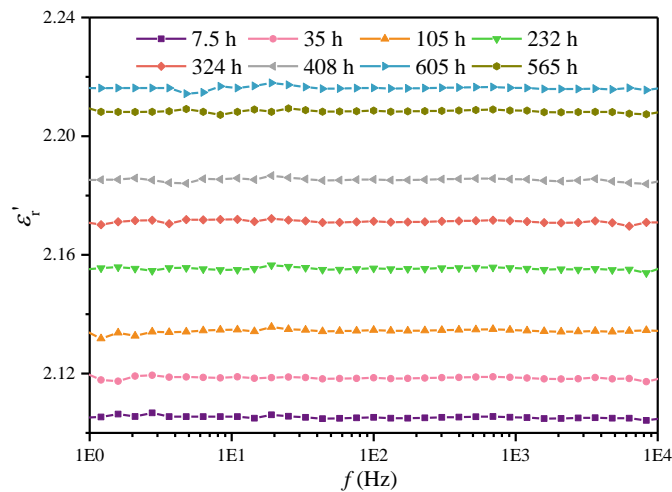


Figure 3.11. The relative permittivity as a function of frequency for selected times of the oxidation experiment.
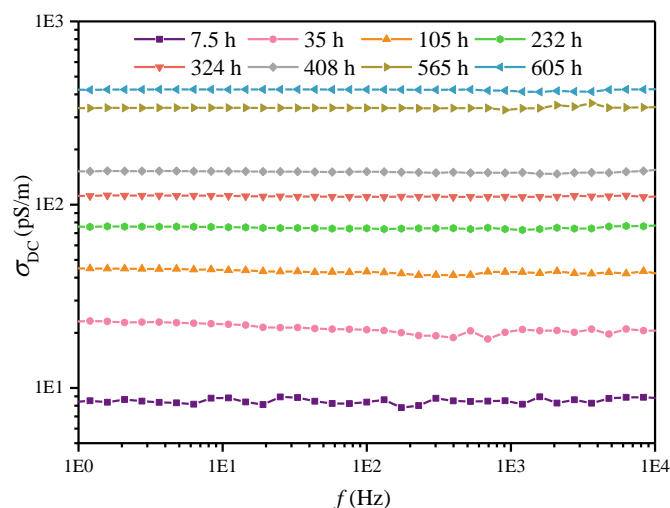
Figure 3.12. The DC conductivity as a function of frequency for selected times of the oxidation experiment.
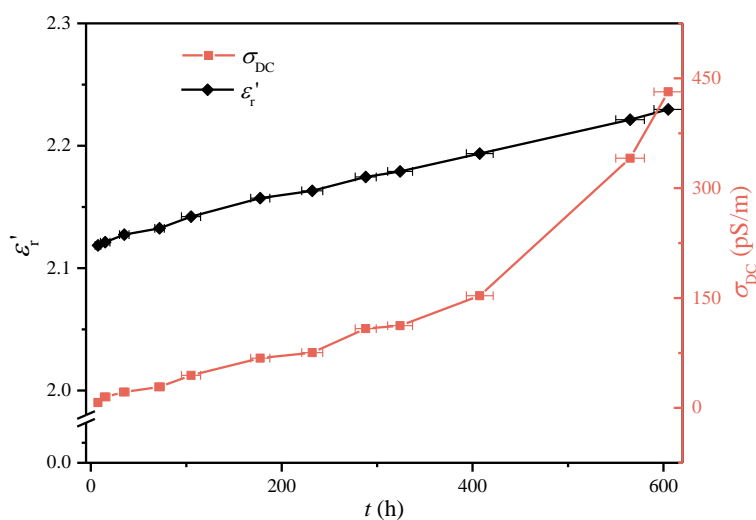


Figure 3.13. Permittivity $\varepsilon_r$' and conductivity over time of the oxidation experiment.

### 3.2.5 Relation between the permittivity $\varepsilon_r$ and infra-red absorbance $A$

This section examines the correlation of the infra-red absorbance with the permittivity. The FTIR analysis has shown that the carbonyl absorbance increased linearly. If the number of dipoles increases, the permittivity must increase as well. Hence, a strong correlation between the two factors is anticipated. This will be checked now in detail. For sufficiently small values of $c$

[33], the infrared absorption $A$ can be written by the Beer-Lambert-law to a wavenumber dependent parameter $\beta(v)$ by

$$A_v = \beta(v)cd \,. \tag{3.4}$$

This is linearly proportional to a concentration $c$ (mol/l) assuming the molecular attenuation coefficient $\beta(v)$ and infra-red liquid cell distance $d$ are constant (see section 2.2 and 3.2.2 for more details about the FTIR measurement). The static permittivity $\varepsilon_r$ can be calculated using the normalized difference of the integrated infra-red absorption,

$$A = (\textstyle\int A_{C=O} - \int A_{C=O,\,base}) / \max(\int A_{C=O}) \,. \tag{3.5}$$

The variable $A$ is the background reduced absorbance for the carbonyl peak, $A_{C=O}$, its base value for unused liquid, $A_{C=O,\,base}$, and its maximum value, $\max(A_{C=O})$. The permittivity can be written as $\varepsilon_r = \chi+1$, where $\chi$ is the susceptibility that represents the degree of polarisation in a dielectric. Values for $\chi_{C=O}$ and the range of the molar concentration $c$ of the oxidation products can be estimated from literature [5, 12, 13, 71]. Defining a maximum concentration $c$ when $A = 1$ and calculating the magnitude of the permittivity according to the infra-red absorbance and $\chi_{base}$ as a base value of the employed insulating liquid;

$$\varepsilon_r = cA\chi_{C=O} + \left(1 - cA_{C=O,\,base}\right)\chi_{base} + 1 \,. \tag{3.6}$$

The susceptibility parameter $\chi_{base} = 1.12$ was obtained from a $\varepsilon_r$ measurement at room temperature of the untreated (0 h) sample. If the oxidization products are a 50:50 ratio of formic acid and 2-decanone, the value for the susceptibility can be evaluated to $\chi_{C=O} = 31$, using the values in Ref. [71]. The value for $\varepsilon_r$ could be reproduced well using a concentration value of $c = 0.0048$ mol/l at the end of the experiment (605 h). The results for the calculated and the measured values of $\varepsilon_r$ are shown in Figure 3.14. A striking similarity between the $\varepsilon_r$-value calculated from the carbonyl absorbance (C=O) and the measured relative static permittivity

has been found. The small fluctuations between the measured and calculated $\varepsilon_r$ could be reproduced precisely having a correlation coefficient of 99.7%.
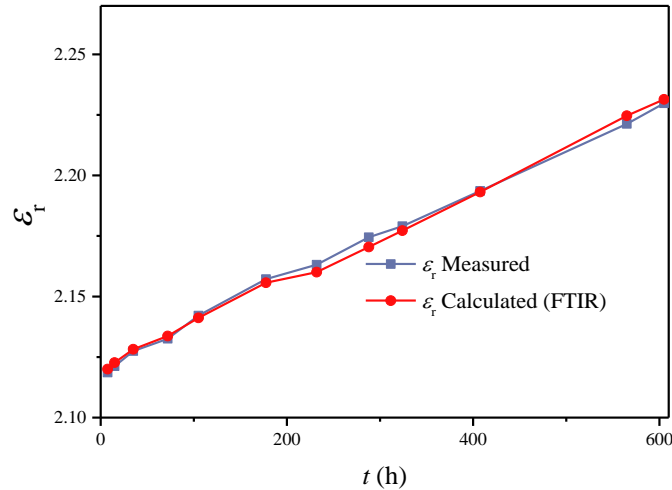


Figure 3.14. Measured magnitude of the relative permittivity vs. calculated relative permittivity from the FTIR absorbance over time of the experiment.

This experiment has shown that there is a relation between the infra-red absorbance and the relative permittivity as anticipated from section 2.4. This is useful as the permittivity and the infra-red absorbance can now be used complementarily in this thesis.

### 3.2.6 Conclusion of the oxidation experiment

An accelerated oxidation experiment of insulating liquid was conducted at 140 °C. In selected intervals, the value of the permittivity and the infra-red absorbance was acquired in the laboratory. The linear increase of $\varepsilon_r$ and the broad carbonyl absorbance $A_{C=O}$, at around $v = 1720 \text{ cm}^{-1}$ suggest that the permittivity is predominantly changed due to a mixture of arising carbonyls in the paraffinic liquid. This is emphasized with a correlation of 99.7% between the infra-red absorbance versus the permittivity. This strong relation requires a more detailed analysis to understand the permittivity and infra-red absorbance in more detail.

## 3.3 FTIR and dielectric properties of potential oxidation products
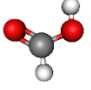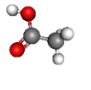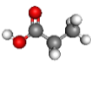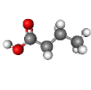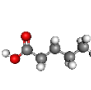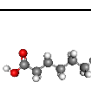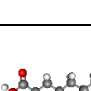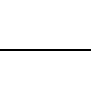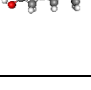
A general increase in the permittivity, moisture content as well as carbonyl content was consistent during the oxidation experiment time. Thus, in this section the measurements were used to evaluate the infra-red and dielectric response for various carbonyls (ketones, acids) and moisture. This was done via diluting these compounds in defined concentrations (0.1 to 0.001 mol/l) among unused insulating liquid. Dielectric measurements were done to evaluate their impact on $\varepsilon_r$. Section 3.3.1 shows measurements of the infra-red absorbance from diluted acids in the liquid. Section 3.3.2 shows the infra-red and dielectric measurements when adding moisture in the liquid. Section 3.3.3 shows the infra-red and dielectric measurements when adding ketones in the paraffinic liquid. Section 3.3.4 shows the infra-red and dielectric measurements when adding organic acids in the liquid.

### 3.3.1 Infra-red absorbance of selected diluted organic acids

Acids are naturally occurring due to the paraffin oxidation process (see section 2.1). Section 3.2 has shown that the infra-red absorbance at 1720 cm$^{-1}$ was increasing with time of the oxidation experiment. It is suspected that this might have originated due to the increasing number of acids in the paraffinic liquid. Hence, in order to evaluate the infra-red response of acids, a range of low to mid molecular weight organic acids were diluted in the unused paraffinic insulating liquid to 0.01 mol/l. The selected organic acids are listed in Table 3.4. These solutions were made using a micro pipette and 1 liter of unused insulating liquid. The error in this process was estimated with ± 5%. Oxopentanoic acid, is shown to be a product when cellulose is subject to decomposition [70, 72]. Formic acid is a product arising from the insulting liquid deterioration. Thus, besides the

separate investigation of nine different acids, a mixture of formic acid and 4-oxopentanoic acid was also measured.

Table 3.4: list of organic acids used for infra-red analysis

| Acid and formula | Structure | Concentration | Sigma-Aldrich number |
|---|---|---|---|
| Methanoic acid <br> HCOOH | | $\geq 85\%$ | Sigma-Aldrich <br> 27002 |
| Ethanoic acid <br> $CH_3COOH$ | | $\geq 99.7\%$ | Sigma-Aldrich <br> 320099 |
| Propanoic acid <br> $CH_3CH_2COOH$ | | $\geq 99.5\%$ | Sigma-Aldrich <br> 402907 |
| Butanoic acid <br> $CH_3(CH_2)_2COOH$ | | $\geq 99\%$ | Sigma-Aldrich <br> B103500 |
| Pentanoic acid <br> $CH_3(CH_2)_3COOH$ | | $\geq 99\%$ | Sigma-Aldrich <br> 240370 |
| Hexanoic acid <br> $CH_3(CH_2)_4COOH$ | | $\geq 98\%$ | Sigma-Aldrich <br> W255904 |
| Heptanoic acid <br> $CH_3(CH_2)_5COOH$ | | $\geq 97\%$ | Sigma-Aldrich <br> H9378 |
| Octanoic acid <br> $CH_3(CH_2)_6COOH$ | | $\geq 98\%$ | Sigma-Aldrich <br> W279900 |
| 4-oxopentanoic acid <br> $CH_3C(O)CH_2CH_2CO_2H$ | | $\geq 97\%$ | Sigma-Aldrich <br> W262706 |
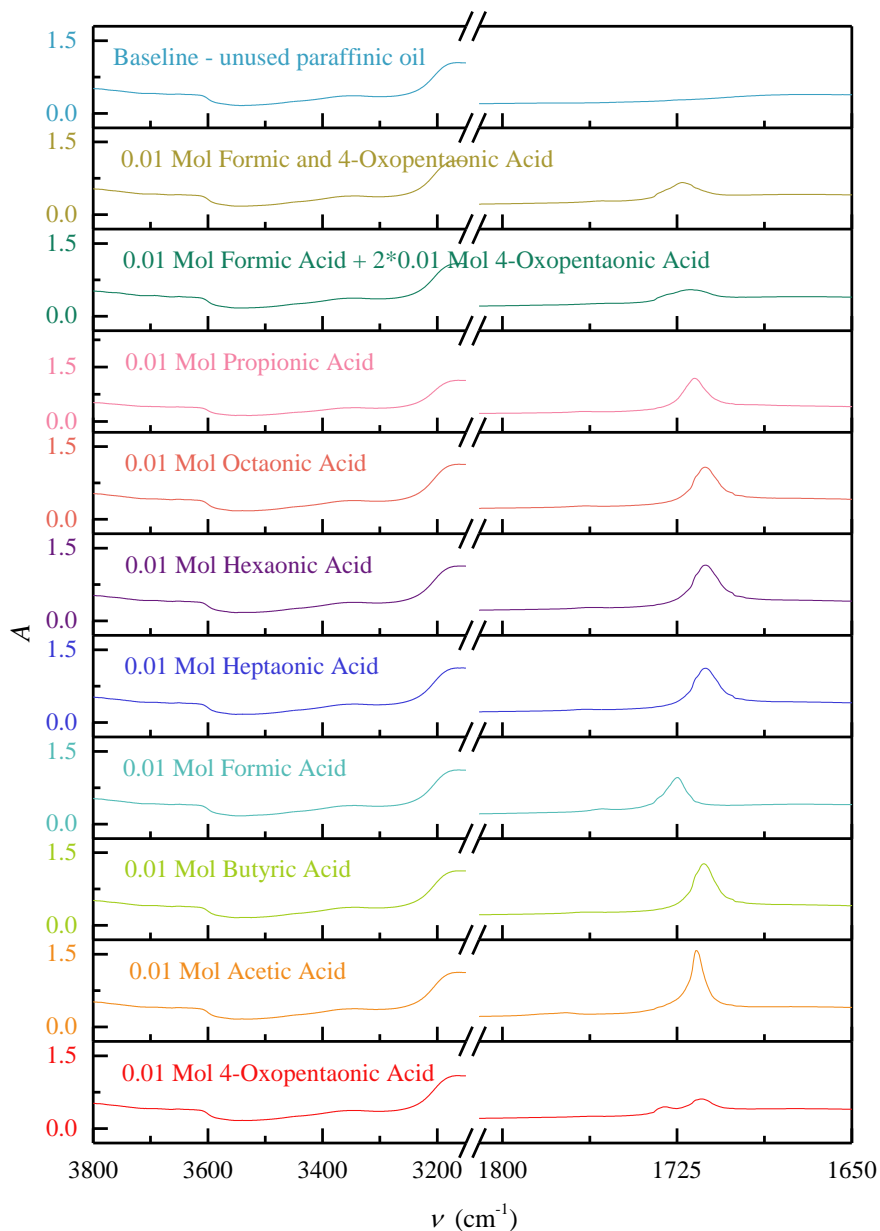
Figure 3.15. Infrared absorbance *A* versus the water and carbonyl infra-red wavenumber region of diluted organic acids from Table 3.4.

The infra-red spectra of the acids were done using the *standard* settings (section 3.2.2) and are shown in Figure 3.15. These measurements are very similar and thus can be summed up as follows: The carbonyl region around 1720 cm⁻¹ exhibited a variety of wavenumber shifts dependent on the kind of the acids present. Lower molecular weight acids are shifted to wavenumbers higher than 1720 cm⁻¹ while higher molecular acids exhibit shift wavenumbers lower than 1720

cm$^{-1}$. This becomes obvious when considering that the molecular weight has an impact on the **C=O** absorbance which was discussed using the potential energy $U(r)$ and force constant $k$ in section 2.2.

In particular, it was found that the 2:1 mixture of 4-oxopentanoic acid and formic acid exhibits a smooth and broad absorbance with a peak at 1720 cm$^{-1}$, well reproducing the experimental value of the oxidation experiment in section 3.2. However, no absorbance change was observed in the water band.

## 3.3.2 Moisture diluted in insulating liquid and its infra-red and dielectric response

Dielectric measurements of insulating liquid with added water were done using three different concentrations of moisture. This was achieved by adding 10 mg de-ionised water per 100 g insulating liquid sample via a micro pipette, giving a concentration of 100 ppm. The solution was heated for 3 hours at 90 °C, with a magnetic stirrer. Three samples were extracted at the end of this mixing process at 90 °C via glass syringes (CADG5177 Aldrich) and filled into sealed vials (nitrogen flushed). These samples were diluted with unused insulating liquid at room temperature. The Karl-Fischer moisture titration method was used and confirm three different moisture concentrations with 42 ppm, 31 ppm and 21 ppm. These are expected values for a moisture concentration of unused paraffinic liquid; the approximate maximum solubility is about 50 ppm at room temperature [18, 73]. A measurement of the moisture was also done after the dielectric experiment, resulting in similar values within the measurement standard deviation of 0.3 ppm.

## 3.3.2.1 Dielectric measurements of the insulating liquid with added moisture

These samples were then measured with dielectric test cell (section 3.1) with regard to their permittivity and conductivity, similar to the dielectric

measurements in section 3.2.4, between 30 to 90 °C in 20 °C steps. The measurement theory is described in section 2.4. The standard deviation of the measurement is shown with error bars. The accuracy of the temperature reading was within ± 10 mK with a precision of ± 1 mK. The dielectric measurements are shown in Figure 3.16a. It can be clearly seen that the relative permittivity changed significantly, proportional with temperature. This slope was negative starting from about 2.1 to 2.05 for 30 to 90 °C respectively. The three samples showed near identical values of the permittivity despite their difference in water content. The measured conductivity was increasing with temperature in a non-linear fashion. For the 21 ppm concentration, the conductivity was about 2.5 pS/m to 0.75 pS/m for 30 to 90 °C respectively. An increase in the moisture to 31 ppm led to an increase in this conductivity to 0.3 pS/m to 1.2 pS/m and 42 ppm yielded 0.6 pS/m to 1.8 pS/m for 30 to 90 °C respectively.
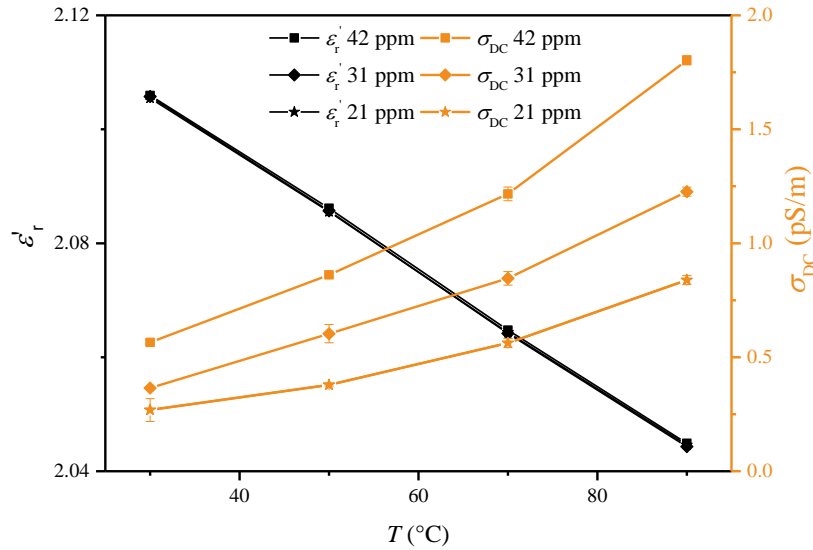


Figure 3.16a. The real part of the relative permittivity and the conductivity versus temperature of unused insulating liquid with added moisture of concentrations 42, 31 and 21 ppm.

### 3.3.2.2 FTIR spectroscopy of the insulating liquid with added moisture
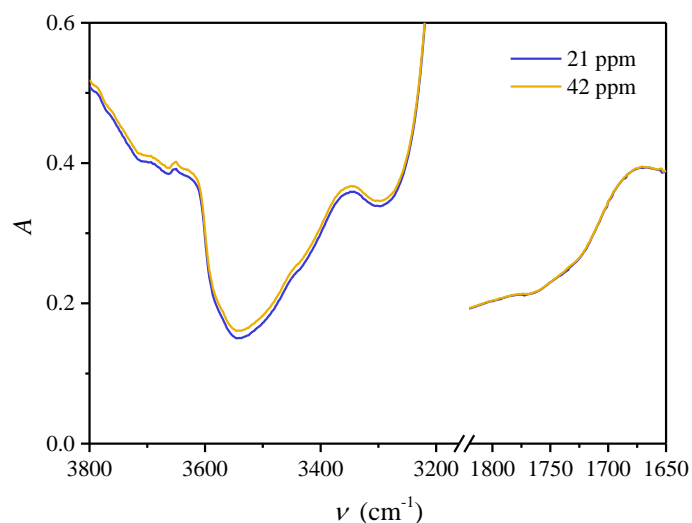


Figure 3.16b. The infra-red absorbance over the wavenumber for insulating liquid having 42 and 21 ppm of moisture.

The FTIR spectroscopy was now used to evaluate the liquid's composition as the thermal treatment to dissolve the moisture could have led to oxidation, and the dielectric measurements would have given false indications. The FTIR spectroscopy confirmed measurable response in the infra-red spectra for the water region around 3500 $cm^{-1}$. No measurable change in the spectrum was present anywhere else between 500 to 4000 $cm^{-1}$ on the spectra, in particular the carbonyl region around 1700 $cm^{-1}$ remained unchanged as shown in Figure 3.16b.

### 3.3.2.3 Modelling of the permittivity, conductivity and moisture concentrations

The slope and the magnitude of the temperature dependent permittivity is examined in this section in more detail. This was done in order to evaluate the impact of the artificially added moisture while aiming to have a measurable quantity relating to determine the concentration of the moisture impurity. This is split into three parts labelled with "A, B, C". Section A examines the temperature slope and magnitude of the permittivity for different moisture

concentrations. The section B studies the resulting conductivity in detail and section C is dedicated to calculating the moisture concentration analytically.

A) The permittivity $\varepsilon_r$

The slope of $\varepsilon_r$ with temperature (see Figure 3.29) is expected to follow inversely to the square dipole moment divided by the temperature $T$ in Kelvin and the Boltzmann constant $k_b$. An acceptable fit can be achieved utilizing a relation to the Clausius-Mosotti equation, $\varepsilon_r(T) \propto (T+2c)(T-c)^{-1}$, where $c$ is the concentration of molecules in $1/m^3$. However, in the region $T = 300$ to $370\,°K$, the $1/T$ dependence is approximately linear. This then can be expressed in a simpler first degree polynomial which is proportional to $T$ and having suitable coefficients. This yields a linear equation having three parameters to fit the experimental data:

$$\varepsilon_r(T) \cong c_1 T + c_2 \qquad (3.7)$$

The value of $\varepsilon_r$ can be readily fit using $c_1$ in units of $K^{-1}$ as temperature coefficient and $c_2$ as an offset value of $\varepsilon_r$ due to the moisture content. The fit parameters for the equation above are listed in Table 3.5. The coefficient of determination was $R^2 \cong 1$.

Table 3.5. The parameter $c_1$ and $c_2$ versus the concentration.

| ppm (µg/g) | $c_1$ (K⁻¹) | $c_2$ |
|------------|-------------|-------|
| 21 | -0.00105 | 2.1359 |
| 31 | -0.00105 | 2.1365 |
| 42 | -0.00105 | 2.1371 |

It can be deduced that added moisture increases the offset $c_2$ proportionally by a small amount. This is visualised with Figure 3.17. The evaluated uncertainties of $c_1$ and $c_2$ are $\pm\,0.0001$.
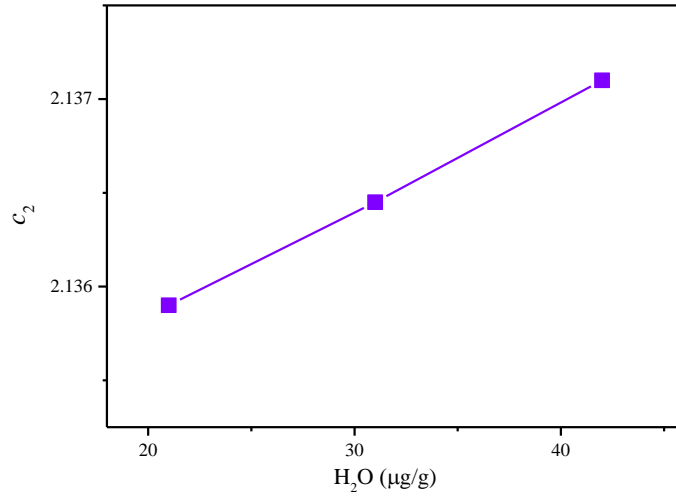
Figure 3.17. The permittivity offset parameter $c_2$ as function of moisture concentration in ppm.

B) The conductivity $\sigma_{DC}$

The conductivity as a function of temperature was measured in section 3.3.2.1 and found to be non-linearly increasing with temperature. The theory for determining the $\sigma_{DC}$ from an impedance measurement is elaborated in section 2.4. The conductivity can be understood as being proportional to the number density of electrons $n$ multiplied by their charge $q$ and mobility $\mu$, $\sigma_{DC} \sim q\, n\, \mu$. A non-linear increase with temperature indicates that the density of charge carriers or their mobility $\mu$ is exponentially proportional to $1/T$. In literature, there are two common models to describe such phenomena.

One model is the Arrhenius-type equation for the conductivity, $\sigma(T) = \sigma_0 \exp(-E_a k_b^{-1} T^{-1})$ [74]. This heuristic model can be used to fit the data points for the conductivity versus temperature. The fit parameter are then $\sigma_0$ and $E_a$. However, while modelling, it was found that the Arrhenius-type equation could not reproduce the experimental data points well enough. Values for the coefficient of determination, $R^2$, were in a reasonable range but only for arbitrary fit parameters. Hence, no consistency to the conducted experiment was found, e.g. the added moisture concentration. For example, the factor $\sigma_0$ was yielding 5.8E-

10 S/m for 42 ppm, 5.2E-10 S/m for 31 ppm and 2.5E-10 S/m for 21 ppm. This yields a weak correlation between $\sigma_0$ and moisture. If the moisture would affect the $\sigma_0$ then a stronger proportionality would be expected. The second fit parameter, $E_a$, was smaller for 31 ppm than for 21 and 42 ppm from which no correlation to the added moisture could be determined. Hence, using the Arrhenius equation, the combination of $\sigma_0$ and $E_a$ does not appear to make much sense in terms of relating this to the changed concentration. Hence, this model fails to describe the experimental data and no useful information could be gained.

A second model is derived analytically in literature [42] which describes that electrons are present in the form of polarons in insulating liquids and electron hopping is the nature of the conduction. The electrons between non-conducting molecules can only 'hop' under certain energy conditions. In Ref. [42] at Chapter 7, the electronic properties of insulating liquids (using polaron hopping theory) is discussed in some detail. It describes that the electron requires an energy, $W_p$, to hop across the (paraffinic) molecules as the molecules state a kind of potential barrier for the electron. These molecules can be understood as a structure of potential barriers which traps the electron inside. An electric field accelerates the electron but fails to hop due to insufficient energy needed to overcome the potential barrier structure. This hopping is a probability dependent on the energy of the electron relative to its surrounding structure. This theory is leading to a derived expression for the charge carrier mobility, $\mu$, [42]

$$\mu(T) = q_{el}a^2 k_b^{-1} T^{-1} P_1 P_2 \qquad (3.8)$$

The $P_1$ term is related to the exponetial probability that conditions are met for an electron hopping, using the energy $W_p$ relative to the thermal energy in the system,

$$P_1 = \omega_0 \pi^{-1} \exp(-W_p k_b^{-1} T^{-1} / 2) / 2. \qquad (3.9)$$

The $P_2$ term is related to the probability of electron transfer in case of a non-adiabatic hopping [42],

$$P_2 = 4\pi^2 h^{-1} \omega_0^{-1} \sqrt{\pi W_p^{-1} k_b^{-1} T^{-1}/2} \ . \tag{3.10}$$

Combined, the electron mobility then becomes,

$$\mu(T) = \sqrt{2}\pi^{3/2} h^{-1} a^2 J^2 k_b^{-3/2} T^{-3/2} W_p^{-1/2} e^{-W_p k_b^{-1} T^{-1/2}} \ \mathrm{cmV^{-1}s^{-1}} \ . \tag{3.11}$$

If the conductivity is propotional to the density of charge carriers per $\mathrm{cm^{-3}}$, their charge and their mobility can then be expressed as

$$\sigma_{DC}(T) = n \cdot q \cdot \mu(T) \ \mathrm{S/m}. \tag{3.12}$$

Simplifying this by using a constant, $c$, as a pre-factor which may be defined as

$$\sigma_0 = n \ q \ \sqrt{2}\pi^{3/2} h^{-1} a^2 J^2 k_b^{-3/2} = n \ c \ , \tag{3.13}$$

which contains constants such as the Boltzmann constant $k_b$, the Planck constant $h$, the intermolecular separation, $a$, proportional to the diffusion constant, $D$; $a = D_{el}/P_1P_2$, the electron charge $q$, the electron transfer integral $J$ and is proportional to the number of charge carriers, $n$, in the system. Hence, $\sigma_0$ is used together with $W_p$ as fit parameters. Here, $W_p$ is the energy of the polaron that is related to the activation energy $E_a$;

$$W_p/2 = E_a \ . \tag{3.14}$$

The conductivity can thus be written as

$$\sigma_{DC}(T) = \sigma_0 T^{-3/2} W_p^{-1/2} e^{-W_p k_b^{-1} T^{-1/2}} \ \mathrm{S/m} \ , \tag{3.15}$$

which has $\sigma_0$ and $W_p$ as fit parameter. Although similar to the Arrhenius equation, the factor $T^{-1.5}$ affects the $T$-dependence of $\sigma_{DC}$.

When fitting the measurements with Equation 3.15, in Figure 3.18, the fit parameter have been determined for $R^2 \cong 1$ as shown in Table 3.6, with an uncertainty of $\pm$ 0.002 of for $W_p$ and $\pm$ 0.01E-5 for $\sigma_0$. It shows clearly that $\sigma_0$ is constant while $W_p$ is changing with the concentration of the moisture. Interpreting the hopping model, adding $H_2O$ may increase the probability of the electron to

hop, as a polar molecule is more likely to 'interact' with an electron than a non-polar molecule due to a different hopping potential barrier. However, adding 21 ppm $H_2O$ may not necessarily introduce significantly more charge carriers and thus is not affecting the charge carrier density $n$ for which $\sigma_0$ then must remain constant.

Table 3.6. The fit parameter $W_p$ and $\sigma_0$ for the moisture solution. While $W_p$ reduces proportionally with $H_2O$, $\sigma_0$ remains constant.

| $H_2O$ (µg/g) | $W_p$ (eV) | $\sigma_0$ (S/m) |
|---|---|---|
| 21 | 0.4926 | 1.06E-5 |
| 31 | 0.4711 | 1.06E-5 |
| 42 | 0.4459 | 1.05E-5 |

These fits for $\sigma_{DC}(T)$ for the three ppm concentrations have been overlaid with the experimental value and are shown in Figure 3.18. Figure 3.19 shows $W_p$ as function of moisture concentration where each $W_p$ value represents one of the three curves in Figure 3.19. The fits correspond well to the experimental data showing that the electron mobility for insulating liquids [42] is a working model to describe the conductivity with temperature dependent on a concentration.
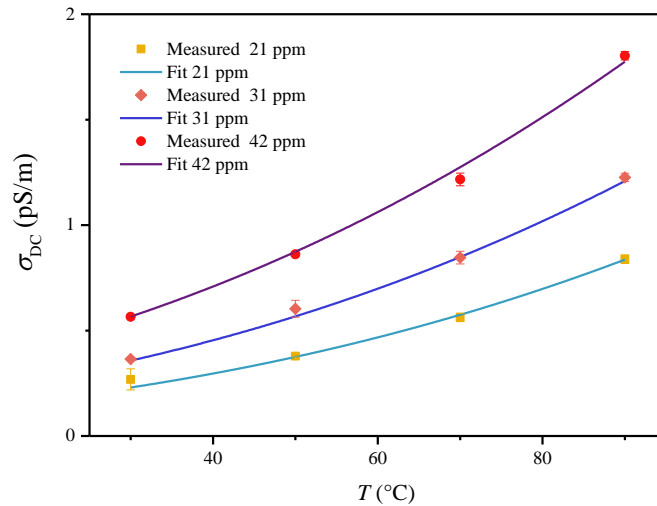


Figure 3.18. Measured conductivity vs. calculated conductivity as a function of temperature of the moisture enriched insulating liquid.
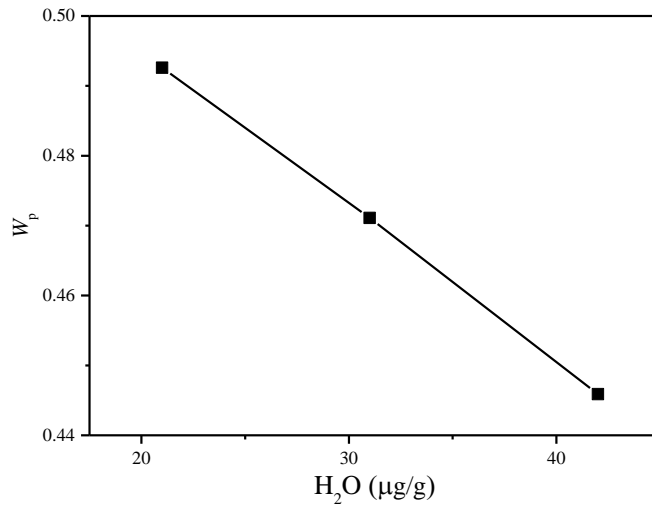
Figure 3.19. $W_{\mathrm{p}}$ as function of moisture content in the moisture enriched insulating liquid.

C) Moisture concentration evaluation

The magnitude of the permittivity was found not to exhibit a significant increase when adding moisture. However, a pronounced impact in the conductivity due to moisture was noticed. Figure 3.19 shows that the activation energy decreases by 0.0022 eV per concentration in ppm value of moisture. Thus, we can write $W_{\mathrm{p}}$ as function of ppm-concentration;

$$W_{\mathrm{p}}(\mathrm{ppm}) \approx (-0.0022\mathrm{ppm} + 0.54)\,\mathrm{eV}\,. \tag{3.16}$$

The ratio $0.0022/0.54 = 0.4$ % shows that in order to affect the conductivity significantly, large quantities of moisture are necessary. However, due to the dissimilar nature of paraffinic liquid and water, only limited concentrations can be achieved. This means that the impact on the conductivity as well as the permittivity of moisture in the insulating liquid is negligible. This will be clearer when discussing ketones in insulating liquid in the next section.

### 3.3.3 Ketones diluted in insulating liquid and its infra-red and dielectric response

A concentration $c$ of 0.1, 0.01 and 0.001 mol 2-decanone (98%, 268194 Aldrich) per 1 liter unused insulating liquid having $20 \pm 1$ ppm moisture was

made in the laboratory by stirring the solution for 2 hours at room temperature. The three decadal dilution step was chosen in order to cover a large range of concentration with a minimal number of samples. Samples of the 1 liter solution were taken at 20 ± 1 °C and filled in the sealed vials. To achieve the desired concentrations in mol per liter, the solutions were diluted with the unused insulating liquid accordingly.

### 3.3.3.1 Dielectric measurements of ketones

These solutions were investigated according to the *standard* settings for the dielectric measurements. Figure 3.20 shows the dielectric measurement of the three different ketone concentrations, in comparison with the unused insulating liquid. The permittivity was similarity affected by the temperature but increased with the concentration. For the lowest concentration, 0.001 mol, the permittivity was about 2.11 to 2.06 for 30 to 90 °C respectively (up from 2.1 at 30 °C and 2.05 at 90 °C). The concentration of 0.01 mol had a moderate effect. The permittivity was about 2.12 to 2.07 for 30 to 90 °C respectively. However, for 0.1 mol, the permittivity increased to 2.19 for 30 °C and 2.14 for 90 °C. The conductivity showed a non-linear behaviour with temperature. The 0.001 mol concentration yielded about 0.4 pS/m at 30 °C and 1.1 pS/m at 90 °C. Similar to that the 0.01 mol concentration yielded approximately 0.5 pS/m to 1.2 pS/m for 30 to 90 °C respectively. The conductivity for the largest 0.1 mol, concentration was significantly increased. It resulted in 1 pS/ at 30 °C and 2.5 pS/m at 90 °C.
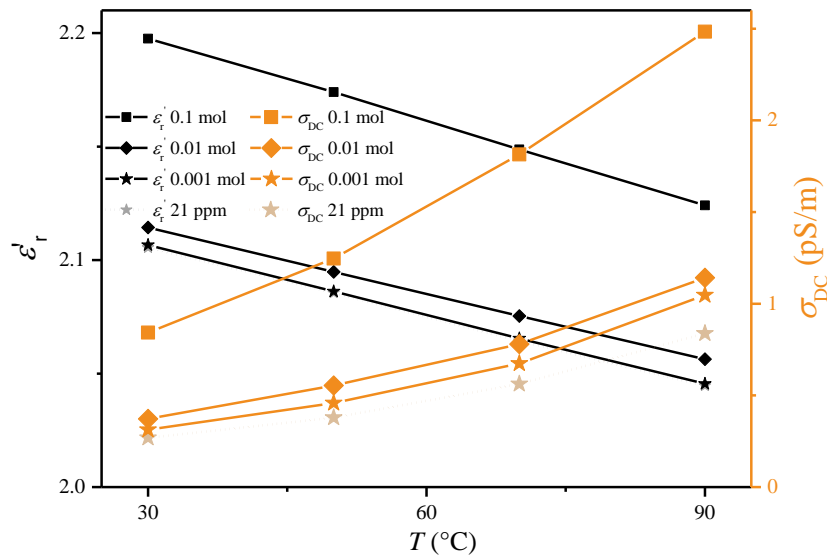
Figure 3.20. The permittivity and the conductivity versus temperature of diluted 2-decanone in unused insulating liquid. As a reference, the moisture value of 21 ppm is shown.

### 3.3.3.2 FTIR measurements of ketones

Now, let us have a look at the infra-red absorbance in order to check whether the permittivity is related to an increase in the ketone concentration. This was anticipated in section 2.4 and indicated in section 3.2. The FTIR spectroscopy of the ketone solution is shown in Figure 3.21 and confirms a measurable response in the infra-red spectra for the carbonyl region. The ketone absorbance peaks at about $\nu = 1726 \text{ cm}^{-1}$.
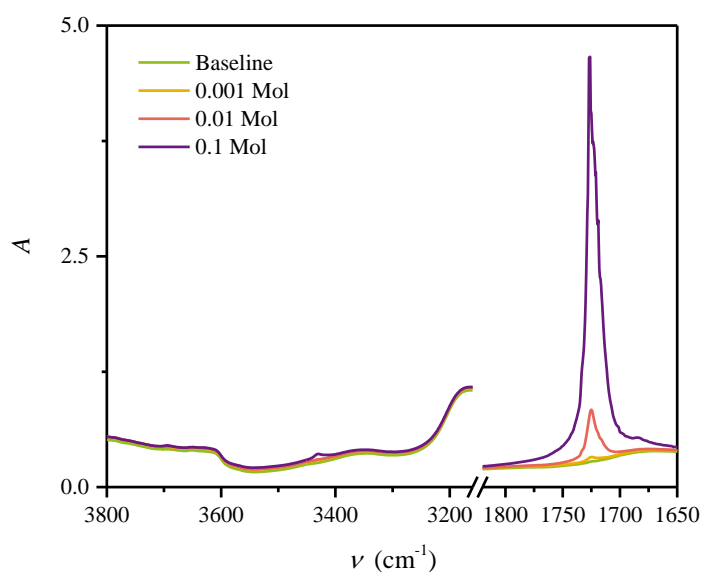
Figure 3.21. Absorbance of insulating liquid with 2-decanone over the moisture and carbonyl mid-infra-red region for three different concentrations; 0.1, 0.01, 0.001 mol/l. The baseline having zero addition is shown as reference value.

The absorbance of the carbonyl region $A_{C=O}$ was significantly increased after the addition of ketones. Defining $\Delta A_{C=O} = A_{C=O} - A_{C=O, Base}$, the absorbance as difference to its baseline value of $A_{C=O, base} = 0.2743$ was $\Delta A_{C=O}(0.001 \text{ mol/l}) = 0.0266$, $\Delta A_{C=O}(0.01 \text{ mol/l}) = 0.2267$ and $\Delta A_{C=O}(0.1 \text{ mol/l}) = 1.9486$. This absorbance follows the target dilution of 100:10:1 approximately as expected: 99:10:1, Figure 3.22. The uncertainty in this analysis was $\pm$ 2%.

A slight increase in the moisture level was also noticed. With the definition $\Delta A_{H2O} = A_{H2O} - A_{H2O, Base}$ and $A_{H2O, Base} = 0.2924$ for 21 ppm the increase is $\Delta A_{H2O}(0.001 \text{ mol/l}) = 0.0273$, $\Delta A_{H2O}(0.01 \text{ mol/l}) = 0.0301$ and $\Delta A_{H2O}(0.1 \text{ mol/l}) = 0.0449$. The measured moisture value for the **0.1 mol/l** ketone concentration was in ppm: **24.8 $\pm$ 0.3 ppm**. Using the **FTIR** absorbance, the moisture concentration can be calculated: $(21 \text{ μg/g}_{H2O}) \cdot A_{H2O}(0.1 \text{ mol/l})/A_{H2O, Base} = 24.2 \pm 0.5$ ppm. This result shows that the increased moisture absorbance is caused by an increased moisture content in the sample and not caused by the ketones. If we consider that the 98% 2-decanone solution was containing 1-2% moisture, these

measurements indicate that the moisture saturation level had increased. This can be due to the increased amount of polar compounds which are more hydrophilic than the insulating liquid.
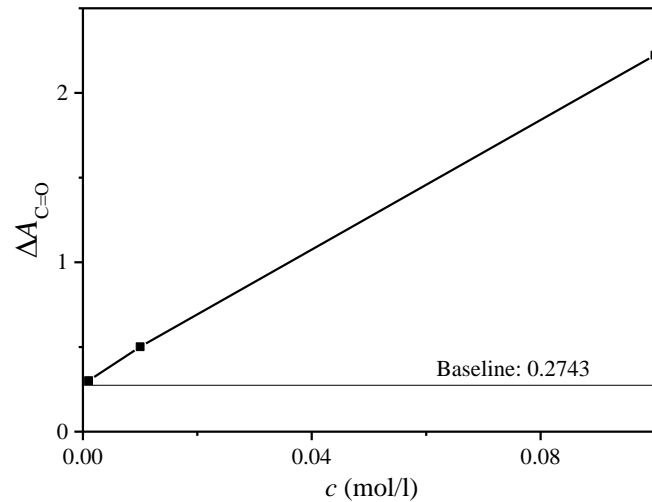


Figure 3.22. The integrated absorbance $A_{C=O}$ for the carbonyl region over the titrated concentration $c$. The baseline represents the sample with 21 ppm moisture content.

### 3.3.3.3 Modelling of the permittivity, conductivity and ketone concentration

This section follows a similar structure for the experiments of the moisture in insulating liquid. In section A the permittivity measurements are shown, section B examines the conductivity and section C shows the modelling of the permittivity and conductivity dependent on the concentration of the ketone in insulating liquid.

A) The permittivity $\varepsilon_r$

The slope and offset coefficients of $\varepsilon_r$ for the ketone experiment (see Figure 3.20) have been calculated with $\varepsilon_r(T) \cong c_1 T + c_2$ similar to section 3.3.2 which are shown in Table 3.7.

Table 3.7. The parameter $c_1$ and $c_2$ versus the concentration $c$.

| $c$ (mol/l) | $c_1$ (K$^{-1}$) | $c_2$ |
|---|---|---|
| **0.001** | -0.0011 | 2.1361 |
| **0.01** | -0.0010 | 2.1449 |
| **0.1** | -0.0012 | 2.2331 |

It can be seen that the slope, $c_1$, remains rather constant and the $c_2$ value is larger than for the moisture experiment (Table 3.5). The $c_2$ value was plotted against the concentration resulting in a linear proportionality, Figure 3.23. Thus, an increase in the ketone compounds increases the permittivity proportionally. The $c_1$ and $c_2$ fitting uncertainties are estimated to be $\pm$ 0.0002.
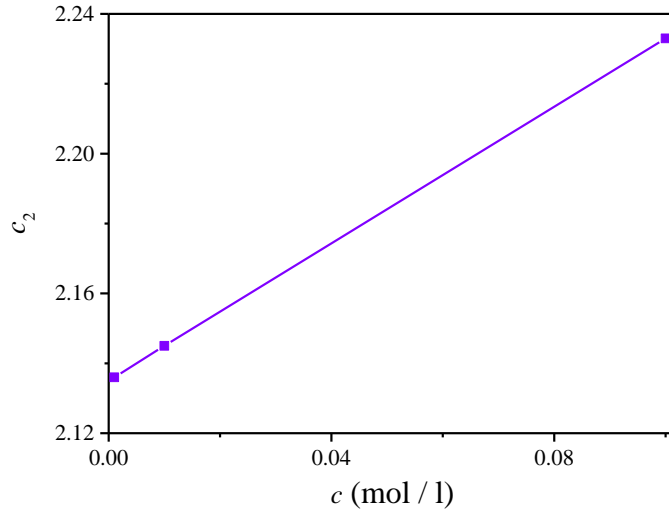


Figure 3.23. The permittivity offset parameter $c_2$ as function of ketone concentration.

This experiment has shown a significant impact on the magnitude of the permittivity when adding ketones to the unused insulating liquid.

B) The conductivity $\sigma_{DC}$

The parameter $W_p$ and $\sigma_0$ to fit $\sigma_{DC}(T)$ are evaluated similar to section 3.3.2 and shown in Table 3.8. Their uncertainties are$\pm$ 0.002 for $W_p$ and $\pm$ 0.02E-5 for $\sigma_0$.

Table 3.8. The parameter $W_p$ and $\sigma_0$ versus the concentration $c$.

| $c$ (mol/l) | $W_p$ (eV) | $\sigma_0$ (S/m) |
|---|---|---|
| **0.001** | 0.4786 | 1.07E-5 |
| **0.01** | 0.4730 | 1.08E-5 |
| **0.1** | 0.4261 | 1.07E-5 |

The fit parameter reveals that the conductivity coefficient remains stable but shows a proportionality to $W_p$. It exhibited a similar dependence as the measurements in the section 3.3.2. These fits have been overlaid with the experimental value and is shown in Figure 3.24. The $W_p$ is plotted subsequently as a function of concentration in Figure 3.25. Also here, the electron mobility can well describe the change in $W_p$ with concentration.
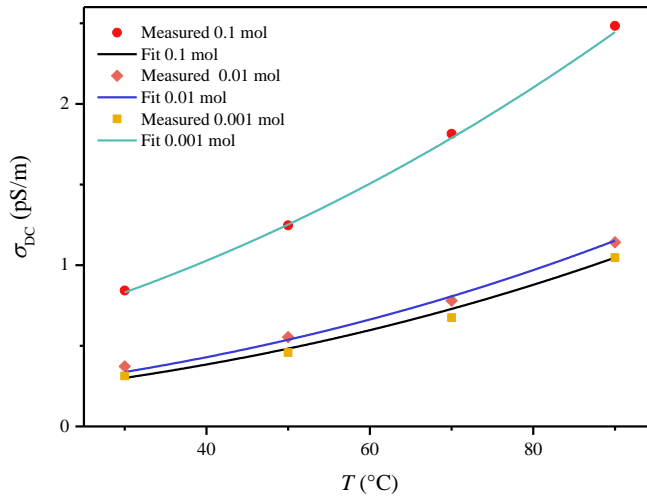


Figure 3.24. Measured conductivity vs. calculated conductivity as a function of temperature of 2-decanone enriched insulating liquid for three different concentrations.
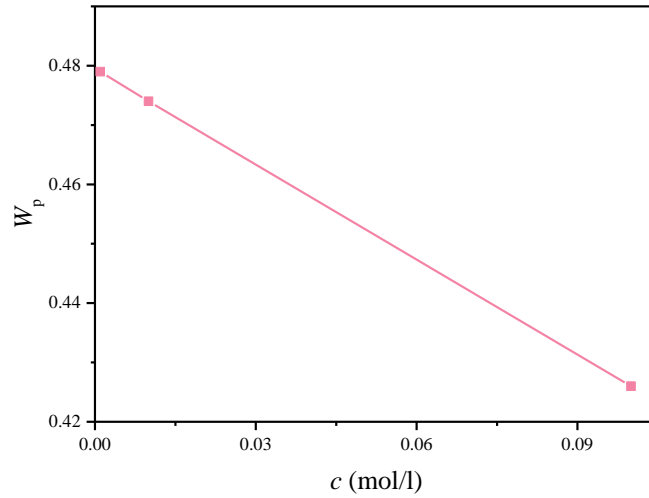
Figure 3.25. $W_\mathrm{p}$ as function the ketone concentration in insulating liquid $c$ (mol/l).

## C) Concentration

The molar mass of 2-decanone was 156 g/mol having a density of $\rho = 0.8215$. Hence, the mole volume can be calculated to $V_\mathrm{m} = 0.19$ l/mol. The permittivity, $\varepsilon_\mathrm{r}(c)$, can be calculated using $\varepsilon_\mathrm{r,\,ins.\,liquid} = 2.1054$ and $\varepsilon_\mathrm{r,\,decanone} = 6.9$ (both measured) through the derived equation in section 3.2,

$$\varepsilon_\mathrm{r}(c) = cV_\mathrm{m}\varepsilon_\mathrm{r,\,decanone} + (1 - cV_\mathrm{m})\varepsilon_\mathrm{r,\,ins.\,liquid} , \tag{3.17}$$

where $c$ was the concentration in mol/l. This function is compared with the experimental data for $\varepsilon_\mathrm{r}(c)$ at 30 °C plotted in Figure 3.26.
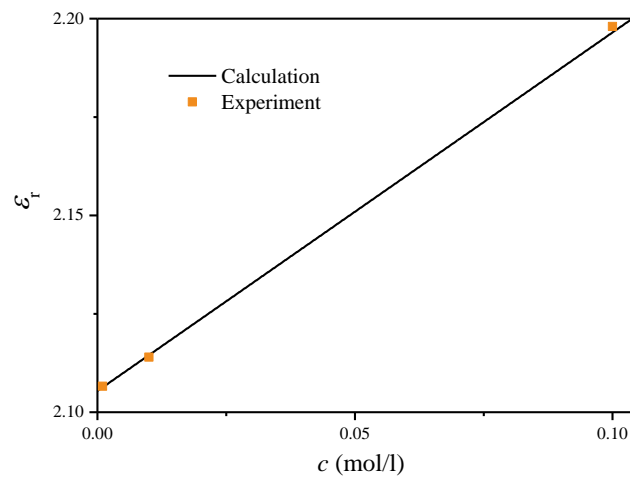


Figure 3.26. The permittivity versus the concentration $c$ as a result of the calculations.

The concentration $c$ of 2-decanone linearly increased the permittivity. The permittivity as function of temperature (in °C) and concentration can be empirically expressed as;

$$\varepsilon_{\mathrm{r}}(c,T) \approx c/c' - 0.001T/T' + 2.135,$$  (3.18)

where $c'$ is 1 mol/l and $T' = 1$ K as this equation, plotted Figure 3.27, has no units.
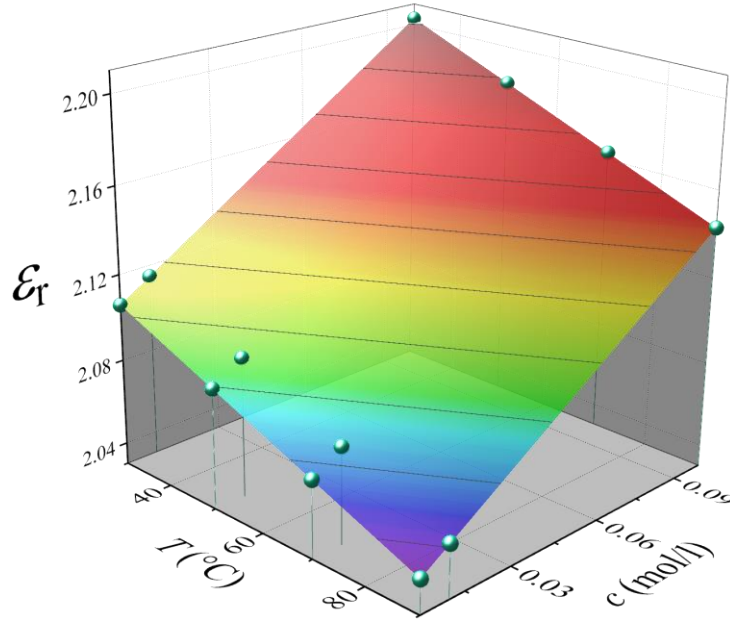


Figure 3.27. The permittivity as function of temperature and 2-decanone concentration $c$, measurement points are shown with marker.

Measuring $\varepsilon_{\mathrm{r}}(c,T)$ can be insightful to relate to its state of oxidation. A similar parameter can be obtained for the conductivity using $W_{\mathrm{p}}$ which is only dependent on $c$,

$$W_{\mathrm{p}}(c) \approx (-0.527c/c' + 0.4786)\,\mathrm{eV},$$  (3.19)

where $c' = 1$ mol/l. This can be used to express

$$\sigma_{\mathrm{DC}}(c,T) = \sigma_0 T^{-3/2} W_{\mathrm{p}}(c)^{-1/2} e^{-W_{\mathrm{p}}(c)k_{\mathrm{b}}^{-1}T^{-1/2}}$$  (3.20)

which is plotted in Figure 3.28.
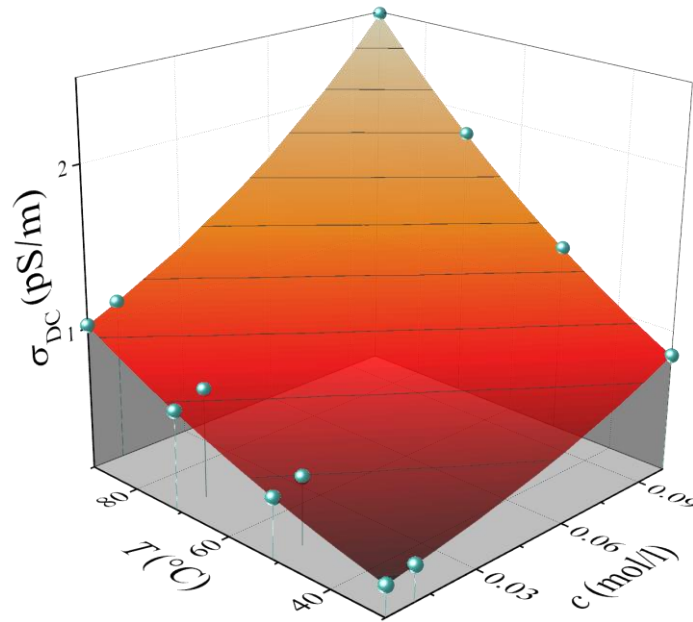
Figure 3.28. The conductivity as function of temperature and 2-decanone concentration $c$ measurement points are shown with marker.

The insulating liquid with added 2-decanone is now characterised regarding its magnitude of the permittivity $\varepsilon_r$ and DC conductivity $\sigma_{DC}$. The Equations 3.18 and 3.20 are each based on 12 accurate and precise data points using the test cell in section 3.1. The lowest concentration (0.001 mol/l) represents the threshold that is measurable, while the largest concentration (0.1 mol/l) represents the maximum anticipated concentration in the insulating liquid. These measurements were consistent with the trend in the experiment in section 3.2. Hence, it is sufficient for the purpose of estimating the permittivity and conductivity of the insulating liquid for the sensor development later in this study as these results provide necessary boundary conditions.

In the next section, the impact of acidic impurities is examined using a similar approach.

### 3.3.4 Acids diluted in insulating liquid and its infra-red and dielectric response

Based on the FTIR data, it was found that a ratio 2:1 of 4-Oxopentanoic acid (> 98% Aldrich L2009) and formic acid (> 95% Aldrich F0507) could

reproduce the infra-red spectra from the oxidation experiment. Thus, a concentration of 0.03, 0.005 and 0.0005 mol/l in the insulating liquid (sample: "21 ppm" in section 3.3.2) was made in the laboratory. These solutions were similarly investigated as the moisture and ketone procedure in regard to its impact on the dielectric response. No special treatment was applied, besides physical mixing at 40 °C. Samples of the 1 liter solution were taken at 40 $\pm$ 1 °C and filled in sealed vials via cleaned glass syringes. The acidity number was measured via an external laboratory, eNZOil Ltd. (Lower Hutt, New Zealand) and is defined as the weight in mg of KOH to neutralize the acidity of a one gram solution. The Table 3.9 shows the acidity number $AN$ in respect to their acid concentrations.

Table 3.9. The measured acidity number $AN$ as versus the concentration.

| $c$ (mol/l) | $AN$ |
|---|---|
| 0.0005 | 0.0073 ± 0.0002 |
| 0.005 | 0.0890 ± 0.0002 |
| 0.03 | 0.6512 ± 0.0002 |

### 3.3.4.1 Dielectric measurements of organic acids

The dielectric measurements were done similar as the ketone and moisture measurements using settings similar to the previous sections. A more detailed analysis of acquiring the dielectric properties is shown in section 2.4. Figure 3.29 shows the dielectric measurement of the three different acid concentrations. The permittivity was less affected by the acids compared to the ketone for the same concentrations. At 0.0005 mol, the permittivity remained at 2.10 for 30 °C and 2.05 for 90 °C, similar to the 21 ppm sample (section 3.3.2). For 0.005 mol the permittivity slightly increased to about 2.106 to 2.05 between 30 and 90 °C. At the highest concentration, 0.03 mol, the permittivity was at 2.14 and decreased to about 2.06 for 30 to 90 °C. Another picture is shown for the conductivity. Here, the conductivity was around 0.4 to 0.6 pS/m for 0.0005 mol and 0.005 mol

at 30 °C. At 90 °C, the 0.0005 mol concentration yielded about 1 pS/m and has risen up to 1.7 pS/m for 0.005 mol. However at 0.03 mol, the conductivity was for 30 °C at a level of 1 pS/m but at 90 °C it increased up to about 8.7 pS/m.
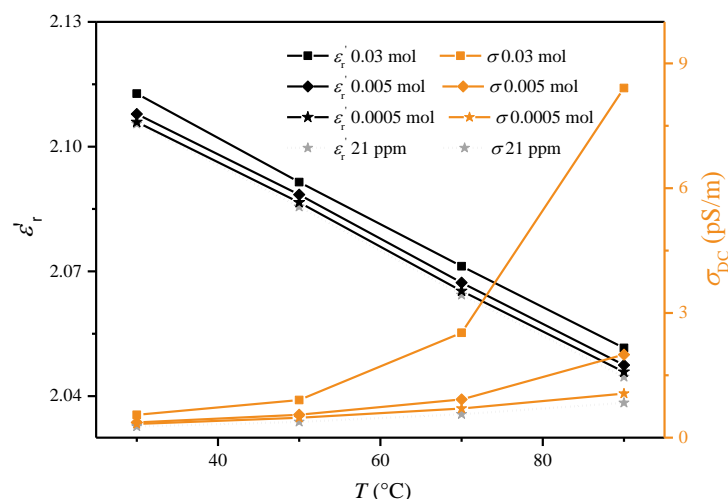


Figure 3.29. The real part of the relative permittivity and its conductivity versus temperature of unused insulating liquid with added concentrations (0.03, 0.005, 0.005 mol/l) of 4-oxopentanoic acid and formic acid. As a reference, the value of the 21 ppm moisture experiment is given.

### 3.3.4.2 FTIR measurements of organic acids

Now we check if the dielectric response can be related to the acids. The FTIR spectroscopy of the organic acid solution confirms a measurable response in the infra-red spectra for the water and acid region, Figure 3.30.
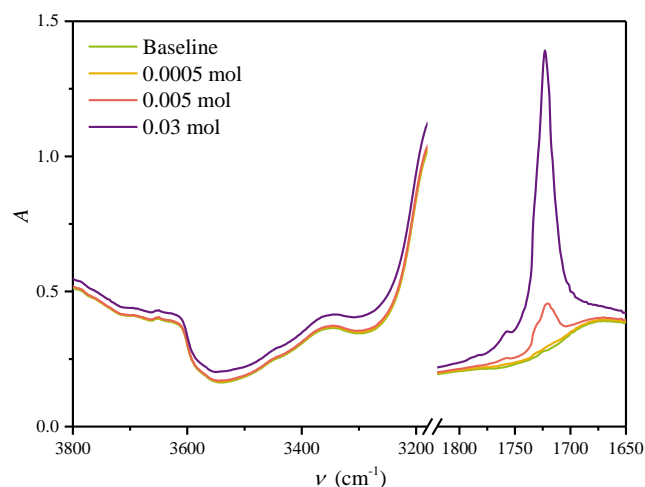


Figure 3.30. The infra-red absorbance as function of the wavenumber of unused insulating liquid with added concentrations (0.03, 0.005, 0.005 mol/l)

of 4-oxopentanoic acid and formic acid. The baseline (sample: 21 ppm) having zero concentration served as base value.

The acid absorbance peaks at about $v = 1724 \ cm^{-1}$. An absorbance of the carbonyl region was significantly increased after addition of acids. The absorbance different to its baseline is defined by: $\Delta A_{C=O} = A_{C=O} - A_{C=O,base}$ where $A_{C=O,base} = 0.274$. Then, the additional absorbance was $\Delta A_{C=O} = 0.0112$ for 0.0005 mol/l, $\Delta A_{C=O} = 0.1142$ for 0.005 mol/l and $\Delta A_{C=O} = 0.6610$ for 0.03 mol/l, Figure 3.31. This absorbance follows the acid target dilution of 1:10:60, confirming the dilution process.
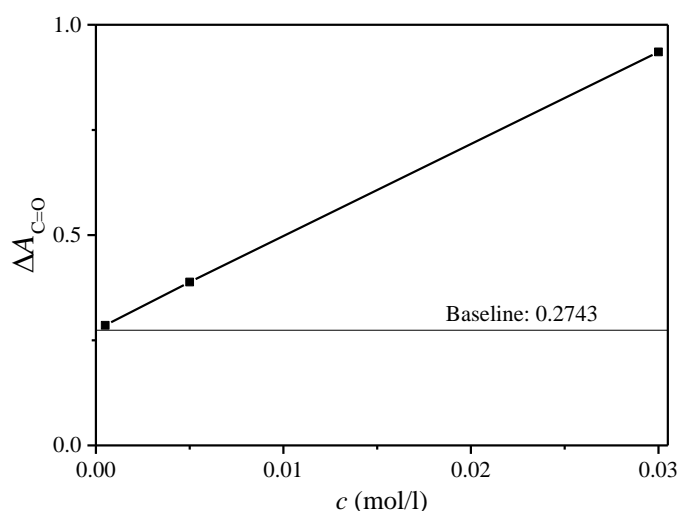


Figure 3.31. The integrated absorbance $A_{C=O}$ for the carbonyl region over the titrated concentration $c$. The baseline represents the sample of having 21 ppm moisture.

In section 3.3.1 the acids were determined not to contribute for a broad water band absorption. The measurements in Figure 3.30 however show that the added acids increase the moisture level. This was also observed for the 2-decanone results in section 3.3.3. The infra-red absorbance for the moisture region was $\Delta A_{H2O} = 0.0036$ for 0.0005 mol/l, $\Delta A_{H2O} = 0.0057$ for 0.005 mol/l and $\Delta A_{H2O} = 0.0385$ for 0.03 mol/l. The moisture value for the 0.03 mol/l concentration was measured via the Karl-Fisher titration (section 3.2) with $24.1 \pm 0.5$ ppm. Then, the concentration value can be calculated as a value similar to that as follows;

83

(21 μg/g$_{H2O}$) $A_{H2O}$(0.03 mol/l)/$A_{H2O,Base}$ = 23.8 ± 0.5 ppm. This result is similar to the results in section 3.3.3 which confirms the tendency of an increased moisture saturation level when adding polar compounds to the non-polar insulating liquid.

### 3.3.4.3 Modelling of the permittivity, conductivity and acid concentration

In this section, it is analysed whether the measured changes on the permittivity and conductivity follow the acidity concentration. This section follows the same structure as for the ketone analysis. In section A the permittivity measurements are shown. Section B examines the conductivity and section C shows a modelling of the permittivity and conductivity dependent on the concentration of the ketone in insulating liquid.

A) The impact of diluted acids on the permittivity $\varepsilon_r$

Similar to the previous section, the slope and offsets of $\varepsilon_r$ for the acidic solution (see Figure 3.29) was calculated which are shown in Table 3.10. Examining this table, it can be seen that the permittivity was less affected by acids than it was by ketones (Table 3.7).

Table 3.10. The parameter $c_1$ and $c_1$ versus their concentration.

| $c$ (mol/l) | $c_1$ (K$^{-1}$) | $c_2$ |
|---|---|---|
| 0.0005 | -0.0011/$T$ | 2.1410 |
| 0.005 | -0.0010/$T$ | 2.1368 |
| 0.03 | -0.0011/$T$ | 2.1361 |

The $c_2$ value was plotted against the concentration resulting in a direct proportionality, Figure 3.32. The respective errors are within the last digit. This figure illustrates that the magnitude of the permittivity is less affected by acids dissolved in the unused insulating liquid.
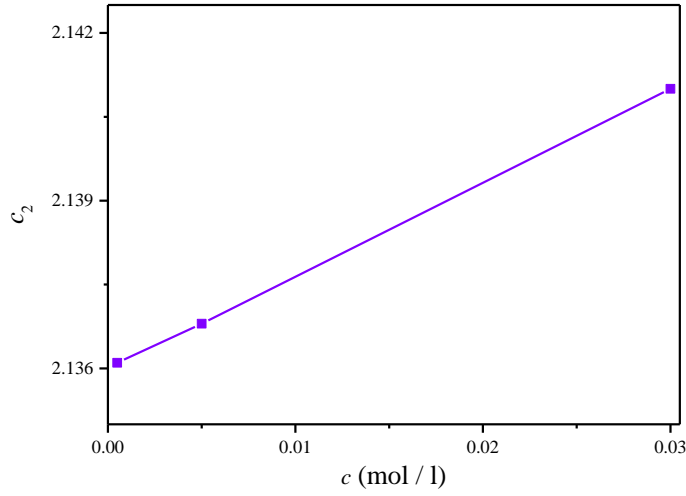
Figure 3.32. The permittivity offset parameter $c_2$ as function of the acid concentration $c$ (mol/l).

B) The impact of diluted acids on the conductivity

The conductivity was significantly increasing in the measurement (see Figure 3.29). This acidic conductivity is different from the observation with added moisture and ketones. The Equation 3.15, used for the electron mobility in section 3.3.2 and 3.3.3, could not fit the measurement satisfactorily anymore. A different expression is required in order to describe the conductivity in this experiment. The measurement in Figure 3.29 shows that adding organic acids to unused insulating liquid has a substantially different impact on the conductivity than in Figure 3.20. Hence, it can be attempted to fit the experimental data using Equation 3.15 for the insulating liquid and the acid separately as an additive term. Then, the conductivity model will be;

$$\sigma(T) = \sigma_0 T^{-3/2} W_p^{-1/2} e^{-W_p k_b^{-1} T^{-1/2}} + \sigma_d T^{-3/2} W_d^{-1/2} e^{-W_d k_b^{-1} T^{-1/2}} \text{ S/m}, \qquad (3.21)$$

where $W_d$ is introduced reflecting a thermally driven process contributing to more charge carriers and $\sigma_d$ represents the coefficient for acids. The expectation is that the dissociation energy $W_d$ is a constant for the specific type of acid mixture used, but $\sigma_d$ is expected to show a proportionality to the acid concentration. $W_p$ still

85

represents the energy due to the insulating liquid and $\sigma_0$ is its coefficient. Since this fit is now overdetermined, $\sigma_0$ was allowed to be varied between 1E-5 to 1.1E-5, as similar to the value from the moisture experiments. The energy $W_d$ was limited to be varied only between 1.85 to 1.9 eV. The necessary fit parameter for the Equation 3.21 $\sigma_0$, $\sigma_d$, $W_p$, and $W_d$ have been determined and are listed in Table 3.11. Figure 3.33 shows that the fit using Equation 3.21 matches the data points for the conductivity from Figure 3.29 well.

The consistency of the fit parameter with the experiment can be illustrated though Figure 3.34, which plots the energy $W_p$ as a function of the molar acid concentration $c$. Subsequently, $\sigma_d$ has been compared with the acidity number $AN$ (method see section 3.2) which is proportional the acid concentration $c$, Figure 3.35.

These data show that the second parameter in Equation 3.21 indeed can represent the presence of acids and $\sigma_d$ is a thermally independent parameter which is directly proportional to the acid concentration. The error margin for $W_d$ is $\pm$ 0.003 and for $\sigma_d$ is about $\pm$ 0.5E3, whereas the errors for the parameter $W_p$ and $\sigma_0$ were $\pm$ 0.002 and $\pm$ 0.02 respectively.

Table 3.11. The fit parameter $W_d$ and $\sigma_d$ versus their concentration.

| $c$ (mol/l) | $W_d$ (eV) | $\sigma_d$ (S/m) | $W_p$ (eV) | $\sigma_0$ (S/m) |
|---|---|---|---|---|
| **0.0005** | 1.8711 | 6.6E3 | 0.4786 | 1.07E-5 |
| **0.005** | 1.8710 | 87.4E3 | 0.4740 | 1.08E-5 |
| **0.03** | 1.8708 | 641.1E3 | 0.4500 | 1.10E-5 |
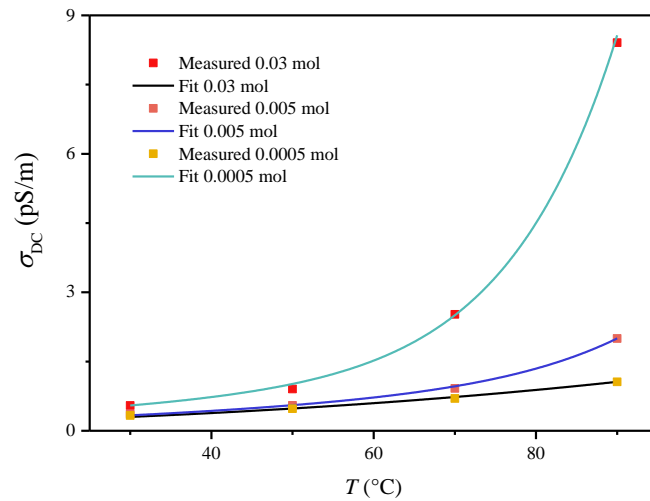
Figure 3.33. Measured conductivity vs. calculated conductivity as a function of temperature $T$ of the acidic solution.
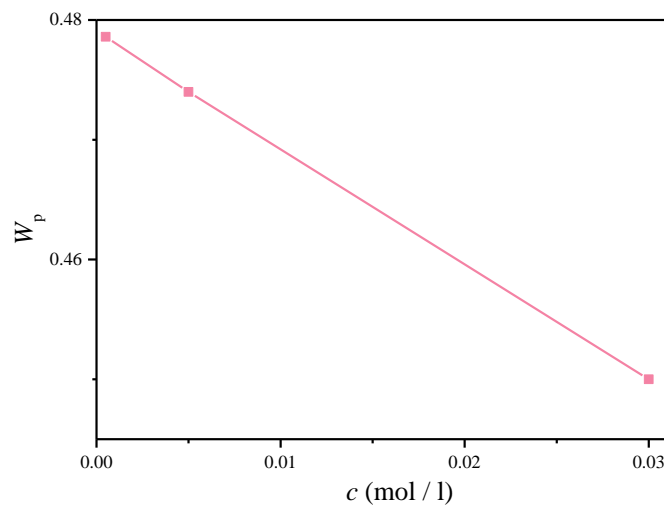


Figure 3.34. $W_p$ as function of the acid concentration $c$.

## C) Concentration

The dependence of the permittivity with temperature and concentration of the used acid-mix can thus be expressed as,

$$\varepsilon_r(c,T) \approx 0.17 c/c' - 0.001 T/T' + 2.136.$$  (3.22)

where $c' = 1$ mol/l and $T' = 1$K. This unit-less function is graphically shown together with the measurements in Figure 3.36.
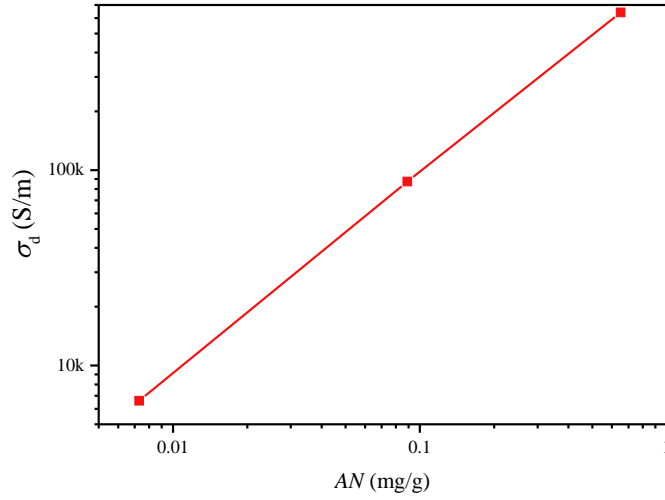
Figure 3.35. Conductivity coefficient $\sigma_d$ as a function of the acidity number $AN$ as log-log scale.

The coefficient $\sigma_d$ is directly proportional to the acidity number ($AN$),

$$\sigma_d\left(AN\right) \approx AN \cdot k \text{ S/m},\tag{3.24}$$

for the investigated acid solution. The factor of $k \sim 1E6$ is an experimentally determined slope in this experiment. It is expected to change when using different solutions.

The DC conductivity can now be written as,

$$\sigma_{DC}\left(c,T,AN\right) = \sigma_0 T^{-3/2} W_p(c)^{-1/2} e^{-W_p k_b^{-1} T^{-1/2}}$$
$$+ \sigma_d(AN) T^{-3/2} W_d^{-1/2} e^{-W_d k_b^{-1} T^{-1/2}} \text{ S/m} \tag{3.25}$$

which is plotted in Figure 3.37.
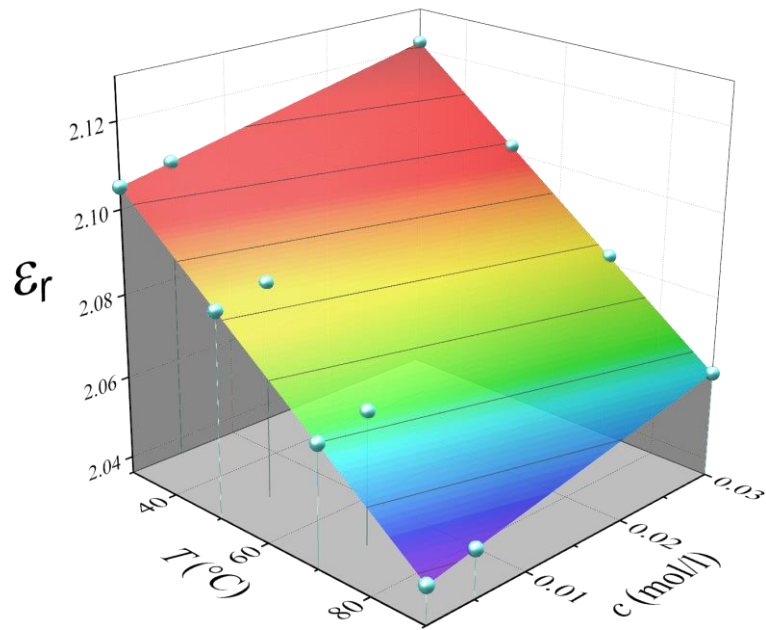
Figure 3.36. The permittivity as function of temperature and acid concentration of a 2:1 ratio of 4-oxopentanoic acid and formic acid.
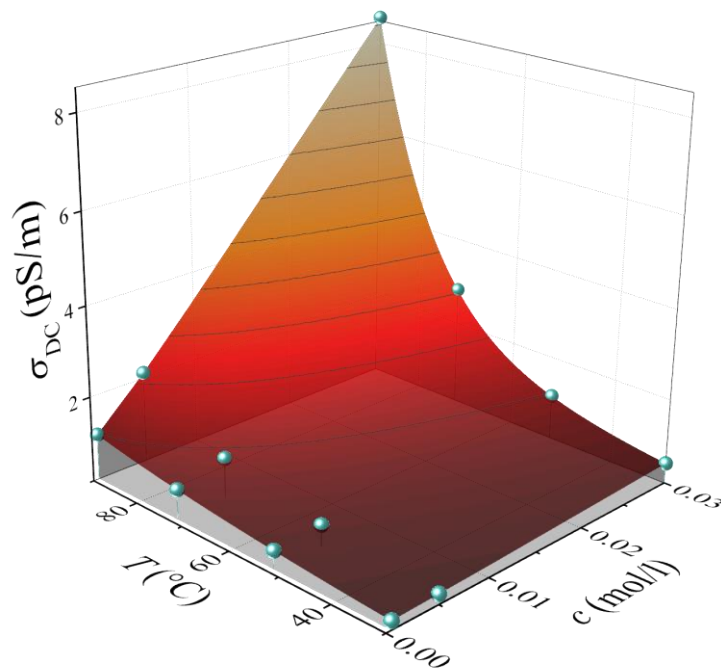


Figure 3.37. The conductivity as function of temperature and acid concentration $c$. measurement points are shown with marker. For large temperatures, the acidic conductivity is proportional to the concentration.

This Equation 3.25 can describe the conductivity based on the concentration $c$ of the impurity, the acidity number $AN$ and the temperature $T$. Thus, if the conductivity was measured, the parameter $c$, $AN$ and $T$ can be determined.

Hence, the complex permittivity can be written as,

$$\varepsilon_r(c,T,AN) = \varepsilon_r^{'}(c,T) + i\omega^{-1}\sigma_{DC}(c,T,AN),$$ (3.26)

where $\varepsilon_r^{'}$ is the real part of the permittivity. There are two parameters this Equation can yield. The first is the degree of oxidation using $c$, and the second parameter is the acidity number using $AN$.

## 3.4  Summary and conclusion

In order to characterize the insulating liquid throughout the thesis, a dielectric test cell was developed, section 3.1, to measure accurately and precisely the dielectric properties of the used insulating liquid in section 3.2.

An accelerated oxidation experiment of the insulating liquid was performed that degraded hydrocarbon insulating liquid at 140 °C for over 600 hours, and the test cell was used to measure the dielectric properties such as the relative permittivity and the conductivity over the experiment time.

The predominant impurities occurring during hydrocarbon deterioration were found to be water, ketones and acids evaluated by FTIR. Their impact on the complex permittivity was determined as follows.

The dissolved water in insulating liquid had a minimal impact on the permittivity. On the other hand, the conductivity exhibited a slight to moderate rise. It was also found that the conductivity $\sigma(T)$ in this liquid can be described using a model for the electron mobility from literature and that a rather classical Arrhenius equation does not yield useful fit parameter such as activation energy $W_p$ and $\sigma_0$. Ketones are paraffinic hydrocarbons with a C=O bond such as 2-decanone. These represent a simple form of oxidised insulating liquid. As low concentrations of ketones were added to the insulating liquid, the permittivity

was found to be strongly proportional to the ketone concentration $c$ in mol/l whereas the conductivity was affected only moderately. As organic acids were added, it was found that they have a smaller impact on the permittivity when compared to ketone at the same concentration. However, the increase in the conductivity was substantially more than for the addition of moisture or ketones. This effect was pronounced in particular at elevated temperatures which required to modify the model for the electron mobility by adding a term containing $W_d$ and $\sigma_d$. The fit parameters for the electron mobility were consistent with the experiment and yielded coefficients determination of $R^2 > 0.99$.

A first oxidation experiment was conducted in order to form an image of the processes during oxidation of the insulating liquid. This yielded values for the permittivity and conductivity which state a kind of boundary condition for the IDS development. Thus, the next chapter discusses the development of a suitable dielectric probe sensing these dielectric properties most accurately in respect to the *in-situ* capability.

# 4 Interdigitated dielectrometry sensor

This chapter is the focus in this thesis. It discusses the development of a suitable interdigitated dielectrometry sensor (IDS). It is a governing requirement to develop an IDS that is capable of sensing the observed changes in the permittivity, $\varepsilon_r$, and conductivity, $\sigma$, from Chapter 3 accurately and precisely. The IDS sensor was developed through a series of four IDS generations, labelled as IDS 1.0, IDS 2.0, IDS 2.5, IDS 3.0, which were modelled, fabricated and measured.

A fundamental understanding of a general working principle can be obtained with very simple structures. Such structures then have the potential to be readily modelled analytically to understand their nature in more detail. At first, a simple interdigitating structure was used to examine the properties of electrodes on a substrate via calculations of the electrostatic physics. This was the IDS 1.0. It was observed that interdigitating electrodes perform badly for measuring $\varepsilon_r$ when placed on a ceramic insulating substrate. The reason for this was that this substrate was also sensed which acted as a parasitic capacitance which was much larger than the capacitance induced by the insulating liquid. The theoretical sensitivity in detecting the insulating liquid relative to its air capacitance was about 10%. The experiments have shown that the IDS 1.0 is practically insensitive to the insulating liquid. This led to the next generation, IDS 2.0, which had an additional conductive ground plane underneath the electrodes which has dramatically improved the accuracy. A Faraday cage for IDS was designed to improve the signal to noise ratio. With the aid of this development, the sensing properties could be systematically improved to a precision of > 99.9% and an accuracy up to 92%. In addition, dependencies of the interdigitating electrode structure could be exploited in a way to manufacture a more suitable IDS 2.5 showing an improved accuracy larger than 99.5% for a specific $\varepsilon_r$ value of a

dielectric. One disadvantage was the need for a prior knowledge of the value of $\varepsilon_r$ to be measured. In order to resolve this issue, the last IDS 3.0 development has a structure that consists of a common ground plane under the electrodes, and a ground electrode (called "deflector electrode") in between the interdigitating electrodes. This improved accuracy for a large range of $\varepsilon_r$ values. The achieved accuracy was 99% across a broad range of $\varepsilon_r$ of insulating liquids. This last development also enabled for the first time to measure the conductivity $\sigma_{DC}$. This finalised the IDS development and provides insight in IDS technology beyond literature, by solving a long overdue issue on how to reliably measure the dielectric properties of insulating liquids using IDS.

An idealized picture of the sensing principle described in section 2.5 is shown in Figure 4.1. It shows electrode pairs for two cases: measuring the air and measuring a material under test (MUT) via an emanated electric field that penetrates the MUT.
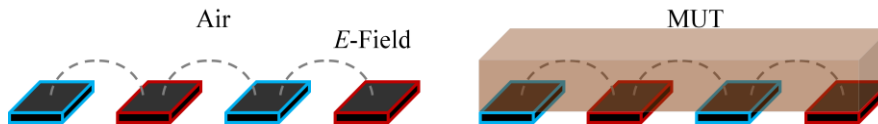


Figure 4.1. Two electro pairs (red and blue) emitting an electrical field (dashed lines) measuring the air or the MUT (opaque box).

## 4.1 IDS 1.0

A simple IDS structure is interdigitated electrodes in free space. One way of keeping the electrodes in a rigid position is bonding them onto a suitable substrate. Previous research had used polymer substrates to create flexible sensors for physical strain applications for non-flat surfaces [15, 19, 75]. Bending of an IDS causes a change in the geometry and thus a change in the capacitance which is exploited in micro technology [8]. However, this is a rather undesired effect as a dielectric change in the surrounding medium will not be satisfactorily distinguishable from a potential strain onto the sensor. Alumina, $Al_3O_2$, is a rigid

material to consider as a substrate; it offers special properties such as high chemical resistivity, low thermal expansion coefficients, high temperature range and high thermal conductivity while being close to a perfect insulator and widely available. In thick film printing technologies, conducting ink is printed directly onto alumina. Firing is a process for bonding the printed conductors onto its surface at temperatures around 500 to 800 °C. Such a method is employed in the first generation of an IDS to investigate its merits in regard to sensing insulating liquid.

### 4.1.1  Structure

A sketch of a design for the first generation IDS1.0 is shown in Figure 4.2. It shows six interdigitating electrodes (red and blue) with gap $g$ and length $l_e$ having a protective coating with thickness $t_c$ (green) onto a substrate with thickness $t_s$ (grey).
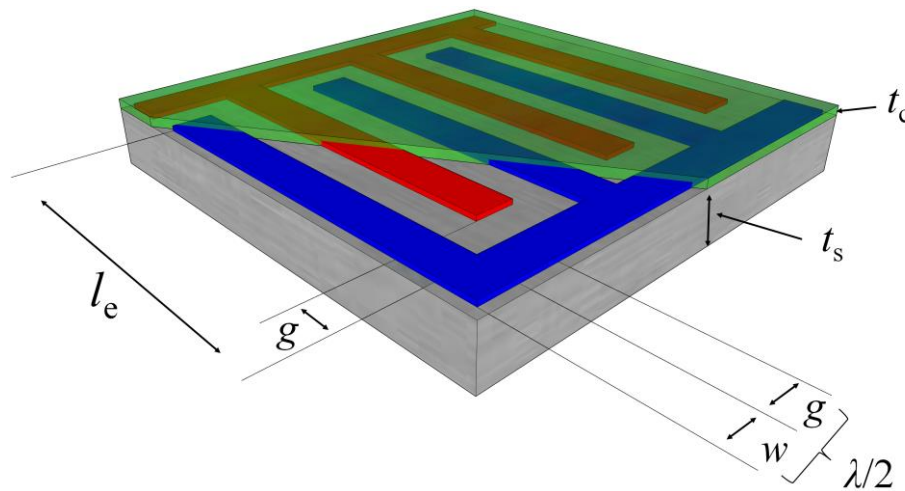


Figure 4.2. The IDS structure 1.0 showing its dimensions of the substrate, electrodes and glass coating.

The dimensions of the manufactured IDS were chosen similar to the structures reported in literature using three IDS having different dimensions on one board. [15, 16, 19-21]. Therefore, the first structure consists of a wavelength $\lambda = 4$ mm and about 40 mm electrode length, the second structure consists of a $\lambda = 2$ mm and about 20 mm electrode length. The third has the dimension $\lambda = 1$

**mm** and an electrode length of about 10 mm. The dimensions are listed in more detail in Table 4.1. To prevent oxidation of the silver electrodes, a thin $SiO_2$ based glass layer (green) was applied onto the electrodes. The manufacturing was done utilizing external laboratories such as the Electronics Design Centre Ltd. (EDS, Cleveland, Ohio, USA), specialized in thick film printing of electrodes onto alumina. The smallest structure ($\lambda$ = **1 mm**) resulted in an electrode width and gap of 250 μm which was the limit of the thick film printing of the EDS facility. Figure 4.3a shows the IDS1.0 made on 0.6 mm alumina substrate having total dimensions of 74 mm by 52 mm.
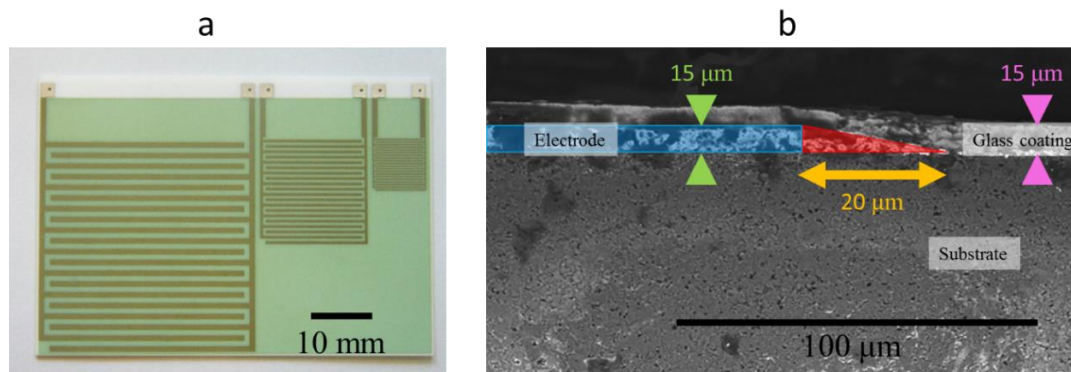


Figure 4.3. (a) Top view of the manufactured IDS board having three IDS showing substrate, electrodes and glass coating. (b) The cross section of the substrate, electrodes (green triangles), glass coating (pink triangles) and their smooth extension (yellow arrow) is highlighted.

The electrode and glass layer height was measured through scanning electrode microscopy (SEM) $t_c$ = 15 ±1 μm (Figure 4.3b). Although the electrode periodicity was accurate, the electrodes did not exhibit a sharp stop, and instead the silver ink liquefied during the firing process. The measured spread into the *g*-region (gap) was about 20 μm (red highlighted in Figure 4.3b).

Table 4.1. The design parameter and properties of the IDS1.0.

| Parameter | Symbol | Value |
|---|---|---|
| **Electrode's width** | $w$ | $\lambda/4$ |
| **Gap between electrodes** | $g$ | $\lambda/4$ |
| **Electrode's height** | $h$ | 10 μm |
| **Electrode's length** | $l_e$ | $9.25\lambda$ |
| **Connect electrode** | $l_c$ | $10\lambda$ |
| **Connect electrode width** | $w_c$ | $\lambda/4$ |
| **Fringe electrode** | $l_f$ | $l_e$ |
| **Fringe electrode width** | $w_f$ | $\lambda/4$ |
| **Sensor substrate thickness** | $t_s$ | 0.6 mm |
| **Sensor substrate rel permittivity** | $\varepsilon_{r,s}$ | ~ 10 |
| **Sensor coating thickness** | $t_c$ | 10 μm |
| **Sensor coating rel permittivity** | $\varepsilon_{r,c}$ | ~ 4 |
| **Sensor's wavelength** | $\lambda$ | 4 mm, 2 mm, 1 mm |

## 4.1.2 The electrical field distribution in space

Electric charges emanate electric fields in space. These fields contribute to the sensing properties. Knowing the distributed electrical field of such a sensor is thus of great importance. This can give us an estimation of the IDS figures of merit. Therefore, this section concentrates on the calculation of the electric field of co-planar strips. With the aid of this electric field distribution, the capacitance, sensitivity and accuracy is determined further utilizing the Schwarz-Christoffel-Mapping (SCM).

Two oppositely charged point electrodes represent an electric dipole for which solutions are readily available. The problem is the physical extension of the dipole electrodes making a prediction of the electric field difficult. This electric field can be calculated readily if we assume a constant total charge $Q$ (in coulombs) onto the electrode as approximation along $x_0 \leq w \leq x_1$, $w$ has units in meters. Each infinitesimal small point along $w$ may follow the electrical field distribution law $E(\mathbf{r}) = q/\mathbf{r}^2$ with $\mathbf{r}$ the vector in a Cartesian space and an arbitrary charge $q$. This charge can be defined to be equal to the total electrode charge divided by its

width $Q/w$, for a unit length in the $z$ direction. The Poisson equation employed, we find the potential $\psi$ from $q$ into space to be

$$\psi(\mathbf{r}) = \int d\mathbf{r}\, \vec{E}(\mathbf{r}) = \frac{q}{\mathbf{r}} + \text{const.} \, . \tag{4.1}$$

The total potential field in $x$ and $y$ direction is then formed by a charge $Q$ distributed along $w$ on the $x$-axis between $w_0$ and $w_1$

$$\Psi(x, y) = \int_{w_0}^{w_1} \psi(\mathbf{r})\, dw = \int_{w_0}^{w_1} dw\, \frac{Q}{\sqrt{\left(x^2 - w^2\right) + y^2}} \, , \tag{4.2}$$

for which we can write a finite sum of $k$-oppositely charged electrodes. We do so and incorporate the electrode periodicity $\lambda$ and the electrode separation $g$ for the integration limits,

$$\Psi_n(x, y) = Q \sum_{n=1}^{k} \int_{\lambda(n-1)/2}^{\lambda n/2 - g} dw\, \frac{(-1)^{n+1}}{\sqrt{(x-w)^2 + y^2}} \, . \tag{4.3}$$

The integration will yield a series of ln-terms such as

$$\Psi_n(x, y) = Q \sum_{n}^{k} (-1)^{n+1} \left\{ \begin{array}{l} \ln\left[ (\lambda n/2 - g) - y + \sqrt{((\lambda n/2 - g) - x)^2 + y^2} \right] \\ + \ln\left[ \lambda(n-1)/2 - y + \sqrt{((\lambda(n-1)/2) - x)^2 + y^2} \right] \end{array} \right\} , \tag{4.4}$$

which defines the potential function having $\pm Q$ charged coplanar strips in space. The gradient of this potential can be computed numerically yielding vector components of the electric field

$$\nabla \Psi_n(x, y) = -\mathbf{E}(x, y) = - \begin{bmatrix} E_x \\ E_y \end{bmatrix} . \tag{4.5}$$

This potential function of Equation 4.4, for the IDS, having 20 electrodes, with $w = g = \lambda/4$ has been calculated in MatLab. This calculation used the numerical value $Q = 1$ for the charges. A mesh, having $\Delta x = \Delta y = 0.0025\lambda$ was set-up. The resulting potential field is shown in Figure 4.4. It shows the horizontally aligned 20 electrodes at zero height. The symmetrical potential field appears to be wider distributed for the electrodes at the interior of the geometry than for

the inner electrodes. The electric field, Equation 4.5, was plotted for the positive upper half plane due to symmetry, Figure 4.5. Even here, the electric field is more distributed in space for electrodes at the outside of the geometry but the electric field is stronger for the electrodes within the geometry. White streamlines indicate the flux lines of the electric field showing that the field is periodically distributed in space.
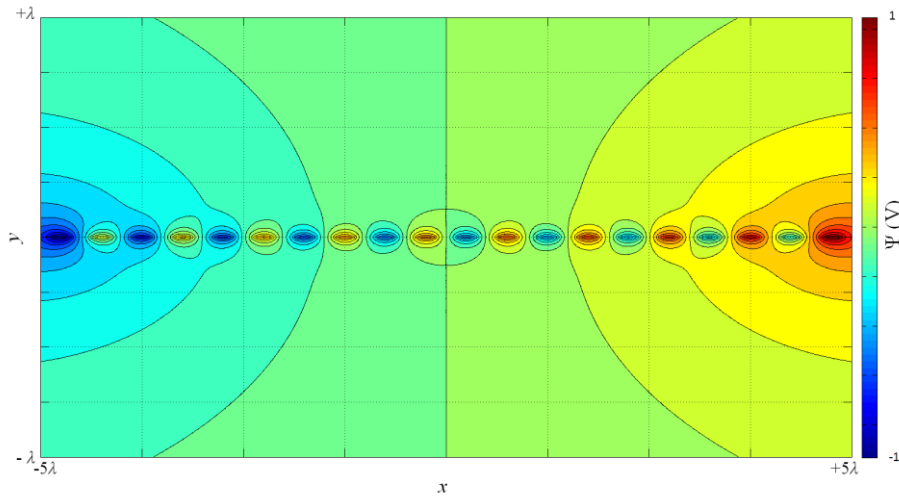


Figure 4.4. Contour plot of the calculated potential function $\Psi$ in $x$ and $y$ direction for the IDS having 20 electrodes at $y = 0$ in free space.
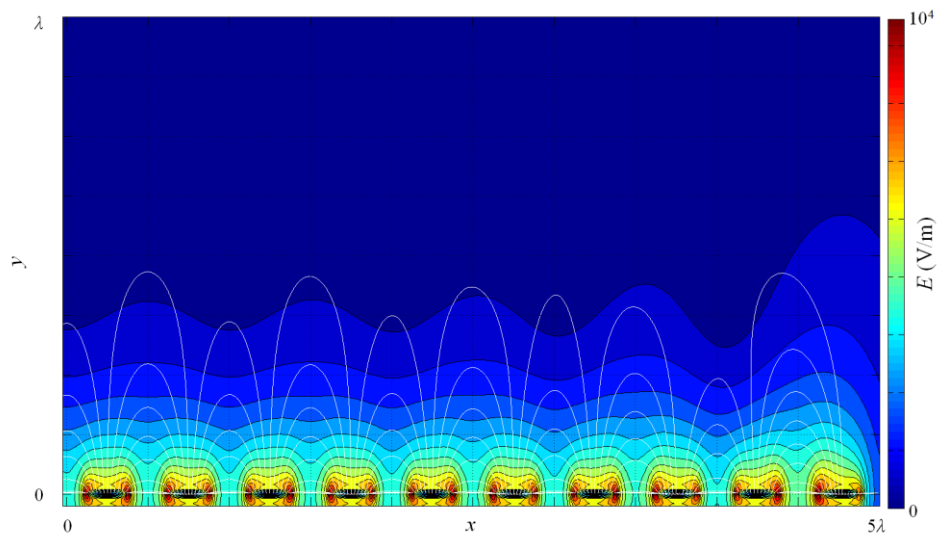


Figure 4.5. The electrical field magnitude $E$ in free space of the potential function $\Psi$ in $x$ and $y$ direction in the positive upper half plane for the IDS having 20 electrodes showing white electric field lines.

It is noticeable that the electric field is not uniform in space. This is contrary to what state of the art literature implies [15, 20, 21, 59]. As stated before, this

electric field is important to get an estimate for the figures of merit. Let us first get a clear function of the electric field dependent on *y* by means of averaging. The averaged electric field, $\bar{E}(y)$, perpendicular to the coplanar electrodes can be obtained by integrating over all *x*-values from *n* to the *k*-th electrode,

$$\bar{E}(y) = c\int_{n}^{k}\left|\mathbf{E}(x,y)\right|dx \;=\; c\int_{0}^{\lambda k/2-g}\left|\mathbf{E}(x,y)\right|dx, \tag{4.6}$$

where $c = 1/L$ with $L = \lambda k/2\text{-}g$. The numerical integral is then,

$$\bar{E}(y) = \sum_{n'=1}^{k'}\tfrac{1}{L}\left|\mathbf{E}(x_{n'},y)\right| = \frac{1}{L}\sum_{n'=1}^{k'}\sqrt{\left(\sum_{n}^{k}\mathbf{E}_{x_{n'}}\right)^{2}+\left(\sum_{n}^{k}\mathbf{E}_{y}\right)^{2}}\;, \tag{4.7}$$

which is plotted in Figure 4.6.
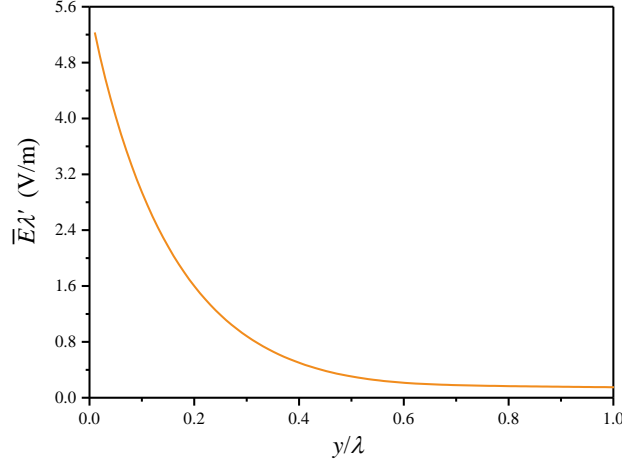


Figure 4.6. The average electrical field $\bar{E}$ times $\lambda$ over the distance $y/\lambda$ above the 20 calculated electrodes.

The electric field is shown as ratios of $\lambda' = \lambda/\Lambda$ over $y/\lambda$ where $\Lambda = 1$ m so that the units stays in V/m and the electric field can be calculated for any $\lambda$ by division. This function can be fit well ($R^2 \cong 1$) through an exponential function,

$$\bar{E}(y/\lambda) = c_1 e^{-ky/\lambda} + c_2 \;, \tag{4.8}$$

having a fit parameter $k \approx 6.72$. Thus, the function is exponentially inversely proportional to the wavelength $\lambda$. The constants $c_1$ and $c_2$ are due to integration of a linear and homogenous ordinary differential equation. Here, $c_n$ has units of V/m and the magnitude of the first constant is $c_1 = E_0 = \bar{E}(y/\lambda = 0)$. The constant

$c_2$ can be neglected, $c_2 = 0$, as the function does not show an offset. A criteria of the extent of the electric field can be found using this exponentially decaying function, with the arbitrary limit were the electric field in $y$ direction is decayed proportional to $e^{-2}$. Thus, employing this limit $\bar{E}(y/\lambda)/\bar{E}_0 = e^{-2}$, we find $y \approx 1/3\lambda$. This finding is consistent to many literature estimations for symmetric electrode design ($g = w$) [15, 19, 20, 59, 60, 62].

### 4.1.3 Figures of merit of the IDS1.0

The capacitance of a plane parallel capacitor is known to be proportional to the ratio of $A/d$. The IDS capacitance is not that straightforward but it can be calculated using the Schwarz-Christoffel-Mapping (**SCM**) method [76] that transforms coplanar strips from the $Z$-plane into a $T$-plane. In order to understand and verify it, the IDS capacitance is derived now. This $T$-plane has then parallel geometries. Figure 4.7 shows the transformation from the coplanar electrode plane (Figure 4.7a) to a plane parallel plate geometry (Figure 4.7b). The coplanar strips are first symmetrically placed between the gap around a coordinate $Z_x = 0$ showing $g/2$ and $w/2$ in a positive and negative direction. The SCM then employs a 90° ($\pi/2$) turning angle at the two edges of this geometry in a positive and negative direction of $Z_x$. That is, the end of $g/2$ (**B**) of the electrode and $w/2$ (**C**). Its transformed height in $T_y$-direction ($\overline{\mathbf{B'C'}}$) via imaginary numbers represents the transformed distance of the strip $w/2$ ($\overline{\mathbf{BC}}$) in the $Z_x$-direction. The real part of the complex number in positive $iT_x$-direction ($\overline{\mathrm{A'B'}}$) represents the electrode separation $g/2$ ($\overline{\mathbf{AB}}$). The symmetrical design is of physical usefulness as this transformation is logically applied on the side for which $Z_x$ holds negative values. This gives an enclosed geometry and thus the geometry ratio $A/d$ where $A$ is per unit length in the $T_z$-direction.

Analytically, from the general SCM definition in common literature, the function (c.f. Refs. [61, 77] and therein)

$$f(Z) = A + C \int_{Z_x} \prod_{k=1}^{n-1} (T - Z_k)^{\frac{\alpha_k - 1}{\pi}} dT , \qquad (4.9)$$

transforms a $Z$ plane to a $T$ plane. This can be written for the upper half plane of coplanar strips in positive and negative $Z_x$ with turning angles $\alpha_k = \pi/2$ to

$$f(Z_x) = A + C \int_{Z_x} (T - Z_B)^{\frac{-1}{2}} (T - Z_C)^{\frac{-1}{2}} (T - Z_B)^{\frac{-1}{2}} (T - Z_C)^{\frac{-1}{2}} dT . \qquad (4.10)$$
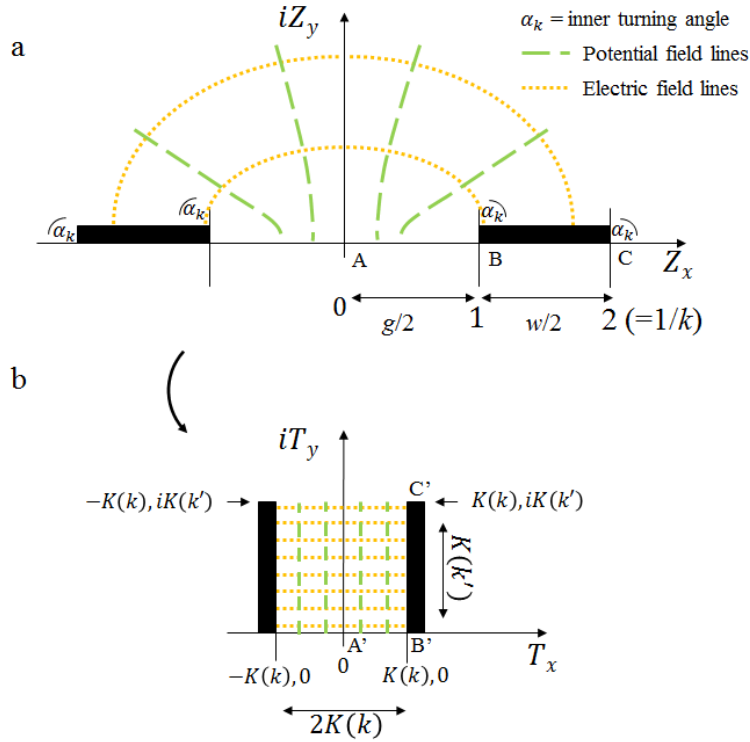


Figure 4.7 (a) The transformation from the physical coplanar electrode structure to a (b) plane parallel electrode structure. The electric and potential field lines from the black electrodes are shown schematically.

Due to symmetry the value, $Z_B = 1$ and $Z_C = 2$. Defining the $k$ variable according to the Figure 4.7a,

$$k := \frac{1}{w_{Z_x}} = \frac{g/2}{g/2 + w/2} = \frac{g}{g + w} = \frac{1}{2} , \qquad (4.11)$$

yields $Z_C = 1/k$. This can then be expressed as,

$$f(Z_x) = A + C \int_0^{Z_x} \frac{dT}{(T-1)^{\frac{1}{2}} (T - 1/k)^{\frac{1}{2}} (T - (-1))^{\frac{1}{2}} (T - (-1/k))^{\frac{1}{2}}} , \qquad (4.12)$$

which is the elliptical integral first kind:

101

$$f(Z_x)/k = \int_0^{Z_x} \frac{dT}{\sqrt{(T^2-1)(k^2T^2-1)}} .$$

(4.13)

This is a function which yields real numbers for the transformed $g/2$ and complex numbers for the transformed $w/2$,

$$f(Z_x)/k = \begin{cases} K(k) & \\ K(k)+iK(k') & \end{cases} \text{if } \begin{matrix} Z_x \in 0...<1 \\ Z_x \in 1...\le 2 \end{matrix} .$$

(4.14)

Now, with the aid of Figure 4.7b (1/2 factor!), the capacitance of the coplanar pair of strips can be readily calculated using $\varepsilon_0$ as the permittivity of free space and $\varepsilon_r$ as the relative permittivity of the material under test,

$$C = \varepsilon_0\varepsilon_r \frac{A}{d} = \varepsilon_0\varepsilon_r \frac{a}{d}l = \varepsilon_0\varepsilon_r \frac{K(k')}{2K(k)}l_e .$$

(4.15)

This result is consistent with literature although $C$ is expressed as $1/C$ in Ref. [61]. This discrepancy needed to be solved by derivation. Introducing the number of electrodes $N$ and the appropriate elliptical integral ratio for the fringe and connect electrodes with their respective values $g_f = g_c = 39$ mm, $w_c = 1$ mm $w_f = 0.5$ mm, the total capacitance of $N = 20$ electrodes will then be,

$$\begin{aligned} C &= 2\varepsilon_0\varepsilon_r \left( \frac{K(k')}{2K(k)}l_e(N-1) + \frac{K(k_c')}{2K(k_c)}l_c + \frac{K(k_f')}{2K(k_f)}l_f \right) \\ &= 17.7\,\varepsilon_r\,\text{pF/m}\left( \frac{K(k')}{2K(k)}l_e(N-1) + \frac{K(k_c')}{2K(k_c)}l_c + \frac{K(k_f')}{2K(k_f)}l_f \right) \\ &= 17.7\,\varepsilon_r\,\text{pF/m}\left( 474.2\text{mm} + 10.8\text{mm} + 9.8\text{mm} \right) \\ &= 8.8\varepsilon_{r,\text{eff}}\,\text{pF.} \end{aligned}$$

(4.16)

This capacitance represents the electrode's free space intrinsic capacitance for $\lambda = 4$ mm dependent on the relative permittivity, denoted as $\varepsilon_{r,\text{eff}}$ for the following section.

As an approximation for the sensor's capacitance in the presence of the dielectric media (substrate), the information of its electric field comes into play here. The substrate thickness is given with $t_s = 0.15\lambda$. Thus, the effective

permittivity contribution of the substrate, "*s*", can be approximated via an effective relative permittivity of the underside, "*u*",

$$\varepsilon_{\text{r,eff, u}} = \frac{A\varepsilon_\text{s} + B\varepsilon_\text{air}}{A + B} = \frac{\int_0^{t_\text{s}} \overline{D}(y)\varepsilon_\text{s}\, \text{d}y + \int_{t_\text{s}}^{\infty} \overline{D}(y)\varepsilon_\text{air}\, \text{d}y}{\int_0^{\infty} \overline{D}(y)\text{d}y} \, . \tag{4.17}$$

The parameter $\bar{D} = \varepsilon\bar{E}$ is the displacement field independent of the total permittivity $\varepsilon$. This can be used to estimate the qualitative electric field penetration though all participating dielectrics. Evaluating this integral yields $A = 0.4$ and $B = 0.24$ and with the substrate permittivity, $\varepsilon_\text{r,s} = 10$, this calculates to the effective permittivity for the underside $\varepsilon_\text{r,eff, u} = 6.3$.

The coating layer is about $t_\text{c} = 10$ μm which is negligible in respect to the employed $\lambda$ dimensions. Thus, the $\varepsilon_\text{r}$ of the top side can be stated as $\varepsilon_\text{r, eff, t} = 1$. Hence, the effective permittivity of the sensor's material is,

$$\varepsilon_{\text{r, eff}} = \tfrac{1}{2}\varepsilon_{\text{r, eff, u}} + \tfrac{1}{2}\varepsilon_{\text{r, eff, t}} = 3.65 \, , \tag{4.18}$$

the IDS vacuum capacitance for $\lambda = 4$ mm is consequently $C = 32.12$ pF. This value will be affected by $\lambda$ as the distributed electric field is proportional to $\lambda$ but $t_\text{s}$ is constant. Based on this, a larger $\lambda$ potentially offers a more sensitive IDS. The theoretical capacitance for the $\lambda = 4$ mm was then compared with the measured capacitance for the sensor having $\lambda = 4$ mm in air. The average value across three measurement sets of each with 51 data points was $C = 31.2 \pm 2.8$ pF. This experimental result lays within the theoretical calculation. For the case of measuring the insulating liquid, $\varepsilon_\text{r, eff,t} \approx 2.1$, the capacitance change is proportional to the ratio of both the effective permittivities. For example, calculating $\varepsilon_\text{r,eff}$ using Equation (4.17): $\varepsilon_\text{r,eff,air} = 3.65$ and $\varepsilon_\text{r,eff,MUT} = 4.2$, thus the capacitance rises about 15%; $\varepsilon_\text{r,eff,MUT}/\varepsilon_\text{r,eff,air} = 4.2/3.65 = 1.15$. The sensitivity for measuring $\varepsilon_\text{r}$ is $S = \partial C/\partial\varepsilon_\text{r}$ $= (C_\text{MUT}\text{-}C_\text{air})/(C_\text{air}[\varepsilon_\text{MUT}\text{-}\varepsilon_\text{air}]) = 14\%$. As a comparison, the test cell (section 3.1) has a sensitivity of 100%.

In order to validate theory and evaluate the sensitivity and accuracy, a series of measurements were done using the IDS1.0 within the dielectric test cell as temperature stable and electrically shielded environment. The IDS was mounted with its underside to the interior of the test cell on one side so that the IDS electrodes were submerged in insulating liquid within the housing of the cell.

The capacitive air measurements of the three different $\lambda$, dependent on the frequency is shown in Figure 4.8a. The three IDS wavelengths are exhibiting an increase in its capacitance for lower frequencies.

The temperature dependence is shown in Figure 4.8b to Figure 4.8c for the respective IDS wavelength $\lambda$. As the temperature increases, the permittivity of the substrate reduces and thus a lower value was observed for $\lambda = 4$ mm and $\lambda = 2$ mm. The opposite was observed for the $\lambda = 1$ mm. A total reduction in the magnitude of the capacitances was due to the electrostatic "confinement" of the cell. Here, the cell was acting as Faraday shield affecting the electric field emanated from the IDS. If the field distribution is sensitive to the substrate permittivity (which is temperature dependent), these field lines will find a different path, due to a change in the substrate temperature affecting the capacitance.

In Figure 4.9a, the measured permittivity is shown as a ratio of the IDS capacitance with an insulating liquid over IDS air capacitance at 21 °C. Ideally, this ration should yield the permittivity of the insulating liquid, $\varepsilon_r = 2.1$, but the measurement showed a sensitivity $S = \partial C/\partial \varepsilon_r$ lower than 1 % across all three sensor wavelengths ($\lambda$). This was consistent with finite element modelling simulations. From this data it is clear that the sensitivity for all wavelengths is weak and this sensor generation does not work. In particular, the theory hypothesized that the largest wavelength is supposed to exhibit the strongest sensitivity. In the measurements within the cell, it was found that the $\lambda = 4$ mm wavelength showed

a negative sensitivity. The scenario of having the IDS within a shielded environment was reproduced in FEM, Figure 4.9b. It could be found that due to a change in the MUT's permittivity, the electric field lines are strongly affected by the shielded underside behind the substrate of the IDS.

Table 4.2 elaborates the measurements in detail and also compares the measured permittivity versus the simulated permittivity (Comsol Multiphysics 4.2, Laplace module). While a consistency was found between theory and experiment, the sensing accuracy $A$, which can be defined trough $A = 1\text{-}D$, for the deviation $D = (\varepsilon_{r,\text{IDS}} - \varepsilon_{r,\text{ref}})/\varepsilon_{r,\text{ref}}$ with $\varepsilon_{r,\text{ref}} = 2.1065$, was determined to be very small for all three wavelengths.
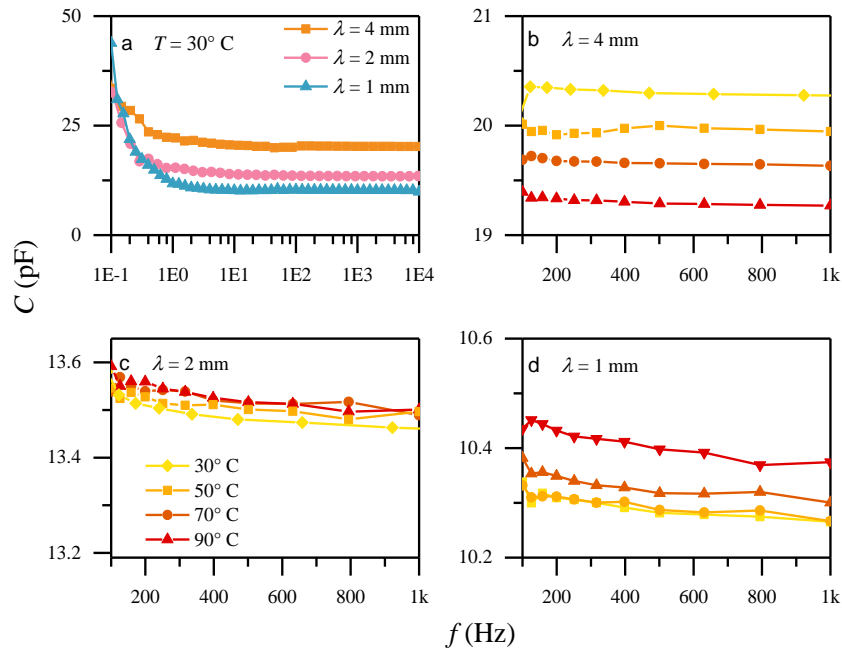


Figure 4.8 (a) The air capacitance over the frequency of the three IDS wavelengths at 30 °C within the test cell. (b) The capacitance over frequency showing its temperature dependency of the wavelengths $\lambda = 4$ mm, (c) $\lambda = 2$ mm and (d) $\lambda = 1$ mm.
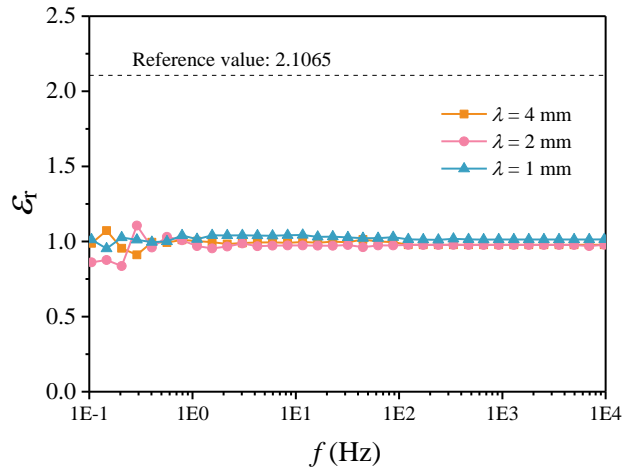
Figure 4.9a. The permittivity of the insulating liquid as measured with the IDS1.0 as function of frequency. The actual (reference) value of the insulating liquid is shown as a dashed line. The value of $\varepsilon_r = 1$ means that the IDS capacitance is unaffected by the presence of the insulating liquid.
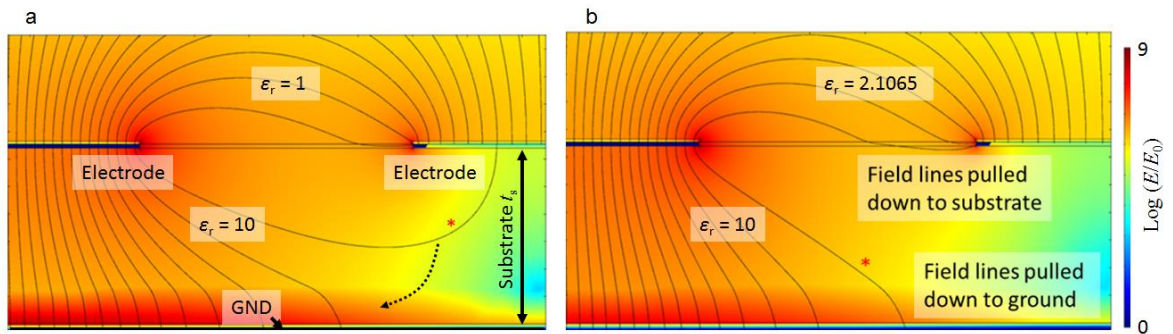


Figure 4.9b. Field lines in presence of a grounded backplane for (a) air and (b) MUT with $\varepsilon_{r,ref} = 2.1065$. The presence of the backplane alters the electric field visually, affecting the sensing properties.

Table 4.2. The figures of merits of the IDS for the three wavelengths compared with simulations.

| Measured | | | | | |
|---|---|---|---|---|---|
| Wavelength | $C_{Air}$ (pF) | $C_{MUT}$ (pF) | $S$ (pF) | $\varepsilon_r$ | $D$ |
| 4 mm | 19.765 ± 0.002 | 19.222 ± 0.005 | -0.491 ± 0.01 | 0.972 ± 0.001 | -54% |
| 2 mm | 12.758 ± 0.001 | 13.285 ± 0.002 | 0.476 ± 0.01 | 1.041 ± 0.001 | -51% |
| 1 mm | 9.926 ± 0.001 | 10.703 ± 0.002 | 0.701 ± 0.01 | 1.078 ± 0.001 | -50% |
| Simulated | | | | | |
| Wavelength | $C_{air}$ (pF) | $C_{MUT}$ (pF) | $S$ (pF) | $\varepsilon_r$ | $D$ |
| 4 mm | 19.782 | 19.321 | -0.4191 | 0.9771 | -54% |
| 2 mm | 12.612 | 13.189 | 0.5246 | 1.0458 | -51% |
| 1 mm | 9.9455 | 10.799 | 0.7759 | 1.0858 | -49% |

### 4.1.4 Conclusion of IDS1.0

A structure of an IDS was designed, manufactured and tested in air as well as in insulating liquid. The electric field distribution was evaluated via analytical expressions using point charges from which a capacitance could be calculated using Schwarz-Christoffel-Mapping method. Subsequent evaluation of the sensitivity and accuracy showed that the capacitance when measuring the insulating liquid only exhibited a minimal sensitivity. This was attributed to the large intrinsic capacitance of the sensor due to the substrate. Effectively, this sensor generation could not measure the insulating liquid.

A substantial redesign of this sensor technology is necessary in order to avoid the determined problems in the first place. Thus, a further exploration of this technology is done in the next section which is about the successor generation IDS2.0.

## 4.2 IDS2.0

The goal in the generation 2.0 is to improve the figures of merit by means of shielding electric fields that contributed detrimentally to the performance of the generation 1.0. In Figure 4.10a, the electric field of the first generation is shown schematically. In this second generation, the effect of a grounded plane which is shielding a large proportion of the intrinsic capacitance is investigated. Such an effect is depicted as a sketch in Figure 4.10b. The improvements made are regarding the sensitivity and accuracy. The fabrication was transferred to PCB technology in order to investigate the fabrication of these sensors in a more cost efficient technology which is readily available. One advantage of choosing PCB technology is the multilayer capability from which a grounded plane can be placed underneath the electrodes. This improved the sensitivity and accuracy by shielding the sensing of the substrate. This idea was continued and an electric shield, serving as a Faraday cage, was applied above the electrodes for improving

the precision. Figure 4.10c and Figure 4.10d shows this Faraday shield and its qualitative effect on the electric field without and with the grounded plane respectively. A quantitative evaluation on the figures of merit, such as the capacitance, sensitivity and accuracy, required an analysis using a particular Green's function.
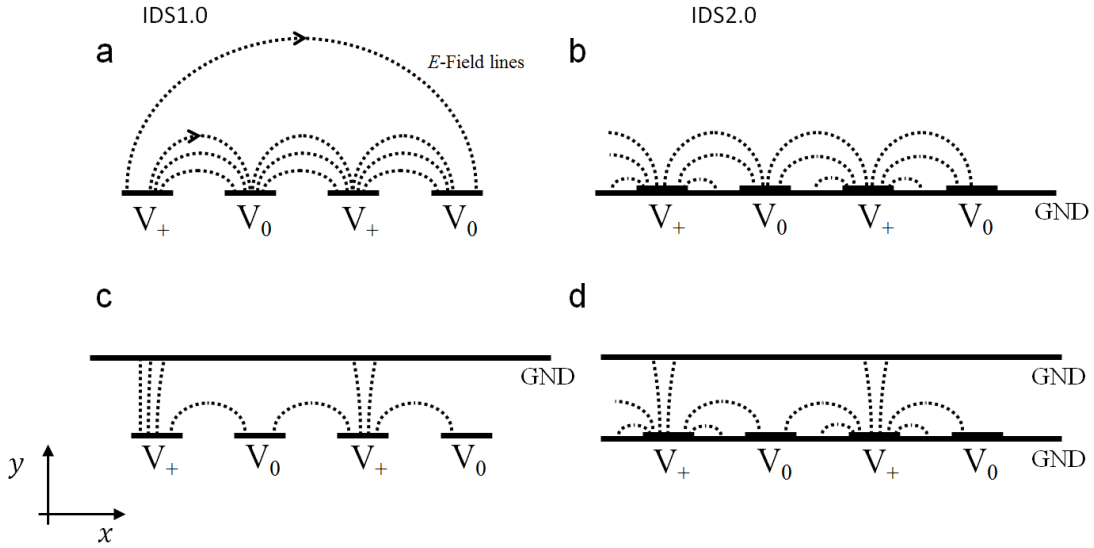


Figure 4.10. Evolution of the IDS generation 1.0 (a) to 2.0 (d). (a) Bare electrodes in free space. (b) Electrodes with a ground plane underneath. (c) Electrodes with a Faraday shield. (d) Electrodes with a Faraday shield and ground plane underneath. Electrodes are infinite in $z$-direction.

Some of these presented figures data and text passages are similar or identical with the open access publication in Ref. [22], published by Alex Risos, Nick Long, Arvid Hunze and Gideon Gouws. The co-authors, Nick Long, Arvid Hunze and Gideon Gouws, agreed with the usage of the publication in this thesis.

### 4.2.1 Analytical approach via Green's function

A Green's function for the Laplace equation [76] was employed to give an solution for the IDS electric field and capacitance. The IDS potential function $\Psi$ without GND underneath the electrodes is found by integrating over three analytical Green's function expressions, $G()$, determined by the surface potential $\psi(\xi)$ dependent on $\xi_a = 0$ depicted in Figure 4.11.

Figure 4.11. The function $\psi(\xi)$ for the IDS <u>without</u> grounded plane.

The surface potential $\psi(\xi)$ for $V_+$ and $V_0$ is 1 and 0 respectively. In between the electrodes $V_+$, and $V_0$ a positive ($\psi_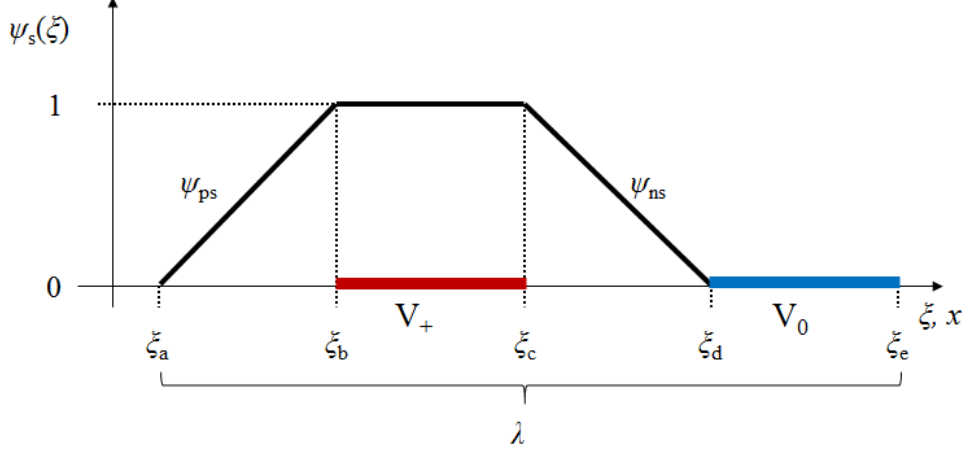{ps}$) and negative slope ($\psi_{ns}$) is assumed as a linear approximation [60]. Starting with the Green's function in the upper half plane in along the $x$-axis at $y = 0$ [76],

$$G\left(x, y|\xi\right) = \frac{1}{\pi} \frac{y}{\left(x - \xi\right)^2 + y^2} . \tag{4.19}$$

The $\psi(\xi)$ in between the electrodes (Figure 4.11) is defined through

$$\psi_{ps}(\xi) = (-n\lambda + \xi)/g , \tag{4.20}$$

and

$$\psi_{ns}(\xi) = ((3/4 + n)\lambda - \xi)/g , \tag{4.21}$$

where $n = 0, 1, 2, ..., N$ determines the number of $\lambda$ in the system, $\xi_a = \xi_b = \xi_d = \xi_e = \lambda/4$ and $g = \lambda/4$ is the gap for this calculation. These $\psi(\xi)$ functions (Equations 4.20 and 4.21) are only valid for appropriate integral limits as shown in Equation 4.22. The potential function is then the superposition of three separate functions as the function for the neutral electrode is zero as $\psi(V_0) = 0$. The surface potential at the active electrode $V_+$ is $\psi(V_+) = 1$;

$$\Psi\left(x, y\right) = \sum_{n=0}^{N} \left[ \begin{array}{l} \int_{\xi_{a+n\lambda}}^{\xi_{b+n\lambda}} G\left(x, y|\xi\right)\left(\psi_{ps}(\xi)\right)d\xi + \int_{\xi_{b+n\lambda}}^{\xi_{c+n\lambda}} G\left(x, y|\xi\right)d\xi \\ + \int_{\xi_{c+n\lambda}}^{\xi_{d+n\lambda}} G\left(x, y|\xi\right)\left(\psi_{ns}(\xi)\right)d\xi \end{array} \right] . \tag{4.22}$$

109

This straightforward integration has solutions as **arctan** and **ln** functions which are omitted for clarity.

The potential function for the electrodes in Figure 4.12, having a grounded plane underneath, simplifies to;

$$\Psi(x,y) = \sum_{n=0}^{N}\left[\int_{\xi_{b+n\lambda}}^{\xi_{c+n\lambda}} G(x,y|\xi)(1)d\xi\right], \tag{4.23}$$

of which its solution can be written as,

$$\Psi(x,y) = \sum_{n=0}^{N} \operatorname{atan}\left(\frac{\xi-x}{y}\right)\Bigg|_{\xi_{b+n\lambda}}^{\xi_{c+n\lambda}}. \tag{4.24}$$

The potential functions can be calculated using MATLAB where its numerical gradient can be computed giving the electric field $E$. This electric field was plotted as its magnitude.
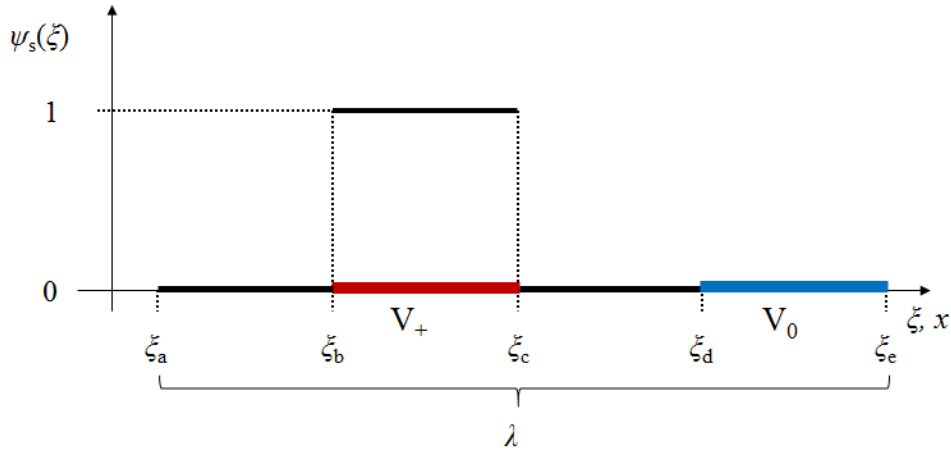


Figure 4.12. The function $\psi(\xi)$ for the IDS <u>with</u> grounded plane.

This is an approximation of having zero distance to the lower ground plane. All geometries have no thickness and the effective length $l$ of the electrodes is infinite [60].

### 4.2.1.1 The calculated potential and electric field in free space

The free space potential $\Psi$ for the IDS having 20 electrodes without a grounded plane underneath the electrodes is shown in Figure 4.13. The potential of 1 V for the $V_+$ electrode falls and rises linearly for the gap $g$ between the

110

electrode(s) $V_0$. The potential is defined zero along $x$ for $0 \le x/\lambda \le 10$ and thus a 'bulge' is occurring at the center of the geometry.



Figure 4.13. The distributed electric potential above 20 electrodes in $x$ and $y$ space for the IDS without a grounded plane underneath the electrodes.

Its electrical field is shown in Figure 4.14. At each point of the electrodes, i.e. the points of each $\xi_{a,b,c,d,e}$, the electric field spikes. This is a phenomenon to a similar reported calculation [60] which is caused by an abrupt change of the $\psi(\xi)$ function due to the derivative at this point. The electric field magnitude is plotted as $E\lambda'$ where $\lambda' = \lambda/\Lambda$ with $\Lambda = 1$ m.
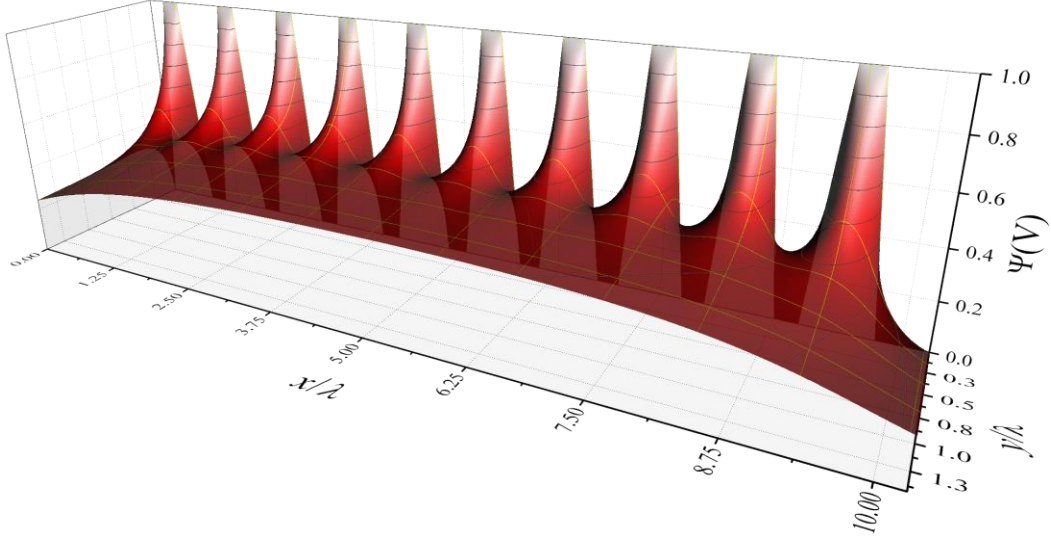
The surface potential from Figure 4.13 and the surface electric field from Figure 4.14 where $y \to 0$ is shown in Figure 4.15. The surface potential function $\psi(\xi)$ shows a positive and negative slope from which its derivative spikes at each non-smooth change of $\psi(\xi)$. The electric field goes up to $\sim 8$ V; i.e. for $\lambda = 4$ mm, the electric field is about 2000 V/m at those spikes. This could not be obtained from the calculation for in $x$ and $y$ direction, Figure 4.14, due to finite meshing size of $y/\lambda = 0.000675\lambda$. The total averaged electrical field (c.f. section 4.1.2), $\bar{E}$, across the 20 electrodes along the $x$-axis which is distributed in free space in shown in Figure 4.16 in terms of $\lambda$ versus the distance $y/\lambda$. It can be deduced that the electrical field decays rapidly. It was found that the definition for the effective

111

electric field distribution distance $\bar{E}(y/\lambda)/\bar{E}_0 = e^{-2}$ yielded $y \approx 0.3\lambda$. This result of the effective electric field distribution is consistent with the calculation for the IDS1.0 using the Poisson equation.



Figure 4.14. The electric field from the calculated potential $\Psi$ without GND below the electrodes.



Figure 4.15. Surface potential and surface electric field of the electrodes without a grounded plane.
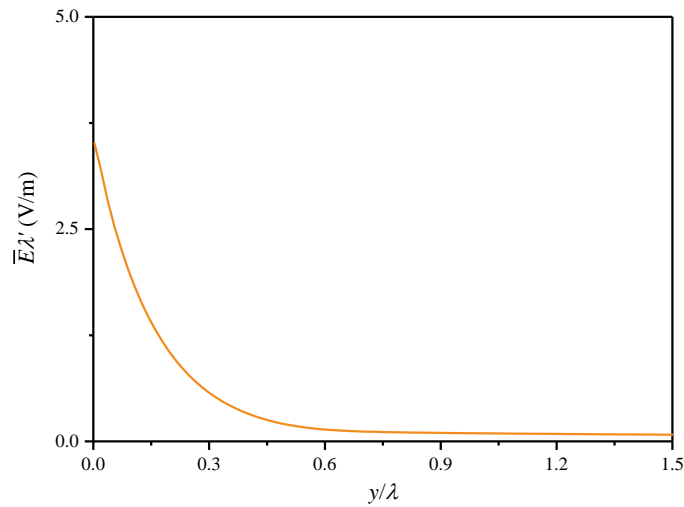
Figure 4.16. The averaged electrode field $\bar{E}$ normalized in terms of $\lambda$ as function of distance above the 20 electrodes *without* GND below the electrodes.

## 4.2.1.2 The calculated potential and electric field in free space with a grounded plane

While the previous section confirmed the calculations for the chapter IDS1.0, the interesting question is how a grounded plane underneath the electrodes affects the physical properties. Figure 4.17 shows that the grounded plane affects the propagated potential; the potential is restricted stronger to the grounded plane, which results in a weaker potential distribution in space. This affects the electric field as plotted in Figure 4.18. Due to the instant change of the potential from 1 to 0, the electric field spikes at those points. It is a matter of numerical uncertainty that the spikes are limited to a value of 20 in this figure.
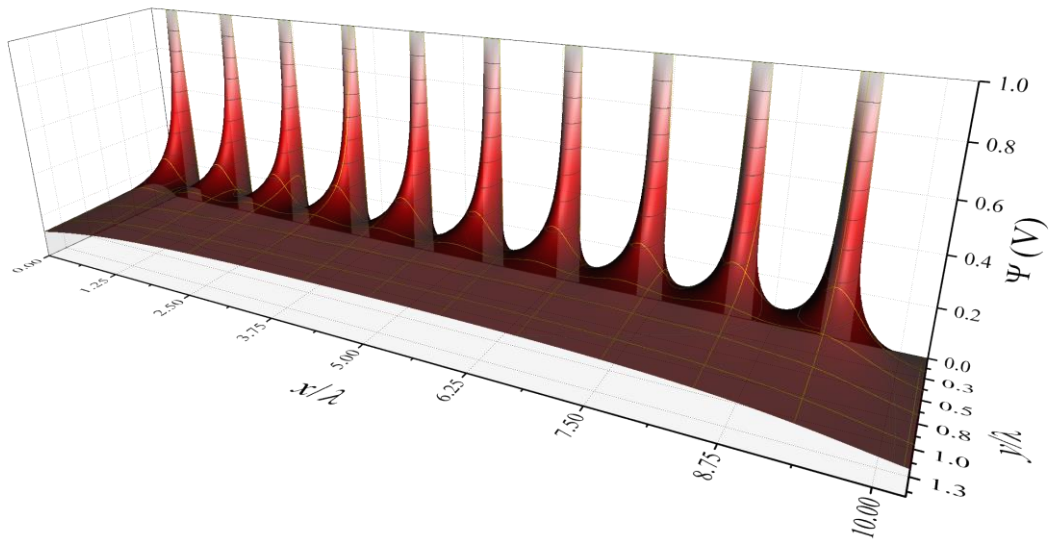
Figure 4.17. The distributed electric potential above 20 electrodes for the IDS with a grounded plane underneath.
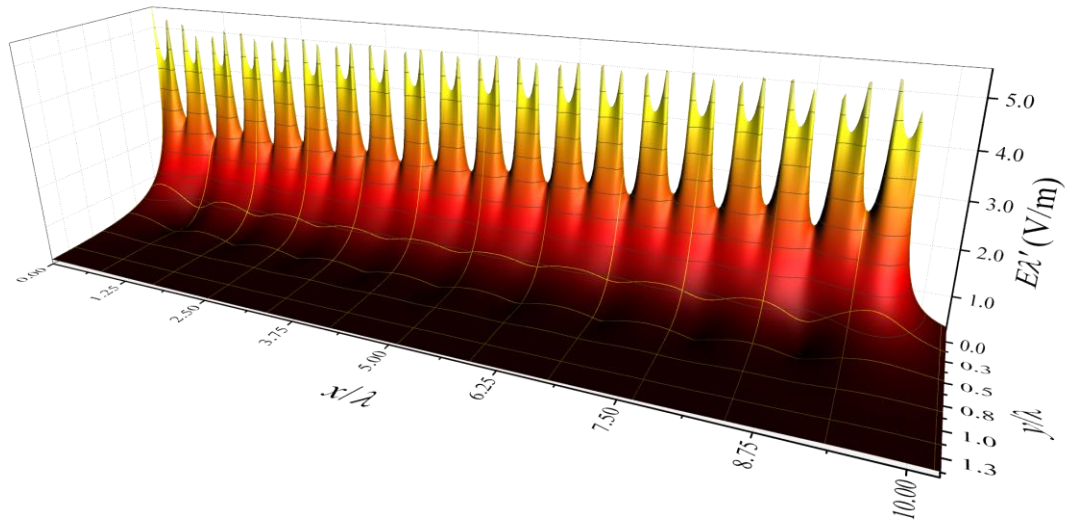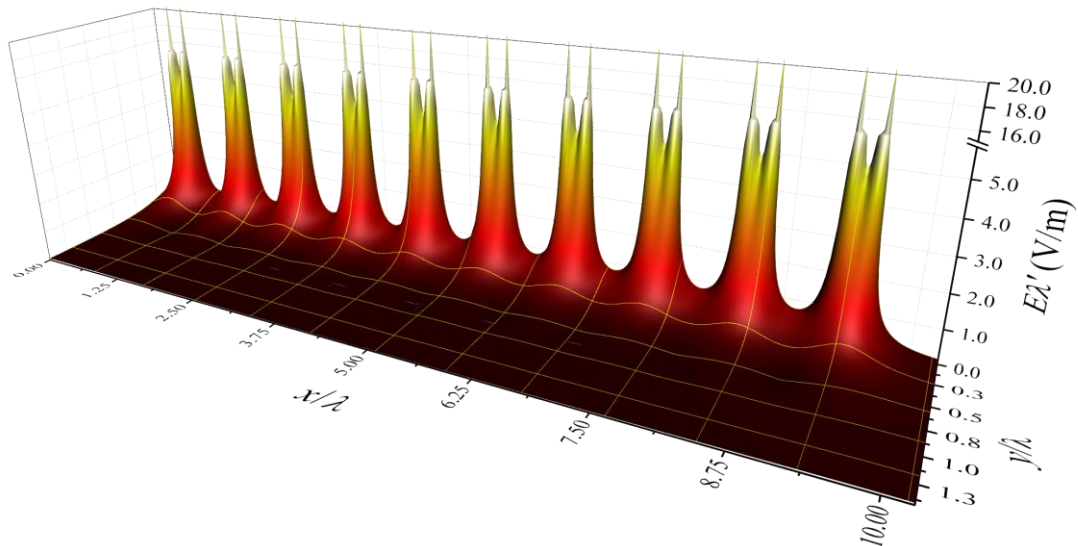


Figure 4.18. The electric field from the calculated potential $\Psi$ with GND below the electrodes.

The surface potential and electric field is plotted in Figure 4.19. At the points of the end of each positive electrode at $\xi_b$ and $\xi_c$, we can examine a high spike in the electrical field. The distributed electrical field, Figure 4.20, is however less affected by those spikes. The effective distance $y \approx 0.3\lambda$ for $\bar{E}(y/\lambda)/\bar{E}_0 = e^{-2}$ could also be reproduced even under the presence of a grounded plane.
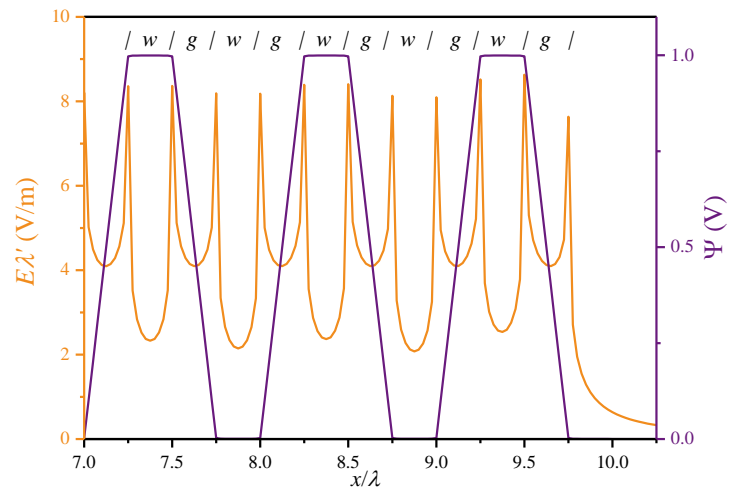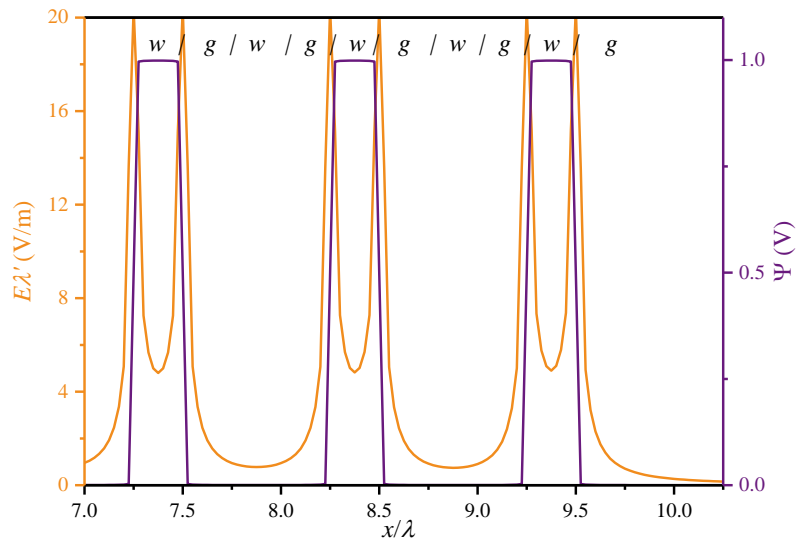
Figure 4.19. Surface potential and surface electric field of the electrodes with GND below.
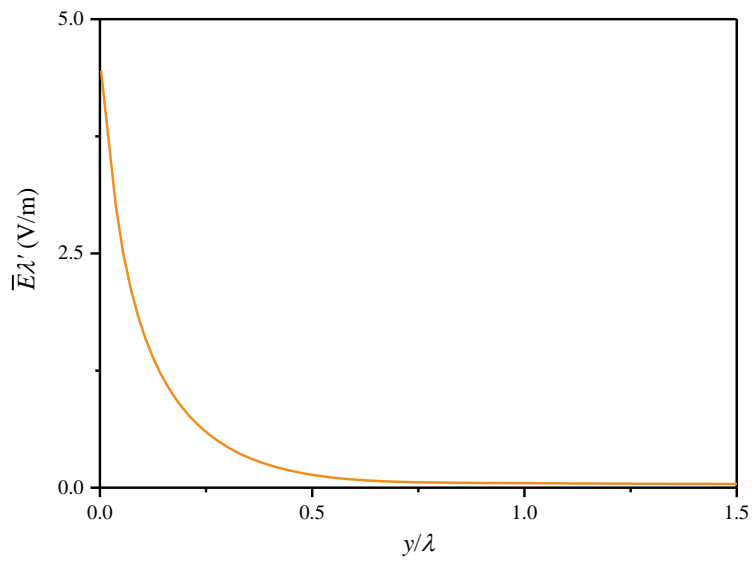


Figure 4.20. The averaged electrode field as function of distance above the 20 electrodes with a grounded plane below.

Comparing the electric field with and without a grounded plane, it can be deduced that for the sensing relevant electric field above the IDS does not vary significantly when applying a grounded plane underneath the electrodes.

## 4.2.2 The manufactured IDS2.0 via PCB technology

As a result of the calculations made, the IDS2.0 is equipped with a grounded plane underneath its electrodes in order to reduce the intrinsic capacitance, which is detrimental for the figures of merit. The IDS was produced via standard commercial multilayer printed circuit board (PCB) technology (Shenzhen JDB Technology Co., Ltd). The wavelengths $\lambda$, having a ratio of $w/g = 1$, were chosen as 1 mm, 2 mm and 4 mm. Also here, $\lambda = 1$ mm required a trace width of 250 µm which was a physical lower limit for the employed PCB technology. The geometry was kept similar to the IDS1.0 for reasons of comparison, the length $l$ of the 20 electrodes were 9.25 mm, 18.5 mm and 37 mm respectively. Figure 4.21a shows the PCB layout of the IDS depicting its multilayer structure. Here, the copper areas are red, while lead separation is shown in black. The IDS electrodes are shown as yellow parallel strips. The manufactured version is shown as photograph with dimensions in Figure 4.21b. This multilayer board structure shields each of the four terminals with a grounded layer to the sides, below and above resulting in a 3D shielded lead design. These leads connect to the IDS electrodes through Vertical Interconnect Accesses (VIA). This approach ensures accurate and precise measurements by reducing parasitic capacitance and mutual inductance of the leads. Figure 4.21c depicts a cross-sectional view obtained via Scanning Electrode Microscope (SEM). The dimensions and dielectric values of these dimensions are listed in Table 4.3.
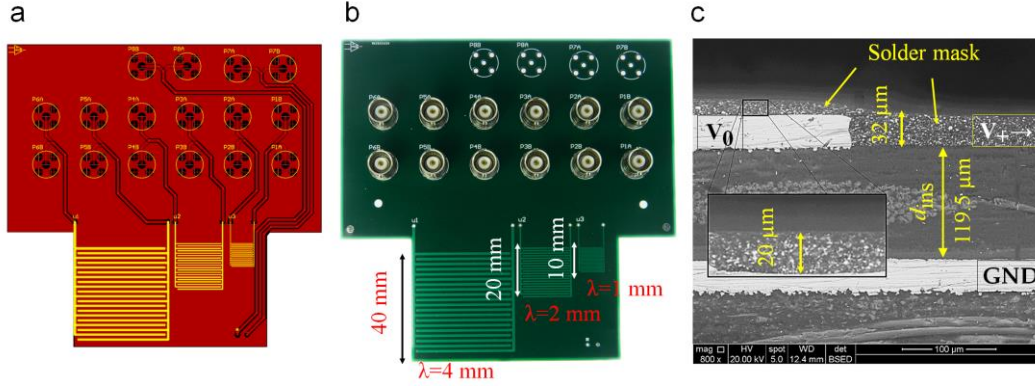
Figure 4.21. (a) The IDS2.0 board as PCB drawing prior manufacturing showing the shielded sensing leads (red) and the IDS electrodes (yellow). (b) The manufactured IDS board showing dimensions of the three IDS electrodes. (c) A SEM cross section view showing spatial dimensions of the relevant layers.

Table 4.3. The dimension and permittivity of the relevant structure of the SEM image.

| Component | Size | Permittivity $\varepsilon_r$ |
|---|---|---|
| **FR4 insulator ($d_{ins}$)** | 119.5 µm | 4.5 |
| **Solder mask between electrodes** | 30 µm | 4.5 |
| **Solder mask above electrode** | 20 µm | 4.5 |
| **Electrode thickness** | 32 µm | - |

### 4.2.3  Measurements of the IDS2.0

The measurements of the sensitivity and accuracy were carried out via a four wire capacitive measurement through the impedance analyser. This four wire BNC setup ensured precise and accurate measurements. Overall 12 BNC connectors were necessary in order to connect all three IDS. Additional four BNC connectors were originally designed for temperature measurements, however, these where not necessary in this setup as the test cell housing (section 3.1) was equipped with a temperature control. The IDS2.0 was placed into the test cell housing as shown in Figure 4.22. The distance to the interior of the grounded housing to the surface of the IDS board was 13.7 ± 0.1 mm - well beyond the effective distributed electric field, $y_{eff} = 0.3\lambda$; for the largest wavelength of $\lambda = 4$ mm, this distance is equivalent to $\approx 3.5\lambda$. The housing was grounded and the served as a Faraday cage so that the measurement was less subject to noise. The

117

measurements at 1 $V_{RMS}$ across the electrodes were carried out a total of three times and the average value was determined.
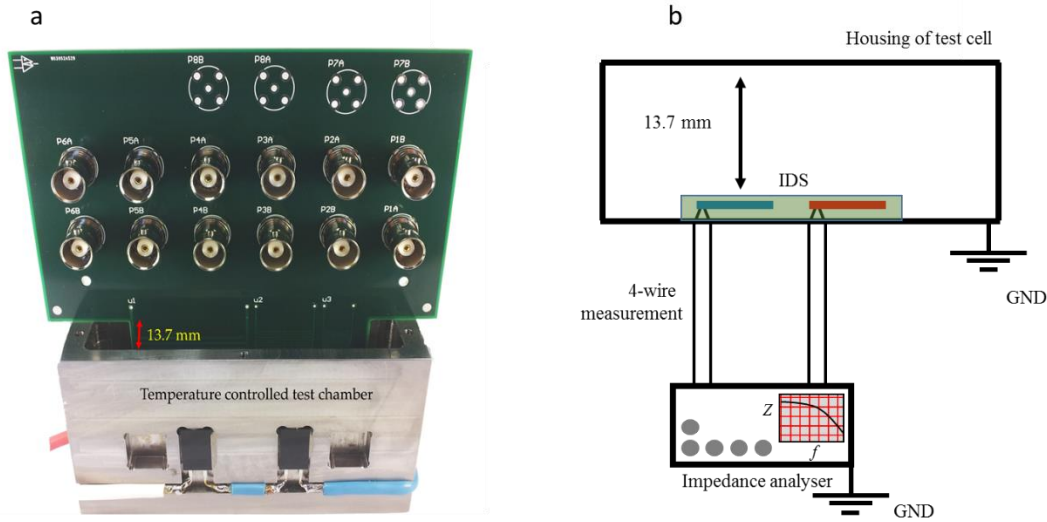


Figure 4.22. (a) Photo and (b) a schematics arrangement of the IDS within the test cell for measuring in an electrically shielded and temperature controlled environment.

### 4.2.3.1 Capacitance, Sensitivity and Accuracy

The measurements presented in Figure 4.23 examine the three IDS on the PCB IDS board. The measurements were carried out in air at temperatures from 30 to 90 °C. For each data point a total of 36 measurements were internally averaged by the measurement instrument. A quantitative evaluation of Figure 4.23 is given in Table 4.4. The frequency dependent air capacitance is shown in Figure 4.23a over the range of 0.1 to 10000 Hz. A significant increase in the capacitance occurs for frequencies below 20 Hz showing frequency limits using this type of IDS which can be attributed to a sensitivity issue of the impedance analyzer. This effect arises for frequencies below 1 Hz for the IDS1.0 as the capacitance is about 20 times larger giving a proportional larger signal to the instrument. The capacitance with frequency is more stable between 100 to 1000 Hz. The temperature dependence is therefore shown across 100 to 1000 Hz. The capacitance for the $\lambda = 4mm$ in Figure 4.23b is constant at about $1.075 \pm 0.01$ pF

between 30 to 90 °C. A measurable relative change in the capacitance of about - 3% occurs with temperature for the $\lambda$ = **2 mm** wavelength as shown in Figure 4.23c. The capacitance decreases with increasing temperature, indicating a presence of a parasitic capacitance. For the $\lambda$ = 1 mm measurements in Figure 4.23d the capacitance also changed with temperature by about -1%. This indicates stronger parasitic capacitances for a smaller $\lambda$.
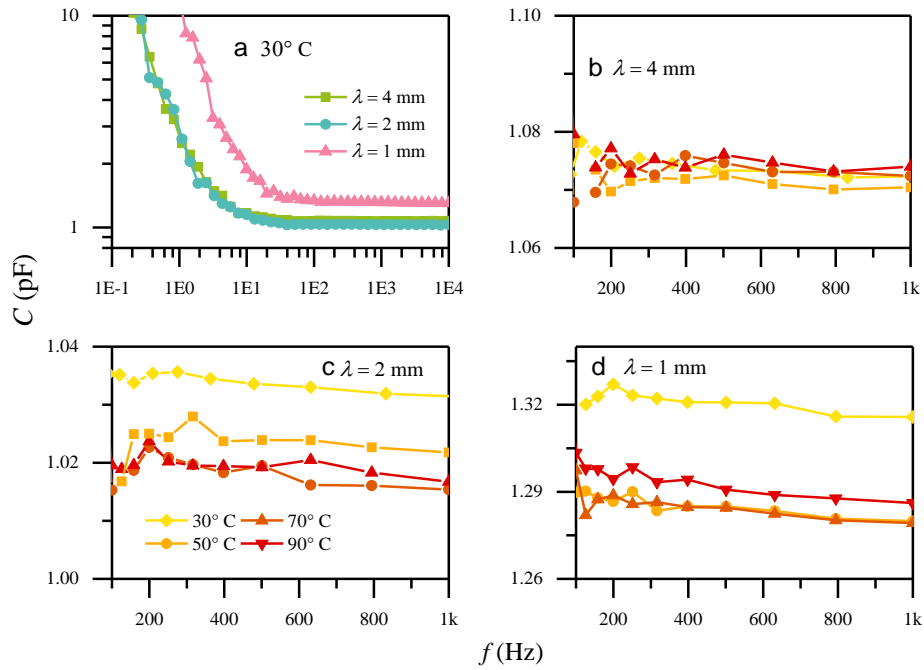


Figure 4.23. (a) The frequency dependent capacitance for $\lambda$ = 4, 2, 1 mm. (b) the $\lambda$ = 4 mm, (c) $\lambda$ = 2 mm, and (d) $\lambda$ = 1 mm capacitance over frequency $f$ from 30 to 90 °C.

An insulating liquid (see section 3.2) having a $\varepsilon_{r,ref}$ = **2.1065** was inserted into the cell covering the IDS electrodes entirely. The resulting permittivity measurement for the three employed wavelengths across a wide frequency range from 0.1 to 10000 Hz is shown in Figure 4.24. The $\varepsilon_r$ value obtained using $\lambda$ = **4 mm** is slightly larger than the reference value $\varepsilon_{r,ref}$ whereas the $\lambda$ = **2 mm** and $\lambda$ = **1 mm** measurements show a smaller value $\varepsilon_r$ than the reference. The fact that the value approaches to $\varepsilon_r \rightarrow 1$ for low frequencies is due to the impedance analyzer. The capacitance of 1 pF below 10 Hz yields an impedance of 15 GOhm which

then is 50% larger than the guaranteed accuracy range (i.e. 10 GOhm) of the impedance analyzer.
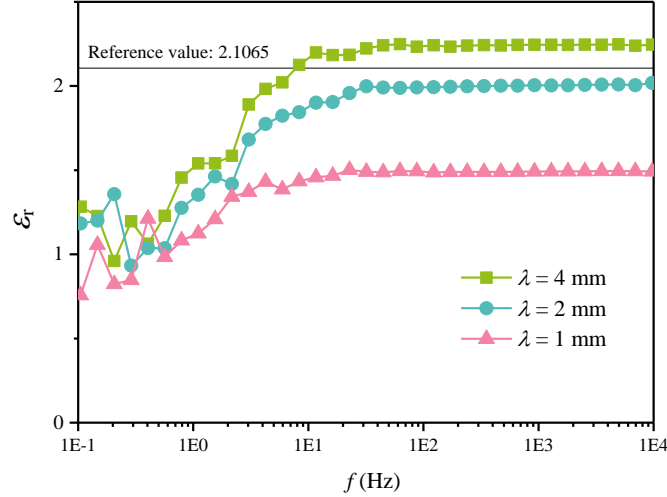


Figure 4.24. The permittivity $\varepsilon_r$ of an insulating liquid measured by the IDS for $\lambda = 4$ mm, $\lambda = 2$ mm and $\lambda = 1$ mm wavelength over the frequency $f$. The reference value of $\varepsilon_{r, ref} = 2.1065$ is shown also.

The findings show that a parasitic capacitance reduces the measured value of $\varepsilon_r$, it is puzzling how a larger permittivity than the reference value can arise. Mathematically, this would mean dealing with a negative parasitic capacitance. This implies that the IDS2.0 possesses dielectrics which have negative permittivities. This appears not to make sense but may be understood via extended FEM simulations.

These simulations are using actual structure values of the IDS2.0 which are given with the SEM image in Figure 4.21c. The permittivity values for the simulation were taken from Table 4.3. The structure for the FEM simulation is shown in Figure 4.25 showing four out of 20 simulated electrodes. Figure 4.26a to Figure 4.26i show how the capacitance, the sensitivity and the accuracy is affected by varying the permittivity of the insulating liquid (or more general the "MUT"), the insulator thickness and the soldermask thickness. In Figure 4.26a the IDS structure having $d_{ins} = 120$ μm and solder mask thickness $d_{SM} = 30$ μm was used.

Here, the $\varepsilon_r$ dependent capacitance $C(\varepsilon_r)$ is shown as being a non-linear function indicating parasitic capacitance behaviour. The capacitance is also affected by a change in the distance $d_{ins}$; $C(d_{ins})$ shown in Figure 4.26b. For small values of $d_{ins}$, the capacitance is low and approaches asymptotically to a maximum at about $d_{ins}$ = $\lambda$ using $\varepsilon_r$ = 2.1065 for the MUT. Figure 4.26c shows the capacitance $C(d_{SM})$ when the soldermask thickness $d_{SM}$ on top of the electrode is varied in its distance using $\varepsilon_r$ = 2.1065 for the MUT. A change on the soldermask has a similar effect on the capacitance as by varying the insulator thickness but is of a lower magnitude and approaches its maximum at about $d_{SM}$ = 0.25$\lambda$. Now, the sensitivity $S(\varepsilon_r)$ in Figure 4.26d deduced from Figure 4.26a, shows an unexpected pattern; the sensitivity moves up linearly, at a certain value of $\varepsilon_r$ the sensitivity maximises and falls down linearly afterwards. By varying the $d_{ins}$ thickness in Figure 4.26e, the sensitivity $S(d_{ins})$ deduced from Figure 4.26b increases smoothly to a maximum at about $d_{ins}$ = 0.1$\lambda$ whereas the sensitivity $S(d_{SM})$ in Figure 4.26f slightly increases but then tends to vanish for large values of $d_{SM}$. The plots 4.26g to 4.26i show the accuracy of the IDS sensor in measuring the exact MUT value of $\varepsilon_r$ = 2.1065 as percent deviation; $D = 100(\varepsilon_{r,\,IDS}\text{-}\varepsilon_r)/\varepsilon_r$. Figure 4.26g shows $D(\varepsilon_r)$ and illustrates a maximum deviation at a point where the sensitivity maximises. The variation in $d_{ins}$ shows a very unexpected pattern of $D$. The accuracy is for small values of $d_{ins}$ approximately zero but rises up to a maximum of about 10% and exhibits a zero crossing for about $d_{ins}$ = 0.01$\lambda$. A similar effect can be achieved by varying the $d_{SM}$ as shown in Figure 4.26i although more detrimental to $S$ and $D$.

The figures of the accuracy $D$ have shown that for certain values of $d_{ins}/\lambda$ the deviation to $\varepsilon_r$ indeed can gain a measured permittivity that is larger than the actual permittivity of the MUT despite parasitic capacitance present. A variation on $\lambda$ in $d_{ins}/\lambda$ shifts $D$ along the horizontal axis, thus for larger values of $\lambda$ this

shifts is towards smaller values of $d_{ins}/\lambda$ having a positive deviation and the measured $\varepsilon_{r, IDS}$ is larger than the actual $\varepsilon_r$. A similar effect is due to the soldermask thickness. Thus the higher measured $\varepsilon_{r, IDS}$ was due to an intrinsic property of the IDS. This demonstrates that IDS are very susceptible in changes of any of its spatial structure parameters. Intuitively, one would design a sensor that shows maximum sensitivity but here it could be determined that this is not always a good choice.
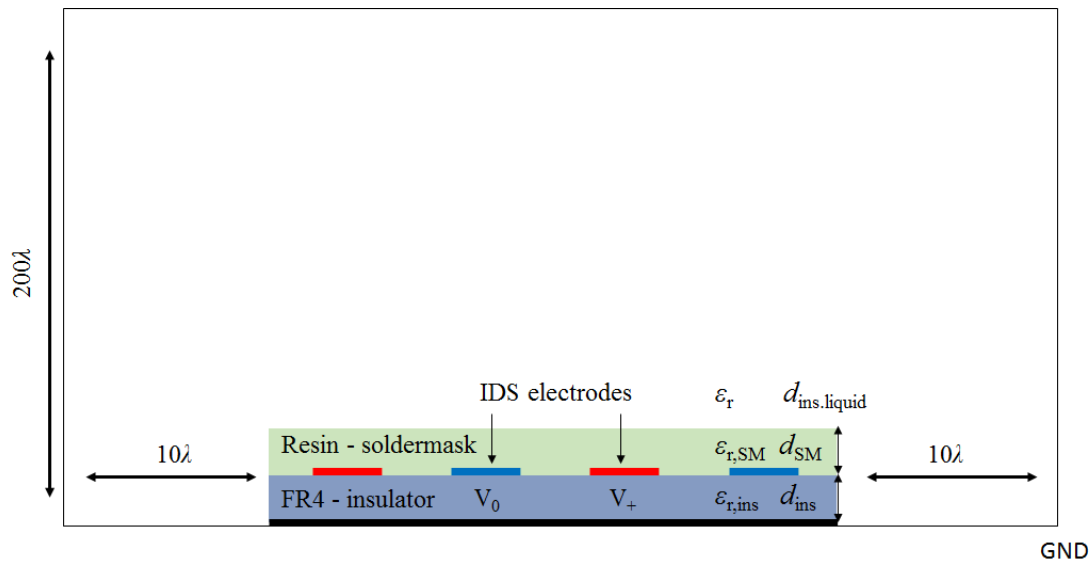


Figure 4.25. The schematics of the simulated structure in FEM showing four out of 20 electrodes, the participating dielectrics soldermask and insulator with their respective thickness $d_{SM}$ and $d_{ins}$.

A quantitative evaluation of the experiments and simulations is given in the Table 4.4. It shows the capacitance $C$ with air, with the insulating liquid and the resulting sensitivity $S$ and accuracy expressed as deviation $D$ from the reference value in percentage. The sensitivity is the largest for the $\lambda = 4$ **mm** and decreases for smaller $\lambda$. Consequently, this affects the deviation progressively. For the $\lambda = 4$ **mm** the deviation is positive and becomes increasingly negative for smaller values of $\lambda$. The FEM simulations confirm these measurements precisely.
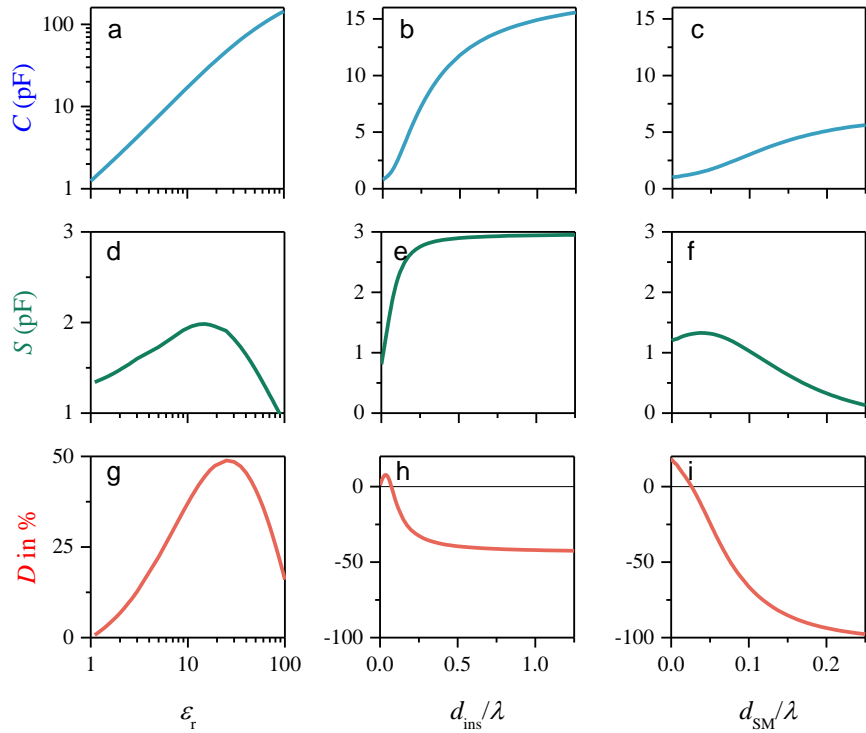
Figure 4.26. The figures of merit ($C$, $S$, $D$) of the IDS2.0 by varying (a, d, g) the permittivity $\varepsilon_r$ of the MUT, (b, e, h) the $d_{ins}/\lambda$ ratio and (c, f, i) the $d_{SM}/\lambda$ ratio as result of the FEM simulations.

Table 4.4. Comparison the measured $C$, $S$, and $D$ with the FEM simulations.

| Measurements | | | | | |
|---|---|---|---|---|---|
| **Wavelength** | **$C_{Air}$ (pF)** | **$C_{MUT}$ (pF)** | **$S$ (pF)** | **$\varepsilon_{r, IDS}$** | **$D$** |
| **4 mm** | $1.066 \pm 0.001$ | $2.414 \pm 0.002$ | $1.22 \pm 0.01$ | $2.264 \pm 0.001$ | 7.49% |
| **2 mm** | $1.016 \pm 0.001$ | $2.063 \pm 0.001$ | $0.95 \pm 0.01$ | $2.030 \pm 0.001$ | -3.65% |
| **1 mm** | $1.316 \pm 0.001$ | $1.956 \pm 0.002$ | $0.58 \pm 0.01$ | $1.486 \pm 0.001$ | -29.45% |
| **Simulations** | | | | | |
| **4 mm** | 1.0730 | 2.4301 | 1.24 | 2.265 | 7.51% |
| **2 mm** | 1.0089 | 2.0398 | 0.94 | 2.022 | -4.02 % |
| **1 mm** | 1.3185 | 1.9331 | 0.56 | 1.466 | -30.40 % |

## 4.2.4  Electric Shielding

A Faraday cage can reduce noise, electromagnetic interferences and thus improve precision. However, such a faraday cage will alter the electric field distribution above the IDS2.0 sensor affecting its sensing properties such as the capacitance. The IDS1.0 and 2.0 measurements were carried out within the test

cell housing in order to reduce potential noise. However, it is not exactly known to what extent the housing affects the IDS sensing properties.

For the calculations in the presence of the two grounded planes, GND ($\mathbf{V} = 0$), below and above the electrodes, the IDS has been simplified to its cross sectional view as depicted in Figure 4.27, showing one period of $\lambda$. An upper boundary such as a shield above the electrodes is located along the *y*-axis at $y = s$. The space between the active and neutral electrodes, labelled $V_+$ and $V_{0,}$ is set to $\mathbf{V} = 0$, which is an approximation of having zero distance to the lower ground plane. As it is usually done, all geometries have no thickness and are infinite in the *z*-direction [60].
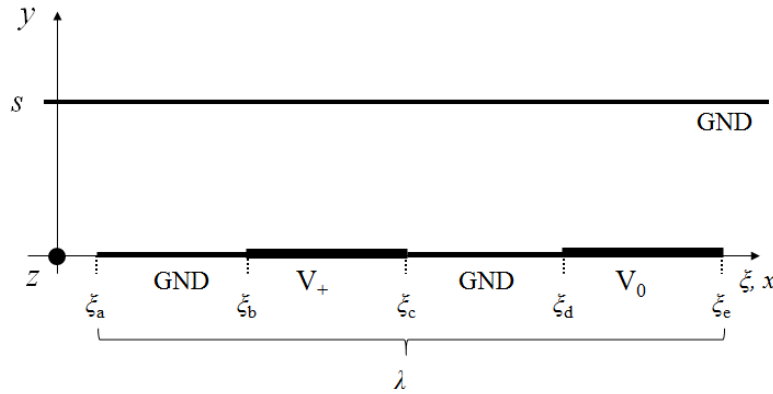


Figure 4.27. Cross section of IDS for the calculation with shield using Green's function. Shown is one period of $\lambda$.

A Green's function method was used to calculate the potential field and subsequently the total charge on the electrodes at $V_0$ to determine $C(s)$. The problem is treated as two-dimensional by treating the *z*-direction as infinite and solving for the capacitance per unit length. This technique works by applying the boundary conditions of the problem under consideration to find the relevant Green's function for the problem geometry. The solution to the potential is then found by an integral over the enclosing surface. General Green's function solutions of the Laplace equation in two dimensions are available for either infinite or finite

$x$ and $y$-boundaries (c.f. p. 710 in [76]). For instance, the electric field problem of an IDS with boundaries at infinity without a ground plane above and below the electrodes has been solved in a previous study [60]. The shield however introduces a new boundary problem where the $x$-direction remains infinite and $y$ is limited by the shield distance. A solution was found via transforming the known series solution for finite boundaries in $x$ and $y$ (c.f. p. 455 in[76]):

$$G\left(x,y|\xi,s\right)=\frac{2}{a}\sum_{n=1}^{\infty}\frac{\sinh[(\pi n/a)(s\text{-}y)]}{\sinh\left(\pi ns/a\right)}\sin\left(\frac{\pi nx}{a}\right)\sin\left(\frac{\pi n\xi}{a}\right) \tag{4.25}$$

with $\pm a$ as the position of the boundary on the $x$-axis and $y = 0$, $y = s$, the $y$-axis boundaries, to a result valid for $a \rightarrow \pm \infty$:

$$G\left(x,y|\xi,s\right) =\frac{1}{\pi}\int_{0}^{\infty}\frac{\sinh k\left(s\text{-}y\right)}{\sinh ks}\cos k(x\text{-}\xi)\mathrm{d}k \tag{4.26}$$

The potential $\Psi(x,y|s)$ of the IDS with $n$ periods of $\lambda$ is given by the integral of the product of the Green's function with the surface potential function $\psi(\xi)$ over the $\xi$-space along $x$ at $y = 0$:

$$\Psi\left(x,y|s\right) =\sum_{n}\int_{\xi_{\mathrm{b}}+n\lambda}^{\xi_{\mathrm{c}}+n\lambda} G\left(x,y|x,s\right)\psi(\xi)\mathrm{d}\xi \tag{4.27}$$

The potential function $\psi(\xi)$ is a step function with amplitude 1 V on the active electrodes and 0 V on the neutral electrodes which is equal to GND which is extended along the $x$-axis to the left and right of the calculated domain.

Employing Gauss's law, the surface charges along $x$ are given by the limit of the gradient of this potential function in $y$-direction [62]

$$\sigma(x) = \varepsilon_0 \lim_{y\to 0}\frac{\partial\Psi\left(x,y|s\right)}{\partial y} . \tag{4.28}$$

The capacitance $C$ is consequently the modulus from the integral of the charges over the neutral electrode, multiplied by the actual electrode length $l$ in the $z$-direction:

$$C(s) = l \sum_{n} \int_{\xi_d + n\lambda}^{\xi_e + n\lambda} |\sigma_x| \mathrm{d}x \qquad (4.29)$$

The experimental setup to determine $C(s)$ is shown in Figure 4.28a and 4.28b. The machined construction (Figure 4.28a) covers and holds the IDS in place while allowing the shield distance $s$ above to be varied. This position varied by a standard micro-meter stage (PT1 from Thorlabs) was read precisely via the installed digital micro-meter. The rigid aluminium construction was grounded throughout the experiment to provide boundaries with $\Psi(\xi) = 0$ V. The IDS was smaller than the grounded $xz$-plane matching the assumption made to have the ground plane extended to infinity. The measurement was carried out via a four wire capacitive measurement through our impedance analyzer Hioki IM3590. This four wire setup ensured precise and accurate measurements (Figure 4.28b). The grounded aluminium construction served at the same time as a Faraday cage, to ensure the measurement was less affected by external noise.
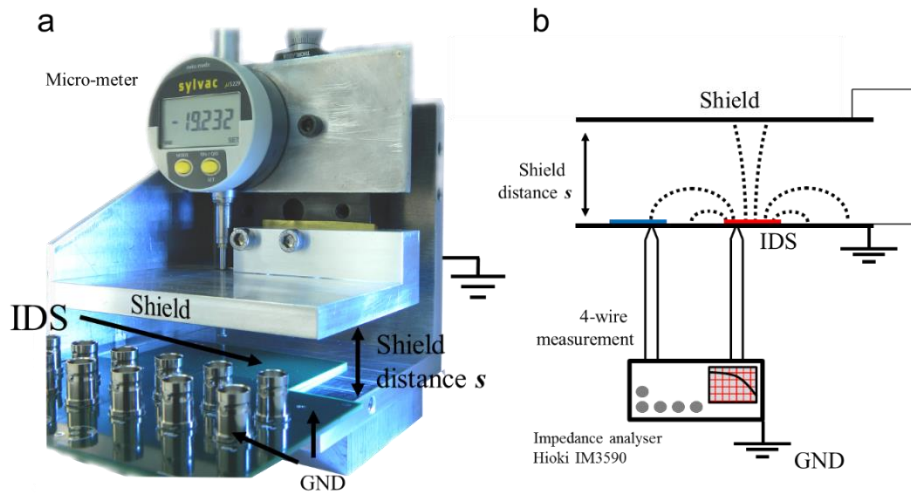


Figure 4.28. (a) Photo of the experimental setup. The photo was taken with an open side for visualization purposes. (b) Schematic of the experiment.

The $s$ dependence of the capacitance was calculated and verified by FEM. The calculations and FEM simulations are shown in Figure 4.29a and Figure 4.29b and plotted versus the distance $s$ and $s/\lambda$ respectively. The capacitance of an IDS scales with the geometry parameters: length $l$ in $z$-direction, $w/g$ ratio,

and *n*. The capacitance is independent of $\lambda$ in the idealized geometry; since the *w/g* ratio and the number of electrodes remained constant, only the varied length *l* changed the capacitance. Hence, the IDS, all with *n* = 10 electrode pairs, have a capacitance ratio of 1:2:4 due to the different lengths *l* in the *z*-direction. Figure 4.29b shows the capacitance versus *s/$\lambda$* and illustrates that, in theory, the capacitance is a function of *s/$\lambda$* and the magnitude is varying with *l*. For small *s/$\lambda$* values this figure also emphasizes a minimum *s/$\lambda$* distance for the shield before which the field lines cannot reach the neutral electrodes ($V_0$) and contribute to the capacitance. In this region, the charge on the active electrodes ($V_+$) is dominated by balanced charges on the upper shield.

The experimental result in Figure 4.29c and Figure 4.29d shows that the capacitance *C(s)* of each of the three sensors is much larger than the theoretical model predicts. As opposed to the prediction, the order of the capacitance magnitudes is reversed over most of the range. The measurements for wavelengths $\lambda$ = 2 mm and $\lambda$ = 1 mm clearly show evidence of parasitic capacitance through a measured offset. The precision of the shield's distance in this measurement was $\pm$ 1 µm. The uncertainty in the absolute distance is about $\pm$ 15 µm due to mechanical factors. The accuracy and precision of the impedance analyzer was about $\pm$ 0.005 pF.
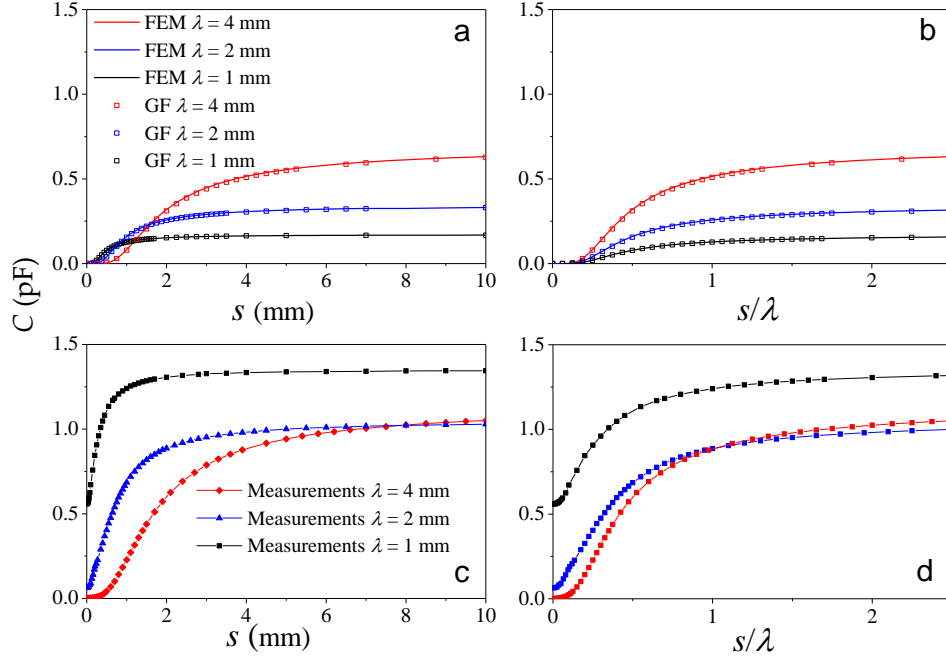
Figure 4.29. (a) Calculation of $C(s)$ and agreement with FEM. (b) Same data plotted vs. $s/\lambda$. (c) Experimental results for three different IDS wavelengths. (d) Same data plotted vs. $s/\lambda$. Clearly visible is the inverted order of $s/\lambda$ in the experiment due to an increased offset in the capacitance.

Table 4.5. Values for the capacitance with shield at $s_0$ in experiment and theory for all three studies wavelengths.

| Wavelength of IDS | Experimental shield distance $s_0$ | Experimental capacitance shielded | Experimental capacitance unshielded | Theoretical shield distance $s_0$ | Theoretical capacitance shielded | Theoretical capacitance unshielded |
|---|---|---|---|---|---|---|
| $\lambda = 4mm$ | 5.8 mm = 1.45$\lambda$ | 0.97 pF | 1.12 pF | 6.5 mm = **1.65$\lambda$** | 0.59 pF | 0.68 pF |
| $\lambda = 2mm$ | 2 mm = $\lambda$ | 0.90 pF | 1.04 pF | 3.25 mm = **1.65$\lambda$** | 0.29 pF | 0.34 pF |
| $\lambda = 1mm$ | 0.65 mm = 0.65 $\lambda$ | 1.16 pF | 1.35 pF | 1.62 mm = **1.65$\lambda$** | 0.15 pF | 0.17 pF |

It is useful to define a distance for the shield at which the capacitance is equal to $1 - e^2 = 86.5\%$ of the unshielded ($s = \infty$) capacitance value. That is, the distance $s_0$ of the shield fulfils the criterion,

$$C(s_0) / C(s = \infty) = 1 - e^2 . \qquad (4.30)$$

The quantified results of the distance $s_0$ and its effect on the capacitance are shown in Table 4.5. One immediate outcome is that the shield distance $s_0$ varies strongly with the parasitic capacitance. In the absence of parasitic capacitance, this would be $s_0 = 1.65\lambda$. From calculations of the idealized geometry it is found

that doubling this distance to $3.3\lambda$ gives 95% of the unshielded capacitance and half this distance $(0.83\lambda)$ reduces this capacitance to 63.2%.

### 4.2.4.1 The difference of the experiment and theory

In the modelling of the sensor, the maximum capacitance achieved was for the 4 mm wavelength sensor and reached 0.7 pF. The experiment shows a considerable difference with an observed maximum of 1.35 pF. As the Green's function result is consistent with the FEM solver, this difference can be explained as due to the simplifications made in the geometry for the calculation. Each sensor's wavelength determines the spatial distribution of the emanated electric field. The dimensions of the insulator layer between the ground plane and electrodes is constant among all $\lambda$, but at smaller $\lambda$ the ground plane is relatively further away and thus less effective at excluding flux from this region. Hence, the insulation layer $d_{ins}$ (FR4) was sensed and added to the total capacitance. For smaller wavelengths than $\lambda = 4$ mm this impact is measurable as a significant offset. In turn, the larger $\lambda$, the less the insulator thickness influences the sensing properties. These observations agree with the literature [21]. As a result, a higher ratio of $\lambda/d_{ins}$ moves the experiment closer to the theoretical geometry. A more realistic modelling in FEM could accurately reproduce the measurement by incorporating the manufactured IDS spatial structure, Figure 4.30.

This simulation of the IDS with $\lambda = 4$ mm could then be used to explore the nature of the parasitic capacitance and magnitude of capacitance compared to theory. Figure 4.31 shows the FEM simulation of the electric field of the IDS cross section. The solder mask is an additional dielectric between the air/MUT and the electrode which contributes to the capacitance. More significantly, the highest field strength adjacent to the electrode occurs in the gap between the active and neutral electrodes. This is the region covered by the solder mask and provides a surface for charges which was approximated to have zero thickness in

the calculations. Also, some field lines from the active electrode are directed below the neutral electrode which agrees with the qualitative findings in the literature [59]. Thus, a large amount of the capacitance occurs within the insulator material surrounding the electrodes instead of within the air above the sensor.

For $\lambda = 4\,\mathrm{mm}$ and a potential of 1 V between the electrodes, the mean electric field strength across the sensor's upper surface could be plotted as a function of distance as shown in Figure 4.32. It shows the unshielded electric field and the shield position at $s_0$, $s_0/2$ and $s_0/4$. The initial electric field strength is about 1100 V/m if the gap between electrodes is $g = 1\,\mathrm{mm}$. Clearly, the electric field decays smoothly with distance and with increasing shield position it approximates the unshielded field distribution.
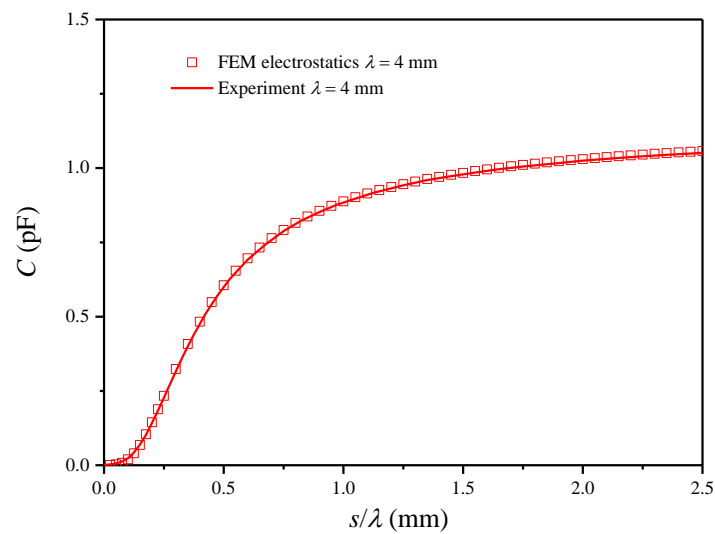


Figure 4.30 Simulated experiment based on the dimensions from the IDS cross sectional record via SEM and their permittivities. Incorporating these in FEM can accurately describe the practical environment.
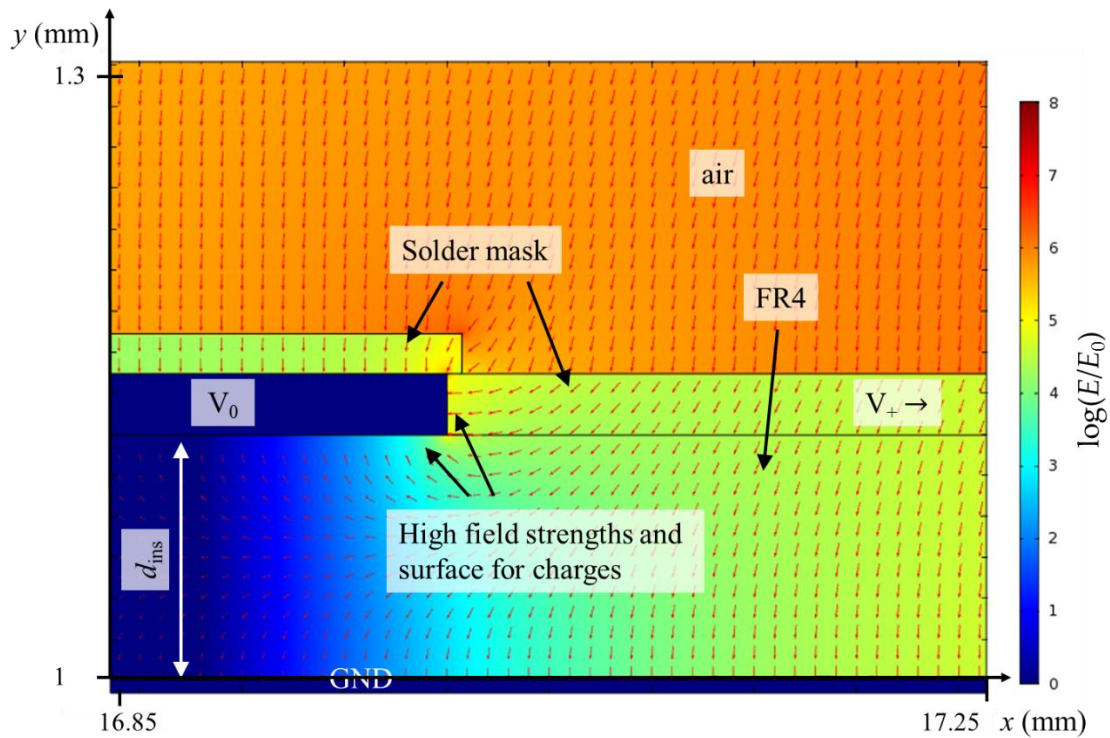
Figure 4.31. Simulated electric field around the neutral electrode $V_0$. The finite thickness of the electrode produces an additional surface directly opposite the active electrode causing charge accumulation. Electric field lines from above the electrodes flow furthermore into the insulator (FR4) above the ground plane and terminate at the underside of the electrode $V_0$. These effects result in increased and parasitic capacitance. The scale is given in $\log(E/E_0)$ where $E_0$ is 1 V/m.
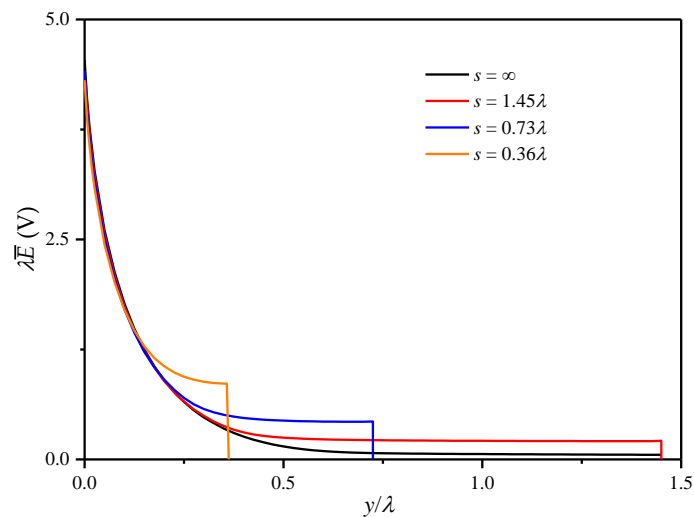


Figure 4.32. Average electric field strength across the IDS with $\lambda = 4$ mm, with a shield distance at $1.45\lambda = 5.8$ mm, $0.73\lambda = 2.9$ mm, $0.36\lambda = 1.45$ mm and at infinity

131

## 4.2.4.2 Validation of the noise reduction

In order to experimentally measure the effects of noise and shielding, a test using the largest wavelength sensor ($\lambda = 4$ mm) with a shield applied at $s_0 = 1.5\lambda$ = 6 mm was conducted. A grounded and electrically conducting box shielded the IDS from external noise sources. This IDS was placed in a glass container, held mechanically 5 cm away from the glass and a standard power cord was arranged above the sensor's surface as an electric noise source, as shown in Figure 4.30. The IDS was located 400 mm from the center of the 800 mm long power cord. The resulting electric field strength from this noise source onto the sensor is estimated to be ~ 500 V/m = 2 $\lambda$V/m which is in the same order of magnitude, shown in Figure 4.33. The insulating liquid was measured using the *standard* settings (section 3.1). The test sequence comprised measurements without applied voltage into the cable and without IDS shield. Subsequently, the power cord was subject to 230 V and the IDS capacitance was measured once in air and once in the insulating liquid. Finally, the shield was applied and the test repeated. The results of the 801 recorded data points, collected at 0.5 s intervals, are shown in Figure 4.34. When unshielded, the measurement exhibited a constant value. The noise is clearly increased when the power cord is subject to power which could be suppressed when the shield was applied.
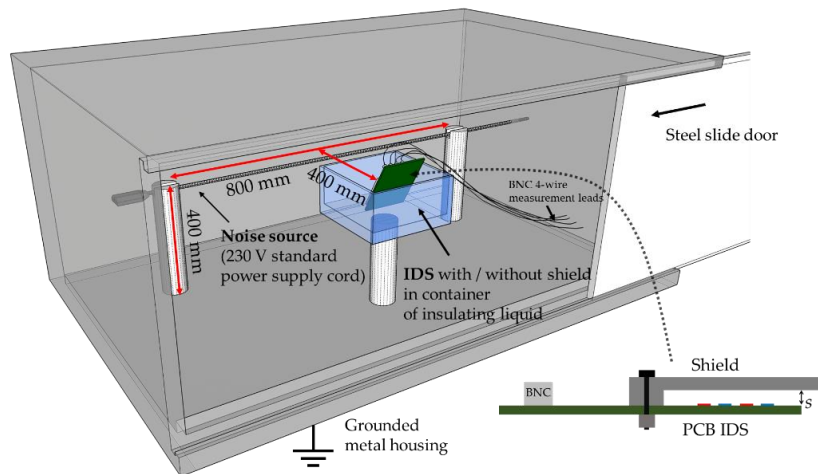


Figure 4.33. Experimental arrangement of the setup to test the function of the shield onto the IDS at distance $s_0 = 1.5\lambda$. Relevant dimensions are shown.
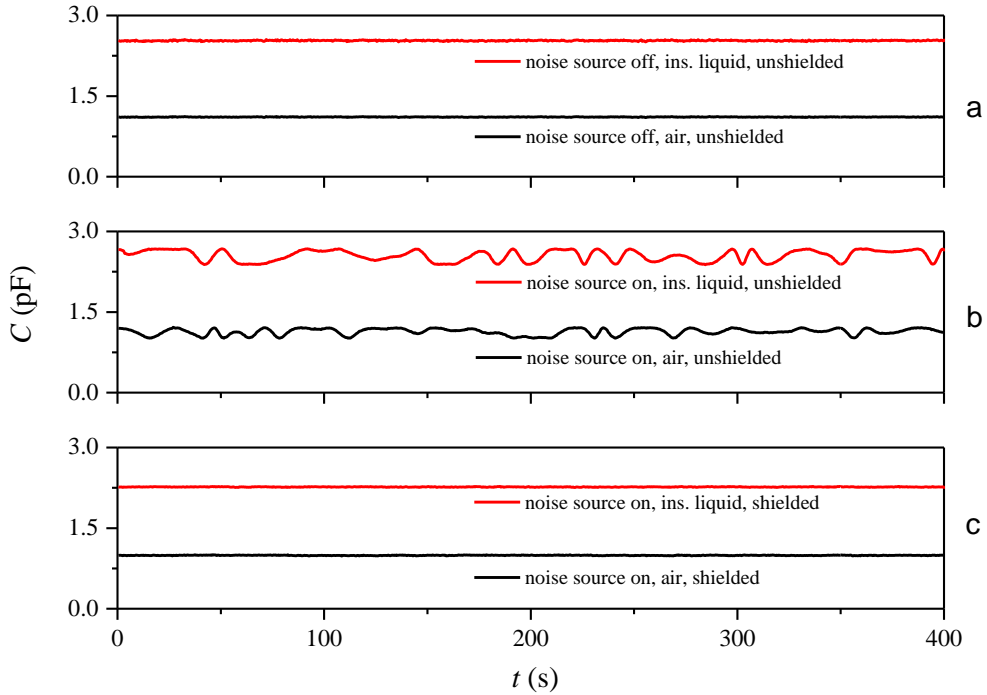
Figure 4.34. The validation of shield function for $\lambda = 4$mm. (a) In the absence of an applied potential on the power supply cord, no instabilities are exhibited. (b) After applying voltage onto the cord, fluctuations are observed. (c) Measurement of capacitance with a Faraday shield in place.

The distribution of measured values have been plotted in Figure 4.35. The capacitance values for the IDS with media air (Figure 4.35a) and insulating liquid (Figure 4.35b), without noise source and unshielded, exhibited a Gaussian distribution. The mean values were $\bar{C}_{air} = 1.11$ pF and $\bar{C}_{ins\ liquid} = 2.53$ pF, with small fluctuations resulting in $\sigma_{air}$ and $\sigma_{oil} \leq 0.35\%$. This behaviour changed when the noise source was turned on. With the noise source, $\bar{C}_{air}$ and $\bar{C}_{ins.\ liquid}$ increases by 0.02 pF (Figure 4.35c and Figure 4.35d) while $\sigma$ increases by a factor of 12-18 relative to the measurement without noise source. The distribution becomes flat and non-Gaussian. The spread of measurement values is due to the inherent frequency fluctuations of the IDS sensing frequency (50.000 ±0.001 Hz) and the fluctuations of the grid (noise source) frequency (50.00 ±0.01 Hz) causing an aperiodic interference pattern as can be seen in Figure 4.35b. With the 3D shield (Figure 4.35e, Figure 4.35f), the lower $\sigma$ values and the observed Gaussian distribution in Figure 4.35 and Figure 4.35b could be recovered. The mean values

133

$\overline{C}_{\text{air}}$ and $\overline{C}_{\text{ins. liquid}}$ have changed due to the impact of the shield on the IDS capacitance. This change of -11.5% is equal for the air and insulating liquid as media. In summary, this histogram analysis shows that the shield reduces the external noise effectively. In order to analyze how the measured permittivity is affected by noise and shield, Table 4.6 shows the calculated values for the permittivity $\varepsilon_r$ using the mean values from Figure 4.35. Mere averaging over 801 data points seems to be an incomplete method to recover the $\varepsilon_r$ value obtained without the noise source. With the noise source, the difference in capacitance remained 0.02 pF affecting the sensed $\varepsilon_r$ value. Due to error propagation, the standard deviation for $\varepsilon_r$ is higher than for the capacitance. Determining $\varepsilon_r$ of the insulating liquid with high certainty is therefore difficult; the standard deviation, $\sigma$, without the shield was as high as 9.5% whereas the shielded standard deviation of 0.6% is similar to the measurement without the noise source.
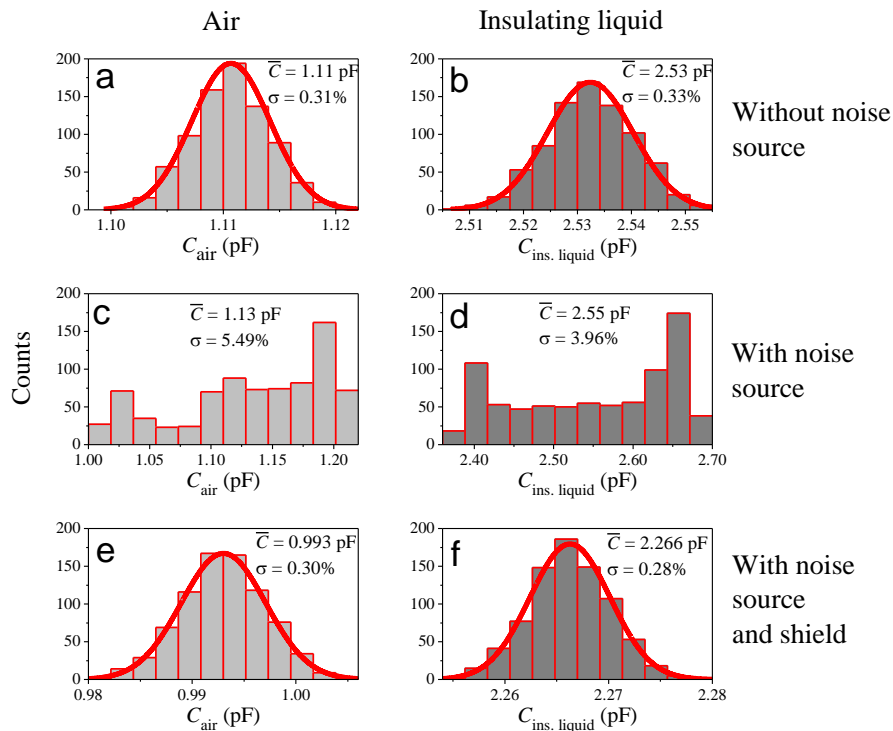


Figure 4.35. The capacitance values plotted as histograms. Capacitance values without the noise source for media of (a) air and (b) insulating liquid. Capacitance with the noise source for media (c) air and (d) insulating liquid. Capacitance with shield and noise source for media (e) air and (f) insulating liquid.

Table 4.6. Influence of noise source and shield on permittivity for $\lambda = 4$ mm

| Measurement | Mean value | Standard deviation σ |
|---|---|---|
| $\varepsilon_r$ **unshielded without noise source** | $\varepsilon_r = 2.28$ | 0.64% |
| $\varepsilon_r$ **unshielded with noise source** | $\varepsilon_r = 2.25$ | **9.45%** |
| $\varepsilon_r$ **shielded with noise source** | $\varepsilon_r = 2.28$ | 0.58% |

The measured $\varepsilon_r$ of insulating liquid with the used $\lambda = 4$ mm IDS ($\varepsilon_r = 2.28$) approximately agrees with literature values [1, 2, 28]. This would not have been the case for $\lambda = 1$ mm and $\lambda = 2$ mm due to the measured offset.

### 4.2.5 Conclusion of IDS2.0

The electric field calculation using Green's function indicated that the electric field distribution above the sensor is insignificantly affected by employing a grounded plane underneath. Thus the IDS2.0 was designed having a grounded plane below the electrodes in order to improve its figures of merit.

The dependence of the IDS capacitance with a grounded shield at a distance above the sensor was predicted also utilizing the Green's function method for finite and infinite boundaries. The manufactured interdigitated dielectrometry sensor differed geometrically from the simplified model, which resulted in a difference between the Green's function model and experimental results. Therefore, FEM was used to model a more realistic situation. FEM matched the obtained experimental solution. The evaluation of the experimental and theoretical data indicates a diminishing parasitic capacitance for larger values of $\lambda$ when dealing with a constant thickness of the insulator, $d_{ins}$.

A parameter $s_0$ was defined as the distance for the shield which retained 86.5% of the capacitance. This ranged in the experiment from $0.65\lambda$ to $1.45\lambda$. The theoretical value for the simplified model, $1.65\lambda$, was only dependent on the sensor's wavelength.

For a demonstration, a shield was manufactured and applied to measure the permittivity of an insulating fluid. A considerable reduction in noise is shown via an experiment with a power cord as noise source. Measuring the permittivity at 50 Hz with the unshielded IDS exhibited a measured standard deviation $\sigma = 9.5\%$ whereas with shield $\sigma = 0.6\%$.

## 4.3  IDS2.5

It was shown in the preceding chapters that an accurate measurement of the relative permittivity, $\varepsilon_r$, of liquids using interdigitated sensors is challenging due to the parasitic capacitance. This was shown to be caused by the IDS spatial structure that uses dielectrics. In particular the observed "negative" parasitic capacitance is a challenging aspect to understand. The expected increase of $\varepsilon_r$ during the insulating liquid's lifetime is generally about $+5\%$ to $+10\%$ [6, 30, 45-47], which can easily be swamped by a parasitic capacitance present in the system. The investigated PCB IDS2.5 structure is similar to the IDS2.0; it consists of a substrate, a ground plane, an insulating layer below the electrodes and a soldermask above the electrodes having a periodicity of $\lambda$. This structure was simulated to determine the influence on the expected values of capacitance $C$, sensitivity $S$ and deviation $D$ (accuracy) for expected values of $\varepsilon_r$ for industrial oils, listed in Table 4.7. It is shown that for particular structure ratios and values of $\varepsilon_r$, the parasitic capacitance can be exploited in order to provide an accurate measurement of $\varepsilon_r$. This was verified during experiments with an optimized IDS2.5 structure on both unused and used insulating liquids. These measurements showed a low deviation from the expected value, yielding a $D < 0.5\%$.

Table 4.7. Typical values of the relative static permittivities for selected insulating liquids at room temperature.

| Oil Type | $\varepsilon_r$ | Reference |
|---|---|---|
| **Paraffinic oil** | 2.1~2.3 | [1, 3, 17, 29, 45-47] |
| **Vegetable oil** | 2.9~3.8 | [29, 49] |
| **Ester oil** | 3.2~5 | [53] |
| **Mineral oil** | 2.5~3 | [30] |

This chapter is based on a publication in the IEEE *Sensors* journal with the authors Alex Risos, Nicholas Long, Arvid Hunze and Gideon Gouws [23]. Therefore, this chapter is widely in consistency with this publication.

## 4.3.1 FEM simulations

The measured value of $C_{oil}$ can be a result of contributions from the dielectric liquid, the sensor structure as well as the sensor environment. The value of permittivity which is calculated will thus be influenced by parasitic capacitances $C_{parasitic}$, and $C'_{parasitic}$ so that

$$\varepsilon_r = \left( C_{MUT} + C_{parasitic} \right) / \left( C_{air} + C'_{parasitic} \right), \tag{4.31}$$

where the definition of the MUT or air capacitance is $C_{MUT/air} = (1/V)\, \varepsilon_0 \int_{s1} E\, dA$ with s1 is the upper surface of the $V_0$ electrode and $C_{parasitic} = (1/V)\, \varepsilon_0 \int_{s2} E\, dA$ where s2 is the lower surface of the $V_0$ electrode [62]. $C'_{parasitic}$ has the same definition but may not necessarily be numerically equal to $C_{parasitic}$. The electrostatic potential between the electrodes was $V = 1$ in the simulations, $E$ is the electric field and $\varepsilon_0$ is the permittivity of free space. A cross sectional view of the simulated IDS structure is shown in Figure 4.36a. This model is transferred to the FEM simulation using the simulated geometry depicted in Figure 4.36b having sharp electrode boundaries. The electric field lines (dotted lines) represent schematically the sensing mechanism; these electric field lines penetrate the MUT as well as IDS dielectric layers - sensing both.
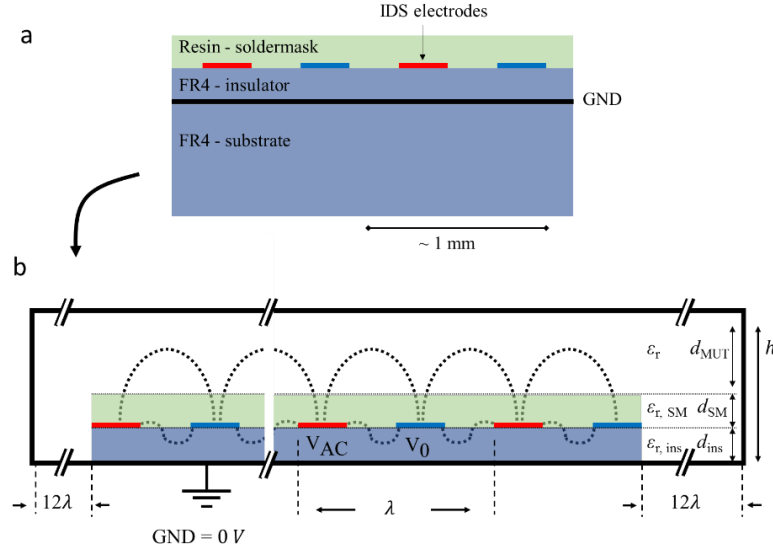
Figure 4.36. (a) A cross section view showing the general structure of the IDS. (b) FEM simulation geometry of the IDS and boundary conditions. Depicted are the relative permittivities and distances for each layer with the IDS surrounded at a distance by a grounded boundary. Electric field lines (dotted) which contribute to the sensing are shown schematically.

The IDS structure employs a common ground plane beneath the electrodes. The electrodes $V_+$ and $V_0$ with a periodicity of $\lambda$ and thickness of 30 μm were separated from this ground layer by an insulator layer with distance $d_{ins}$. A soldermask (an epoxy resin) is a standard protection coating for PCBs. In order to investigate its effects of the IDS figures of merits it was considered with thickness $d_{SM}$ in the simulations.

Simulations were performed for a structure of 20 electrodes ($10\lambda$). The first figure of merit considered in the simulation is the capacitance $C$, which is important for maximizing the signal to noise ratio (S/N). From this capacitance, the sensitivity is defined as: $S = \Delta C_{IDS}/\Delta \varepsilon_{r,\,IDS}$, the deviation $D$ from a reference value (accuracy) is determined by the ratio of the IDS permittivity, $\varepsilon_{r,\,IDS}$, over the reference value $\varepsilon_{r,\,ref}$: $D = (\varepsilon_{r,ref} - \varepsilon_{r,\,IDS})/\varepsilon_{r,ref}$, with the measured permittivity by the IDS given by: $\varepsilon_{r,\,IDS} = C_{MUT,\,IDS}/C_{air,\,IDS}$ and the reference value, measured as: $\varepsilon_{r,\,ref} = C_{MUT,ref}/C_{air,ref}$.

The geometry in Figure 4.36 depicts the Dirichlet FEM boundary held at zero potential (= GND). This surrounds the IDS structure with spacing to the

grounded structure of $12.5\lambda$. This mimics a grounded plane to the left and to the right at infinity. Therefore a comparison of the defined permittivity as entered in the simulation as material under test above the IDS electrode structure $\varepsilon_r$ was possible. The electrodes were set to a potential of $V_+ = 1$ V and $V_0 = 0$ V. The insulating liquid was located above the IDS geometry. The thickness of the soldermask was modeled for values of $d_{SM}/\lambda = 0$ to 0.1 and the insulator distance was varied from $d_{ins}/\lambda = 0$ to 0.2. The MUT layer, $d_{MUT} = h - (d_{SM} + d_{ins}) \cong 25\lambda$, was effectively infinite relative to the soldermask and insulator distances. While the relative permittivity of the soldermask $\varepsilon_{r, SM}$ and insulator $\varepsilon_{r,ins}$ was held constant at 4.5, the permittivity of the MUT, $\varepsilon_r$, was varied from 2 to 5. Figure 4.37 shows the results of our simulations presented as contour plots.

The first set of simulations, Figure 4.37a to Figure 4.37c, show the impact that changes in $\varepsilon_r$ and $d_{ins}/\lambda$ have on $C$, $S$ and $D$. The value of $d_{SM}/\lambda$ was held constant at 0.007 and the values of $C$, $S$ and $D$ were calculated as shown in Figure 4.37a. The results show an increase in the capacitance $C$ as both $\varepsilon_r$ and $d_{ins}/\lambda$ increase. The sensitivity $S$ is predominantly affected by an increase in $d_{ins}/\lambda$, and is less sensitive to $\varepsilon_r$, as is seen in Figure 4.37b. The accuracy $D$, shown in Figure 4.37c, is also primarily affected by $d_{ins}/\lambda$. At low values of $d_{ins}/\lambda$, $D$ is rising for $d_{ins}/\lambda \cong 0.03$ up to $\approx 15\%$, then follows a linear decrease to -30 % at $d_{ins}/\lambda \cong 0.2$. This results in a zero crossing at $d_{ins}/\lambda \cong 0.075$ resulting in high accuracy at this ratio.

The second set of simulations, shown in Figure 4.37d to Figure 4.37f, illustrates the change of $C$, $S$ and $D$ when $\varepsilon_r$ and $d_{SM}/\lambda$ are varied. Here the value of $d_{ins}/\lambda$ was held constant at 0.03. In Figure 4.37d it can be seen that the capacitance $C$ is predominantly affected by a change in $\varepsilon_r$ and less by $d_{SM}/\lambda$, contrary to the previous observation varying $d_{ins}/\lambda$. The sensitivity $S$ in Figure 4.37e varies with $\varepsilon_r$ and $d_{SM}/\lambda$. This occurs in a way that low values for $d_{SM}/\lambda$

increase the sensitivity with increasing $\varepsilon_r$, whereas this pattern is the opposite at high values of $d_{SM}/\lambda$. The sensitivity decreases as the parasitic capacitance through this soldermask gradually increases. This does not appear to affect the accuracy $D$ as shown in Figure 4.37f very much; it exhibits a similar behaviour as observed in Figure 4.37c, exhibiting a steady decrease with increasing $d_{SM}/\lambda$. More specifically, $D$ decreases throughout $d_{SM}/\lambda$ from approximately +10% down to -30%. This in turn also exhibits a zero crossing for the deviation at around $d_{SM}/\lambda = 0.025$.

The third set of figures, Figure 4.37g to Figure 4.37i, shows the impact of varying $d_{SM}/\lambda$ and $d_{ins}/\lambda$ on $C$, $S$ and $D$ when $\varepsilon_r = 3.5$ is held constant. Figure 4.37g plots an increase in capacitance $C$ with increasing $d_{ins}/\lambda$ while $d_{SM}/\lambda$ has a less significant effect on $C$. However, Figure 4.37h demonstrates an opposite behaviour as can be seen via the contour lines. The sensitivity $S$ generally increases with $d_{ins}/\lambda$ but at high $d_{SM}/\lambda$ this is a weak effect. The accuracy $D$ was affected by both, $d_{SM}/\lambda$ and $d_{ins}/\lambda$, Figure 4.37i. In general, high values of $d_{SM}/\lambda$ and $d_{ins}/\lambda$ produce a large $D$ of more than -25% in the negative space. However, small values of $d_{SM}/\lambda$ increase $D$ with increasing $d_{ins}/\lambda$ similar to Figure 4.37c. It is possible to find a zero deviation for a certain combination of $d_{SM}$ and $d_{ins}$, as well as when $d_{SM}$ and $d_{ins}$ is equal to zero which would represent an IDS having no substrate dielectrics – as this is commonly assumed in approximations [61].

The simulations show that the spatial structure strongly affects the figures of merit of an IDS. The soldermask decreases the sensitivity throughout as it provides a direct parasitic capacitance in between the sensed insulating liquid and electrodes. Increasing the insulator distance in turn increases $C$ and $S$, as a larger separation of the electrodes to the ground plane results in fewer field lines being pulled downwards to the ground. The insulator thickness can control the accuracy while maintaining a high sensitivity.

In order to facilitate a measurement of $\varepsilon_r$ with high accuracy, one aim of the work was to find the design for an IDS with the best possible accuracy, ideally $D = 0$.
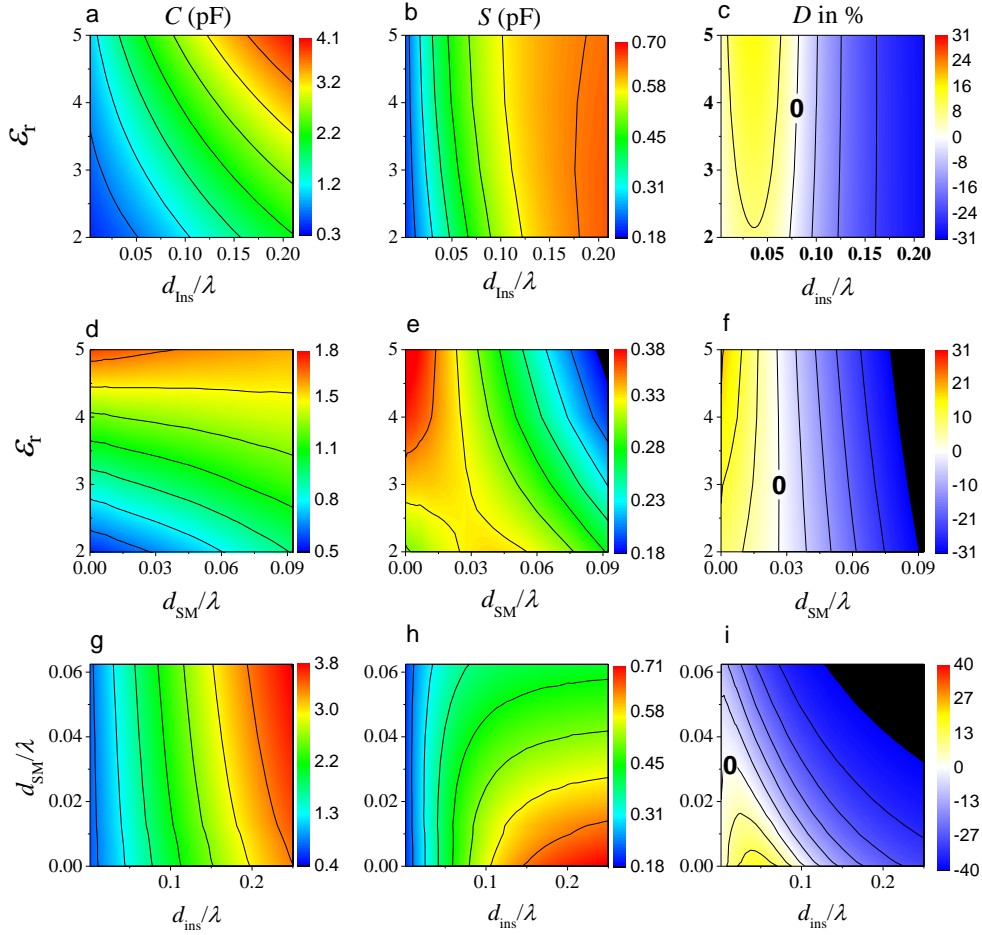


Figure 4.37. FEM Simulations for the capacitance $C$, sensitivity $S$ and accuracy $D$ of the IDS. The first row (a, b, c) shows the figures of merit while varying $\varepsilon_r$ and $d_{ins}$. The second row (d, e, f) shows the figures of merit when altering $\varepsilon_r$ and $d_{SM}$. The third row (g, h, i) shows the figures of merit dependent on $d_{SM}$ and $d_{ins}$ having $\varepsilon_r = 3.5$.

For an experimental verification of these simulations, the practical design for a possible IDS was informed with the aid of the data shown in Figure 4.37i. It can be seen clearly that a particular ratio of $d_{ins}/\lambda$ is needed in order to achieve a high accuracy. With aid of this knowledge, a suitable IDS measuring accurately a specific value of $\varepsilon_r$ in practice can be created. An unused insulating liquid (see section 3.2) having $\varepsilon_{r,ref} = 2.1065$ at 21 °C was used to simulate this specific case,

Figure 4.38. This Figure 4.38 shows a similar pattern as Figure 4.37i. With aid of the FEM simulations, it could be identified that the presence of a soldermask, $d_{SM}$, is detrimental to the sensitivity. Therefore, $d_{SM}$ was removed in the manufactured IDS2.5. The insulator layer thickness is fixed by the manufacturer at $d_{ins} \cong 120\ \mu m$. From Figure 4.35, a $D = 0\%$ can be created for $d_{ins}/\lambda \cong 0.096$ when making an IDS having an electrode periodicity of $\lambda = 1.247\ mm$.
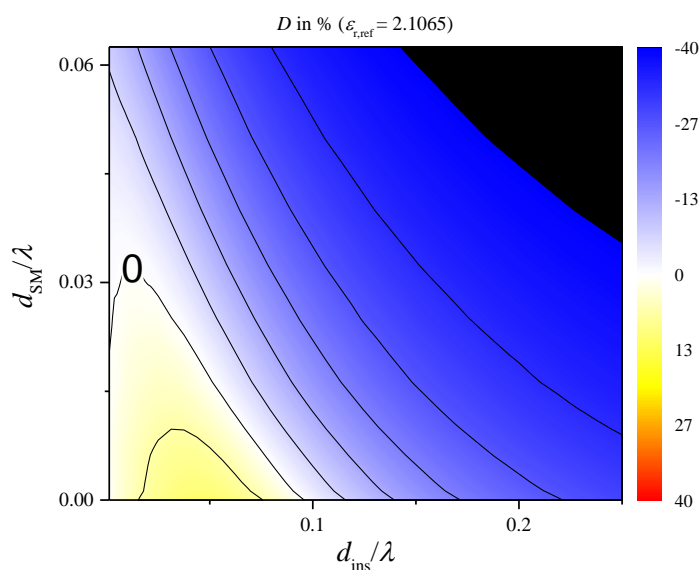


Figure 4.38. Simulation results for the deviation $D$ dependent on $d_{SM}$ and $d_{ins}$ as a specific case for the MUT having $\varepsilon_r = 2.1065$. The zero '0' deviation line $D$ is numerically highlighted.

This simulated $D = 0\%$ is achieved by a sensing mechanism which is dependent on the dimensions and dielectric properties of the IDS and $\varepsilon_r$. The electric field distribution changes for different values of $\varepsilon_r$, as shown in Figure 4.39. This affects the sensed capacitance and thus $\varepsilon_r$ in a convoluted manner. The $\varepsilon_r$ can be measured accurately when no parasitic capacitance is present or when a particular set of $C_{parasitic}$, $C'_{parasitic}$, $C_{MUT}$ and $C_{air}$ compensates a present parasitic capacitance. The latter is case of the IDS; choosing $\lambda = 1.247$ for $\varepsilon_r = 2.1065$ has such an effect on $\varepsilon_{r,\ IDS}$.
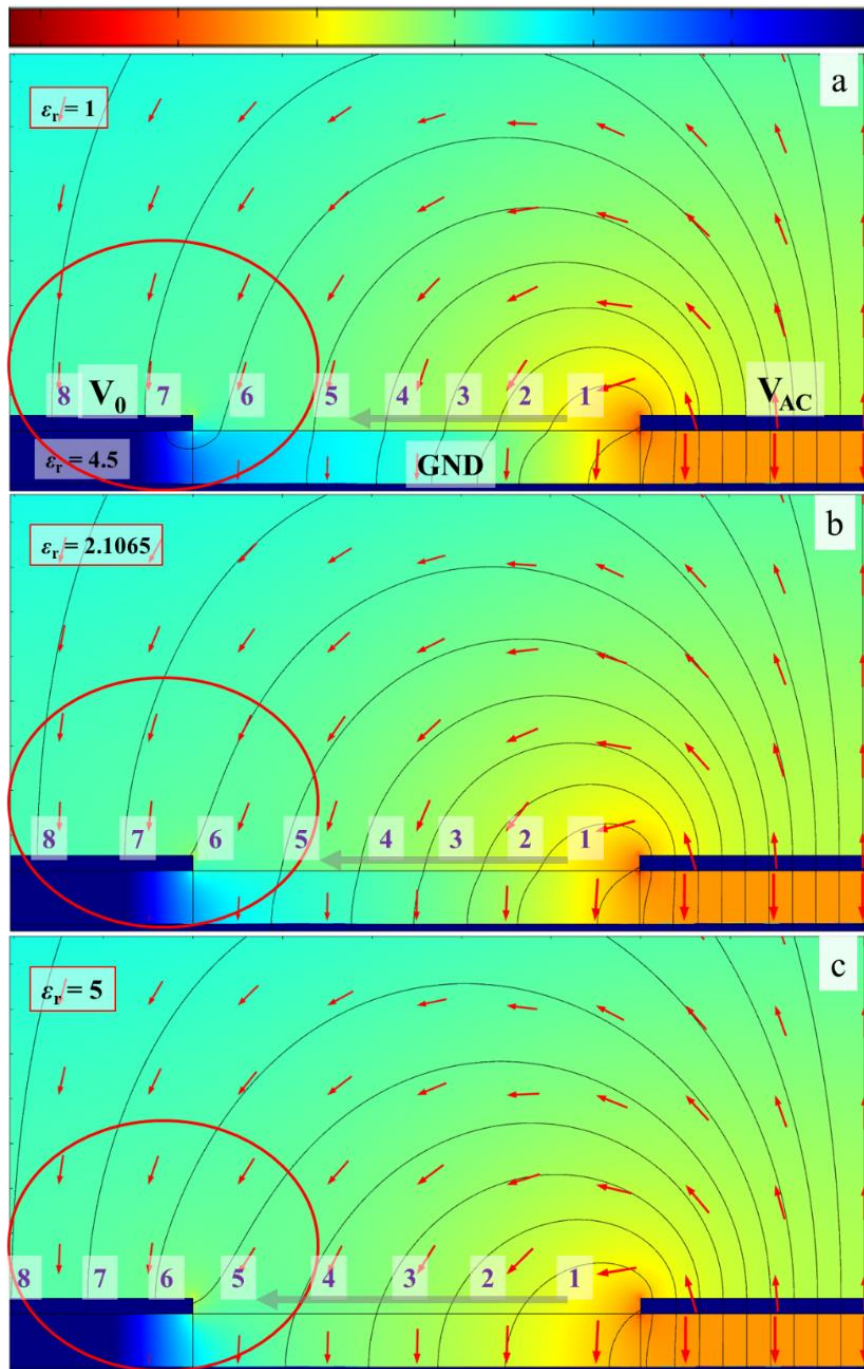
Figure 4.39. Electric field lines (1 to 8) depicted for one pair of the simulated electrodes in $\mathrm{Log}(E/E_0)$ where $E_0$ is 1 V/m. The field lines curl above the electrodes and reconnect to the opposite electrode dependent on the permittivity under test (red circle). A grey arrow supports the visual field line tracking representatively between 1 and 5. (a) Two field lines connected to the upper side of $V_0$ while one reconnects to the underside. (b) Three field lies connect to the upper side when measuring a MUT. (c) For higher $\varepsilon_\mathrm{r}$, the increasing relative field intensity above the sense electrodes is responsible for a non-constant parasitic capacitance.

The physics in this case is predominantly based on two effects, illustrated with Figure 4.39. For the capacitance with $\varepsilon_r = 1$ (Figure 4.39a), the field lines emanated from $V_+$ are strongly pulled downwards to the ground plane (GND) due to the vicinity of the FR4 dielectric ($\varepsilon_{r,\,FR4} = 4.5 > \varepsilon_{r,\,air}$). This is causing a lowered air capacitance, $C_{air}$, and a strong parasitic capacitance, $C'_{parasitic}$, through field lines connecting to the underside of $V_0$ (see circle in Figure 4.39a). When measuring the insulating liquid ($\varepsilon_r > 1$) the field distribution changes as illustrated in Figure 4.39b. This is yielding an increased E-field density through the insulating liquid than air. This produces an increased capacitance, $C_{oil}$, through $\varepsilon_r$ and weak parasitic capacitance, $C_{parasitic}$. This parasitic capacitance vanishes for $\varepsilon_r = \varepsilon_{r,\,FR4}$ and becomes negative for $\varepsilon_r > \varepsilon_{r,\,FR4}$ as more field lines progressively connect to $V_0$ than to GND, Figure 4.39c, causing a capacitance over-proportional to $\varepsilon_r$. This special interaction is dependent on the insulator thickness $d_{ins}$ allowing an optimal value of $\lambda$ in the sensor design.

## 4.3.2 Characterisation of the manufactured IDS2.5

With the aid of these findings, a PCB IDS based on $\lambda = 1.247$ for a target deviation $D = 0\%$ was designed and fabricated without soldermask as it was found that this is detrimental to the sensing properties. A gold finish onto the electrodes provided sufficient electrochemical inertness in the insulating liquid environment. Measurements on this IDS were done using guarded four wire BNC connectors to the impedance analyzer. Figure 4.40 shows the manufactured IDS. The four BNC connectors provided shielded measurement leads. These four leads merge onto the PCB board surface in a shielded manner at the electrodes. The SEM image in Figure 4.41 shows a cross sectional view of the electrodes and indicates the actual dimensions. The ground layer is indicated with GND. This confirms the designed parameter of $w = g = 312\,\mu m$ for $d_{ins} = 120\,\mu m$. The SEM image is accurate within

±1 μm. These dimensions were consistent within ±1 μm for three examined IDS cross sections.

In order to verify the functionality of the IDS in $\varepsilon_r$ of the unused and used insulating liquid accurately, the insulating liquid used for the oxidation experiment (section 3.2) was used. Two vials, one containing the unused insulating liquid and the other the used insulating liquid, were prepared. In Figure 4.42, the air, unused insulating liquid and used insulating liquid was measured with our optimized IDS. The procedure was as follows: after measuring the air capacitance $C_{air}$ with the IDS, the IDS was placed in a vial containing the unused liquid for about 20 seconds. The IDS was removed and exposed to air for 10 seconds. Subsequently, the IDS was inserted into the vial containing used insulating liquid for about 20 seconds. This process was repeated without cleaning of the IDS between these steps. This sensor exhibited an instantaneous response without lag or hysteresis effect to the air and different insulating liquids. This shows that this IDS is capable of reflecting changes in the insulating liquid instantaneously. This is possible when the capacitance is directly and linear proportional to $\varepsilon_r$. In this experiment, the capacitance of the IDS followed $\varepsilon_r$ accurately within the measurement uncertainty of 0.5%.

For a comparison of the measured vs. simulated figures of merit $C$, $S$ and $D$, the capacitance was measured. Both results of $C$ and $S$ are shown in Figure 4.43. The capacitance $C$ (Figure 4.43a) and the sensitivity $S$ (Figure 4.43b) are slightly larger than simulated. The measured permittivity of the insulating liquid with the IDS is compared to reference values ($\varepsilon_{r, IDS}$ vs. $\varepsilon_{r, ref}$) for the unused ($\varepsilon_{r, ref, unused}$ = 2.1065) and used insulating liquid ($\varepsilon_{r, ref, used}$ = 2.2453), Figure 4.44. The mean value yields a slight consistent positive deviation $D$ of about +0.45% due to the manufacturing tolerances. The experiment was conducted using three sensors from which we observed a consistent deviation of 0.4 - 0.5% emphasising a

manufacturing issue in the $d_{\text{insulator}}$. We did not observe any capacitance fluctuations dependent on the environment or sensor's temperature. An explanation for this lays in the thermal expansion of $d_{\text{insulator}}$. The thermal expansion of the FR4 insulator layer may result in a dimensional change of not more than 100 nm per 10 °C which is well below the 1 μm manufacturing tolerance causing the 0.5% deviation. This is a valuable outcome and confirms standard PCB production being suitable for manufacturing such sensors.
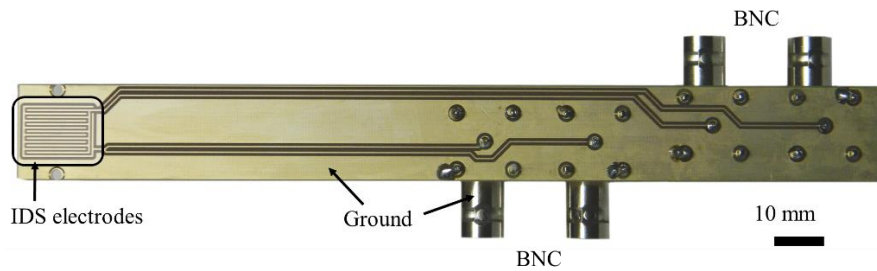


Figure 4.40. Designed IDS in standard PCB technology with four point measurement principle through shielded BNC connectors. Sensor surface is Ni as diffusion barrier for copper and subsequently Au plated as corrosion reduction. Active IDS sensing area is highlighted and electrically grounded areas are marked.
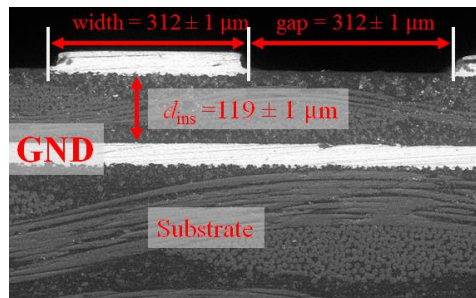


Figure 4.41. A SEM cross sectional image of the manufactured IDS as a cross sectional view showing the electrode width, thickness and separation from the common ground layer as $d_{\text{ins}}$.
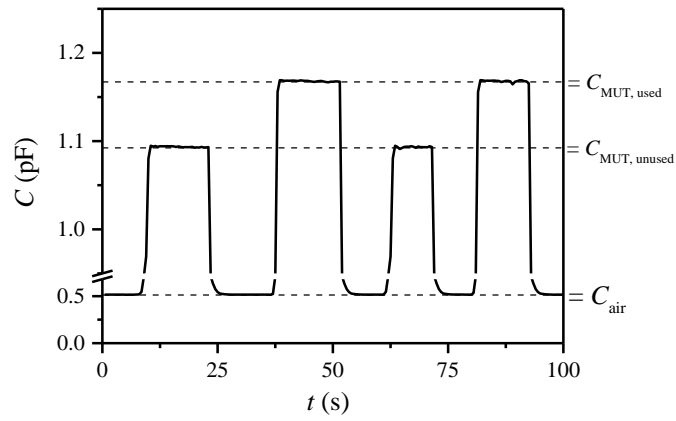
Figure 4.42. Repeatability and response of the sensor showing capacitance of air, with unused insulating liquid and used insulating liquid without a sensing hysteresis effect. The IDS was exposed to air and manually inserted into vials containing unused and used insulating liquid (each two times).
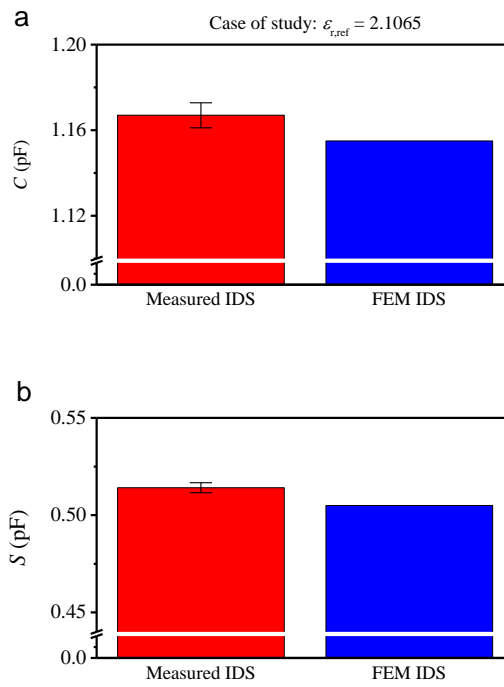


Figure 4.43. (a) Capacitance $C$ measured vs. simulated. (b) Sensitivity $S$ ($\approx$ air capacitance) measured vs. simulated. FEM simulation showing similar values to the experimental data.
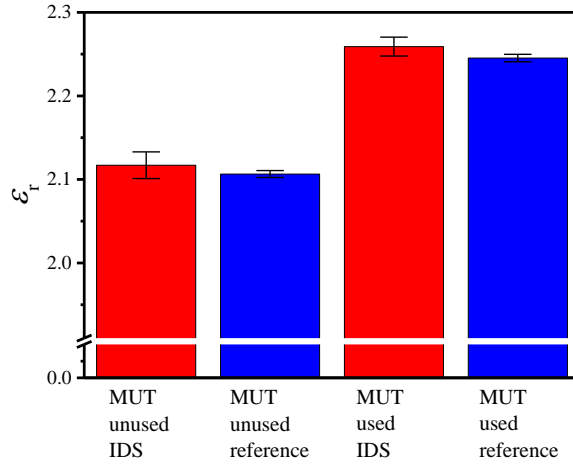
Figure 4.44. Permittivity via IDS measured $\varepsilon_{r,\,IDS}$ compared with reference values $\varepsilon_{r,\,ref}$ showing a good agreement. The exact value for the unused insulating liquid was $\varepsilon_{r,ref} = 2.1065$ and for the used insulating liquid $\varepsilon_{r,ref} = 2.2453$ from which the $\varepsilon_{r,\,IDS}$ exhibits a $D = 0.5\%$.

### 4.3.3 Conclusion of IDS2.5

A procedure has been demonstrated for the development of an interdigitated sensor for measuring insulating liquids accurately. This design procedure simulated figures of merit of the sensor for particular combinations of dimensions and sensor structure. The examined figures of merit (capacitance, sensitivity and accuracy) are strongly affected by the spatial structure of the IDS making it important to know the dimensions and permittivities of the physical layout. It was found that the soldermask throughout has a negative impact on the sensitivity, but if this layer thickness is well controlled it can improve accuracy. A similar result regarding accuracy was obtained from a variation of the insulator distance $d_{ins}$ between the IDS electrodes and a common ground plane (GND) without a soldermask. This also exhibited a positive impact on the sensitivity. The high accuracy emerges from parasitic capacitances which get recompensed by choosing a right combination of the IDS insulator $d_{ins}$ and wavelength $\lambda$ for a given $\varepsilon_r$ of the insulating liquid. The accuracy is achieved at the ratio of $d_{ins}/\lambda \cong 0.095$ without the soldermask. Standard PCB technology was then used to manufacture an IDS with this given ratio. The efficacy of this design in

discriminating changes in the properties of industrial insulating liquid during degradation was shown by a measurement of the permittivity on unused and aged insulating liquid and by comparing measured values to the values from a calibrated instrument. Subsequent measurements were consistent with the FEM predictions in this research, verifying the possibility to manufacture an IDS with PCB technology measuring $\varepsilon_r$ accurately using $d_{ins}/\lambda \cong 0.096$. This particular ratio will change when a different material is used for the insulator. The changed insulator permittivity yields a new $d_{ins}/\lambda$ for the $D = 0$ condition.

## 4.4  IDS 3.0

It was shown that the $\varepsilon_r$ of a MUT changes the electric field distribution above the sensor and therefore affecting the parasitic capacitance. This parasitic (positive and negative) capacitance was due to an interaction with the grounded plane separated underneath by an insulator from the electrodes. This was an essential outcome of the IDS2.5 development. The next generation of an interdigitated sensor minimized this parasitic capacitance. The hypothesis then is that a compensation of $C_{parasitic}$ and $C'_{parasitic}$ in,

$$\varepsilon_r = \left(C_{MUT} + C_{parasitic}\right)/\left(C_{air} + C'_{parasitic}\right), \tag{4.32}$$

is not necessary anymore and this equation reduces to,

$$\varepsilon_r + \varepsilon_{r,int} = \varepsilon_{r,IDS} = (C_{MUT} + C_{int})/(C_{air} + C_{int}), \tag{4.33}$$

where $C_{int}$ is the intrinsic capacitance of the IDS yielding an offset such as $\varepsilon_{r,int}$. If $C_{int}$ is comparably small to $C_{air}$, then the permittivity measured by the IDS is the permittivity of the MUT;

$$\varepsilon_r = C_{MUT}/C_{air}. \tag{4.37}$$

This will enable to directly measure the relative permittivity and potentially the conductivity of the insulating liquid. In order to achieve this, the third design generation of the IDS is equipped with a deflector electrode $V_D$ in between both

sensing electrodes, $V_+$ and $V_0$. The $V_D$ function as a Faraday shield towards the grounded plane (GND) beneath having potential $V_D \rightarrow$ GND ($= 0$ V). This reduces the electric field interaction with the insulator which was found responsible for $C_{parasitic}$ and $C'_{parasitic}$ dependent. The investigation on the impact on the figures of merit such as $C$, $S$, and $D$ using this deflector electrode is shown via FEM.

For the manufacturing of the IDS3.0 sensor, an aluminium PCB technology was chosen. Aluminium PCB technology provides a rigid 2 mm aluminium base plate which also serves as a common GND plane. The same IDS manufacturer as the IDS2.0 and IDS2.5 was chosen. The minimal possible trace size for the electrodes and their separation was constrained by the manufacturer with $d_{min} =$ 150 μm. Further restrictions for the simulations were $d_{ins} = 120$ μm and an electrode thickness of 30 μm. The permittivity of the insulator was set to 4.5 in the simulations as an approximation for epoxy laminates, similar as in the IDS2.0 and IDS2.5 chapter.

### 4.4.1 Structure and FEM simulations

In the IDS2.5 simulations (section 4.3) the intention was to compensate the parasitic capacitance. But here, the aim of the simulation for the IDS3.0 is to find a design parameter which affect the figures of merit in respect to $w_D$ and $g_D$ of $V_D$, in order to minimise the parasitic capacitance. The IDS3.0 structure was simulated similar to the IDS2.5 simulations using Figure 4.45a, showing one electrode pair and the placement of the deflector electrode. However, no soldermask was applied onto the electrodes as this was found to be detrimental to the sensing properties (section 4.3.1). The deflector electrode, $V_D$, potential was having the ground potential (GND) and not electrically connected to the sensing electrodes $V_+$ and $V_0$.

Figure 4.45b shows the simulated cross section with its dimensions using 20 sensing electrodes, $V_+$ and $V_0$. The electrode periodicity is defined by $\lambda/2 = w + 2g_D + w_D$. A grounded plane, $s$, was at a distance of $12\lambda$ to the left and right of the IDS electrode structure. An upper boundary was set to a distance of $s = 20\lambda$. The boundary $s$ was also extended on the left and right walls, defining the simulation effectively with a Dirichlet boundary condition entirely.
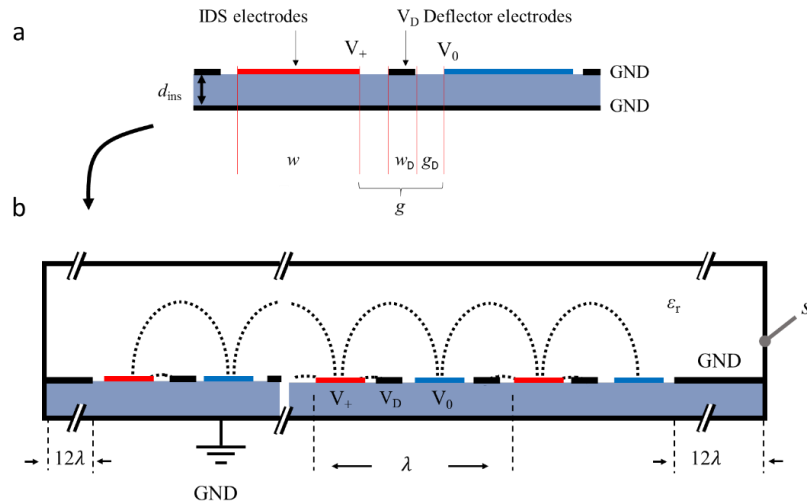


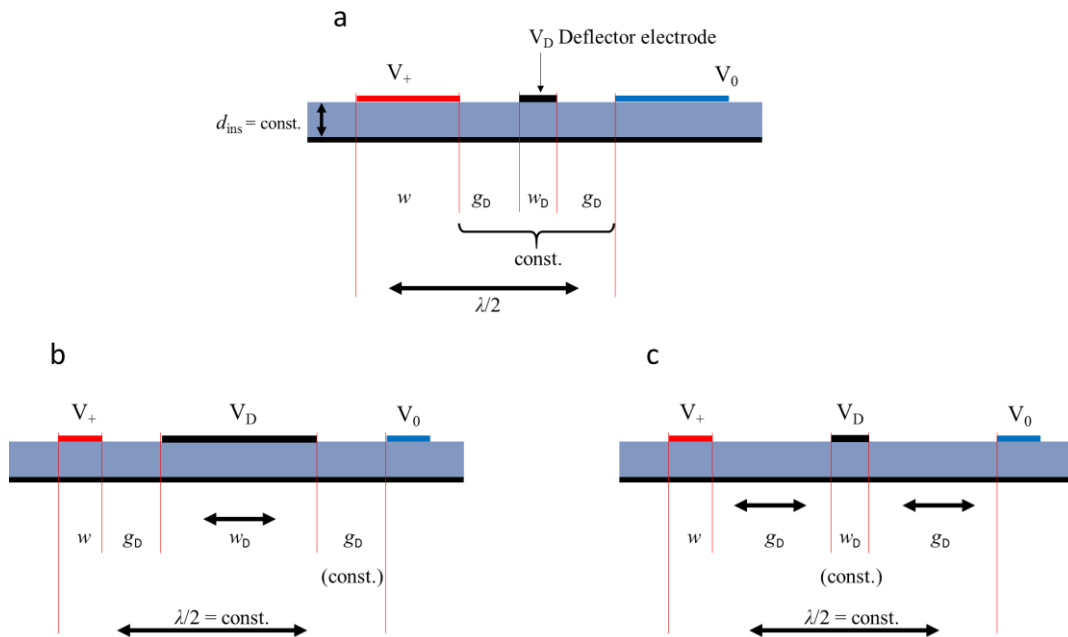Figure 4.45. The structure of the IDS and its boundary conditions for the FEM simulation.



Figure 4.46. Three different cases for the simulation for a constant $d_{ins}$. (a) A variation on $\lambda$ while having $g_D$ and $w_D$ constant. (b) A variation on $w_D$ while having $\lambda$ and $g_D$ constant. (c) A variation on $g_D$ while having $\lambda$ and $w_D$ constant.

The simulation uses the structure as shown in Figure 4.45. It focussed on three variations on the geometry and its impact on the capacitance $C$, sensitivity $S$ and accuracy $D$. Firstly, in Figure 4.46a, the effect of a variation of the wavelength $\lambda = 1$ to $6$ mm, using the minimal possible structure for $g_D = w_D = 150$ μm is investigated. Secondly, in Figure 4.46b, a dimensional variation on $w_D = 0.0025\lambda$ to $0.125\lambda$ is expected to have an impact on these figures of merit when $g_D = 0.0375\lambda$ and $\lambda = 4$ mm is kept constant. Thirdly, a set of simulations investigates the effect of a variation on $g_D = 0.0025\lambda$ to $0.125\lambda$ while keeping $w_D = 0.0375\lambda$ and $\lambda = 4$ mm constant, Figure 4.46c.

The first set of simulations examines the capacitance $C$ as a function of $\varepsilon_r$ for a variation in $\lambda$, $w_D/\lambda$ and $g_D/\lambda$ in Figure 4.47a to Figure 4.47c. The capacitance in Figure 4.47a increases for larger $\lambda$ but saturates around $\lambda > 4$ mm. This capacitance increases for a larger value of $\varepsilon_r$. The capacitance, as a function of $\varepsilon_r$, when varying $w_D/\lambda$, exhibits an increase for lower ratios of $w_D/\lambda$ due to the effective increase in the electrode width $w$ and diminishing effect of the grounded electrode $w_D$. The opposite occurs for larger ratios of $w_D/\lambda$, Figure 4.47b. A similar picture is plotted in Figure 4.44c showing the capacitance as a function of $\varepsilon_r$ when $g_D/\lambda$ is varied. Smaller ratios of $g_D/\lambda$ effectively increases the electrode width $w$ while the $g_D$ increasingly vanishes. The magnitude of this effect is similar to the dependence $w_D/\lambda$. This examines that the capacitance is predominantly affected by the IDS sensing electrode width.

The second set of figures determines the sensitivity $S$ in Figure 4.47d to Figure 4.44f as function of $\varepsilon_r$. The sensitivity as function of $\varepsilon_r$ while varying $\lambda$ can be regarded as constant in respect to $\varepsilon_r$ as shown in Figure 4.47d. The sensitivity however increases as the capacitance increases with $\lambda$. Figure 4.47e shows an increased sensitivity as function of $\varepsilon_r$ when reducing the ratio $w_D/\lambda$. The sensitivity does not vary significantly across $\varepsilon_r$. The sensitivity in Figure 4.47f as

a function of $\varepsilon_r$ is shown for a variation on $g_D/\lambda$. Smaller values of $g_D/\lambda$ causes an increase in the sensitivity but the overall sensitivity remains nearly constant with $\varepsilon_r$, although large values of $g_D/\lambda$ leading to a decrease in the sensitivity as a function of $\varepsilon_r$. A reduction on $S$ can be attributed due to an increased parasitic capacitance.

The third set of figures, Figure 4.47g to Figure 4.47i, explores the accuracy expressed as the deviation $D$ in percentage as function of $\varepsilon_r$. Using a variation on $\lambda$, Figure 4.47g, the deviation remains more constant for larger values of $\lambda$. Smaller values of $\lambda$ causes the deviation $D$ to increase strongly with $\varepsilon_r$ and does not remain constant. When varying $w_D/\lambda$ but holding $g_D$ constant does not affect the accuracy very much, Figure 4.47h. A zero crossing is highlighted via a turquoise line. This zero crossing occurs for very small values of $w_D/\lambda$.

As a conclusion to these simulations, $C$ and $S$ increase with $\lambda$, and increases for small values of $w_D/\lambda$ and $g_D/\lambda$. For $\lambda = 1\,mm$ within the range $\varepsilon_r = 2$ to $2.5$ the deviation is about 5.1 to 5.8%. For $\lambda = 4\,mm$ this deviation reduces to 1 and 1.3% whereas for $\lambda = 6\,mm$ the deviation is between 0.8 and 1.1%. Essentially, the $g_D$ controls the parasitic capacitance. Small values of $g_D/\lambda$ lead to a small deviation and are nearly constant with $\varepsilon_r$, whereas large values of $g_D/\lambda$ increase the deviation, which are not only dependent on $g_D/\lambda$ but also are a function of $\varepsilon_r$.
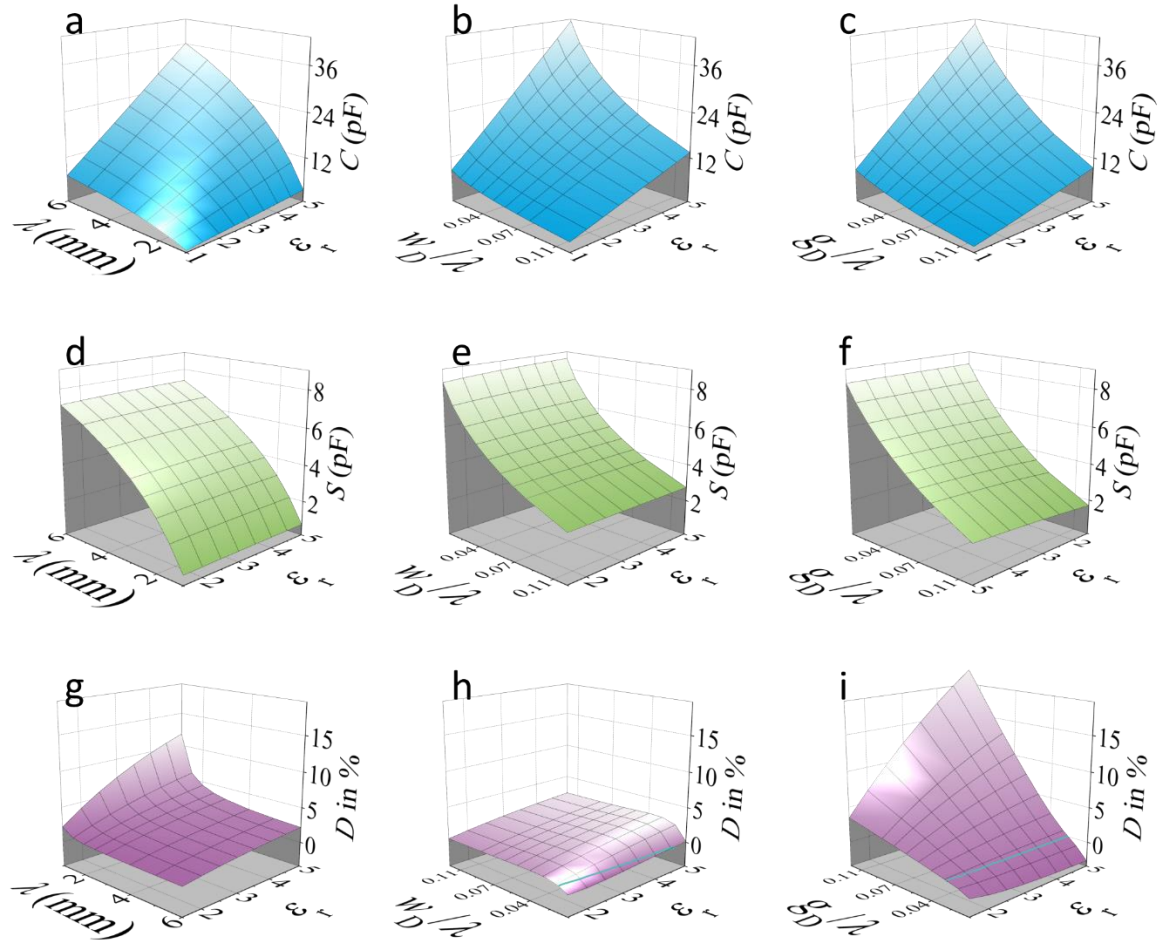
Figure 4.47. The figures of merit capacitance *C*, sensitivity *S* and deviation *D* versus $\varepsilon_r$ when $\lambda$, $w_D$ or $g_D$ of the IDS3.0 structure is varied.

The electric field dependence for a variation on $\varepsilon_r$ and $g_D$ is explored in Figure 4.48 and 4.49. Figure 4.48a shows in more detail the field lines for $\varepsilon_r = 1$, $w_D = 0.15$ mm and $g_D = 0.01$ mm having $\lambda = 4$ mm. The electric field above the electrode's surface is visible and a small fraction reconnects to the underside of the $V_0$ electrode emanated from $V_+$. In Figure 4.48b, the $\varepsilon_r$ is increased to $\varepsilon_r = 5$. The electric field distribution does not change visually when comparing this figure with Figure 4.48b, but the electric field from $V_+$ to $V_0$ beneath the electrodes causes a parasitic capacitance in the system.
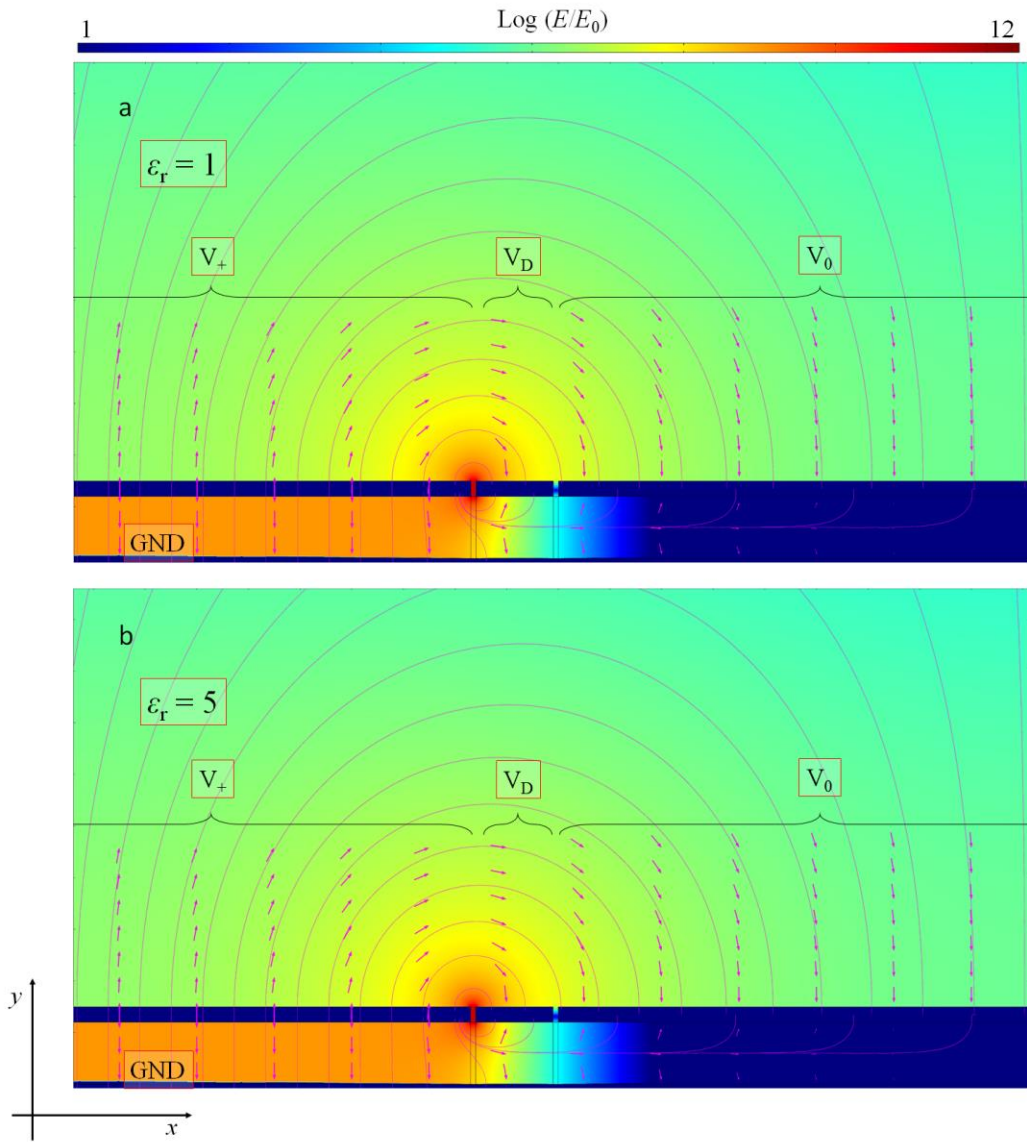
Figure 4.48. The electric field distribution around the electrodes $V_+$, $V_0$ and $V_D$ having $g_D = 0.01$ mm for the case (a) $\varepsilon_r = 1$ and (b) $\varepsilon_r = 5$. The electric field does not visually vary between both cases.
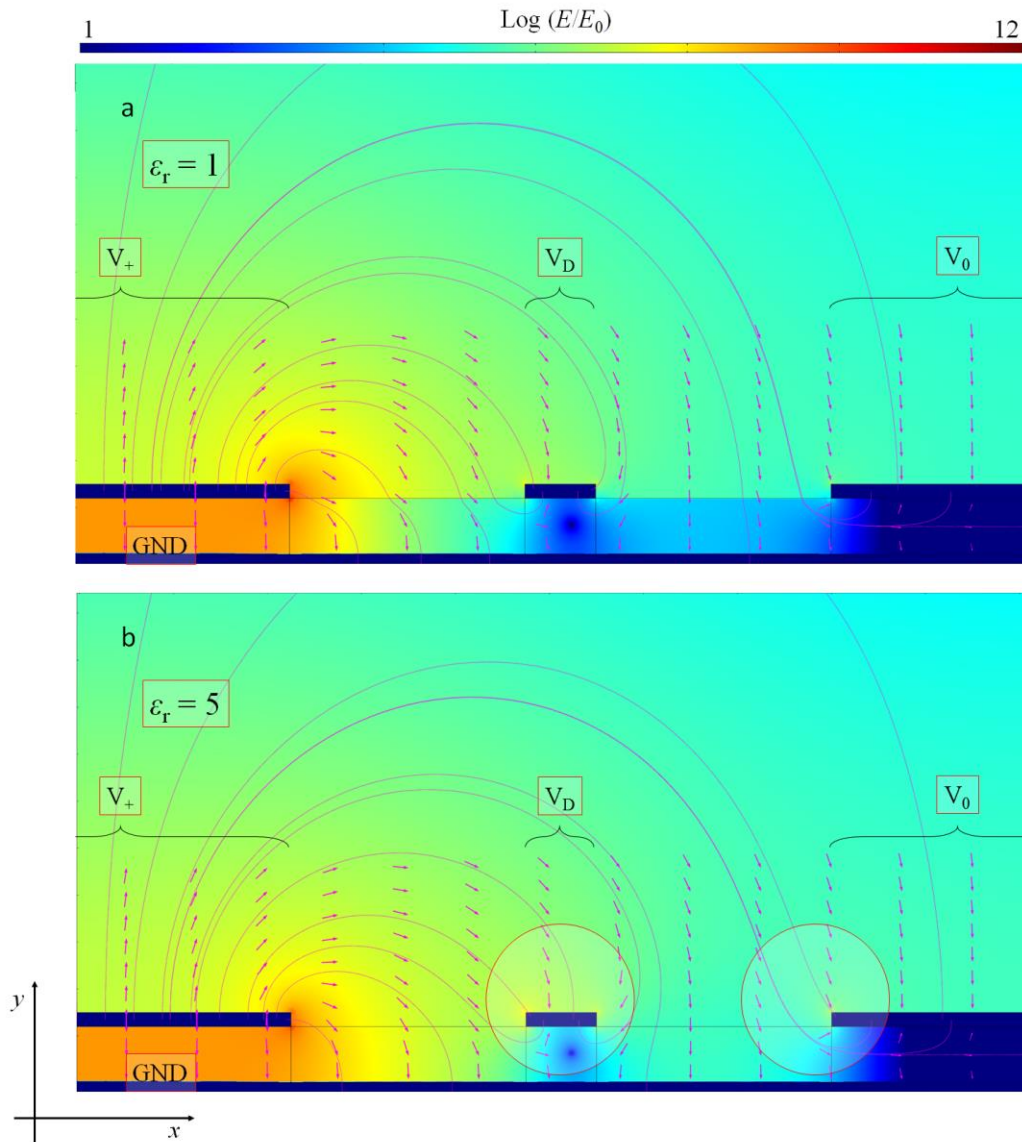
Figure 4.49. The electric field distribution around the electrodes $V_+$, $V_0$ and $V_D$ having $g_D = 0.5$ mm for the case (a) $\varepsilon_r = 1$ and (b) $\varepsilon_r = 5$. The electric field varies visually between both cases, red circles.

A different image is plotted when using $g_D = 0.5$ mm, Figure 4.49. Figure 4.49a shows the case for $\varepsilon_r = 1$. The electric field, emanated from $V_+$, shows a strong affinity to GND through $d_{ins}$. In addition to that effect, the electric field is visually altered by the deflector electrode. The wide gap $g_D$ permits the electric field to penetrate the underside of $V_0$. Figure 4.49b shows the case for $\varepsilon_r = 5$, highlighting the changed electric field via circles. When comparing the electric field lines between 4.49a and 4.49b, one notices a preference towards the upper

side of $V_0$. This causes the effect of having a negative parasitic capacitance which was present in the IDS2.0 design and exploited in the IDS2.5 version.

Exploring the Figure 4.47i, one might examine that a zero deviation can be achieved at the ratio $g_D/\lambda$ = 0.025 and thus adjusting $\lambda$. However, for this particular ratio the appropriate wavelength would be $\lambda$ = 6 mm given that the minimal possible $g_D$ is set by the manufacturer with 150 µm. This case is shown in Figure 4.47g and proves that a zero crossing on $D$ cannot be achieved with a deflector electrode, rather than having a constant positive 1%-offset to $\varepsilon_r$. A $D \cong 0$ for all $\varepsilon_r$ will be only possible if $g_D \cong 0$ and $d_{ins} \cong 0$.

## 4.4.2  Manufacturing of PCB IDS3.0

The $\lambda$ is a parameter that essentially controls the capacitance per area size of such a sensor. Utilizing $\lambda$ = 4 mm is a practical choice as a larger value of $\lambda$ yields proportionally less capacitance per unit area and a lesser improvement on $S$ or $D$. A smaller value than $\lambda$ = 4 mm causes a non-linear increase in $D$. As dimensions for the electrodes, the deflector electrode $w_D$ = 0.15 mm, the gap $g_D$ = 0.15 mm and, as $\lambda$ = 4 mm and $w$ = 1.55 mm were evaluated according to the simulations to be the most suitable parameter.

Figure 4.50 shows the PCB drawing of the IDS3.0 board, focussing on the generic layout. The IDS was designed to fit in a standard dimension of 100 mm by 100 mm, from which about one half of 50 by 100 mm is designed for the IDS electrodes (Figure 4.50a (bottom)). The other upper half is designed for proper electrode connection via BNC connectors, Figure 4.50a (top). The IDS sensor board was designed to be equipped with a four wire PT100 temperature probe. Therefore, a total of eight 50 $\Omega$ BNC connectors had to be placed on the board in order to connect the electrodes and the PT100 with a four wire system. Figure 4.50b shows the structure having the deflector electrode in between the IDS electrodes in more detail. The resulting length of the electrodes $l_e$, was designed

to be 84 mm on this board. Together with an effective electrode number, $N_{e,eff} = 23$, both these determine the total capacitance of the IDS.

The manufactured IDS3.0 is shown in Figure 4.51a. A 50 nm gold coating above the 1 μm Nickel diffusion barrier onto the Cu electrodes improves inertness for potential chemical electrode reactions with the MUT. A Faraday shield at $s = 1.5\lambda$, Figure 4.51b, was applied onto this IDS improving the precision of the measurement. The structure was investigated via a scanning electron microscope, Figure 4.52, from which its gathered dimensions are listed in Table 4.8. These dimensions were consistent with the design sent to the PCB manufacturer and used in the FEM simulation.

Table 4.8. IDS3.0 dimensions.

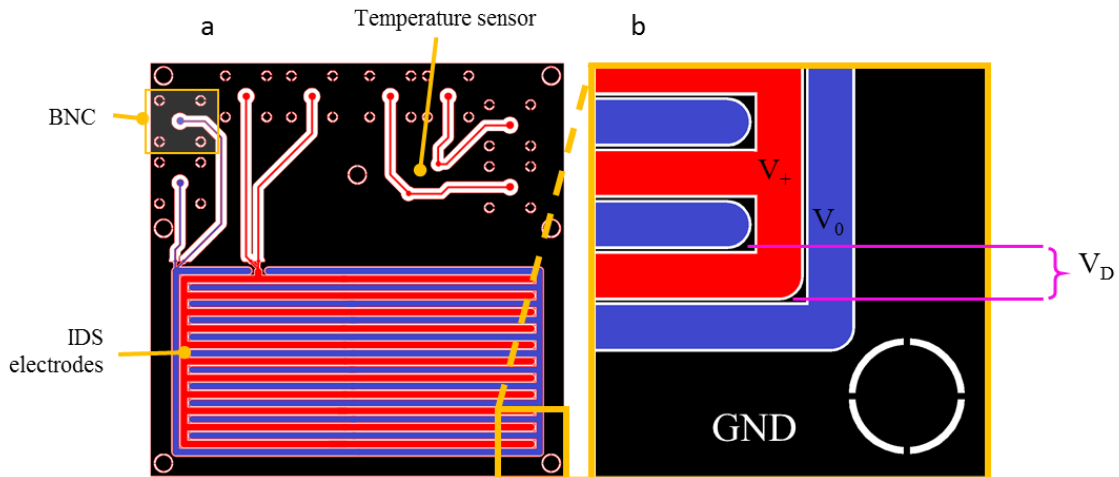| Part | Dimension |
| --- | --- |
| $w$ | 1.55 mm |
| $g_D$ | 0.15 mm |
| $w_D$ | 0.15 mm |
| $d_{ins}$ | 0.12 mm |
| $l_e$ | 84 mm |
| $N_{e,eff}$ | 23 |



Figure 4.50. The PCB drawing of the manufactured IDS3.0. (a) The top view of the 100 by 100 sensor board with designed placement of a PT100 temperature probe and (b) a close view of the fine structure resolving the placement of the deflector electrode $w_D$.
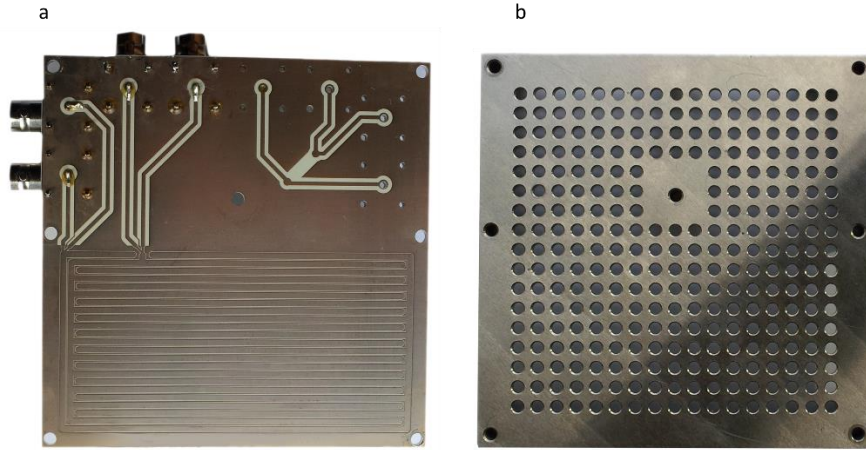
Figure 4.51. (a) The manufactured IDS3.0 with BNC connectors and (b) its Faraday shield.
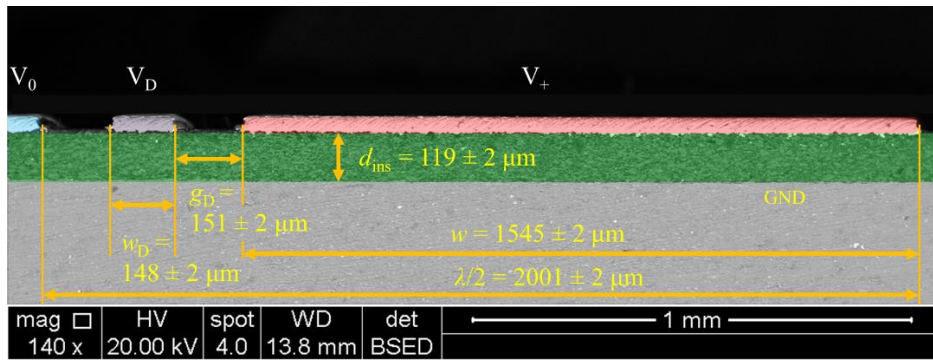


Figure 4.52 Dimensions of the IDS3.0 via the SEM image of the IDS cross-section.

### 4.4.3  Measurements of the IDS3.0

Three IDS3.0 were randomly selected out of a manufactured batch of 20 samples. These IDS were assembled and measured in air at 30 and 90 °C. The test was conducted in a laboratory oven from which its temperature was controlled and verified by a separate thermometer. The vertical temperature gradient within the oven was measured as $\pm$ 1 °C, thus all three IDS were placed on the same horizontal layer within the oven. In order to remove potential adsorbed moisture from the electrodes, the IDS were heated up to 90 °C for 3 hours prior any measurement. The oven was subsequently set to 30 °C and the air capacitance was measured. The mean capacitance and its spread due to the manufacturing tolerances is $C = 6.28 \pm 0.02\,\text{pF}$ after reaching a stable 30 °C in the oven, Figure 4.53. The change in the capacitance when heated from 30 to 90 °C

159

was $\Delta C$ = - 0.0094 pF with a mean value and spread of $C$ = 6.27 ± 0.02 pF. In regard to the total capacitance at 30 °C this decrease is about 0.1 % and thus yielding $\partial C/\partial T$ = 0.15 fF/K which is below the possible resolution of the impedance analyzer. Therefore it can be said that within about ± 10 °C, this IDS3.0 is thermally stable. The conductivity measured is shown in Figure 4.54. The value of the measured conductivity at $T$ = 30 °C was $\sigma$ = 11.63 ± 0.03 pS/m while the value at $T$ = 90 °C was $\sigma$ = 9.77 ± 0.01·pS/m.
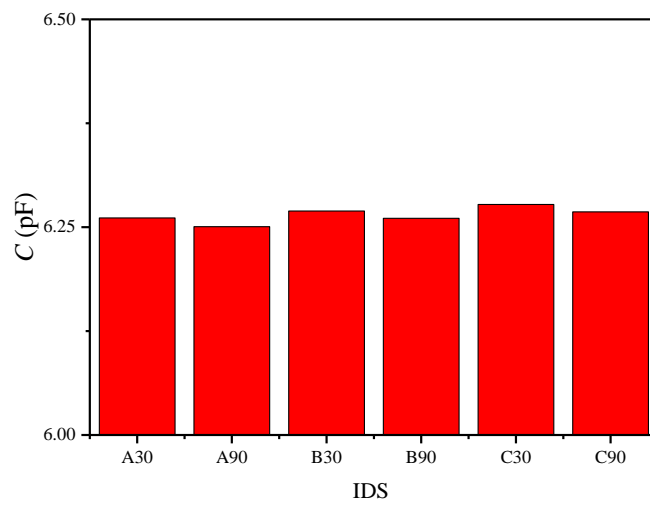


Figure 4.53. The IDS capacitance in air versus three different IDS for 30 °C and 90 °C
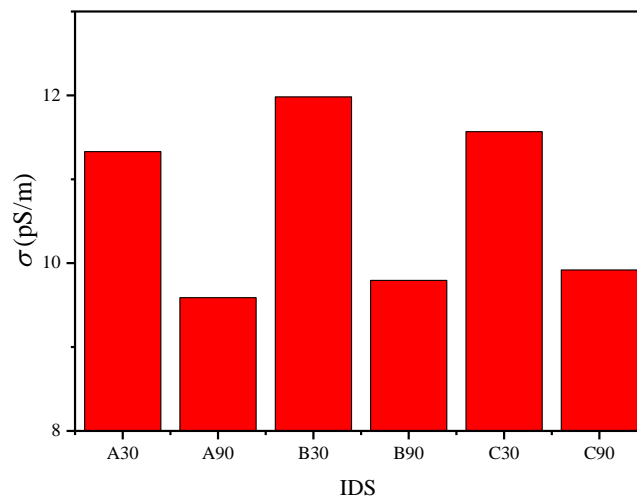


Figure 4.54. The IDS conductivity in air versus three different IDS for 30 °C and 90 °C

The measurement of the three IDS in insulating liquid examines the accuracy using reference values $\varepsilon_{r,ref}$. The test cell housing (section 3.1) was used to measure with the IDS by inserting the IDS with the Faraday cage into the housing. Then the housing was filled with the liquid so that the IDS electrodes were covered with the liquid, Figure 4.55. The IDS in the housing is essentially a large heat sink. The test cell with IDS inside was placed in a laboratory oven which was heated to temperatures of 25, 45, 65 and 85 °C, so that the housing heating elements served as temperature fine control for achieving a MUT temperature of 30, 50, 70, and 90 °C. The four wire BNC measurement leads to the impedance analyzer and the PT100 probe leads were fed though the rubber sealing of the door of the laboratory oven. The permittivity was determined by $\varepsilon_{r,IDS} = C_{MUT}/C_{air}$ where $C_{air}$ is the experimental value of the respective IDS in air.

Temperature controlled laboratory oven
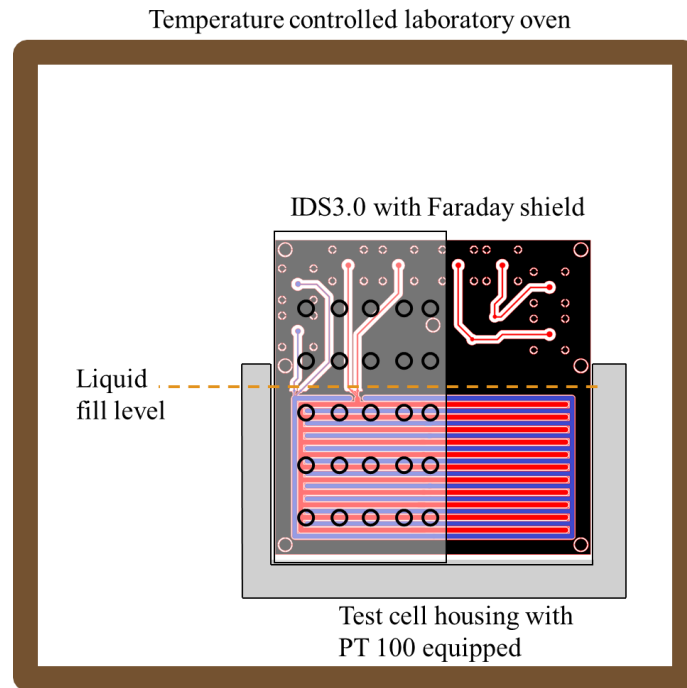


Figure 4.55. Sketch of the measured IDS in the laboratory oven.

The measurement of the permittivity $\varepsilon_r$ with the IDS is shown in Figure 4.56. The measured permittivity of each of the three IDS at 30 °C shows a mean value of $\varepsilon_{r,IDS} = 2.130 \pm 0.001$. The difference to the reference value is $\varepsilon_{r,IDS} - \varepsilon_{r,ref} = 2.130 - 2.1054 = 0.025$ which yields to a deviation of $D = 1.14\%$. This value is well within

the simulated deviation, which is $D_{FEM} = 1.04\ \%$, using $\varepsilon_{r,\ ref} = 2.1054$. A measurement at 90 °C yielded a mean value of $\varepsilon_{r,\ IDS} = 2.059 \pm 0.001$. Compared to the reference value at 90 °C of $\varepsilon_{r,\ ref} = 2.045$, this yields a deviation of $D = 0.69\%$ which is -0.29% different from the FEM simulations of $D_{FEM} = 0.98\%$. This deviation is slightly larger and negative. This may be due to the approximations made in determining $\varepsilon_r$. The air capacitance for larger temperatures was reduced by 0.0094 pF. This affected the measured $\varepsilon_{r,\ IDS}$. Using the air capacitance value for 90 °C instead, consistently increases the $\varepsilon_{r,\ IDS}$ value of about 0.2% in average. Thus, the experiment shifts closer to the simulated value having a $D'' = 0.84\%$ yielding a difference $D_{FEM} - D'' = 0.14\%$ which is in turn well within the predicted values.
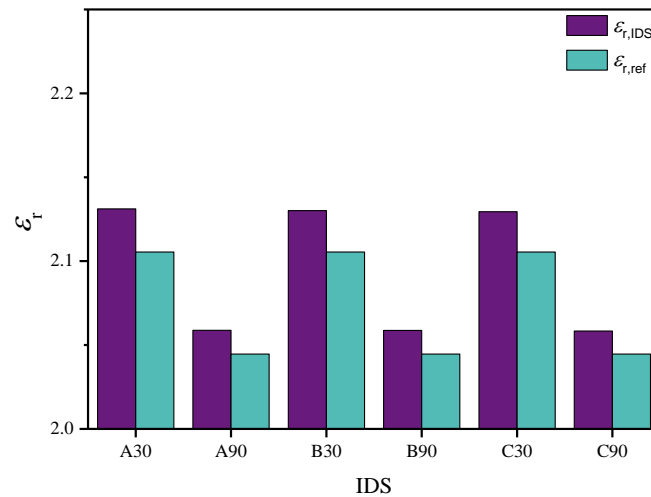


Figure 4.56. The $\varepsilon_r$ of insulating liquid as measured for the IDS (A, B, C) versus the reference value $\varepsilon_{r,\ ref}$ at 30 °C and 90 °C.

The conductivity of the insulating liquid was measured with the IDS, $\sigma_{IDS}$, and is compared with the reference value, $\sigma_{ref}$. The mean conductivity for the three sensors at 30 °C was measured: $\sigma_{IDS} = 5.8 \pm 0.4$ pS/m in Figure 4.59. This value increased for 90 °C to: $\sigma_{IDS} = 8.4 \pm 0.8$ pS/m. Compared with the reference value obtained via the test cell for 30 °C; $\sigma_{ref} = 0.21 \pm 0.01$ pS/m and its increased value at 90 °C; $\sigma_{ref} = 0.84 \pm 0.02$ pS/m. The Figure 4.59 shows that the IDS3.0 was

inaccurate for measuring very low conductivities of an unused insulating liquid. The measurement was repeated by diluting the insulating liquid from the oxidation experiment (section 3.2) in order to investigate the accuracy on the conductivity for used insulating liquids. The used insulating liquid was measured pure 1/1 (Test 5) and diluted in a ratio of approximately 1/2 (Test 4), 1/4 (Test 3) and 1/8 (Test 2) into unused insulating liquid (Test 1). These three solutions were filled into 100 ml glass containers. The conductivity was then measured via the IDS and compared with the test cell results at 30 °C. It was found that a very low concentration (ratio 1/8) of used insulating liquid into unused insulating liquid changes the conductivity of unused insulating liquid significantly. The measurement suggests that the IDS possesses an intrinsic conductivity which vanishes when the insulating liquid reaches a value of about > 5 pS/m. Hence, for most practical environments, where slight impurities are unavoidable, the IDS3.0 shows a sufficient accuracy for the conductivity.
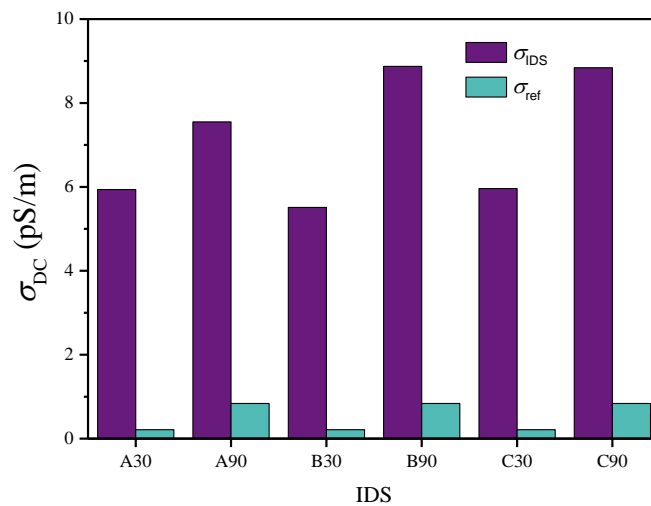


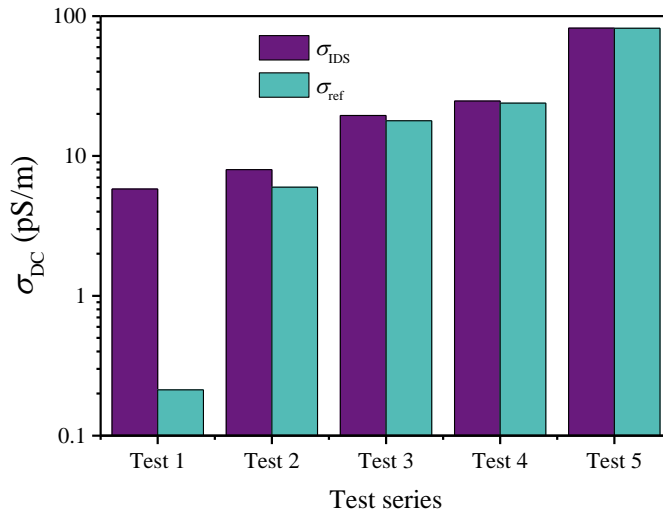Figure 4.59. The $\sigma_{DC}$ of the insulating liquid as measured for the IDS versus the reference value $\sigma_{ref}$.

Figure 4.60. The $\sigma_{DC}$ of an aged insulating liquid as measured for the IDS versus the reference value $\sigma_{ref}$.

### 4.4.4  Conclusion of IDS3.0

In this section 4.4, the generation IDS 3.0 was presented. This generation has shown significant improvements, such as temperature insensitivity and a dramatic reduction in the parasitic capacitances. It has also shown a high accuracy and precision through a deflector electrode and a faraday shield.

When the temperature was varied from 30 to 90 °C the capacitance remained stable within ± 0.05%. The accuracy was as high as 99%. Simulations show a variation in $\varepsilon_r$ of about 0.2% across the expected permittivity range (section 3.2) of $\varepsilon_r = 2$ to 3. This can be regarded as a constant offset when measuring the insulating liquid. A measured precision of the capacitance was within the instrument error of 0.05% regardless when measuring the air capacitance or the permittivity $\varepsilon_r$, indicating this is attributed to the measurement instrument. The capacitance spread and thus the manufacturing tolerances were lower than 0.5%.

These figures of merit are remarkable when comparing previous generations in this thesis and with the state of the art in the literature. This new development uniquely allows the measurement of the conductivity with a standard one-layer

aluminium based PCB technology. This is a critical step towards measuring acidity content in insulating liquids.

The electric field plots have shown how the electric field is affected by the presence of a deflector electrode. The deflector electrode is still required even if the gap is very small as it shields the parasitic capacitance from within the insulator. Thus, $w_D$ detrimentally affects the accuracy if chosen too small.

The next chapter will apply this IDS3.0 as a prototype in an environment which deteriorates the insulating liquid at 140 °C, for examining the performance in measuring *in-situ* the permittivity at elevated temperatures.

## 4.5  IDS development overview

The extensive chapter about the IDS development can be summarized in Table 4.9. Each sensor generation eliminated the predecessor disadvantage. IDS1.0 was practically insensitive for measuring insulating liquid. The unshielded electrodes were susceptible to external electric fields. This was reduced with the development of the IDS2.0 using a grounded plane underneath the electrodes and a faraday shield above the electrodes. All further generations used a Faraday shield and a grounded plane. A further development step was to optimise the electrode structure to yield a high accuracy for a known value of the relative permittivity. The last development, IDS3.0, adapts deflector electrodes to shield the sensors own electric field. This reduced the susceptibility to temperature dramatically and enabled to measure the conductivity. The latter was not possible with previous generations in this thesis and in literature using cost efficient printed circuit board technology.

Table 4.9. The IDS generations and their key aspects.

| IDS | Feature | Advantage | Disadvantage | Accuracy |
|-----|---------|-----------|--------------|----------|
| 1.0 | Simplicity | Robust | Insensitive, noisy | Not applicable |
| 2.0 | Grounded plane and Faraday shield | High precision | Inaccurate | 80 % |
| 2.5 | Special electrode geometry | High accuracy | Temperature sensitivity | 99.5% |
| 3.0 | Deflector electrodes | Temperature insensitive | Physical sensor size | 99% |

# 5 *In-situ* insulating liquid measurements with IDS3.0

The section 4.4 has shown that the IDS 3.0 performs well when measuring the permittivity and conductivity of selected liquids. A logical step now is to examine how such a sensor performs when measuring a liquid which is continuously degrading. Immersing such a sensor in the insulating liquid at high temperatures for long periods has not yet been done. Hence, in order to measure *in-situ* with IDS, a more realistic experiment setup than in section 4.4 was required to permanently measure the dielectric properties.

## 5.1 Experiment

This experiment was similar to the oxidation experiment in section 3.2 but in a 5-fold larger scale to facilitate three IDS3.0. In addition to the insulating liquid, winding insulation paper strips were added to this experiment. It is expected that this paper decomposes, which may have a relationship with the relative permittivity. This could enable to estimate the physical strength of the winding insulating paper via a measurement with the IDS 3.0. Hence, the experiment was designed as follows. Figure 5.1 shows a 40 liter large aluminium container that was used to accommodate three IDS3.0 with a Faraday shield. Within the 30 liters of paraffinic insulating liquid, 2.5 kg of winding paper as a roll and 30 winding paper strips of each 280 mm by 30 mm for tensile strength testing were placed (Weidmann Diamond Dotted 250 µm). The winding paper and insulating liquid weight ratio is about 10%. In addition, the liquid was continuously stirred via a magnetic stirrer to reduce potential temperature gradients which was monitored via a PT100 temperature probe. An air headspace of about 10 liters volume was present.
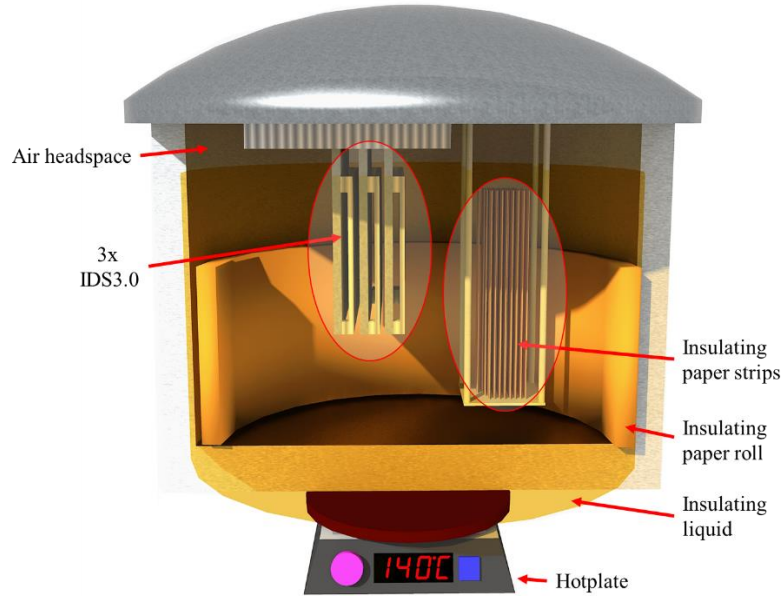
Figure 5.1. Experimental setup of *in-situ* measuring the deteriorating of insulating liquid with IDS3.0. The three IDS and a paper strip holder were mounted at the lid to immerse the IDS and the paper strips in the liquid.

The experimental procedure is described now. After a vacuum drying process of the included paper at 90°C for 48h, the experiment was fully assembled and the IDS were electrically connected to the impedance analyzer Hioki IM3590 via shielded BNC connectors. The air capacitance, $C_{air}$, for the three IDS at room temperature was measured prior to the assembly (as shown in section 4.4, the IDS capacitance can be considered as temperature independent). The experiment was filled with the insulating liquid of about 30 ±0.5 liters (see section 3.2). An initial settling time of 72 hours was given to fully settle the experiment and impregnate the paper samples. The measurements were done in the following structure. At 21 °C, a 100 ml insulating liquid sample was taken via glass syringes and three paper strips were extracted. These strips of 0.25 mm thickness were then cut into the dimensions of 15 mm width and length of 180 mm according to the standard for tensile testing [78] and measured with a tensile test machine (H110kT, Tinus Olsen Ltd., UK). The measurements of the assembled and shielded three IDS were done using the standard settings having 1 $V_{RMS}$ across the IDS electrodes and 0 V for all relevant grounded parts, i.e. the 40 liters

container, the Faraday shield, the IDS grounded plane and deflector electrodes. The temperature was increased to 140 °C for periods of about 100 h. After this period, the temperature was turned off and the setup cooled down to 21 °C over a period of 72 h. This process was repeated for the number of measurement points.

## 5.2  Measurements and Results

The measured permittivity of the liquid at 21 °C and 90°C, measured as $\varepsilon_r = C_{ins.liquid}/C_{air}$, is shown as an averaged value for the three IDS in Figure 5.2. The permittivity linearly increased during this experiment with the time of the experiment. The $\varepsilon_r$ value for the 21 °C is larger throughout, due to the *T*-dependence of the liquid. However, both lines are in parallel. This result was expected and is consistent with the conducted laboratory analysis in Chapter 3. It suggests that the permittivity may be used as a linear indicator for the deterioration of the employed components. The standard deviation of $\varepsilon_r$ was < 0.05%.
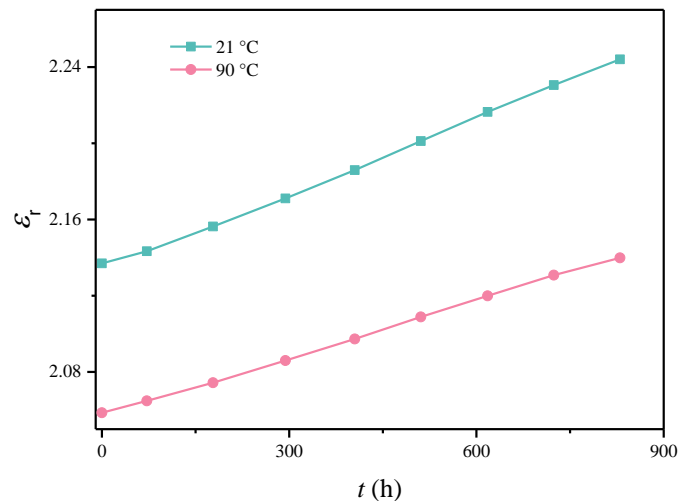


Figure 5.2. The measured permittivity as an average value obtained via three IDS3.0 versus the time of the experiment at two difference temperatures.

The insulating liquid moisture concentration with experiment time was measured at room temperature via a Karl-Fischer titration method and is shown

in Figure 5.3. Similar to the oxidation experiment in section 3.1, this value increased approximately linearly proportional to the experiment time. The magnitude of this increase shows a factor of two with a maximum concentration of about 50 ppm ($\pm$ 3%) which does not affect the permittivity much (section 3.3.1). This low change in the moisture value excludes itself as a cause for the increase in $\varepsilon_r$.
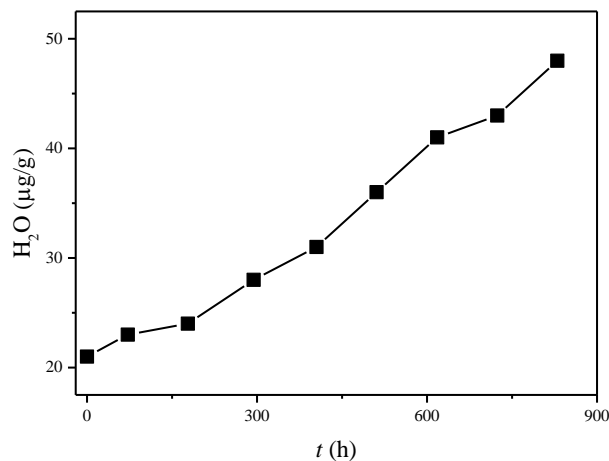


Figure 5.3. The amount of moisture in ppm in insulating liquid with time of the experiment.

The average cardboard paper tensile strength $\sigma_{TS}$ values of the three measured paper samples are plotted normalized over the experiment time in Figure 5.4. The tensile strengths $\sigma_{TS}(t)$ were measured with an average standard deviation of about $\pm 3.5\%$ for three samples per data point. The initial stress at which the insulating paper broke was at $\sigma_{TS}(0) = 1050 \pm 27$ N/mm$^2$. It exhibits a large drop in its value for the first measurements up to 300 hours and settles to a value of about 65% after about 400 hours. Similar results can be found in literature; such a settling is often attributed to a remaining value of the degree of cellulose polymerisation [31, 79].

Figure 5.4. The tensile strength of the insulating paper as function of time of
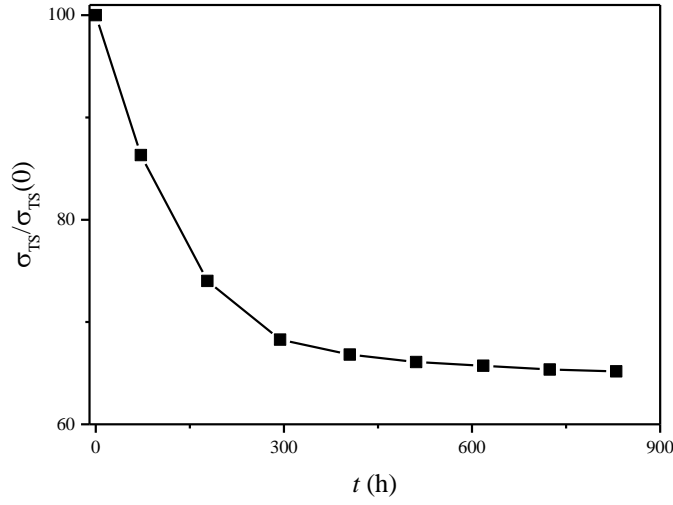the experiment.

The tensile strength can be plotted against the permittivity as the permittivity is a proportional indicator for the progressed deterioration. The heuristic tensile strength as a function of $\varepsilon_r$ is: $\sigma_{TS}(\varepsilon_r)$, can be derived. When this function exhibits a negative slope dependent on $\varepsilon_r$, then $\sigma_{TS}(\varepsilon_r)$ must be equal to a negative derivative of itself,

$$\sigma_{TS}(\Delta\varepsilon_r) \;=\; -1/k\frac{\partial\sigma_{TS}(\Delta\varepsilon_r)}{\partial\Delta\varepsilon_r}. \tag{5.1}$$

Using straightforward algebra we find,

$$\sigma_{TS}(\Delta\varepsilon_r) = c_1 e^{-\Delta\varepsilon_r k} + c_2, \tag{5.2}$$

where $c_n$ are integration constants which have units of $N/mm^2$. The constant $k$ is an experimental fit constant which can depend on parameter such as the paper material and manufacturing treatment, moisture value and the physical thickness of the paper. A comparison of the normalized experimental and theoretical function fitted using $c_1 = 1/e$, $c_2 = 0.65$ and $k = 90$ is shown in Figure 5.5. This shows that the permittivity can be utilized to predict the remaining tensile strength of the employed cardboard paper.
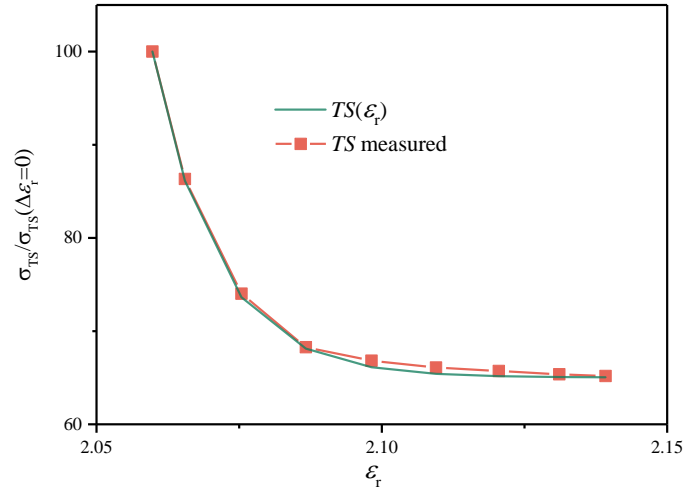
Figure 5.5. The experimental tensile strength of the paper and the fitted tensile strength as function of the relative permittivity measured via the IDS3.0.

The standard for transformer lifetime prediction states that the transformer life is a function of time and temperature (for various moisture, oxygen and paper conditions)[31]. With Eq. 2.2, it was shown that the chosen aging temperature of 140 °C versus 60 °C operating temperature of the oil yields an aging acceleration factor of 870 and thus 1 year at 60 °C was found to be equivalent to 10 h at 140 °C. It was also found that the oil permittivity increased and this increase is a function of time and temperature. That means that the transformer life is a function of the permittivity. Therefore, the transformer life $TL = (-\varepsilon_r(t) + \varepsilon_r(t = x))/(-\varepsilon_r(t = 0) + \varepsilon_r(t = x))$ where $x$ is the time, e.g. 400 h (equivalent 30~40 years, see E.q. 2.2), can be plotted as function of the permittivity as shown in Figure 5.6. A $TL = 0$ represents the approximated value of a designed service time of 30 years. This figure then shows that the conducted experiment comprised about 60 years of an oil filled transformer service time. Thus at a value of $\Delta\varepsilon_r \approx 0.05$, which is about half the experiment time, the service time of an oil filled transformer is reached. This model is an agreement of the measured tensile strength which

172

settles at about half the experiment time. This value is in turn in agreement with literature values for determining the end of life of oil filled transformers [79].
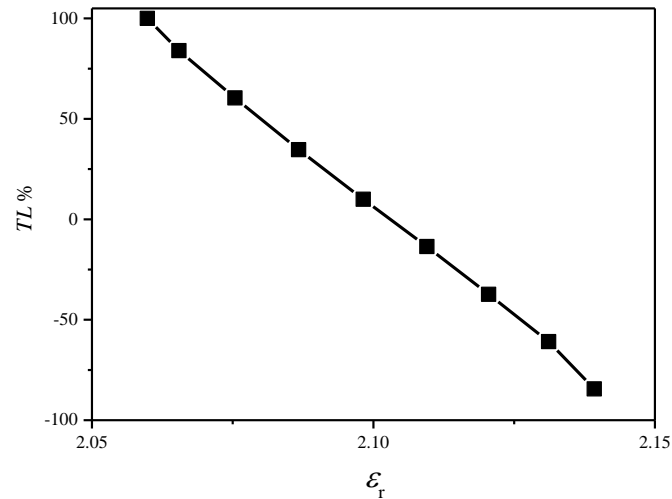


Figure 5.6. The transformer life in percent versus the permittivity measured through the IDS3.0.

The increase in the conductivity $\sigma(T)$, measured with the IDS using the standard setting (c.f. section 3.3), with experiment time being non-linear for both temperatures (21 and 90 °C), Figure 5.7. However at 90 °C, the magnitude of the increase was larger. The measurement threshold of the IDS3.0 was determined to be about 5 pS/m but the smallest measured value was 11 pS/m. This value for unused insulating liquid is substantially different from the value from unused insulating liquid which had 0.5 pS/m (section 4.4.3) at 21 °C. At $t = 0$, this insulating liquid was not yet degraded and it shows that after assembly and settling, the conductivity of insulating liquid increases by one order of magnitude. The thermal increase up to 15 pS/m for 90 °C is consistent with section 3.3.2. Therefore, in such practical environments, the sensor is sensitive for the conductivity insulating liquid.
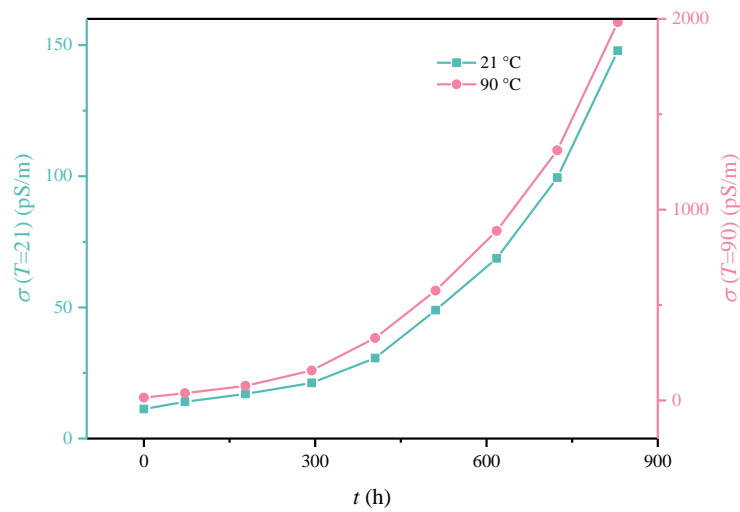
Figure 5.7. The measured conductivity for 21 and 90 °C measured via the IDS3.0 as function of the time of the experiment.
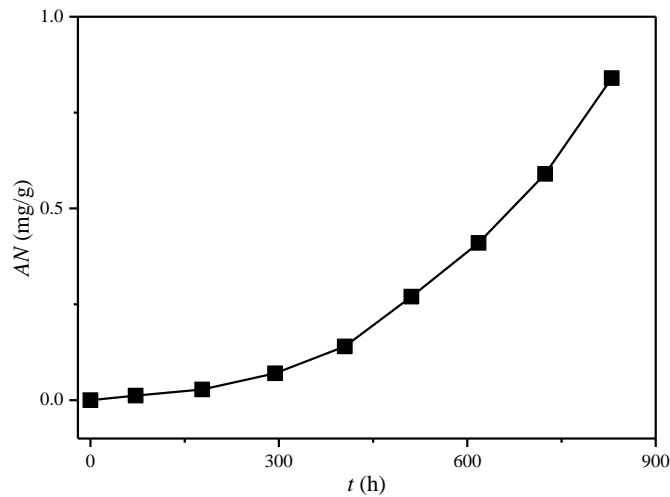


Figure 5.8. The acidity number *AN* as function of the time of the experiment.

According to the analysis in Chapter 3, the conductivity $\sigma(T)$ value at 21 °C represents the intrinsic base liquid more, whereas the value at 90 °C is relatively more proportional to the acidity content. In order to verify this, the acidity value, *AN*, was measured via the external laboratory (eNZOil, Lower Hutt, New Zealand) according to the standard ASTM D664-2009 and is shown in Figure 5.8. This standard also describes the procedure of neutralizing the acid with KOH. The *AN* value of the insulating liquid increased somewhat exponentially with the

experimental time. Comparing this curve with the non-linear curve for $\sigma(T)$, strong similarities can be found. Hence, the conductivity was taken and plotted as a function of $AN$, Figure 5.9. This picture is similar to the laboratory analysis in section 3.3.3. The conductivity is also proportional to the acidity number using IDS in practical environments which degrade the insulating liquid gradually.
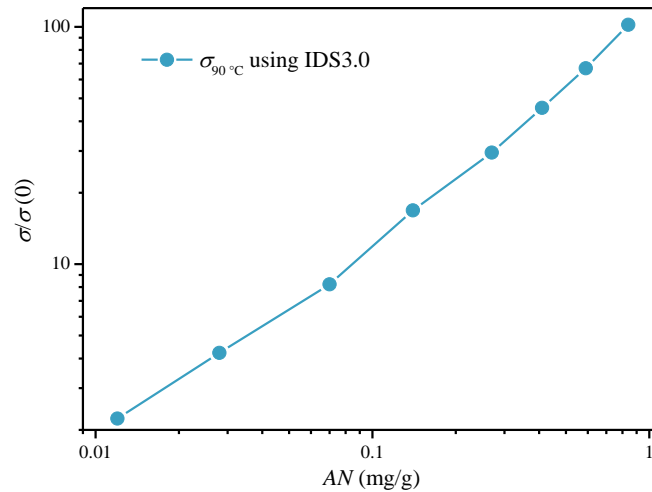


Figure 5.9. The relative change of the conductivity for $\sigma_{DC}$ as measured via the IDS at 90 °C as function of the acidity number $AN$.

## 5.3 Conclusion

The *in-situ* experiment with the IDS3.0 illustrates a remarkable utilization of the complex permittivity measurement of only the insulating liquid. It is shown that the relative permittivity could be tracked over the entire experiment period of over 800 hours in an acidic solution at 140 °C without showing deterioration effects on the sensor itself. These 800 hours correspond to an approximated lifetime for oil filled transformers of about 60 years. Thus this sensor is stable, accurate and precise for long periods, only requiring a one-time calibration measurement using air ($C_{air}$).

The monitored positive permittivity change was found to be a linear indicator of progressed system deterioration (the insulating liquid and the insulating winding paper) which is a function of time and temperature. Thus, this accurate

measurement yielded valuable information of the aforementioned transformer life *TL*, the oil moisture concentration and the tensile strength of the employed winding insulation cardboard paper. These parameters could be expressed as a function of the permittivity, giving novel insight in the interpretation of an observed change in the permittivity.

The measured conductivity gained deep insight into the acid formation during this experiment. In the laboratory analysis it was measured that the conductivity $\sigma$ follows the acidity concentration. This was also observed in this experiment using IDS. Thus, the acidity number, *AN*, can be directly related to the measured conductivity via the IDS3.0.

# 6 Summary of the work and conclusion

## 6.1 Overview

This work focussed on the design of interdigitated dielectrometry sensors for the *in-situ* monitoring of oil in distribution transformers. This was done in order to provide a health characterization of the used insulating liquid, e.g. a paraffinic hydrocarbon oil, which is useful for transformer engineers to evaluate the transformer's lifetime. The successful implementation of such a sensor can potentially eliminate off-line analysis of the oil by chemical methods, and even more importantly prevent expensive transformer failures.

## 6.2 Predictions

A literature survey was completed on the chemical changes that can be expected during the oxidation of the employed insulation liquid. Oxidation products were found to consist predominantly of ketones, organic acids and small amounts of moisture. Ketones for instance can dissolve organic materials whereas acids are harmful for metals. Moisture is a problem in large concentrations when it comes to the electrical insulating capability of the oil.

The oxidation products as described in the literature were confirmed by an accelerated aging experiment and a subsequent analysis using infra-red spectroscopy. This showed that the concentrations of these oxidation products increased with the time of the experiment. It then was expected that a gradual increase in these products will affect the dielectric properties of the oil.

## 6.3 Oil oxidation findings

A novel dielectric test cell was designed and constructed in order to measure the impact on the dielectric properties of this oil with a very high accuracy and precision. The oil from the accelerated aging experiment was measured in regard to its permittivity and conductivity. It was found that the permittivity linearly increased with experiment time. The conductivity was increasing non-linearly

177

with time. Importantly, the conductivity could now be described by a modification of the known polaron theory. This was not shown in literature before.

The aforementioned ketones, acids and moisture were then added to an unused oil sample and the permittivity and the conductivity was measured to identify their roles on the dielectric properties of the oil. It was found that ketones substantially increased the relative permittivity of the insulating liquid, whereas acids significantly contributed to the conductivity. Moisture was found to have an overall negligible impact due to its very low concentration.

## 6.4 Interdigitated dielectrometry sensor development

The previous section stated the boundary condition for the novel type of sensor that needed to be developed in order to sense the degree of transformer deterioration. When using a sensor responding to one type of acids or ketones only, this would require to know with certainty that this specific compound occurs in all hydrocarbon deterioration processes. However, the large variety of ketone and acid molecules made it difficult to employ such a sensor. Instead, measuring the relative permittivity and its conductivity was expected to yield the presence of all ketones and all organic acids, and thus be an advantage for determining the general degree of "transformer aging".

Interdigitated dielectrometry sensors were chosen as candidates for sensing these dielectric properties. In contrast to other interdigitated platforms that utilize active polymers, these dielectrometry sensors directly measure the material under test, i.e. the oil. This has the advantage that the chemical changes which affect the dielectric properties such as the permittivity and conductivity can be measured. In order to achieve a high degree of confidence that the measured value is the value of the material under test, a suitable sensor needed to be developed. After a series of four iterations using finite element modelling and analytical

functions, a highly accurate and a very cost efficient sensor could readily be manufactured using a standard printed circuit board technology.

## 6.5 In-situ testing of the sensor

For the first time, this sensor was then used in an *in-situ* accelerated aging experiment to degrade the insulating liquid at 140 °C over 800 hours. It was found that the permittivity linearly increased with the experiment time. The conductivity was increasing more exponentially. The conductivity was compared to the increase in the acidity value. It was found that both, the conductivity and the acidity increased in the same manner and yielded a linear relationship. The acidity is a well-known standard for health determination of those transformers. From this experiment, there were three crucial outcomes - a) the sensors were shown to be durable over an experiment time that is approximately equal to the lifetime of a distribution transformer, b) the accurate measurement of the relative permittivity allowed to infer the state of degradation of the oil and c) the conductivity yielded the value for the acidity.

## 6.6 Novelty

The major contribution in this thesis is twofold. Firstly, the detailed oil analysis showed the impact on the complex permittivity when mixing unused insulating oil with moisture and oxidised oil components such as ketones and organic acids. Secondly, the development of a suitable capacitive sensor sensing the complex permittivity *in-situ*. These robust, accurate, and cost effective interdigitated dielectrometry sensors were successfully used to determine the health of the oil *in-situ* that reflects the ageing of a distribution transformer.

## 6.7 Future work

The future work is to test these sensors in a real world environment such as in a transformer in the field. These sensors were measured with high quality laboratory equipment. In practice, microcontrollers are small and cost effective

mini-computers which can determine these dielectric properties. An idea for the future is to fabricate these interdigitated dielectrometry sensors with microcontrollers and their accessory electronics onto the printed circuit board. By means of energy harvesting, the electric field from the transformer core can be tapped to power a microcontroller. An attached radio frequency or infra-red transmitter can wirelessly transmit the dielectric properties to a receiver station outside, while the sensor remains inside. This may enable to mass-produce capsulated mini sensors, which can be applied in a large variety of applications where liquids need to be remotely measured. This goes beyond pure transformer applications, such as for marine or exoplanet research.

This concludes the work, which yielded several publications, talks and conference presentations as listed in the introduction.

# 7 Appendix A

The appendix A shows the raw measurements for the impedance $Z$ and the phase $\varphi$ of the oil as an example.

The raw data for the magnitude of the impedance $Z$ is shown in Fig. A1. The impedance from the accelerated aging experiment in section 3.2 changes for the lower frequency but for the upper frequency band, the $Z$ for the different experiment times is visually not distinguishable.
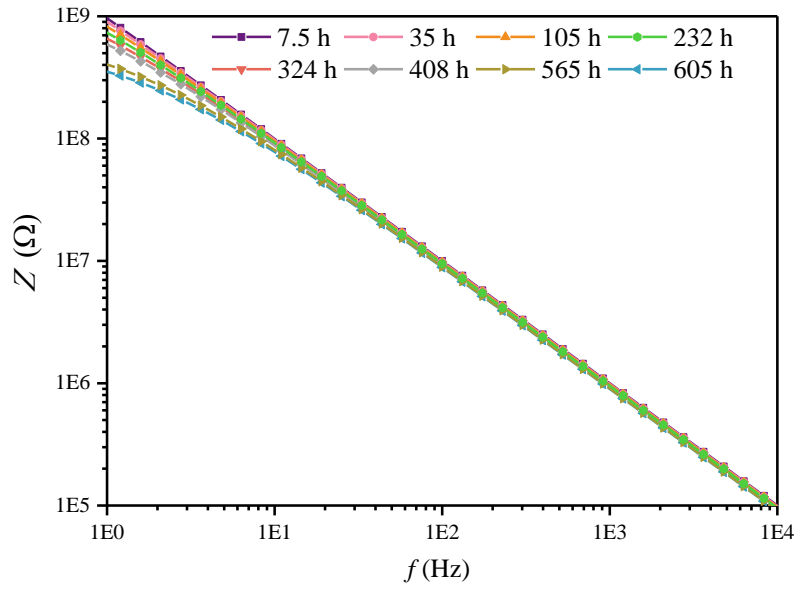
Fig A1. The measured impedance as function of the frequency from the accelerated oxidation experiment.

The raw data for the measured phase angle φ from the same aging experiment (section 3.2) between voltage and current is shown in Fig A2. The phase is nearly as constant for larger frequencies.



Fig A2. The measured phase angle as function of the frequency from the accelerated oxidation experiment.

This states a problem when presenting the data. It was solved by plotting the permittivity, $\varepsilon_r$, and the DC conductivity, $\sigma_{DC}$, over the frequency in section 3.2 and for the ensuing content. This convenience to choose the permittivity and the DC conductivity parameter was also in their frequency independence.

# 8 References

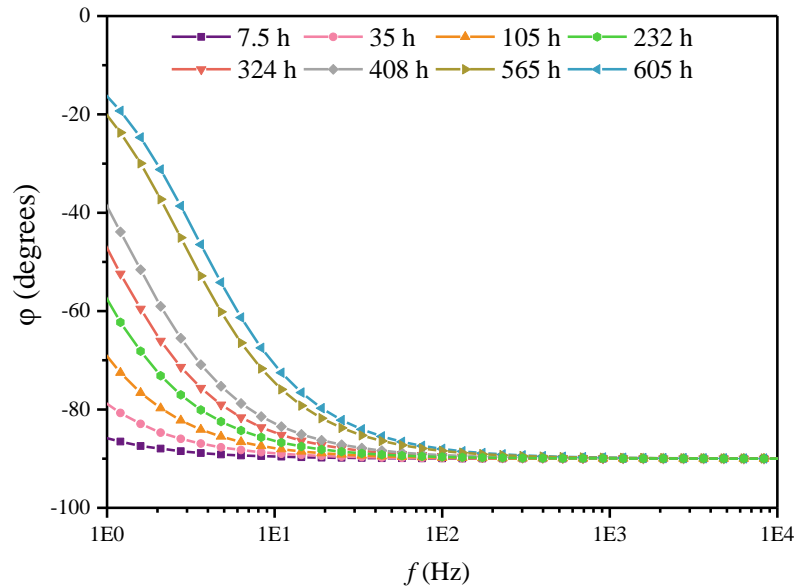[1]     C. T. Dervos, C. D. Paraskevas, P. Skafidas, and P. Vassiliou, "Dielectric characterization of power transformer oils as a diagnostic life prediction method" *IEEE Electrical Insulation Magazine,* vol. 21, pp. 11-19, 2005.

[2]     C. F. Ten, M. A. R. M. Fernando, and Z. D. Wang, "Dielectric properties measurements of transformer oil, paper and pressboard with the effect of moisture and aging" in *2007 Annual Report - Conference on Electrical Insulation and Dielectric Phenomena,* Vancouver, BC, Canada, pp. 727-730, 2007.

[3]     I. Fofana, "50 years in the development of insulating liquids" *IEEE Electrical Insulation Magazine,* vol. 29, pp. 13-25, 2013.

[4]     T. Bley, E. Pignanelli, and A. Schütze, "Multi-channel IR sensor system for determination of oil degradation" *J. Sens. Sens. Syst.,* vol. 3, pp. 121-132, 2014.

[5]     A. Georgiev, I. Karamancheva, and L. Topalova, "Determination of oxidation products in transformer oils using FT-IR spectroscopy" *Journal of Molecular Structure,* vol. 872, pp. 18-23, 2008.

[6]     C. Dervos, C. Paraskevas, P. Skafidas, and P. Vassiliou, "A Complex Permittivity Based Sensor for the Electrical Characterization of High-Voltage Transformer Oils" *Sensors,* vol. 5, p. 302, 2005.

[7]     M. Kitsara, D. Goustouridis, S. Chatzandroulis, M. Chatzichristidi, I. Raptis, T. Ganetsos, *et al.,* "Single chip interdigitated electrode capacitive chemical sensor arrays" *Sensors and Actuators B: Chemical,* vol. 127, pp. 186-192, 2007.

[8]     C.-F. Fong, C.-L. Dai, and C.-C. Wu, "Fabrication and Characterization of a Micro Methanol Sensor Using the CMOS-MEMS Technique" *Sensors,* vol. 15, pp. 27047-27062, 2015.

[9]     T. Yang, Y. Z. Yu, L. S. Zhu, X. Wu, X. H. Wang, and J. Zhang, "Fabrication of silver interdigitated electrodes on polyimide films via surface modification and ion-exchange technique and its flexible humidity sensor application" *Sensors and Actuators B: Chemical,* vol. 208, pp. 327-333, 2015.

[10]    V. F. Lvovich, C. C. Liu, and M. F. Smiechowski, "Optimization and fabrication of planar interdigitated impedance sensors for highly resistive non-aqueous industrial fluids" *Sensors and Actuators B: Chemical,* vol. 119, pp. 490-496, 2006.

[11]    Y. Zhang, X. Liu, C. Ru, Y. L. Zhang, L. Dong, and Y. Sun, "Piezoresistivity Characterization of Synthetic Silicon Nanowires Using a

MEMS Device" *Journal of Microelectromechanical Systems,* vol. 20, pp. 959-967, 2011.

[12]    P. R. Dugan, "Hydrocarbon Oxidation" in *Biochemical Ecology of Water Pollution,* ed Boston, MA: Springer US, 1972, pp. 87-96.

[13]    B. K. Warren and S. T. Oyama, *Heterogeneous Hydrocarbon Oxidation* vol. 638. Washington, DC American Chemical Society, 1996.

[14]    K. A. Yegorova, "Use of IR spectroscopy for the study of oxidation properties of hydrocarbon mixtures" *Petroleum Chemistry U.S.S.R.,* vol. 16, pp. 185-189, 1976.

[15]    Y. Sheiretov and M. Zahn, "Dielectrometry measurements of moisture dynamics in oil-impregnated pressboard" in *International Symposium on Electrical Insulation,* pp. 33-36, 1994.

[16]    A. V. Mamishev, B. C. Lesieutre, and M. Zahn, "Optimization of multi-wavelength interdigital dielectrometry instrumentation and algorithms" *IEEE Transactions on Dielectrics and Electrical Insulation,* vol. 5, pp. 408-420, 1998.

[17]    A. E. Seaver, A. V. Mamishev, Y. Du, B. C. Lesieutre, and M. Zahn, "Development and applications of fringing electric field dielectrometry sensors and parameter estimation algorithms" *Journal of Electrostatics,* vol. 46, pp. 109-123, 1999.

[18]    Y. Du, A. V. Mamishev, B. C. Lesieutre, M. Zahn, and S. H. Kang, "Measurements of moisture solubility for differently conditioned transformer oils" in *International Conference on Dielectric Liquids, 1999. (ICDL '99) Proceedings of the 1999 IEEE 13th* pp. 357-360, 1999.

[19]    A. V. Mamishev, S. R. Cantrell, Y. Du, B. C. Lesieutre, and M. Zahn, "Uncertainty in multiple penetration depth fringing electric field sensor measurements" *IEEE Transactions on Instrumentation and Measurement,* vol. 51, pp. 1192-1199, 2002.

[20]    A. V. Mamishev, K. Sundara-Rajan, Y. Fumin, D. Yanqing, and M. Zahn, "Interdigital sensors and transducers" *Proceedings of the IEEE,* vol. 92, pp. 808-845, 2004.

[21]    A. Mamishev, D. Yanqing, and M. Zahn, "Measurement of dielectric property distributions using interdigital dielectrometry sensors" in *Conference on Electrical Insulation and Dielectric Phenomena,* pp. 309-312, Virginia, U.S.A., Oct. 22-25, 1995.

[22]    A. Risos, N. Long, A. Hunze, and G. Gouws, "A 3D Faraday Shield for Interdigitated Dielectrometry Sensors and Its Effect on Capacitance" *Sensors,* vol. 17, p. 77, 2017.

[23]    A. Risos, N. Long, A. Hunze, and G. Gouws, "Interdigitated Sensors: A Design Principle for Accurately Measuring the Permittivity of Industrial Oils" *IEEE Sensors Journal,* vol. 17, p. 4, 2017.

[24] A. Risos, N. Long, A. Hunze, and G. Gouws, "MID-IR absorbance and its relation to static permittivity as a robust in-field tool tracking oil deterioration" in *SPIE Defence + Commercial Sensing 2017*, Anaheim, CA, p. 1, 2017.

[25] A. Risos, N. Long, and G. Gouws, "A temperature compensated dielectric test cell for accurately measuring the complex permittivity of liquids" *Review of Scientific Instruments,* vol. 88, p. 105105 2017.

[26] T. O. Rouse, "Mineral insulating oil in transformers" *IEEE Electrical Insulation Magazine,* vol. 14, pp. 6-16, 1998.

[27] I. R. Kaplan, J. Rasco, and S.-T. Lu, "Chemical Characterization of Transformer Mineral-Insulating Oils" *Environmental Forensics,* vol. 11, pp. 117-145, 2010.

[28] J. w. Jung, Y. b. Lim, J. s. Jung, G. h. Yi, and H. y. Park, "The Analysis of Dielectric Characteristics of Transformer Oil Suffering Ageing Treatment" in *2006 IEEE 8th International Conference on Properties & applications of Dielectric Materials*, Bali, Indonesia, pp. 848-851, 2006.

[29] M. Rafiq, Y. Z. Lv, Y. Zhou, K. B. Ma, W. Wang, C. R. Li*, et al.*, "Use of vegetable oils as transformer oils – a review" *Renewable and Sustainable Energy Reviews,* vol. 52, pp. 308-324, 2015.

[30] Suwarno and J. Marbun, "Effect of thermal aging on the dielectric properties of mixture between mineral oil and natural ester" presented at the TENCON 2015 - 2015 IEEE Region 10 Conference, Macao, China, 2015.

[31] Standard "Loading Guide for Mineral-Oil-Immersed Power Transformers (IEC 60076-7)", ed: British Standards Institution, United Kingdom, p. 88, 2016.

[32] M. Karimian, M. Schaffie, and M. H. Fazaelipoor, "Determination of activation energy as a function of conversion for the oxidation of heavy and light crude oils in relation to in situ combustion" *Journal of Thermal Analysis and Calorimetry,* vol. 125, pp. 301-311, July 01 2016.

[33] B. H. Stuart, *Infrared Spectroscopy: Fundamentals and Applications*: John Wiley & Sons, Ltd, 2004.

[34] F. R. v. d. Voort, A. Al-Alawi, J. Sedman, and A. Ghetler, "Automated FTIR Analysis of Free Fatty Acids or Moisture in Edible Oils" *JALA: Journal of the Association for Laboratory Automation,* vol. 11, pp. 23-29, 2006.

[35] W. S. Struve, *Fundamentals of Molecular Spectrocopy* vol. 1. New York, NY, U.S.A.: John Wiley & Sons, Inc, 1989.

[36] R. N. Clark, J. M. Curchin, T. M. Hoefen, and G. A. Swayze, "Reflectance spectroscopy of organic compounds: 1. Alkanes" *Journal of Geophysical Research: Planets,* vol. 114, p. 1, 2009.

[37] C. J. F. Böttcher and O. C. v. Belle, *Theory of Electric Polarization: Dielectrics in Static Fields* vol. 1. Amsterdam, Netherlands: Elsevier, 1973.

[38] G. G. Raju, *Dielectrics in Electric Fields (Second Edition)*. Basel, Switzerland: Marcel Dekker, Inc, 2003.

[39] Y.-B. Huang, Z.-S. Zhong, and Q. Fu, "Study on Aging Characteristics and Chemical Composition of Hydrogenated Transformer Oil" *Journal of Electrical Engineering & Technology,* vol. 8, 2013.

[40] A. Singh, R. T. Gandra, E. W. Schneider, and S. K. Biswas, "Studies on the Aging Characteristics of Base Oil with Amine Based Antioxidant in Steel-on-Steel Lubricated Sliding" *The Journal of Physical Chemistry C,* vol. 117, pp. 1735-1747, 2013.

[41] S. O. Kasap, *Principles of Electronic Materials and Devices* vol. 3. New York: McGraw-Hill, 2006.

[42] W. F. Schmidt, *Liquid State Electronics of Insulating Liquids*: CRC Press, 1997.

[43] F. Kremer and A. Schönhals, *Broadband Dielectric Spectroscopy* vol. 1: Springer 2003.

[44] Standard "Insulating liquids. Measurement of relative permittivity, dielectric dissipation factor (tan $\delta$) and d.c. resistivity (BS EN 60247:2004)", ed: British Standards Institution, United Kindom, p. 27, 2004.

[45] Y. Du, T. Wu, and J. Cheng, "Age detection of lubricating oil with on-line sensors" presented at the 2015 IEEE Sensors, Busan, Korea, 2015.

[46] D. Yang, X. Zhang, Z. Hu, and Y. Yang, "Oil Contamination Monitoring Based on Dielectric Constant Measurement" in *2009 International Conference on Measuring Technology and Mechatronics Automation,* Zhangjiajie, Hunan, China, China pp. 249-252, 2009.

[47] A. Agoston, N. Dorr, and B. Jakoby, "Online Application of Sensors Monitoring Lubricating Oil Properties in Biogas Engines" in *2006 5th IEEE Conference on Sensors,* pp. 1099-1102, 2006.

[48] U. Kaatze, "Reference liquids for the calibration of dielectric sensors and measurement instruments" *Meas. Sci. Technol,* vol. 18, p. 967, 2007.

[49] J. Ulrych and V. Mentlík, "Dielectric properties of sunflower, rapeseed and commonly used mineral oil" in *2016 17th International Scientific Conference on Electric Power Engineering (EPE),* Prague, Czech Republic p. 44, 2016.

[50] L. Lomba, B. Giner, I. Bandres, C. Lafuente, and M. a. R. Pino, "Physicochemical properties of green solvents derived from biomass" *Green Chemistry,* vol. 13, pp. 2062-2070, 2011.

[51] J. N. Wilson, "The Dielectric Constants of Polar Liquids" *Chemical Reviews,* vol. 25, pp. 377-406, 1939.

[52] M. Tjahjono, T. Davis, and M. Garland, "Three-terminal capacitance cell for stopped-flow measurements of very dilute solutions" *Review of Scientific Instruments,* vol. 78, p. 23902, 2007.

[53] T. A. Prevost, "Dielectric properties of natural esters and their influence on transformer insulation system design and performance " in *2009 IEEE Power & Energy Society General Meeting*, pp. 1-7, 2009.

[54] T. Judendorfer, A. Pirker, and M. Muhr, "Conductivity measurements of electrical insulating oils" in *2011 IEEE International Conference on Dielectric Liquids*, Trondheim, Norway, p. 86, 2011.

[55] N. Perini, A. R. Prado, C. M. S. Sad, E. V. R. Castro, and M. B. J. G. Freitas, "Electrochemical impedance spectroscopy for in situ petroleum analysis and water-in-oil emulsion characterization" *Fuel,* vol. 91, pp. 224-228, 2012.

[56] I. C. Halalay, "Versatile cell for complex permittivity measurements on liquids" *Review of Scientific Instruments,* vol. 70, pp. 3432-3434, 1999.

[57] L. Rae Duk, K. Han Jun, and Y. P. Semenov, "Precise measurement of the dielectric constants of liquids using the principle of cross capacitance" *IEEE Transactions on Instrumentation and Measurement,* vol. 50, pp. 298-301, 2001.

[58] J. D. Piper, D. E. F. Thomas, and C. C. Smith, "Liquid Dielectrics: Effect of Soluble Oxidation Products on Power Factor and Conductivity of Liquid Paraffin" *Industrial & Engineering Chemistry,* vol. 28, pp. 309-312, 1936/03/01 1936.

[59] X. B. Li, S. D. Larson, A. S. Zyuzin, and A. V. Mamishev, "Design principles for multichannel fringing electric field sensors" *IEEE Sensors Journal,* vol. 6, pp. 434-440, 2006.

[60] D. S. Clague and E. K. Wheeler, "Dielectrophoretic manipulation of macromolecules: The electric field" *Physical Review E,* vol. 64, pp. 26605-26613, 2001.

[61] L. Yu Chin and R. A. Moore, "Properties of alternately charged coplanar parallel strips by conformal mappings" *IEEE Transactions on Electron Devices,* vol. 15, pp. 173-180, 1968.

[62] M. W. den Otter, "Approximate expressions for the capacitance and electrostatic potential of interdigitated electrodes" *Sensors and Actuators A: Physical,* vol. 96, pp. 140-144, 2002.

[63] F. I. Mopsik, "Dielectric constant of n-hexane as a function of temperature, pressure, and density " *National Bureau of Standards* vol. 71A, p. 287, 1967.

[64]  A. M. Thompson, "The cylindrical cross-capacitor as a calculable standard" *Proceedings of the IEE - Part B: Electronic and Communication Engineering,* vol. 106, pp. 307-310, 1959.

[65]  D. G. Lampard, "A new theorem in electrostatics with applications to calculable standards of capacitance" *IET,* vol. 104, pp. 271-280, 1957.

[66]  Y. Sun, Y. Tu, J. Sun, and D. Niu, "Effect of temperature and composition on thermal properties of carbon steel" in *2009 Chinese Control and Decision Conference,* Guilin, China pp. 3756-3760, 2009.

[67]  Y. Araki, "Thermal expansion coefficient of polytetrafluoroethylene in the vicinity of its glass transition at about 400°K" *Journal of Applied Polymer Science,* vol. 9, pp. 421-427, 1965.

[68]  Y. Araki, "Transitions of polytetrafluoroethylene at about 90 and 130°C. studied by x-ray diffraction and infrared spectra" *Journal of Applied Polymer Science,* vol. 11, pp. 953-961, 1967.

[69]  H. Kirk, H. Ludewig, L. Mausner, N. Simos, P. Thieberger, R. Weggel*, et al.,* "Super-Invar as a target for a pulsed high-intensity proton beam" in *Proceedings of the 2003 Particle Accelerator Conference,* Portland, OR, USA pp. 1628-1630 vol.1623, 2003.

[70]  F. D. Klingler and W. Ebertz, "Oxocarboxylic Acids" in *Ullmann's Encyclopedia of Industrial Chemistry.* vol. 1, ed: Wiley-VCH Verlag GmbH & Co. KGaA, 2000.

[71]  W. M. Haynes, *CRC Handbook of Chemistry and Physics* vol. 97. Boca Raton, FL, U.S.A.: CRC Press, 2016.

[72]  Y. Shen, J.-K. Sun, Y.-X. Yi, B. Wang, F. Xu, and R.-C. Sun, "One-pot synthesis of levulinic acid from cellulose in ionic liquids" *Bioresource Technology,* vol. 192, pp. 812-816, 2015 2015.

[73]  E. Mladenov, S. Staykov, and G. Cholakov, "Water saturation limit of transformer oils" *IEEE Electrical Insulation Magazine,* vol. 25, pp. 23-30, 2009.

[74]  E. A. Davis, *Electronic Properties of Non-Crystalline Semiconductors.* Dordrecht: Springer Netherlands, 1984.

[75]  S. Cao, S. Pyatt, C. Anthony, A. Kubba, A. Kubba, and O. Olatunbosun, "Flexible Bond Wire Capacitive Strain Sensor for Vehicle Tyres" *Sensors,* vol. 16, pp. 929-946, 2016.

[76]  P. M. M. a. H. Feshbach, *Methods of Theoretical Physics* vol. 1. New York: McGraw-Hill, 1953.

[77]  M. Khan and S.-W. Kang, "Highly Sensitive Temperature Sensors Based on Fiber-Optic PWM and Capacitance Variation Using Thermochromic Sensing Membrane" *Sensors,* vol. 16, pp. 1064-1078, 2016.

[78]    Standard "Paper and board - Determnination of tensile properties - Part 2: Constant rate of elongation method (ISO 1924-2:2008)", ed. Bruessles: CEM European Committee for Standardization, Bruessels, p. 10, 2008.

[79]    M. Duval, A. D. Pablo, I. Atanasova-Hoehlein, and M. Grisaru, "Significance and detection of very low degree of polymerization of paper in transformers" *IEEE Electrical Insulation Magazine,* vol. 33, pp. 31-38, 2017.